NASA CR-72378
AGC-7977-T1

INDUCER DYNAMICS
FULL-FLOW, FULL-ADMISSION HYDRAULIC TURBINE DRIVE

By

J. Farquhar
B. K. Lindley
E. B. McKinney
G. K. Olson
P. S. Buckmann

Prepared for

National Aeronautics and Space Administration

Contract NAS 3-7977

AEROJET-GENERAL CORPORATION

SACRAMENTO, CALIFORNIA

Requests for copies of this report should be referred to:

National Aeronautics and Space Administration
Office of Scientific and Technical Information
Attention: AFSS-A
Washington, D. C. 20546

NASA CR-72378
AGC-7977-T1

TECHNOLOGY REPORT

INDUCER DYNAMICS

FULL-FLOW, FULL-ADMISSION HYDRAULIC TURBINE DRIVE

Interim Report for Tasks I, II, and III

Prepared for

NATIONAL AERONAUTICS AND SPACE ADMINISTRATION

CONTRACT NAS 3-7977

Prepared by:

AEROJET-GENERAL CORPORATION
LIQUID ROCKET OPERATIONS
SACRAMENTO, CALIFORNIA

AUTHORS: J. Farquhar
Project Engineer

B. K. Lindley
Pump Design

E. B. McKinney
Turbine Design

G. K. Olson
System Dynamics

P. S. Buckmann
Bearing Design

APPROVED: W. W. Heath
Project Manager

Technical Management:

NASA LEWIS REASEARCH CENTER
CLEVELAND, OHIO

APPROVED: W. A. Rostafinski
Large Engine Technology
Branch
Project Manager

ABSTRACT

This report describes the work performed by the Liquid Rocket Operations, Aerojet-General Corporation, Sacramento, California, to complete Tasks I, II, and III of Contract NAS 3-7977 (Inducer Dynamics - Full-Flow, Full-Admission Hydraulic Turbine Drive), which is under the cognizance of the NASA Lewis Research Center, Cleveland, Ohio.

Contractual effort was initiated during March 1967 and is scheduled for completion during September 1968. The three tasks described herein encompass the hydrodynamic and mechanical design layout; the formulation and demonstration of both the pumping system and the test facility steady-state as well as transient performance computer models; and the parametric studies performed using these computer models.

A two-speed inducer system was designed. The low-speed inducer is driven by a hydraulic turbine, the power source for which is the flow supplied by a rotor connected to a high-speed drive. The high-speed rotor blading is mounted between the low-speed inducer and the turbine blading. Essentially, all of the delivered flow passes through each row of blades. The system is designed to operate in liquid hydrogen at a flow rate of 4900 gpm with a net positive suction head at 25 ft and an over-all cavitating head rise of 5453 ft. The high-speed rotor is designed to operate at 44,500 rpm while the low-speed rotor is designed to operate at 18,800 rpm.

The remaining three tasks in the contract (IV, V, and VI) consist of the detailed design and fabrication of a test unit followed by both steady-state and transient demonstration tests in water at high-speed rotor speeds (up to 8500 rpm). The results from these tests will be used to refine and verify the analytical performance models.

TABLE OF CONTENTS

TABLE OF CONTENTS (cont.)

TABLE OF CONTENTS (cont.)

APPENDICES

LIST OF TABLES

LIST OF FIGURES

LIST OF FIGURES (cont.)

LIST OF FIGURES (cont.)

LIST OF FIGURES (cont.)

I. SUMMARY

The objective of the Inducer Dynamics - Full-Flow, Full-Admission Hydraulic Turbine Drive Program is to formulate an analytical computer model for the transient performance of a two-speed inducer system that is hydraulically designed for liquid hydrogen. This model will be experimentally verified using water as the test fluid. Three of the six program tasks have been completed and the accomplishments in Tasks I, II, and III are summarized in the following discussions.

A. TASK I - HYDRODYNAMIC DESIGN AND MECHANICAL LAYOUT

A two-speed inducer system was designed. The low-speed inducer is driven by a hydraulic turbine, the power source for which is the flow supplied by a rotor connected to a high-speed drive. The high-speed rotor blading is mounted between the low-speed inducer and the turbine blading. Essentially, all of the delivered flow passes through each row of blades. The design parameters are as follows:

NPSH - 25 ft (LH_2)
Flow Rate - 4900 gpm
High-Speed Shaft Rotational Speed - 44,500 rpm
Low-Speed Shaft Rotational Speed - 18,800 rpm
Head Rise (Cavitating) - 5435 ft
Efficiency (Cavitating) - 61.3%

The design layout for an 8500 rpm high-speed shaft water test demonstration unit was completed. The low-speed shaft of this assembly is supported by hydrostatic bearings and can be braked by means of a Prony Brake to alter the normal operating speed ratio. This Prony Brake also is designed to be utilized as a dynamometric device for measuring torque. In addition, design layouts were completed of the assemblies for driving the high-speed shafts with an electric motor for steady-state testing and with a gaseous nitrogen turbine for transient testing. The test unit is designed to permit its conversion to liquid hydrogen operation without any need for major modifications.

B. TASK II - FORMULATION AND DEMONSTRATION OF COMPUTER SIMULATION

A model was formulated which describes the design and off-design pumping system performance. Along with this model, an associated digital computer Fortran IV program was formulated for use with the IBM 360 Model 65 computer. This program also is compatible with the Model 67 computer.

The steady-state and transient dynamics of the flow of fluids in lines that are external to the pumping system are described using the method of characteristics to evaluate an elastic column "waterhammer" model. An adequate number of test cases were run to verify the capability of the model and the computer program. In this program, the major content parameters are plotted automatically as functions of time.

C. TASK III - PARAMETRIC STUDIES

Parametric studies were accomplished to evaluate the following:

1. Changes in the high-speed rotor speed ramp rate.
2. Changes in the mass moment of inertia of the low-speed inducer and hydraulic turbine.
3. Changes in the pump suction pressures.
4. Changes in the suction line geometry.
5. Changes in the discharge line geometry.
6. Changes in the discharge valve position.
7. Changes in the fluid acoustic velocity.
8. Changes in the pumping system size.

Start transients wherein the system operates at relatively high flow coefficients (flow rate/speed ratios) were evaluated. These were selected as being representative of typical liquid rocket engines operating under a "tank-head" start condition.

D. MAJOR CONCLUSIONS AND RECOMMENDATIONS

Based upon the results from Tasks I, II, and III, the following are the major conclusions and recommendations.

1. Torque/speed matching characteristics of the low-speed inducer and hydraulic turbine must be evaluated to ensure stable (hydraulically-locked) system operation.

2. Lower head rise (under 5000 ft) designs have more conventional high-speed rotor blade geometries and can be more easily mated to the downstream pumping elements.

3. Parametric study cases for one type of liquid rocket engine start transient ("tank-head" type) were evaluated. Other types of starting, particularly those where the pumping system is operated at low or zero flow coefficient, are recommended for further investigation.

4. The pumping system exhibited satisfactory operation for engine start transients through initial "bootstrapping" of the low-speed shaft assemblies. Flow rate convergence problems were experienced while the pump was accelerating to the final operating point. While it was established that

this problem was not caused by hydrogen compressibility effects, the cause of the problem was not isolated. A radial vane impeller, centrifugal pump was used as the main stage pumping element and it is possible the steepness of the head flow curve at high flow coefficient conditions contributed to the convergence difficulty. Further investigation of the effect of this type of main stage pumping system upon staging characteristics appears to be warranted as a result of this experience.

The three remaining tasks in the contract (IV, V, and VI) consist of the detailed design and fabrication of a test unit followed by both steady-state and transient demonstration tests in water at high-speed rotor speeds (up to 8500 rpm). The results from these tests will be used to refine and verify the analytical performance models.

II. INTRODUCTION

This report delineates the work performed by the Liquid Rocket Operations, Aerojet-General Corporation, Sacramento, California, to complete Tasks I, II, and III of Contract NAS 3-7977 (Inducer Dynamics - Full-Flow, Full-Admission Hydraulic Turbine Drive), which is under the cognizance of the NASA Lewis Research Center, Cleveland, Ohio.

Contractual effort was initiated during March 1967 and is scheduled for completion during September 1968. The three contractual tasks described herein are as follows:

Task I - Hydrodynamic Design and Mechanical Layout of Hydraulic-Turbine-Driven Low-Speed Inducer/High-Speed Inducer Pump System

Task II - Formulation and Demonstration of Computer Simulation to Predict Transient and Steady-State Behavior

Task III - Parametric Studies

The remaining three contractual tasks are as follows:

Task IV - Detailed Design

Task V - Fabrication

Task VI - Pump System Tests to Determine Performance and to Develop the Computer Simulation

The full-flow, hydraulic-turbine-driven inducer concept, which is shown on Figure No. 1, incorporates a two-speed power transmission and pumping system. The low-speed inducer is driven by a hydraulic turbine, the power source for which is the flow supplied by a rotor connected to a high-speed drive. The high-speed rotor blading is mounted between the low-speed inducer and the turbine blading. Essentially, all of the delivered flow passes through each row of blades. In a rocket engine feed system, the high-speed rotor would be attached directly to the main pump rotor. The operation of the low-speed inducer at speeds below those of the main pump results in feed system NPSH requirements that are less than those of the directly-coupled inducer systems.

The full-flow, hydraulic-turbine-driven inducer concept has been considered for the advanced NERVA nuclear rocket application(1)(2). Designs of

---

(1) Beveridge, J. H., Campbell, W. E., and Fitts, J. J., <u>NPSP Selection for a Nuclear Rocket</u>, AIAA Paper 67-467, July 1967

(2) Campbell, W. E., et al., (U) <u>NPSP Evaluation</u>, Aerojet-General Report RN-S-388, March 1967 (Confidential Report)

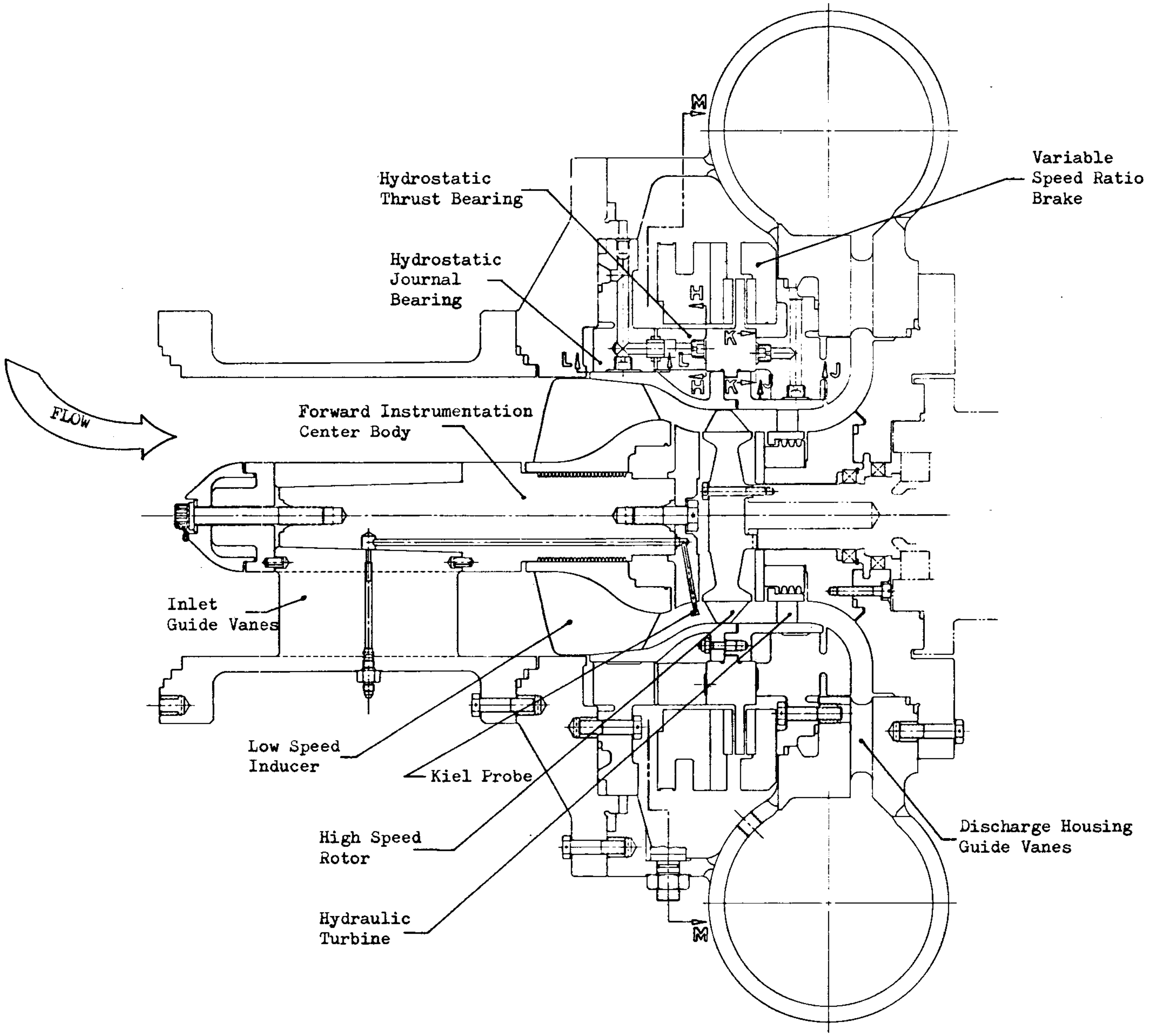

Figure 1. Full-Flow, Hydraulic-Turbine-Driven Inducer (Axial Section)

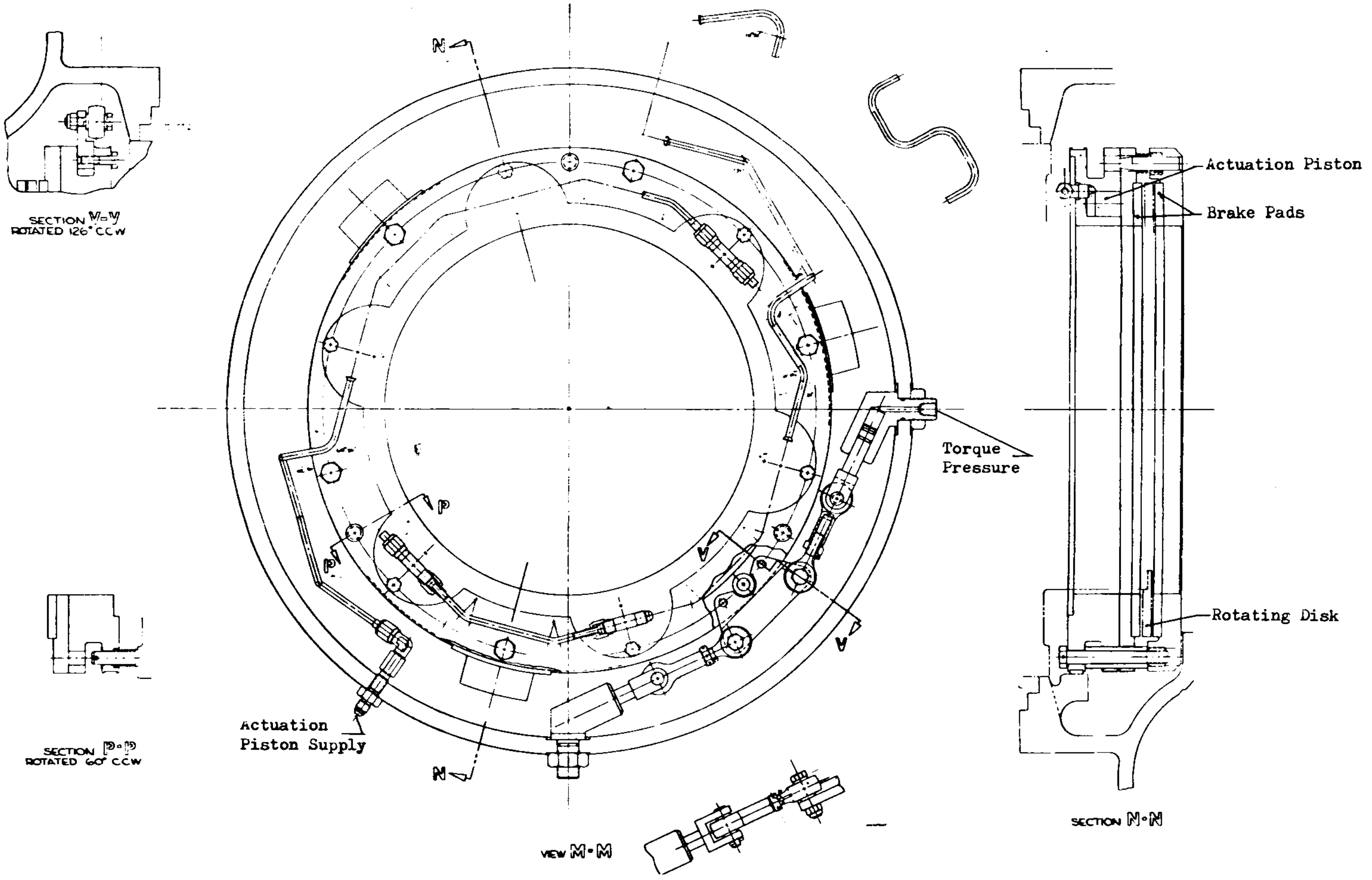

Figure 1. Full-Flow, Hydraulic-Turbine-Driven Inducer
(Prony Brake Radial Section)

this type also are being considered for the Aerospike Nozzle Concept in the Advanced Cryogenic Rocket Engine Program(3).

Aerojet-General has previously designed, built, and tested hydraulic-turbine-driven inducers wherein the hydraulic turbine operated using only a portion of the delivered flow(4), which is supplied by means of recirculation from the main stage pump. The test program associated with these pumps consisted of steady-state tests at Aerojet-General and transient tests conducted by the Air Force Rocket Propulsion Laboratory(5) using the same hardware.

Testing of the inducer during Task VI will be accomplished using water as the test fluid; however, the unit will be designed so as to comply with the specification in the contract that the design of the test unit will be such that testing in liquid hydrogen can be accomplished without extensive modifications. These Task VI pump system tests will involve both steady-state and transient testing. The steady-state operating range of the pump will be from 80% to 120% of the nominal design flow coefficient (flow rate/shaft speed) with the high-speed shaft operating at speeds of up to 8500 rpm.

The contractual requirements for the test system hydraulic design point are:

Fluid:	Liquid Hydrogen
Flow Rate:	4900 gpm to 11,400 gpm
Minimum Head Rise:	5000 ft (at hydraulic turbine exit)
Net Positive Suction Head:	25 ft
Off-Design Performance:	To 120% of design flow coefficient (flow rate/high-speed shaft speed) without cavitation in the high-speed rotor when operating at design speed

The ensuing sections of this report detail the technical effort for Tasks I, II, and III as well as present the conclusions and recommendations resulting from this effort.

---

(3) Lary, F. B., (U) Advanced Cryogenic Rocket Engine Program, Aerospike Nozzle Concept, Contract AF 04(611)-11399, Quarterly Progress Reports, RPL TR-66-138, June 1966; RPL TR-66-242, September 1966; RPL TR-66-348, December 1966; RPL TR-67-91, March 1967; RPL TR-67-188, June 1967 (Confidential Reports)

(4) (U) Phase II Final Report on the Design and Evaluation of a Low Speed Hydraulic Turbine-Driven, Pump Discharge Fed Inducer Stage, Aerojet-General Corp., Sacramento, California; Contract AF 04(611)-7446 (Confidential Report)

(5) Chlapek, J. D., Start Transient Testing of a Low-Speed Hydraulic Turbine Driven Inducer Stage in Combination with a Rocket Engine Turbopump, Report AFRPL-TR-66-124, June 1966

III. TASK I - HYDRODYNAMIC DESIGN AND MECHANICAL LAYOUT

The design of the demonstration test unit is detailed in this section. The design effort was divided into the following three subtasks:

- Hydraulic design of a hydrogen test unit.
- Design of a water test unit driven by an electric motor to be used for the steady-state performance testing.
- Design of a water test unit driven by a gas turbine to be used for the transient performance testing.

The detailed design, fabrication, and testing of these water test units will be accomplished during the remaining program tasks.

A modified MARK III, MOD 4 NERVA Experimental Engine turbopump turbine will be used to drive the water test unit for the transient testing. Only the first stage of this two-stage turbine will be used with gaseous nitrogen at ambient temperature as the driving fluid. In addition, the turbopump/bearing housing will be modified to accept grease-packed bearings.

Adequate design work has been accomplished to ensure that the test unit can be converted to liquid hydrogen testing without need for any extensive modifications. The single-stage turbine would be utilized in combination with the unmodified, liquid-hydrogen-lubricated bearing system. However, the maximum operating speed of the turbine is approximately two-thirds that of the selected hydrogen hydraulic design speed as a result of turbine stress and vibration limitations.

A. DESIGN POINT SPECIFICATION

1. Over-All Performance

The following values were selected as a design point:

Flow rate:	4900 gpm
High-Speed Shaft Speed:	44,500 rpm
Head Rise (Cavitating):	5435 ft

The contractually-required minimum flow rate was selected to minimize liquid hydrogen consumption for potential hydrogen test applications. In addition, the selection of this flow rate permits partial-speed testing of the full-scale hardware in available test facilities.

An analysis of existing as well as planned hydrogen pumps was made to select the high-speed shaft rotational speed. A preliminary value of 30,000 suction specific speed was selected for the low-speed inducer based upon the use of working fluids without thermodynamic vapor head depression characteristics. However, the contractually-specified NPSH of 25 ft is for hydrogen, which exhibits head depression characteristics; therefore, a correction of 80 ft was applied to obtain a value of 105 ft. This latter value was used for the calculations of suction specific speed. Both the 30,000 suction specific speed and 80 ft liquid hydrogen head depression values are representative of current liquid hydrogen inducer design values. The 80 ft value was used in designing the M-1 engine fuel pump.(6)

An equivalent low-speed inducer speed was calculated for each of the pumps shown on Table I using the above indicated values and flow rates. The ratio of turbopump speed to low-speed inducer speed also was calculated using the actual operating speeds of the turbopumps. Then, the various pumps were categorized by speed ratio as shown on Table II. A speed ratio of 3.15 (corresponding to that obtained in a large NERVA turbopump study) was selected as being representative of current turbopump applications. The high-speed shaft design rotational speed was calculated using the selected design flow rate and based upon the 3.15 speed ratio, the low-speed inducer suction specific speed of 30,000, and the 105 ft NPSH values.

Further analysis, subsequently discussed, indicate that the full-flow inducer device would not operate in a stable condition (low-speed inducer speed hydraulically-locked to the high-speed rotor speed) at the originally selected design speed ratio of 3.15. Reduced design speed ratios were required to obtain stable operation. Rather than alter the selected high-speed shaft speed, the low-speed inducer speed was increased. This corresponds to a suction specific speed increase from 30,000 to 40,000, and a speed ratio decrease of from 3.15 to 2.37. Analysis indicates that stable operation is obtained at this condition.

An evaluation of typical boost pumping system head rise requirements was made to ascertain a suitable design head rise value. Table III summarizes the results. The contractual minimum requirement of 5000 ft is a reasonable intermediate value for the various possible applications. A non-cavitating head rise value of 5600 ft was selected to establish blade mean line design parameters. The additional 600 ft of head was added to allow for low-speed inducer head loss resulting from cavitation; the differences between the preliminary mean line and the final blade element, integrated head rise; and prediction uncertainties. The final cavitating head rise obtained from blade element predictions is 5435 ft (see Section III,B).

---

(6) Farquhar, J. and Lindley, B. K., Hydraulic Design of the M-1 Liquid Hydrogen Turbopump, NASA CR-54822, 15 July 1966.

TABLE I

SHAFT SPEED RATIO FOR DUAL PUMP CONCEPT APPLIED TO CURRENT AND FUTURE LIQUID HYDROGEN ROCKET ENGINES

STATUS	LIQUID HYDROGEN HIGH SPEED TURBOPUMPS	APPROX. VOLUMETRIC FLOW RATE (GPM)	HIGH SPD. TURBOPUMP APPROX. SHAFT SPEED (RPM)	PARAMETER(S) LIMITING FURTHER INCREASE OF SHAFT SPEED	SHAFT SPEED(1) LOW SPEED INDUCER (RPM)	SHAFT SPEED RATIO(2)
TESTED UNITS	RL10 Fuel Pump	600	28,400	Pinion Gear Speed/Load	40,000	0.7
	NERVA I Turbopump (Contract SNP-1)	7,600	22,500	Turbine Stress	11,300	2.0
	J-2 Fuel Turbopump (Contract NAS 8-19)	7,300	25,600	Critical Speed	11,000	2.3
	Mark 25 Turbopump (Phoebus Program)	10,000	34,000	Turbine Stress Bearing Speed/Load Critical Speed	9,800	3.4
	M-1 Fuel Turbopump (Contract NAS 3-2555)	60,000	13,200	Turbine Stress Bearing Speed/Load Critical Speed Pump Rotor Stress	4,000	3.3
STUDY UNITS	Fuel Turbopump 250K AGC Study Engine (1965)	8,600	47,500	Turbine Stress Bearing Speed/Load Critical Speed	10,600	4.5
	Advanced J-2 Fuel Turbopump (Typical, 1966)	10,300	28,000	Turbine Stress	9,700	2.9
	HG-3 Fuel Turbopump (Contract NAS 8-11427)	11,000	37,300	Turbine Stress Bearing Speed/Load	9,400	4.0
	NERVA Large Turbopump Study (Contract SNP-1)	33,000	17,000	Turbine Stress Critical Speed Bearing Speed/Load	5,400	3.15

(1) Shaft speed based upon a suction specific speed of 30,000, a net positive suction head of 25 feet plus a thermodynamic head depression correction of 80 feet.

(2) Ratio main pump rotor speed to low speed inducer rotational speed.

TABLE II

CATEGORIES OF TURBOPUMPS ADAPTABLE TO DUAL-SPEED PUMP CONCEPTS

Category No.	Category Descriptions	Rocket Engine Designation and Type	Pump Speed Ratio*
1	Turbopumps not suitable for dual-speed pump concept because of gearing constraints of high-speed turbomachinery.	RL-10, LO_2/LH_2 Engine	0.7
2	Turbopumps suited for dual-speed pump concept (conservative turbomachinery technology).	NERVA Technology, Nuclear Engine	2.0
		J-2, LO_2/LH_2 Engine	2.3
3	Turbopumps suited for dual-speed pump concept (current turbomachinery technology).	Advanced J-2, LO_2/LH_2 Engine Large NERVA Turbopump Study, Nuclear Engine M-1, LO_2/LH_2 Engine "KIWI", Non-Flight Nuclear Engine	2.9 3.15 3.3 3.4
4	Turbopumps suited for dual-speed pump concept (advanced turbomachinery technology).	H-3 Study Engine	4.0
		Aerojet-General Advanced LO_2/LH_2 Study Engine	4.5

---

*Ratio of main pump speed to inducer pump speed.

TABLE III

TYPICAL MAIN STAGE HIGH-SPEED PUMP PARAMETERS

	Type of Main Stage Pump		
	Centrigugal or Axial with 20,000 Suction Specific Speed Inducer	Centrifugal or Axial With 5000 ft Head Rise Full Flow Inducer System	Axial with No Inducer or Transition Type Inlet Staging
Flow Rate, gpm	4900	4900	4900
Main Stage Pump Speed, rpm	44,500	44,500	44,500
Low-Speed Inducer Speed, rpm	18,800	18,800	18,800
Low-Speed Inducer Suction Eye Diameter, in.	7.72	7.72	7.72
Main Stage Pump Suction Eye Diameter, in.	3.9	3.9	3.9
Main Stage Pump Suction Eye Blade-Root Diameter, in.	1.95	1.95	3.22
Inducer System Head Rise Requirement	1100	5000	8700

2. Stage Work Split Selection

The following factors were considered in selecting the stage work split:

- stage efficiency and blade loading
- interstage power/speed matching characteristics
- stage cavitation

Analyses were conducted using blade mean line calculations. Design is restricted to staging, which consisted of rotors only because preliminary analyses indicated that stators offered no significant design point performance advantage while they reduced off-design cavitation performance capability. The presence of stators in the staging also complicates the mechanical design (see Section III,II,C). To further simplify design and fabrication of the test unit, the high-speed rotor blade and the hydraulic turbine blade annulus dimensions were made identical (i.e., blade height and mean line radius were equal and constant). Preliminary analyses indicated that reasonable designs could be achieved with such geometries.

a. Stage Efficiency and Blade Loading

For the low-speed inducer stage, available test data for inducers were correlated by plotting loss coefficient and relative velocity retardation factor versus theoretical head coefficient as shown on Figure No. 2. The parameters are defined as:

$$\overline{\omega} = (H_{ideal} - H_{actual})/(W_{1m}^2/2g)$$

$\overline{\omega}$ - loss coefficient

H_{ideal} - ideal (isentropic) head rise, ft

H_{actual} - actual head rise, ft.

W_{1m} - inlet mean (rms radius) relative velocity, ft/sec

g - acceleration due to gravity, ft/sec^2

$\Psi_{ideal} = H_{ideal}/U_{2m/g} = Cu_2/U_{2m}$ - ideal head coefficient

Cu_{2m} - exit mean (rms radius) tangential absolute velocity, ft/sec

U_{2m} - exit mean rotor velocity, ft/sec

W_{2m}/W_{1m} - relative velocity retardation factor

W_{2m} - exit mean relative velocity, ft/sec

W_{1m} - inlet mean relative velocity, ft/sec

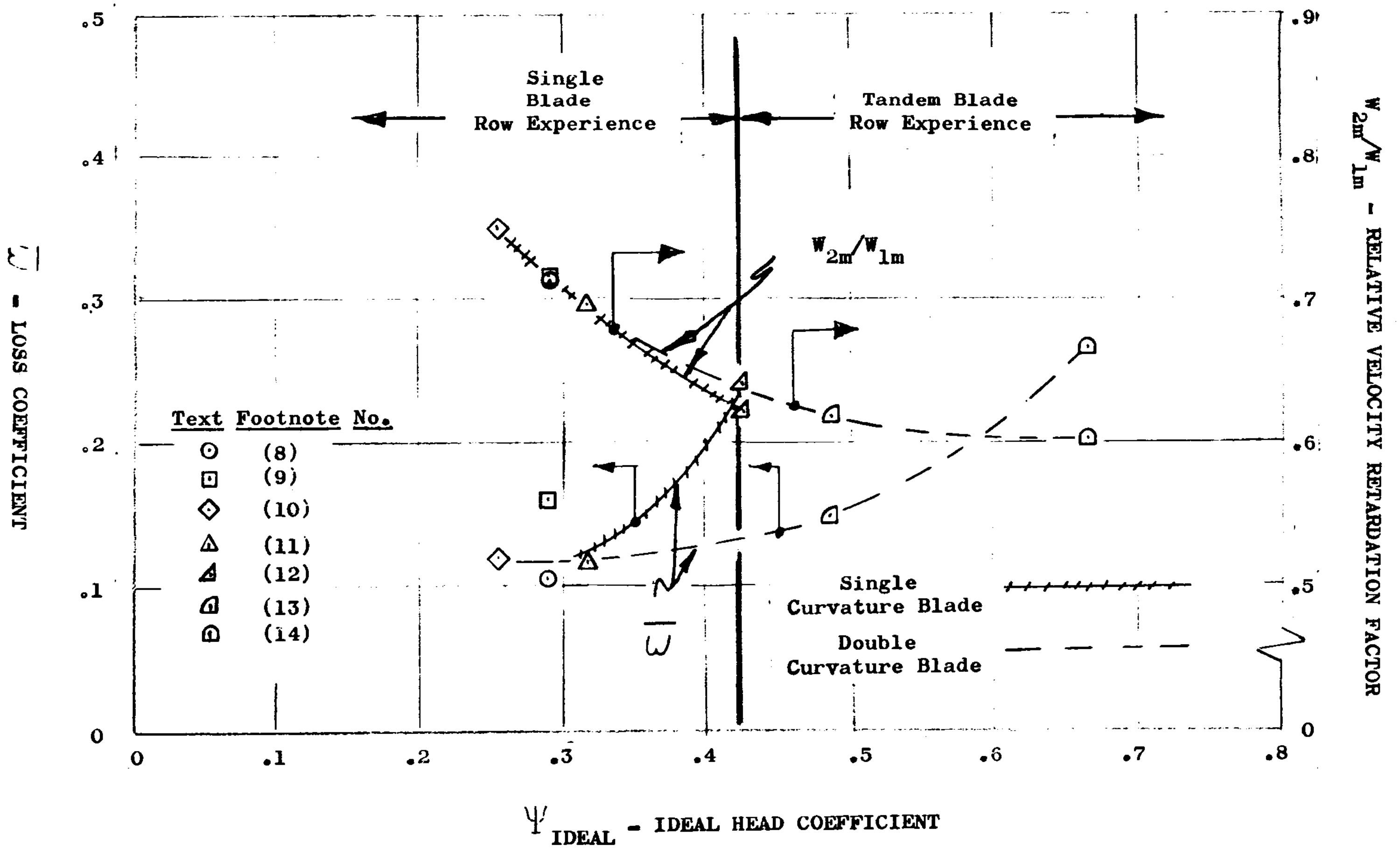

Figure 2. Loss Coefficient and Relative Velocity Retardation Factor vs Ideal Head Coefficient - Inducer Type Inlet Staging

The relative velocity factor was utilized, rather than the diffusion factor, D,(7)to simplify calculations. Because of the low coefficients, high blade stagger angles, and larger secondary flows in inducers, there appeared to be no advantage in using the more rigorous two-dimensional correlation. Data for helical inducers(8)(9)(10)(11) and inducers with larger head rise, including single blade row(12)and tandem blade row(13)(14)designs are shown. The cross-hatched line represents single curvature (straight element) blades and includes helical inducers as well as the cambered M-1 fuel pump(15). The dashed lines represent the tandem row designs having double curvature blading in the vane exit regions. These dashed lines were utilized to establish losses for the stage loading considered in the work split analysis. Ideal head coefficients for .29 to 0.5 were considered. The lower value is a typical one for helical inducers while the higher value represents a tandem row design.

---

(7) Lieblein, S., Schwenk, F. C., and Broderick, R. L., Diffusion Factor for Estimating Losses and Limiting Blade Loadings in Axial-Flow Compressor Blade Elements, NASA RME53D01, 8 June 1953

(8) Anderson, D. A., Soltis, R. F., and Sandercock, D. M., Performance of 84° Flat-Plate Helical Inducer and Comparison with Performance of Similar 78° and 80.6° Inducers, NASA TN D-2553, December 1964

(9) Acosta, A. J., "An Experimental Study of Cavitating Inducers," Second Symposium on Naval Hydrodynamics, Washington, D. C., August 1958

(10) Sandercock, D. M., Soltis, R. F., and Anderson, D. A., Cavitation and Non-Cavitation Performance of an 80.6° Flat-Plate Helical Inducer at Three Rotational Speeds, NASA TN D-1439, November 1962

(11) Sandercock, D. M., Soltis, R. F., and Anderson, D. A., Investigation of the Performance of a 78° Flat-Plate Helical Inducer, NASA TN D-1170, March 1962

(12) Lindley, B. K., Test Report, M-1 Fuel Subscale Pump Water Tests 1.2-05-EHP-008 through 019 (Inducer Stage, Transition Stage Configuration). Aerojet-General Report TPR 0028, August 1965

(13) Sandercock, D. M. and Crouse, J. E., Design and Over-All Performance of a Two-Stage Axial-Flow Pump with a Tandem-Row Inlet Stage, NASA TN D-2879, June 1965

(14) Edlebeck, N. A., "(U) The Design and Testing of Axial-Flow Blading for High-Head, High Capacity Liquid Hydrogen Pumps," AIAA Propulsion Specialists Conference, Colorado Springs, Colorado, June 1965 (Confidential Paper)

(15) Lindley, B. K., Aerojet-General Report TPR 0028, op. cit.

Conventional axial-flow compressor blade correlations of the total pressure loss parameter with diffusion factor D(16) were used for the high-speed rotor analysis. The loss parameter is defined as follows:

$$\bar{\omega} \frac{\cos\beta_2}{2\sigma}$$

$\bar{\omega}$ - loss coefficient as defined previously for inducer blading

β_2 - blade exit relative flow angle (measured from axial direction), degrees

σ - blade solidity (chord length blade space)

Existing values(17) for streamlines other than those near the rotor tip were increased by 23% to account for the tip loss effects shown for the outer streamlines.

The hydraulic efficiency of the hydraulic turbine was estimated using a fixed total head loss coefficient (based upon exit mean radius relative velocity) of .177. In addition, a leakage factor of .975 (ratio of power actually obtained to power obtained from velocity diagram calculations) was utilized. Experience with the design(18) and testing(19) of turbines having a moderate degree of reaction indicates that these are reasonable values.

b. Interstage Power/Speed Matching Characteristics

To evaluate the stage matching characteristics of the system, it was assumed that the exit relative velocity of each blade row was constant regardless of the operating flow coefficient.

Writing the expression for the low-speed inducer/turbine energy balance at design or off-design flow coefficient assuming zero inlet whirl to the inducer stage as follows:

$$U_i \, Cu_i + \frac{K \, U_i^2}{(\phi/\phi_D) \, R_R} = TLFF \left(\frac{N_i}{N_R} \, U_R \, C_{uR} - U_T/Cu_T \right)$$

---

(16) Lieblein, S., et. al., NASA RME 53D01, op. cit.

(17) Aerodynamic Design of Axial-Flow Compressors, NASA Sp-36, 1965, Figure 203

(18) Beer, R., Aerodynamic Design and Estimated Performance of a Two-Stage Curtis Turbine for the Liquid Oxygen Turbopump of the M-1 Engine. NASA CR-54764, 1965

(19) Roelke, R. J., Stable, R. G., and Evans, D. G., Cold Air Performance Evaluation of Scale Model Oxidizer Pump Drive Turbine for the M-1 Hydrogen-Oxygen Rocket Engine. NASA TN D-3368, March 1966

U - tangential rotor velocity at mean diameter, ft/sec

Cu - fluid exit tangential velocity, ft/sec

N - rotor speed, rpm

R - ratio of actual high-speed rotor/low-speed rotor rotational speed to design point high-speed rotor/low-speed rotor rotational speed

K - factor to account for low-speed shaft parasitic losses (mechanical and shroud or film bearing fluid friction), ft/sec

ϕ - flow coefficient (C_m/u)

Cm - fluid axial velocity

TLFF - turbine leakage flow factor

Subscripts:

D - refers to design point value

i - refers to low-speed inducer

R - refers to high-speed rotor

T - refers to hydraulic turbine

To simplify calculations, the second term on the left side of the equation, which accounts for non-pumping losses, is assumed to be independent of the flow coefficient but proportional to the speed squared. Fluid and mechanical friction effects do not follow such a speed relationship; however, the assumption follows the usual dynamic similarity assumptions and is sufficiently accurate for analyses in the region of design operating speed

Dividing the above expression by U_i^2 to obtain a relationship in terms of ideal head coefficients, based upon inducer wheel velocity:

$$\frac{Cu_i}{U_i} + \frac{K}{(\phi/\phi_D)_R \, R} = \text{TLFF} \left(\frac{r_R}{r_i} \frac{Cu_R}{U_i} - \frac{r_T}{r_i} \frac{Cu_T}{U_i} \right)$$

r - mean line radius

Writing expressions for the individual blade row ideal head coefficinet-flow coefficient relationships as follows:

$$\frac{Cu_i}{U_i} = 1 - \left(\frac{\phi}{\phi_D}\right)_R R \left[1 - \left(\frac{Cu}{U}\right)_{Di}\right]$$

$$\frac{Cu_R}{U_i} = \frac{N_R \, r_R}{N_i \, r_i} \left\{1 - \left(\frac{\phi}{\phi_D}\right)_R \left[1 - \left(\frac{Cu}{U}\right)_{DR}\right]\right\}$$

$$\frac{Cu_T}{U_i} = \frac{r_T}{r_i} \left\{1 - \left(\frac{\phi}{\phi_D}\right)_R R \left[1 - \left(\frac{Cu}{U}\right)_{DT}\right]\right\}$$

Substituting the above three relationships into the ideal head coefficient expression:

$$1 - \left(\frac{\phi}{\phi_D}\right)_R R \left[1 - \left(\frac{Cu}{U}\right)_{Di}\right] + \frac{K}{(\phi/\phi_{DR})R}$$

$$= \mathrm{TLFF}\left\{\frac{N_R}{N_i}\left(\frac{r_R}{r_i}\right)^2 \left\{1 - \left(\frac{\phi}{\phi_D}\right)_R R \left[1 - \left(\frac{Cu}{U}\right)_{DR}\right]\right\}\right.$$

$$\left. - \left(\frac{r_T}{r_i}\right)^2 \left\{1 - \left(\frac{\phi}{\phi_D}\right)_R R \left[1 - \left(\frac{Cu}{U}\right)_{DT}\right]\right\}\right\}$$

At the design point $(\phi/\phi_D)_R = R = 1$ and the above expression can be simplified and solved for N_R/N_i to obtain:

$$\frac{N_R}{N_i} = \left(\frac{N_R}{N_i}\right)_D = \frac{\frac{1}{\mathrm{TLFF}}\left[\left(\frac{Cu}{U}\right)_{Di} + K\right] + \left(\frac{r_T}{r_i}\right)^2 \left(\frac{Cu}{U}\right)_{DT}}{\left(\frac{r_R}{r_i}\right)^2 \left(\frac{Cu}{U}\right)_D}$$

The above expression can be used together with the definition of R

$$N_R/N_i = (N_R/N_i)_D \; R$$

to eliminate N_R/N_i from the general energy balance equation to obtain a quadratic expression in R, the normalized speed ratio parameter. The equation then can be solved for R to obtain a general expression in terms of blade row geometry, design point parameters, and normalized high-speed rotor flow coefficient:

$$R = \frac{-B + \sqrt{B^2 - 4AC}}{2A}$$

$$A = \left(\frac{N_R}{N_i}\right)_D \left(\frac{r_R}{r_i}\right)^2 - \left(\frac{\phi}{\phi_D}\right)_R D$$

$$D = \left(\frac{N_R}{N_i}\right)_D \left(\frac{r_R}{r_i}\right)^2 \left[1 - \left(\frac{Cu}{U}\right)_{DR}\right] - \left(\frac{r_T}{r_i}\right)^2 \left[1 - \left(\frac{Cu}{U}\right)_{DT}\right] - \frac{1}{TLFF}\left[1 - \left(\frac{Cu}{U}\right)_{Di}\right]$$

$$B = -\frac{1}{TLFF} - \left(\frac{r_T}{r_i}\right)^2$$

$$C = \frac{-K}{\left(\frac{\phi}{\phi_D}\right)_R TLFF}$$

The relationships derived above define general design and off-design high-speed shaft/low-speed shaft rotational speed ratio values; however, the torque speed matching characteristics of the low-speed shaft components must be examined to ensure that stable (hydraulically-locked) operation will be obtained.

At any given operating point, it is necessary that the constant-speed hydraulic turbine torque coefficient-flow coefficient curve intersects the corresponding inducer curve at a slope which is greater than that of the inducer curve. This is illustrated on Figure No. 3(a). If the flow coefficient is displaced from the torque-matched values (resulting from such possible causes as flow disturbances or varying hydraulic turbine torque requirements resulting from rotor inertia during speed transients) in a decreasing direction, the speed will decrease because the inducer torque requirement will exceed the turbine torque and the unit will tend to return to the original torque and flow coefficient values. If the flow coefficient is displaced in an increasing direction, the speed will tend to increase because the turbine torque exceeds the inducer torque requirement; again, tending to return the unit to the original flow and torque coefficients.

Figure No. 3(b) illustrates the opposite situation wherein the hydraulic turbine curve slope is less (more negative) than that of the inducer. In this case, if the unit is operated below the matched torque-flow coefficient value, the low-speed shaft will tend to increase because the turbine torque will exceed the inducer requirement and the flow coefficient will diverge from the matched value, resulting in a "run-away" speed condition. If the flow coefficient is greater than the matched value, the inducer torque requirement will exceed the turbine torque, which results in a decrease in speed and divergence in an increasing direction of the flow coefficient. Actually, steady-state operation of the inducer/turbine unit at the condition shown on Figure No. 3(b) would not be possible. The unit would either "run away" to an undesirable high speed with a corresponding low flow coefficient or it would not "bootstrap" and would operate at low or zero speed with correspondingly high flow coefficients.

To define conditions and limits for stable operation in terms of blade geometry, design parameters, and operating flow coefficient, the head coefficient expression previously derived can be differentiated with respect to the normalized flow coefficient, $(\phi/\phi_D)_R$, holding the speed ratio, R, fixed; and then solved for $(N_R/N_i)_D$, making use of the relationship between $(N_R/N_i)_D$, (N_R/N_i) and R:

$$\left(\frac{N_R}{N_i}\right)_D = \frac{\frac{1}{TLFF}\left\{\left[1-\left(\frac{Cu}{U}\right)_{Di}\right]+\frac{K}{R^2(\phi/\phi_D)_R^2}\right\}+\left(\frac{r_T}{r_i}\right)^2\left[1-\left(\frac{Cu}{U}\right)_{DT}\right]}{\left(\frac{r_R}{r_i}\right)^2\left[1-\left(\frac{Cu}{U}\right)_{DR}\right]}$$

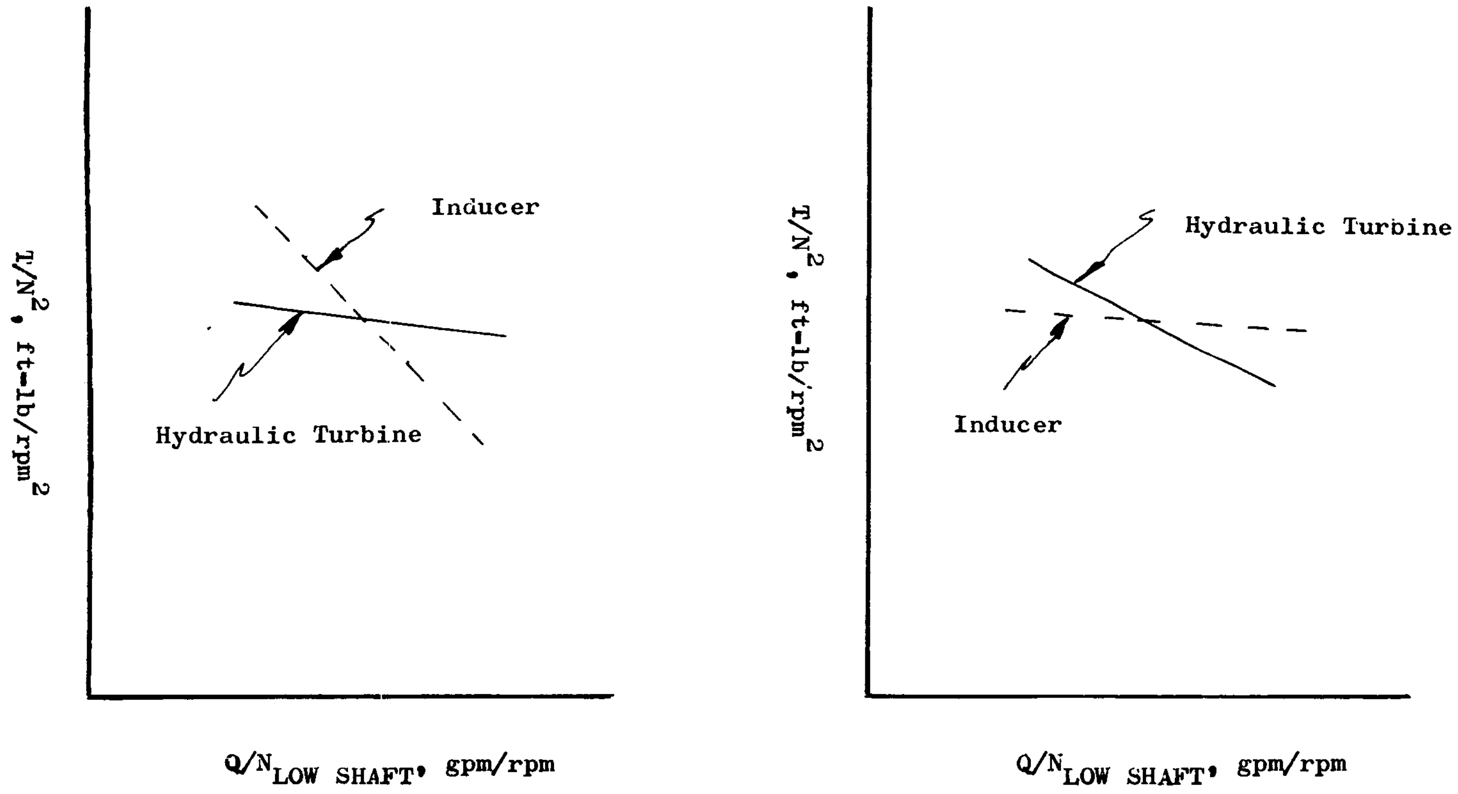

(a) STABLE

(b) UNSTABLE

Figure 3. Low-Speed Shaft Torque Matching

This expression defines the critical value of speed ratio for stability. To ensure stable operation, the design speed ratio must be less than this value. Analysis indicated that the value of R does not vary greatly from unity for designs of interest over the operating flow coefficient region. In addition, the term $\frac{K}{R^2 (\phi/\phi_D)_R^{\,2}}$ has a relatively minor influence upon the speed ratio value. Consequently, the stability of candidate designs was evaluated at the design point, although the minimum stability margin is generally obtained at the maximum flow coefficient.

In estimating the required design margins to ensure stable operation, a calculation of the speed ratio variance was made using the following design parameter values:

$$(Cu/U)_{Di} = .425$$

$$(Cu/U)_{D_R} = .500$$

$$(Cu/U)_{DT} = .524$$

$$K = .02$$

and the following estimated variance attributable to prediction uncertainties:

Cu/U - 10%

K - 100%

The calculated variance in $(N_R/N_i)_D$ was approximately 13%. This value does not vary appreciably in the range of design interest and was used to establish stability margins. The only designs considered were those where the critical speed ratio for stability was at least 13% larger than the design value.

The above analyses are based upon ideal head characteristics, assuming the blade exit relative flow angle and fluid deviation angle are fixed. The analysis for stability is probably conservative for conditions where the flow coefficient is less than the design value. This is based upon consideration that in this region, the recirculation caused by boundary layer separation will generally result in higher than ideal inducer torque requirements, which permit higher operating speed ratio values than those indicated by the ideal analysis limits. The ideal analysis is believed to be accurate for estimating design parameters and also for operation at above design-flow-coefficient conditions.

c. Stage Cavitation

It was necessary to examine estimated cavitation performance of the blade rows prior to selecting the stage work split to ensure that the contractual design requirement for cavitation-free operation of the high-speed rotor at 120% of the design flow coefficient would be satisfied. This requirement was interpreted to mean that at the 120% design flow coefficient point, cavitation performance of the system would be limited by the low-speed inducer rather than the high-speed rotor performance. It was assumed that the operation of the high-speed rotor at partially-cavitating (vapor present) conditions was permissible provided that head or torque reductions resulting from cavitation occur initially in the low-speed inducer as NPSH is reduced.

The design cavitation performance requirements for the low-speed inducer do not directly influence the work split selection; however, criteria for the inducer performance at 120% of the design flow coefficient had to be selected to permit calculation of the available head for the high-speed rotor. The non-cavitating head coefficient of the helical portions of the inducer was estimated from available data for 6 degree to 12 degree inducers(20)(21)(22) to be .135 (based upon rms rotor velocities). This value was reduced by 10% to allow for performance loss resulting from cavitation. Using the loss coefficient data shown on Figure No. 2, reductions in NPSH caused by fluid heating were calculated for a range of flow coefficients. The conservative assumption that the inducer was operating at 25 ft NPSH was used to calculate high-speed rotor suction head.

The total of the combined corrections for head degradation, fluid heating, and inducer suction NPSH is plotted as a function of inducer ideal head coefficient on Figure No. 4. This correction was applied to the estimated inducer head coefficient at 120% of the flow coefficient to obtain the available NPSH at the inducer discharge. The off-design head coefficient at 120% of the flow coefficient was estimated from the flat-plate inducer data previously referred to as well as data for the higher head coefficient designs(23)(24)(25). The estimate is shown on Figure No. 5 in terms of head coefficient as a function of design point ideal head coefficient.

To calculate available NPSH for the high-speed rotor, an additional reduction of low-speed inducer discharge NPSH was made to account for interstage flow passage losses and fluid heating. A NPSH reduction equivalent to 10% of the inducer exit absolute velocity head was made.

---

(20) Anderson, D. A., et. al., NASA TND-2553, op. cit.
(21) Sandercock, D. M., et. al., NASA TND-1439, op. cit.
(22) Sandercock, D. M., et. al., NASA TND-1170, op. cit.
(23) Lindley, B. K., Aerojet-General Report TPR 0028, op. cit.
(24) Sandercock, D. M., and Crouse, J. E., NASA TND-2879, op. cit.
(25) Edlebeck, N. A., op. cit.

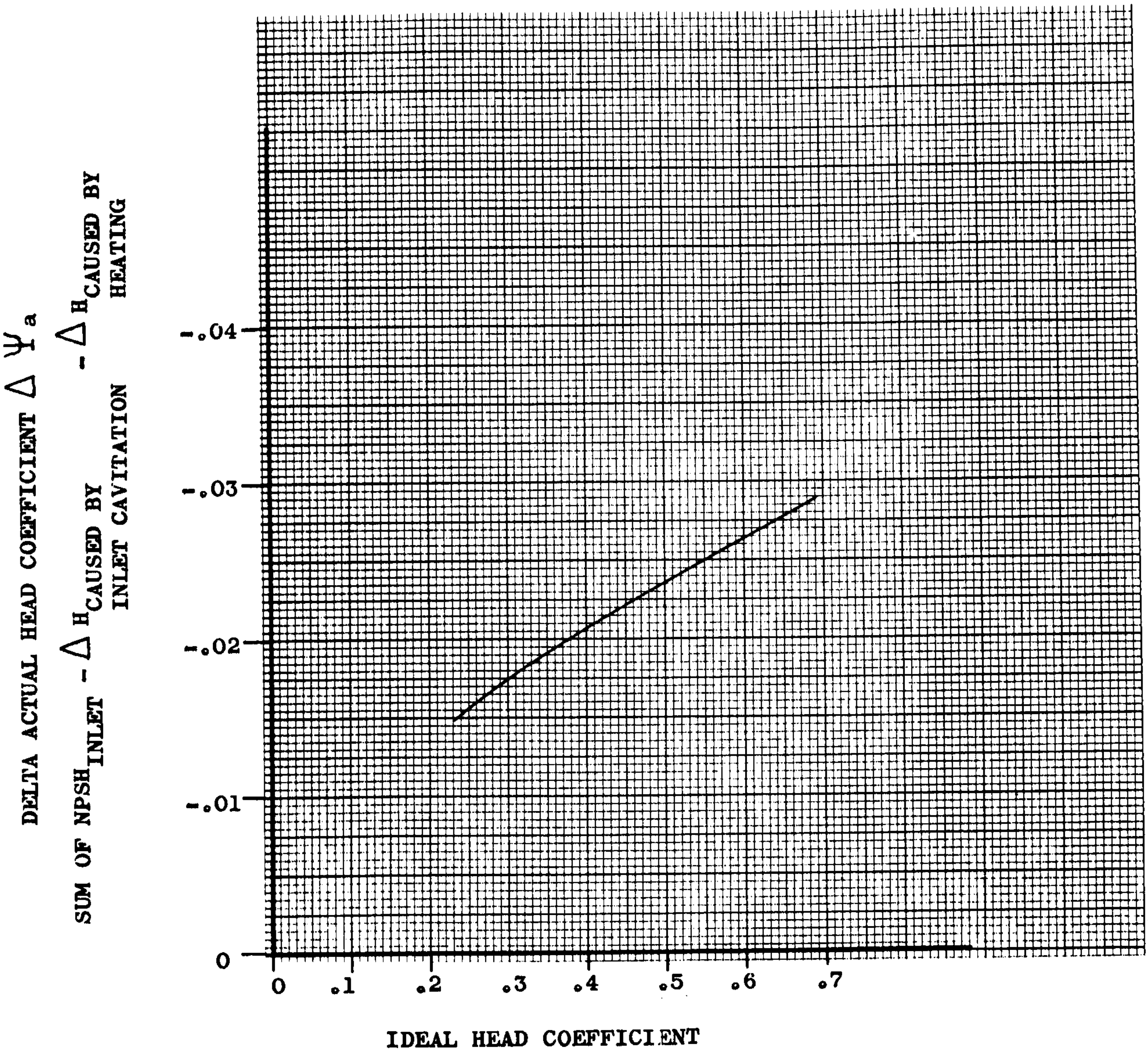

Figure 4. Calculated Head Losses, Sum of Inlet NPSH, Inlet Cavitation, and Fluid Heating Effect

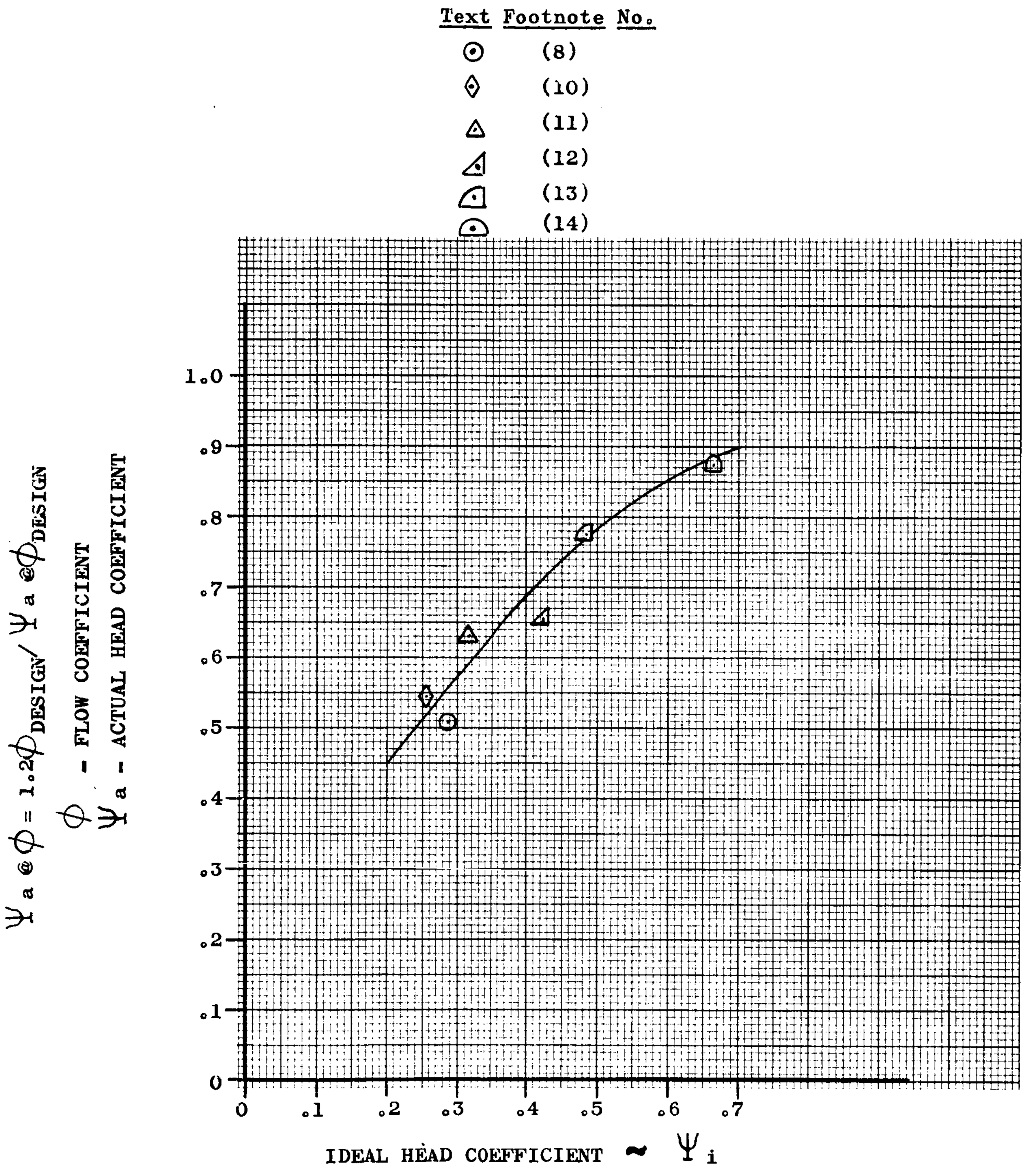

Figure 5. Off-Design Head Coefficient for Inducer Rotors

The high-speed rotor inlet relative flow angle and flow coefficient are important design parameters because they establish the high-speed rotor inlet blade angle and blade height requirements. In view of the assumption that the high-speed rotor and hydraulic turbine would have identical annulus dimensions, the above parameters establish the annulus for both blade rows.

To obtain the high-speed rotor inlet design parameters, criteria for the cavitation performance as a function of inlet flow conditions must be established. The available data for inducers and axial pumps concern the zero pre-whirl condition only. This data must be corrected and extrapolated for the current application where some pre-whirl exists. Available test data were compared upon the basis of equivalent cavitation number, K, (based upon inlet relative velocity):

$$K = \frac{H_T - H_v - C_1^2/2g}{W_1{}^2/2g}$$

H_T - inlet total head, ft

H_v - vapor head, ft

C_1 - inlet absolute velocity, ft/sec

W_1 - inlet relative velocity, ft/sec

g - acceleration caused by gravity, ft/(sec)^2

and inlet relative flow angle (measured from axial direction):

$$\beta = \cos^{-1} \frac{C_{m1}}{W_1}, \text{ degrees}$$

C_{m1} - inlet axial velocity, ft/sec

Three methods of correlation, based upon no fluid thermodynamic head effects were evaluated for this purpose. In the first method, blade surface velocity correlations proposed by Lieblein(26) were used to estimate blade low-pressure surface, minimum pressures, and corresponding cavitation number as a function of diffusion factor, D, and inlet relative flow angle. This correlation was originally developed to correlate losses with blade boundary layer thickness. It cannot be expected to give accurate estimates of actual low-pressure surface velocities; however, it is useful to obtain gross indications of surface velocities for empirical data correlations. The cavitation number can be written:

---

(26) Lieblein, S., et. al., NASA RME53D01, op. cit.

$$K = \left(\frac{W_{MAX}}{W_1}\right)^2 - 1$$

W_{MAX} - blade maximum surface velocity

and W_{MAX}/W_1 can be expressed in terms of diffusion factor and discharge/inlet relative velocity ratio:

$$\frac{W_{MAX}}{W_1} = D + \frac{W_2}{W_1} + 0.1$$

D - diffusion factor

W_2 - exit relative velocity, ft/sec

The W_2/W_1 ratio can be expressed in terms of diffusion factor, inlet relative flow angle, and blade solidity. The following is a listing of comparisons of experimental cavitation test data for the incipient head-breakdown point:

Reference	Inlet Relative Flow Angle $\beta 1$ (degrees)	Diffusion Factor D	① $\left(\frac{W_{MAX}}{W_1}\right)_{TEST}$	② $\left(\frac{W_{MAX}}{W_1}\right)_{THEORY}$	RATIO ①/②
(27)	70.1	.370	1.082	1.234	.876
(28)	71.9	.504	1.118	1.261	.888
(29)	63.5	.631	1.175	1.326	.886

The parameters are based upon the mean (rms) radius station; however, the diffusion factor was calculated using the ideal, integrated design head rise rather than the local value. An average value of test/theory velocity ratio of .883 was used to obtain data correlation curves.

---

(27) Crouse, J. E., Soltis, R. F., and Montgomery, J. C., Investigation of the Performance of an Axial Flow-Pump Stage Designed by the Blade Element Theory, NASA TN D-1109, December 1966

(28) Crouse, J. E., and Sandercock, D. M., Design and Over-All Performance of an Axial Flow-Pump Rotor with a Blade Tip Diffusion Factor of 0.43. NASA TN D-2295, May 1964

(29) Miller, M. J. and Crouse, J. E., Design and Over-All Performance of an Axial-Flow Pump Rotor with a Blade Tip Diffusion Factor of 0.66, NASA TN D-3024, September 1965

A second performance correlation which can be used is that of Gongwer(30):

$$\frac{NPSH}{Cm^2/2g} = 1.4 + 0.085 \left(1 + \frac{1}{\phi^2}\right)$$

Gongwer found that this relationship correlated the complete head breakdown point for centrifugal pumps with inlet relative flow angles (based upon tip geometry) of 7 degrees to 11 degrees. However, Wood and his associates(31) found that this correlation could be used to estimate the incipient head loss point for mixed-flow impellers with inlet tip relative flow angles of approximately 16-degrees.

A third correlation, which correlates the incipient head loss point for helical inducers with tip inlet relative flow angles of 3.5 degrees to 7.5 degrees, is the Brumfield(32) criteria:

$$\frac{NPSH}{Cm^2/2g} \doteq 3$$

The three methods of correlation are plotted on Figure No. 6. The correlation based upon the Lieblein surface velocity analysis has the advantage of taking into account blade fluid loading. However, the results of the work split analysis indicate that inlet relative flow angles in excess of 75 degrees are required to satisfy design specifications. In this region, blading of high solidity generally is used. A mean line solidity of 1.8 was selected for both the preliminary mean line analysis and the final design. This is an intermediate value between the airfoil type blade and the high-solidity helical, non-airfoil type blade; therefore, existing cavitation data for both were utilized. The solidity value of 1.8 was used to calculate the dashed-line curves shown on Figure No. 6. Because of the lack of data for high solidity blading and high inlet relative flow angles, an envelope established by using the Brumfield and Gongwer correlations was used to estimate the high-speed rotor inlet geometry and flow conditions. These curves follow the trends established by the lower relative flow angle, low solidity (1.1 to 1.3) air-foil blade data correlations which are based upon surface velocities. Analyses of the relative inlet flow angles to the high-speed rotor at 120% of the design flow coefficient indicates that the value obtained did not vary greatly from the design point value. The curves shown on Figure No. 6 were used to establish the design inlet relative flow angle. The cavitation number, K, was calculated for the 120% design point because this is the point of minimum cavitation margin.

---

(30) Gongwer, C. A., "A Theory of Cavitation Flow in Centrifugal Pump-Impellers," Trans. ASME, Vol. 66, 1941, pp 29-40

(31) Wood, G. M., Murphy, J. S., and Farquhar, J., "An Experimental Study of Cavitation in a Mixed Flow Pump Impeller," Trans. ASME, Journal of Basic Engineering, Vol 82, Series D, December 1960, pp 929-940

(32) Brumfield, R. G., Optimum Design for Resistance to Cavitation in Centrifugal Pumps U. S. Naval Ordinance Test Station, Inyokern, California, 1948

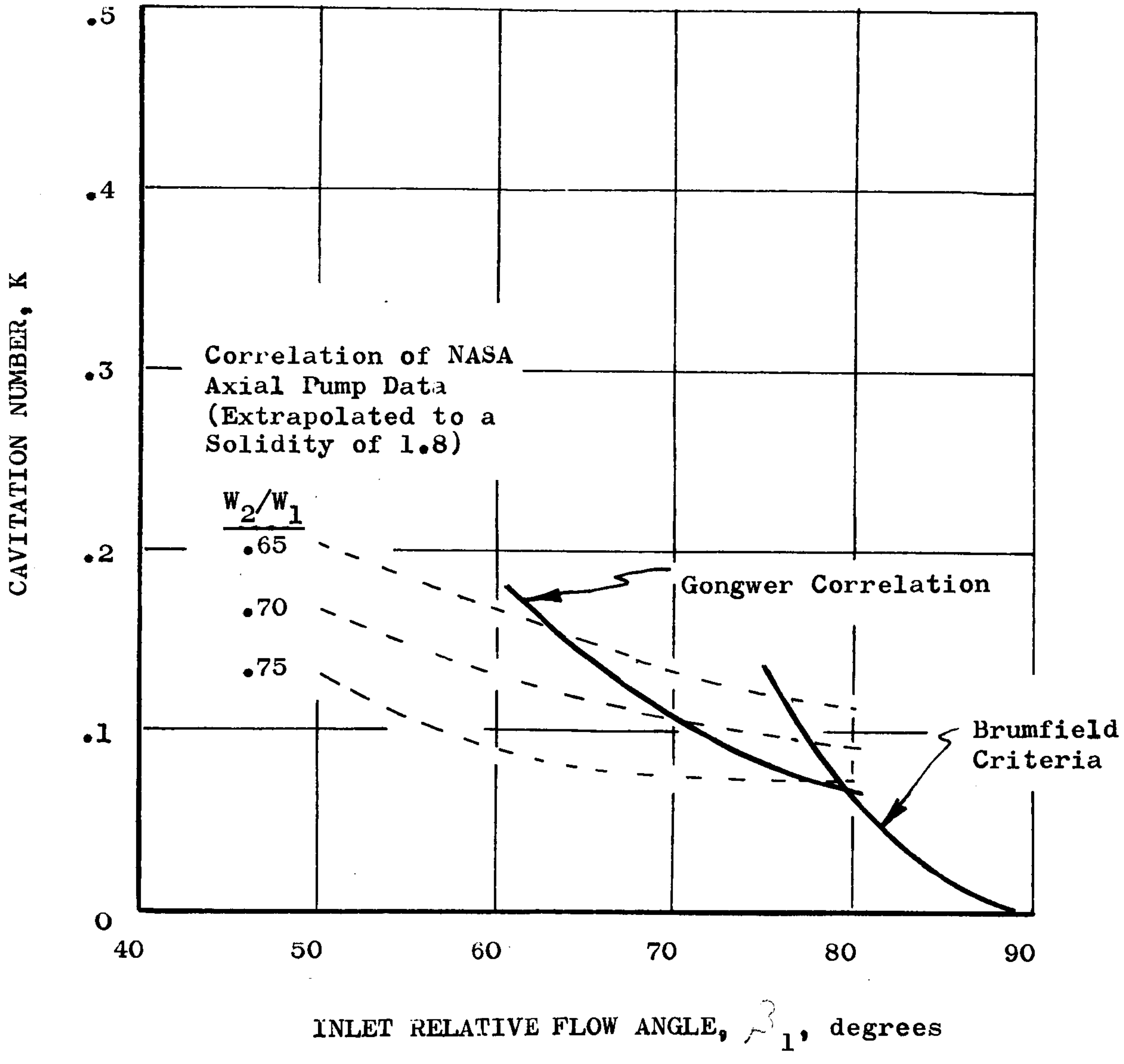

Figure 6. Correlations of Inlet Cavitation Number as a Function of Inlet Relative Flow Angle

Estimates of hydraulic turbine cavitation margins indicated that large margins existed for designs compatible with the low-speed inducer and high-speed rotor designs. Calculated design point cavitation numbers, based upon Lieblein's surface velocity correlations, are on the order of 0.3 for the deisgns of interest (using inlet head and exit relative velocities). Operating cavitation numbers based upon estimates of head delivered by the high-speed rotor are on the order of 4.0. This allows more than an adequate margin for design and off-design operation.

d. Work Split and Annulus Geometry Selection

It was convenient to perform both the calculations for the power/speed matching analysis as well as the analysis for the high-speed rotor and hydraulic turbine flow coefficients and the annulus geometry using a single program written for the IBM 1130 computer. (Appendix A is a listing for this program). The program input variables are defined below, together with those values of each, for which calculations were performed. The value selected for the final design is shown in parenthesis for those parameters where more than one value was evaluated.

Parameter	Definition	Units	Value
Ind Speed	Low-Speed Inducer Rotational Speed	rpm	14,100 (18,800)
Flow	Flow Rate	gpm	4,900
--	High-Speed Rotor Rotational Speed	rpm	44,500
--	High-Speed Rotor Ideal Head Rise	ft	1500 and up in 1500 ft increments (8800)
SR-STA-MR	Ratio: Critical Speed Ratio for Stability to Actual Speed Ratio	--	1.13
IND-R-M1	Inducer Inlet Mean Radius (rms)	in	2.94
IND-R-N2	Inducer Discharge Mean Radius (rms)	in	2.94 (3.24) 3.52
IND-R-MAX	Inducer Maximum Discharge Tip Radius	in	3.70
DRUM FHC	Low-Speed Rotor Shrouded Bearing Friction Coefficient	--	(.0770) .02

Parameter		Units	Value
TURB-R-FA	Ratio of Turbine Pitch Line Radius to Calculated High-Speed Rotor or Main Axial Pump Stage Mean Lines	---	1.0 to high rotor; 1.0 and 1.2 Main Axial Pump Stages (1.1)
TURB-L-FA	Ratio of Turbine Output Power to Hydraulic (Velocity Diagram) Power	---	.975
I-STAGE-F	Inducer/High-Speed Rotor Interstage Passage Loss Coefficient	---	0.1
W2/W1	High-Speed Rotor Discharge/Inlet Relative Velocity Ratio	---	0.60 (0.65) 0.70 0.75
HCI	Inducer Head Coefficient	---	.29 to .5 (.425)

The low-speed inducer rotational speeds of 14,100 rpm and 18,800 rpm correspond to suction specific speeds of 30,000 and 40,000, respectively, for the design NPSH of 105 ft (25 ft NPSH and LH_2) plus 80 ft thermodynamic suppression head). Calculations indicated that the 14,100 rpm designs would have unsatisfactory torque/speed stability characteristics; consequently, the 18,800 rpm speed was selected.

Values of high-speed rotor ideal head rise from 1500 ft to a maximum value determined from the low-speed shaft inducer/hydraulic turbine torque/speed stability limits were evaluated. This portion of the study included ideal head rise values that yield less than the contractual minimum over-all actual head rise values. A study of the lower head rise value was mutually agreed upon by NASA and Aerojet-General when preliminary calculations indicated a more desirable design might be achieved by decreasing the minimum to a lower value. The results of the study are summarized on Figures No. 7 through No. 10. The following parameters are plotted against the delivered over-all head rise for all three blade rows (non-cavitating):

R_R/R_I

R_R - High speed rotor and hydraulic turbine mean line (rms) radius
R_I - Inducer exit mean line (rms) radius
β - High rotor inlet fluid relative velocity (measured from axial direction), degrees

Efficiency - Over-all efficiency for three blade rows, %

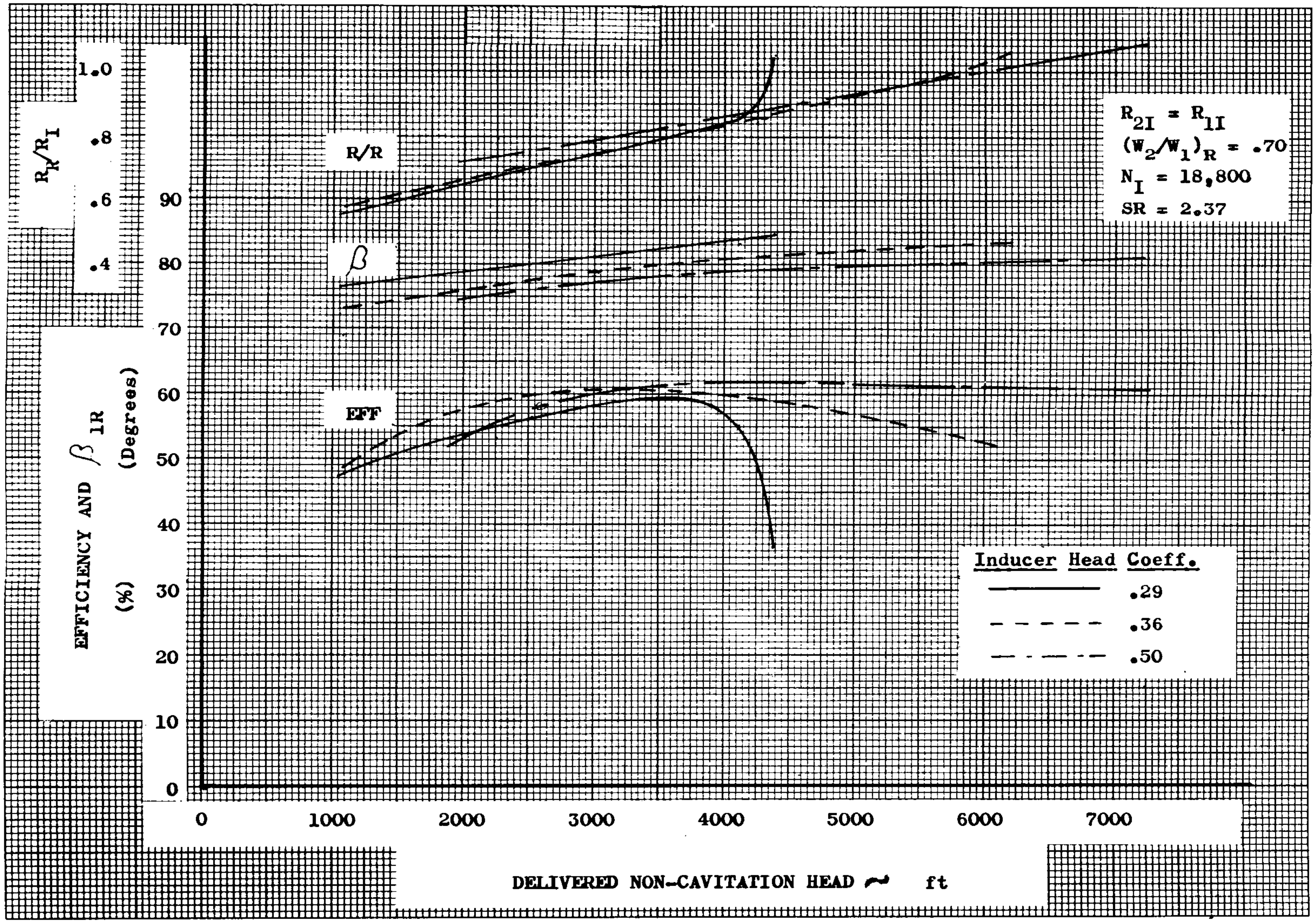

Figure 7. One-Dimensional Design Parameters vs Delivered Head, $R_{2I}=R_{1I}$, $(W2/W1)_R = 0.70$

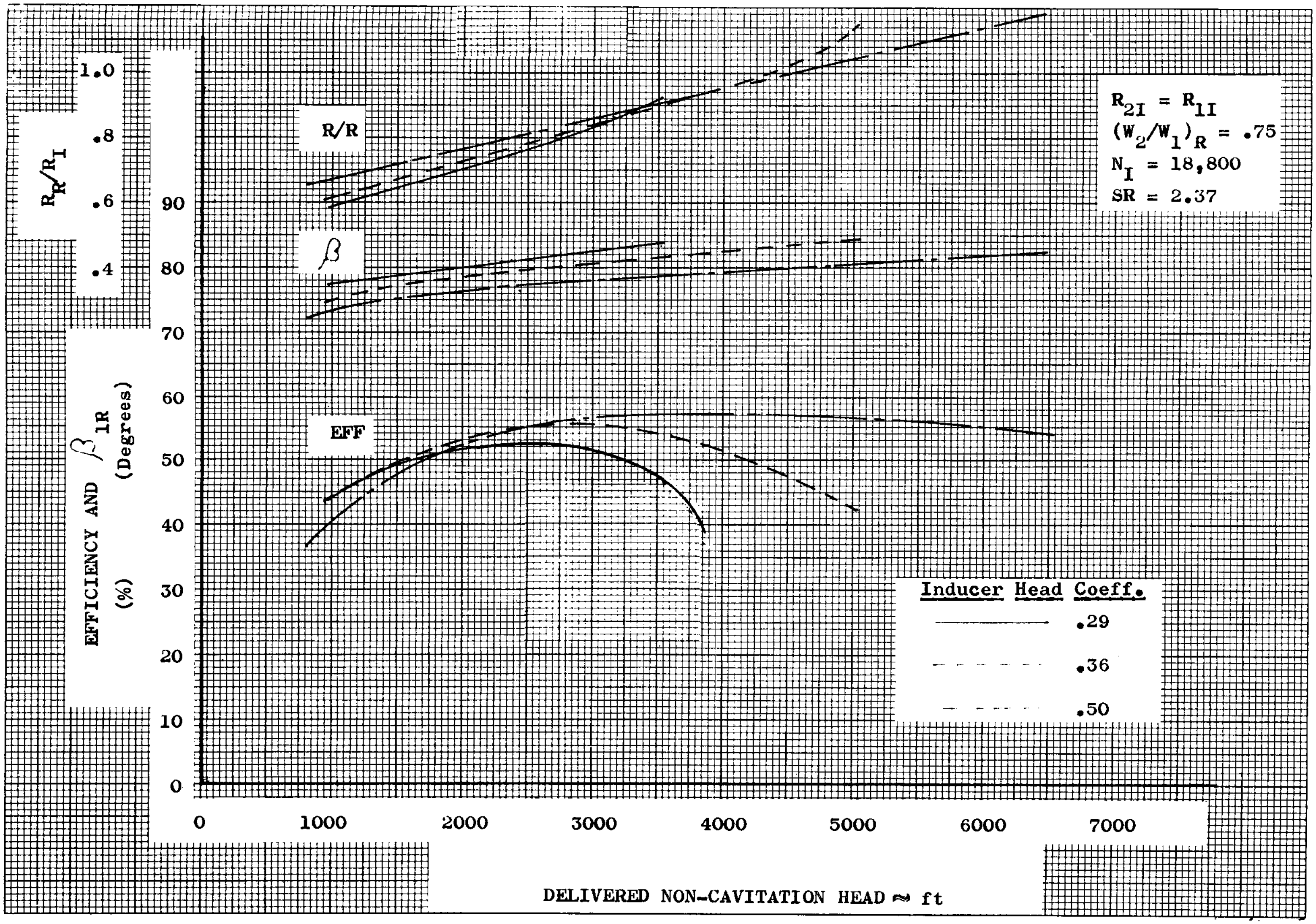

Figure 8. One-Dimensional Design Parameters vs Delivered Head, $R_{2I}=R_{1I}$, $(W2/W1)_R = 0.75$

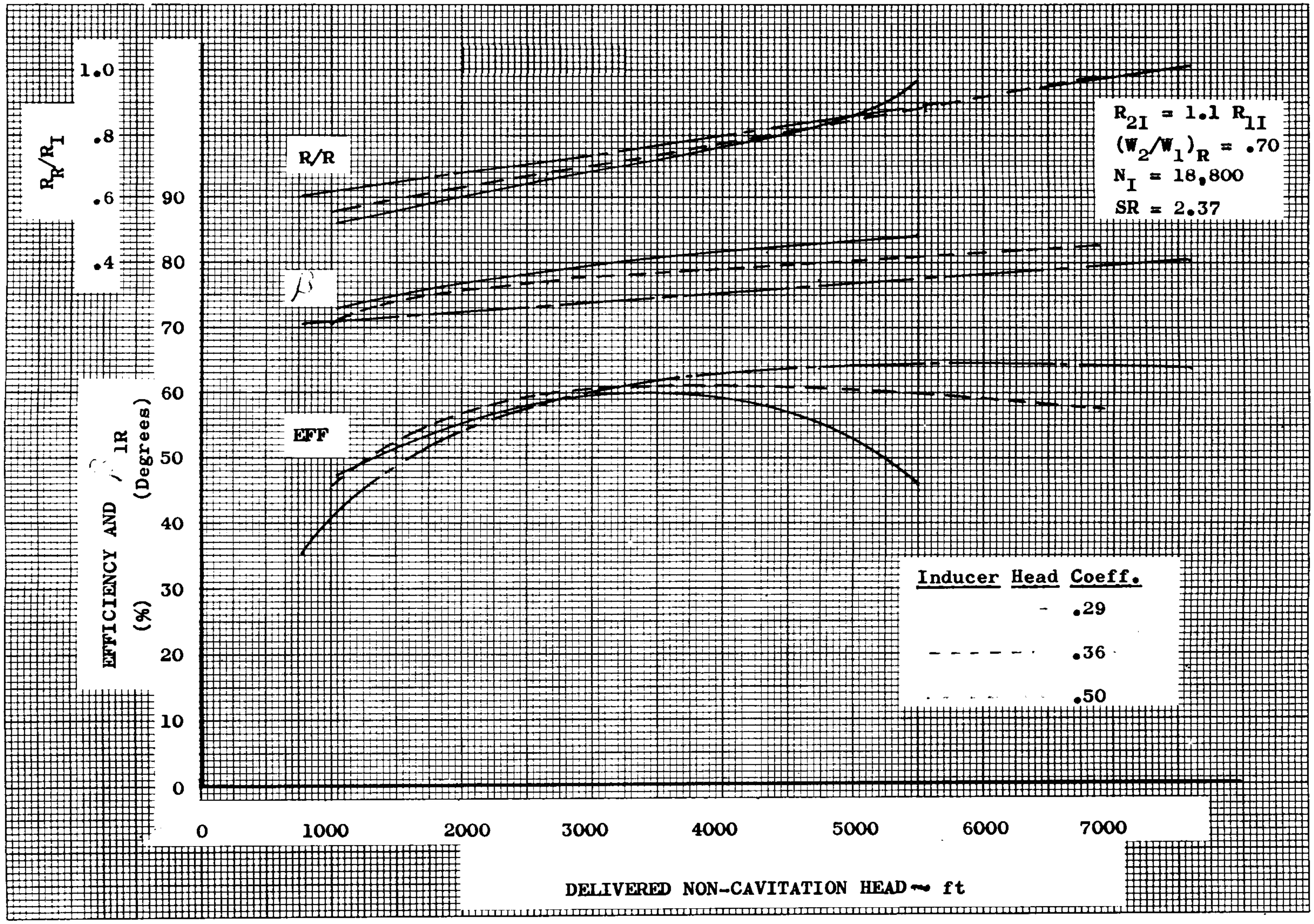

Figure 9. One-Dimensional Design Parameters vs Delivered Head, R_{2I}= $1.1R_{1I}$, $(W2/W1)_R$= 0 70

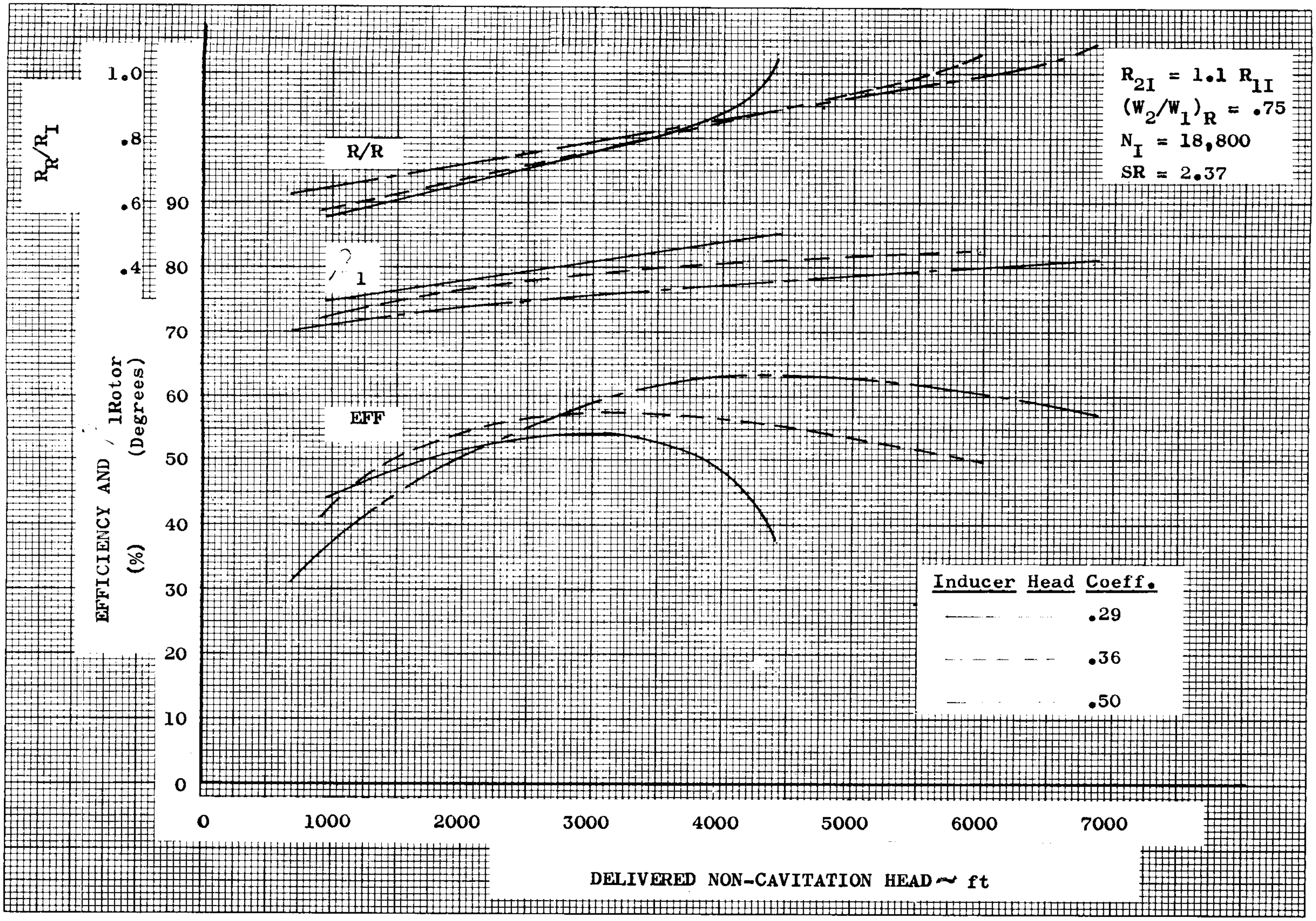

Figure 10. One-Dimensional Design Parameters vs Delivered Head, $R_{1I} = 1.1 R_{1I}$, $(W2/W1)_R = 0\ 75$

The calculations are performed for a low-speed shaft speed (N_I) of 18,800 rpm and a high-speed shaft/low-speed shaft speed ratio (SR) of 2.37. Results for three values of inducer head coefficient are shown in each figure. Two values at low inducer exit mean line radius (R_{2I}) and two values of high-speed rotor relative velocity retardation factor $(W_2/W_1)_R$ were evaluated. The four plots encompass the various combinations of these latter parameters:

Figure No.	R_{2I}/R_{1I}	$(W_2/W_1)_R$
7	1.0	.70
8	1.0	.75
9	1.1	.70
10	1.1	.75

The calculations indicate that the higher head rise designs have higher predicted efficiencies; however, the lower head rise designs have lower high-speed rotor inlet relative flow angles, which provide improved high-speed rotor cavitating and non-cavitating performance predictability. The lower head rise designs may have lower discharge annulus radii (corresponding to lower R_R/R_I values) and annulus dimensions, which more nearly correspond to downstream pumping elements.

The efficiency predictions are based upon the previously discussed loss coefficients. The high-speed rotor inlet relative flow angles are based upon the limit curves shown on Figure No. 6. The R_R/R_I values are calculated from the high-speed rotor ideal head rise and the W_2/W_1 value.

While lower design head rise values would provide more conventional high-speed rotor blade geometries, it was believed that a feasible design could be achieved for the originally-selected design non-cavitating head rise of 5671 ft. The calculations indicated that maximum inducer exit radius and inducer ideal head coefficient as well as minimum $(W_2/W_1)_R$ values yield the most desirable designs. The primary criterion was the magnitude of the high-speed rotor inlet relative flow angle. A $(W_2/W_1)_R$ value of .65 was selected as the lowest value which provides reasonable blade velocity diffusion and diffusion factors. A value of inducer mean discharge radius 10% larger than the inlet radius was selected. The inlet radius is obtained from cavitation performance considerations (see Section III,B,1). Values of exit radius, which are significantly larger than this would result in inducer exit tip radii that are larger than the inlet tip radius. This was undesirable from the mechanical design arrangement aspect as well as for matching the inducer exit annulus to the high-speed rotor inlet. An inducer ideal head coefficient:

$$\frac{\Delta H_I}{U_{2I}^2/g}$$

ΔH_I - Inducer ideal head rise, ft

U_{2I} - Inducer exit mean (rms) wheel velocity, ft/sec

g - Acceleration caused by gravity, ft/sec^2

of 0.425 was selected. This is the maximum value, for which there is design experience with single blade rows.

Initial calculations for the study were based upon the .02 value of the low-speed inducer shroud and bearing friction coefficient. The final calculations (see Figures No. 7 through No. 10) are based upon final estimates for the shroud and bearing friction in LH_2. The values for water will be somewhat higher. The coefficient is defined to be consistent with the equation format shown in Section III,A,2,b.

The selected design values are listed on Tables IV, V, and VI for LH_2 hydraulic design, LH_2 test, and water test, respectively.

TABLE IV

DESIGN SPECIFICATION SHEET, HYDROGEN HYDRAULIC DESIGN

PUMPS	DIMENSIONS	OVER-ALL	LOW-SPEED INDUCER	HIGH-SPEED ROTOR
Propellant Temperature	°F	-420.3	-420.3	-420.3
Propellant Density	lb/ft3	4.3	4.3	4.3
Shaft Speed	rpm	44,500.0	18,800.0	44,500.0
Total Discharge Pressure	psia	187.9	115.5	329.4
Total Suction Pressure	psia	23.7	23.7	112.9
Total Pressure Rise	psi	164.2	91.8	216.5
Total Head Rise (cavitating)	ft	5000.0	3078.0	7250.0
Weight Flow	lb/sec	47.0	47.0	47.0
Capacity	gpm	4900.0	4900.0	4900.0
Specific Speed (Based on Cavitating Head)	$\frac{\text{rpm x gpm}^{1/2}}{\text{ft } 3/4}$	4860.0	3200.0	3950.0
Efficiency	%	61.9	82.5	81.7
Fluid Horsepower	h.p.	470.0	263.0	630.0
Shaft Horsepower	h.p.	760.0	319.0	760.0
Net Positive Suction Head	ft	25.0	25.0	3004.0
Suction Specific Speed	$\frac{\text{rpm x gpm}^{1/2}}{\text{ft } 3/4}$	*94,600.0	*40,000.0	7700.0

* (80 Ft. Thermodynamic Head)

TURBINE	DIMENSIONS	HYDRAULIC TURBINE
Gas		LH_2
Shaft Power	h.p.	377.0
Gas Weight Flow	lb/sec	47.0
Gas Inlet Total Temperature	°F	-420.3
Shaft Speed	rpm	18,800.0
Efficiency	%	93.0
Gas Inlet Total Pressure	psia	329.4

TABLE V

DESIGN SPECIFICATION SHEET, HYDROGEN OPERATION

PUMPS	DIMENSIONS	OVER-ALL	LOW-SPEED INDUCER	HIGH-SPEED ROTOR
Propellant Temperature	°F	-420.3	-420.3	-420.3
Propellant Density	lb/ft3	4.3	4.3	4.3
Shaft Speed	rpm	27,600.0	11,650.0	27,600.0
Total Discharge Pressure	psia	86.7	58.6	141.0
Total Suction Pressure	psia	23.3	23.3	57.6
Total Pressure Rise	psi	63.4	35.3	83.4
Total Head Rise (cavitating)	ft	2120.0	1180.0	2790.0
Weight Flow	lb/sec	29.2	29.2	29.2
Capacity	gpm	3040.0	3040.0	3040.0
Specific Speed (Based on Cavitating Head)	$\frac{rpm \times gpm^{\frac{1}{2}}}{ft\ 3/4}$	4860.0	3200.0	3950.0
Efficiency	%	61.9	82.5	81.7
Fluid Horsepower	h.p.	113.0	62.9	148.0
Shaft Horsepower	h.p.	182.0	76.1	182.0
Net Positive Suction Head	ft	9.6	9.6	1130.0
Suction Specific Speed	$\frac{rpm \times gpm^{\frac{1}{2}}}{ft\ 3/4}$	*94,500.0	*40,000.0	7700.0

* (30.8 Ft. Thermodynamic Head)

TURBINE	DIMENSIONS	HYDRAULIC TURBINE	HIGH-SPEED DRIVE TURBINE
Gas		LH_2	GH_2
Shaft Power	h.p.	89.6	211.4
Gas Weight Flow	lb/sec	29.2	0.95
Gas Inlet Total Temperature	°F	-420.3	60.0
Pressure Ratio			1.43
Static Back Pressure	psia		30.0
Shaft Speed	rpm	11,650.0	27,600.0
Efficiency	%	93.0	87.5
Gas Inlet Total Pressure	psia	141.0	42.9
Nozzle Area (Effective)	in.2		4.15
Specific Heat	BTU/lb°R		3.47
Specific Heat Ratio			1.417
Gas Constant	ft/°R		766.0

TABLE VI

DESIGN SPECIFICATION SHEET, WATER OPERATION

PUMPS	DIMENSIONS	OVER-ALL	LOW-SPEED INDUCER	HIGH-SPEED ROTOR
Propellant Temperature	°F	70.0	70.0	70.0
Propellant Density	lb/ft3	62.4	62.4	62.4
Shaft Speed	rpm	8500.0	3590.0	8500.0
Total Discharge Pressure	psia	88.9	50.5	163.6
Total Suction Pressure	psia	2.02	2.02	49.1
Total Pressure Rise	psi	86.9	48.5	114.5
Total Head Rise (cavitating)	ft	200.5	112.0	264.0
Weight Flow	lb/sec	130.0	130.0	130.0
Capacity	gpm	935.0	935.0	935.0
Specific Speed (Based on Cavitating Head)	$\frac{\text{rpm x gpm}^{\frac{1}{2}}}{\text{ft } 3/4}$	4860.0	3200.0	3950.0
Efficiency	%	61.9	82.5	81.7
Fluid Horsepower	h.p.	47.5	26.5	62.7
Shaft Horsepower	h.p.	76.9	32.1	76.9
Net Positive Suction Head	ft	3.83	3.83	110.0
Suction Specific Speed	$\frac{\text{rpm x gpm}^{\frac{1}{2}}}{\text{ft } 3/4}$	94,500.0	40,000.0	7700.0

TURBINE	DIMENSIONS	HYDRAULIC TURBINE	HIGH-SPEED DRIVE TURBINE
Gas		Water	GN_2
Shaft Power	h.p.	37.9	84.6
Gas Weight Flow	lb/sec	130.0	4.40
Gas Inlet Total Temperature	°F	70.0	-10.0
Pressure Ratio			2.15
Static Back Pressure	psia		20.0
Shaft Speed	rpm	3590.0	8500.0
Efficiency	%	93.0	62.3
Gas Inlet Total Pressure	psia	163.6	43.0
Nozzle Area (Effective)	in.2		4.15
Specific Heat	BTU/lb°R		0.248
Specific Heat Ratio			1.4
Gas Constant	ft/°R		55.1

B. DETAILED HYDRODYNAMIC DESIGN

1. Low-Speed Inducer

The low-speed inducer speed and head rise were established as a result of the stage work split discussed in Section III,A,2. In general, the maximum speed of the low-speed inducer will be limited by the suction performance. Higher inducer speeds mean greater cavitation margin for the high-speed rotor and less cavitation margin for the low-speed inducer while with lower inducer speeds, the reverse is true. The suction eye was sized for a 40,000 suction specific speed with the inlet fluid velocity head equal to the design NPSH of 25 ft. Then, the speed was calculated from the suction specific speed, flow, and the effective NPSH (the sum of the design or apparent NPSH plus the thermodynamic NPSH). A thermodynamic NPSH of 80 ft at 36.7°R was scaled from existing 37°R data(33) and was found to be consistent with previous Aerojet-General experience.(34)

The discharge mean radius was limited to a value that is 10% greater than the inlet mean radius. The discharge annulus was obtained from the blade element design consideration (viz., relative velocity ratios).

The inlet blade angle of 6.3 degrees at the tip was obtained from criteria for optimum suction performance(35). The blade angle from tip to hub was established with $r \tan \beta$ being constant, which is the condition of a flat-plate or helix inducer. The back portion of the inducer was made of twisted airfoil sections. The flow was analyzed at the end of the flat-plate portion and again, at the discharge of the airfoil section. In both cases, it was assumed that the flow satisfied simple radial equilibrium. The flow leaving the flat-plate portion of the inducer was assumed to be following the blade angle without deviation. Figure No. 11 shows the axial and tangential velocities at this station. The losses were obtained from data for similar types of inducers(36). The computer program needed to obtain these results is outlined in Appendix B.

The rear portion of the inducer was then analyzed using the same computer program with different boundary conditions. These conditions were:

---

(33) Ball, C. J., Meng, P. R., and Reid, L., (U) Cavitating Performance of 84° Helical Pump Inducer Operated in 37° and 42°R Liquid Hydrogen, NASA TMX-1360, February 1967 (Confidential Report)

(34) Farquhar, J. and Lindley, B. K., NASA CR-54822, op. cit.

(35) Stripling, L. B., "Cavitation in Turbopumps - Part 2," Trans. ASME, Journal of Basic Engineering, Vol. 84, 1962, pp. 339-350

(36) Farquhar, J. and Lindley, B. K., NASA CR-54822, op. cit., Section III,A,1, Figure 19, p. 28

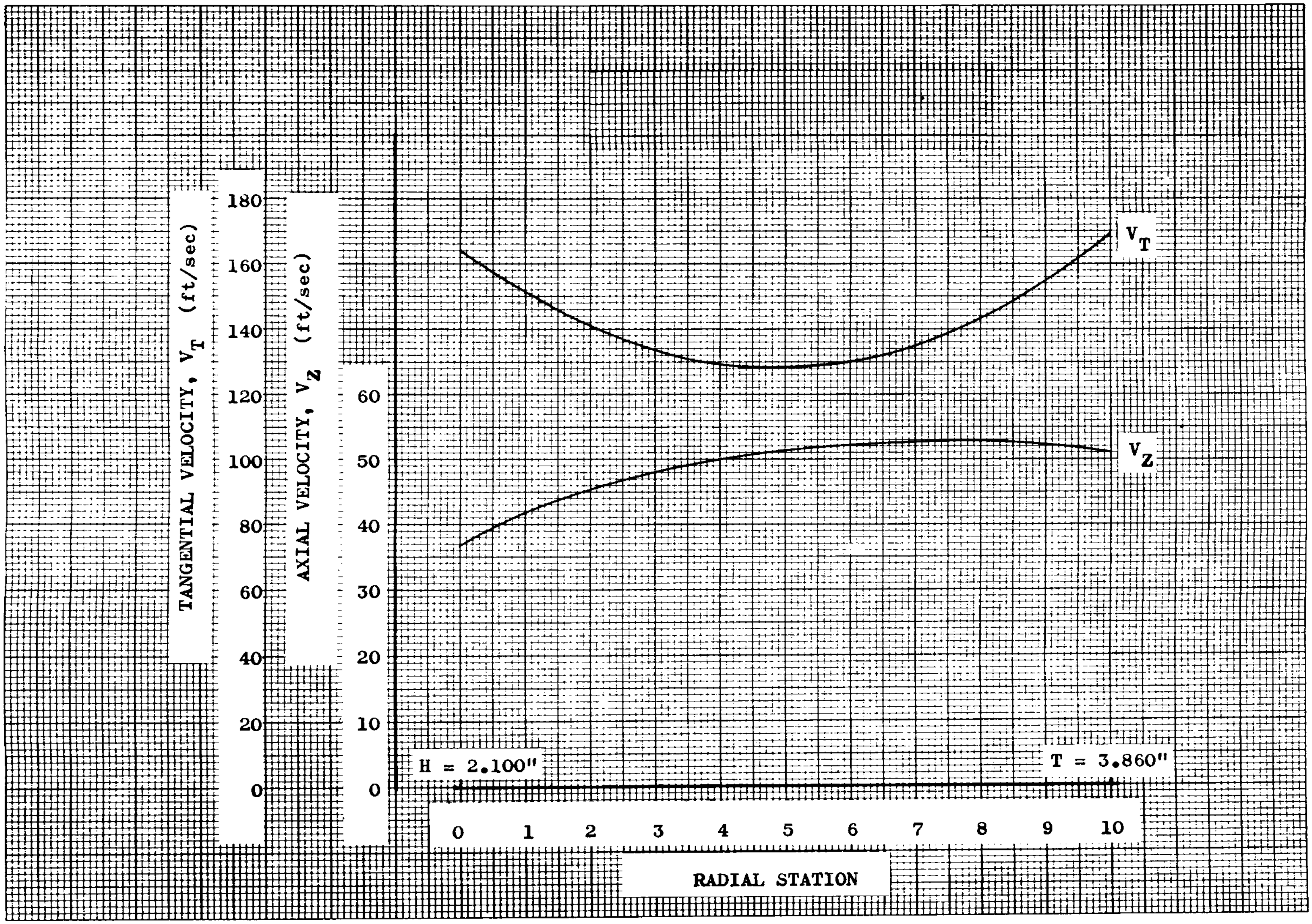

Figure 11. Low-Speed Inducer, Tangential, and Axial Velocity Distribution at Exit of Flat-Plate Portion

a. The flow entering the airfoil portion was the same as that leaving the flat-plate portion.

b. The mass averaged input head would be the difference between the over-all inducer input head (as determined by the work split) and the flat-plate input head.

c. The losses would be considerably less than found in normal airfoil data because there would be no entrance loss.

The over-all inducer losses would be consistent with those for similar inducers (see Figure No. 2).

The discharge axial and tangential velocity as well as the total and static head are shown on Figure No. 12 in relationship to passage height.

With the flow conditions defined, blade stagger and camber angles could be established which would satisfy this flow. The inlet flow conditions were assumed to be the same as the flat-plate discharge flow condition; therefore, camber and stagger angles could be determined from the Reid flow angles and some deviation angle distribution. This deviation angle distribution was obtained from traverse data for similar types of inducers (see Figure No. 13). Figure No. 14 shows the smoothed setting and turning angles.

The inducer was laid out so that the three flat-plate vanes blended into three of the airfoil blades. This required that the airfoil sections be stacked on the center-of-gravity in the radial plane but shifted forward (from hub to tip) in the axial plane. The other three blades were considered as nearly true airfoils and would serve as partial blades. A schematic of this blade layout is shown as Figure No. 15.

2. High-Speed Rotor

The high-speed rotor supplements the work done by the inducer and provides the input power to the low-speed shaft. The work split analysis established the two major blade design criteria; the cavitation coefficient at the blade inlet and the blade loading resulting from the required head rise. The flow analysis obtained from the methods outlined in Appendix B was used to calculate the blade element performance. The input head to the high-speed rotor was adjusted until the mass averaged input head agreed with the one-dimensional input head.

Figure No. 16 shows both the inlet and outlet high-speed rotor blade performance parameter. To obtain the inlet flow conditions, it was assumed that conservation of angular fluid momentum at any given streamline existed between the low-speed inducer discharge and the high-speed rotor inlet. With the angular or tangential velocity known, an axial velocity

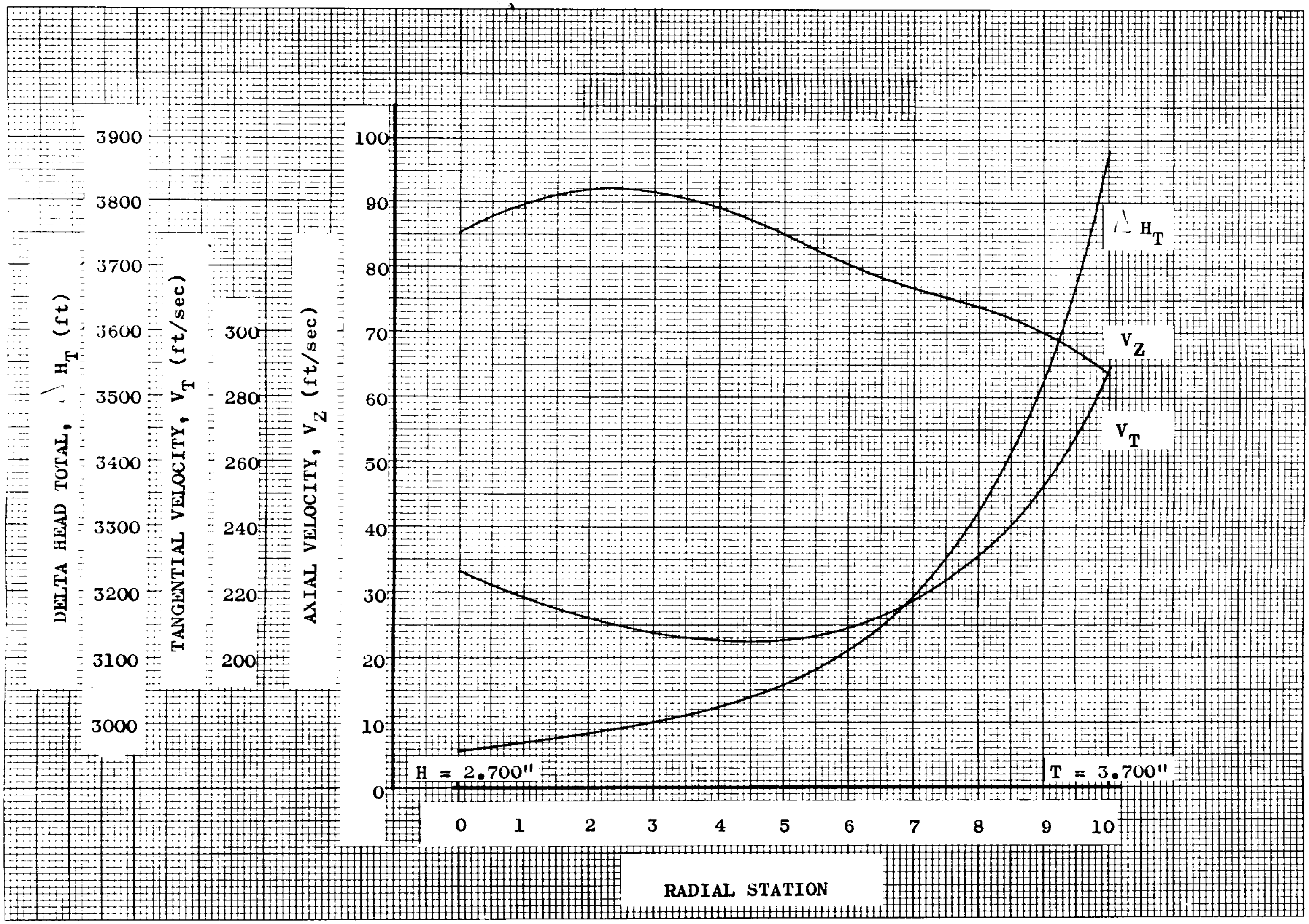

Figure 12. Low-Speed Inducer Blade Element Data

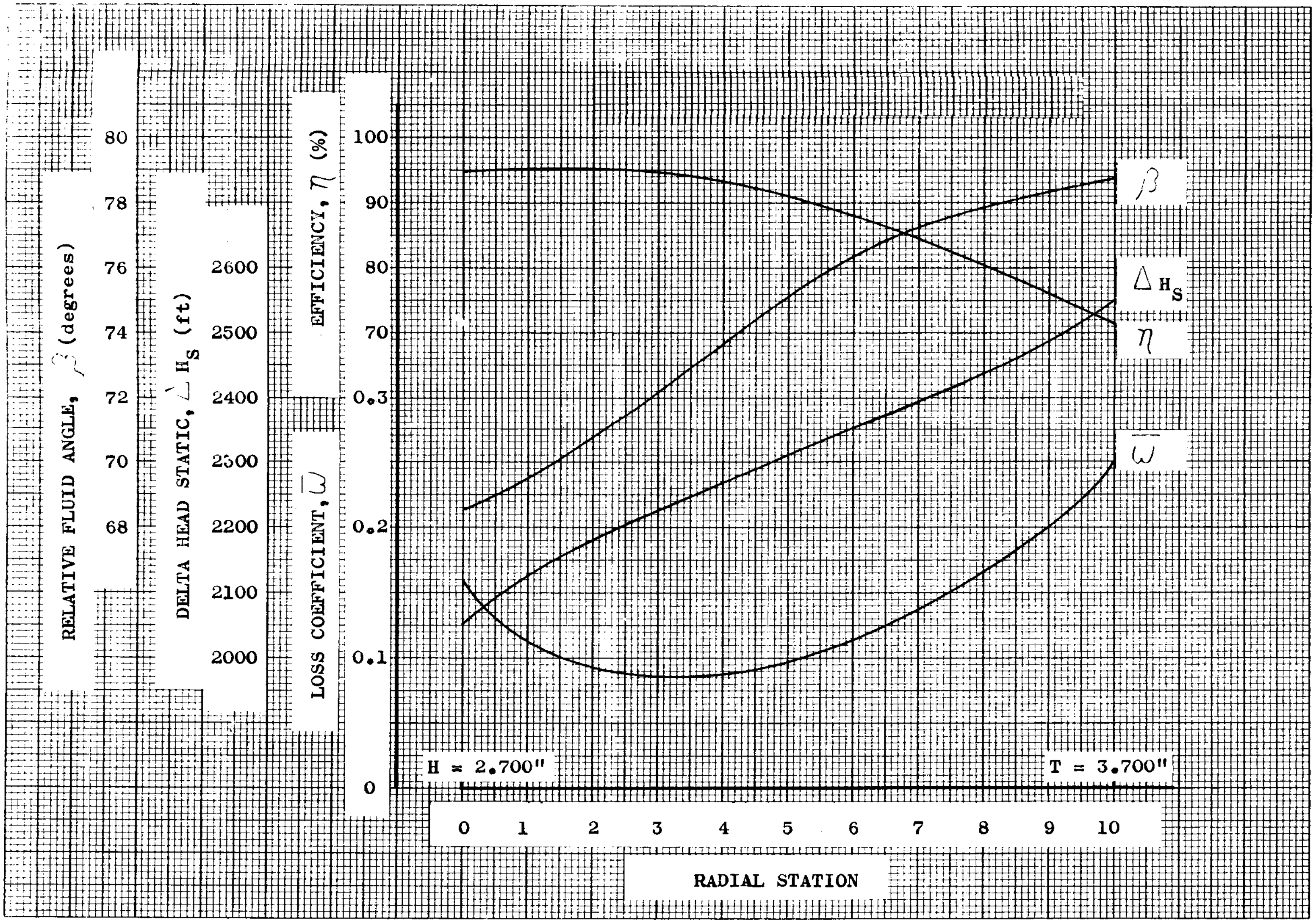

Figure 12. Low-Speed Inducer Blade Element Data

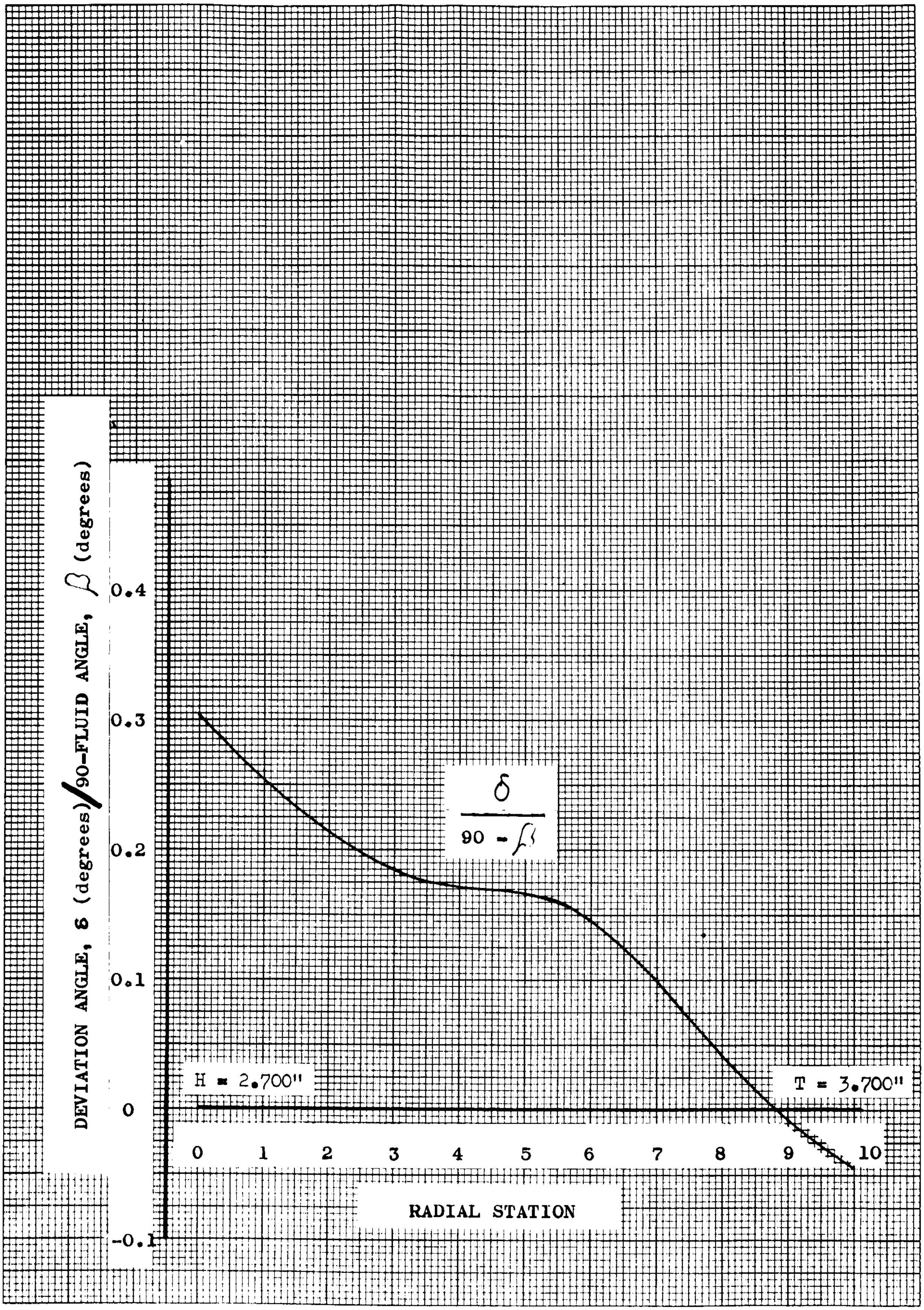

Figure 13. Inducer Blade Exit Flow Deviation Angle Correlation

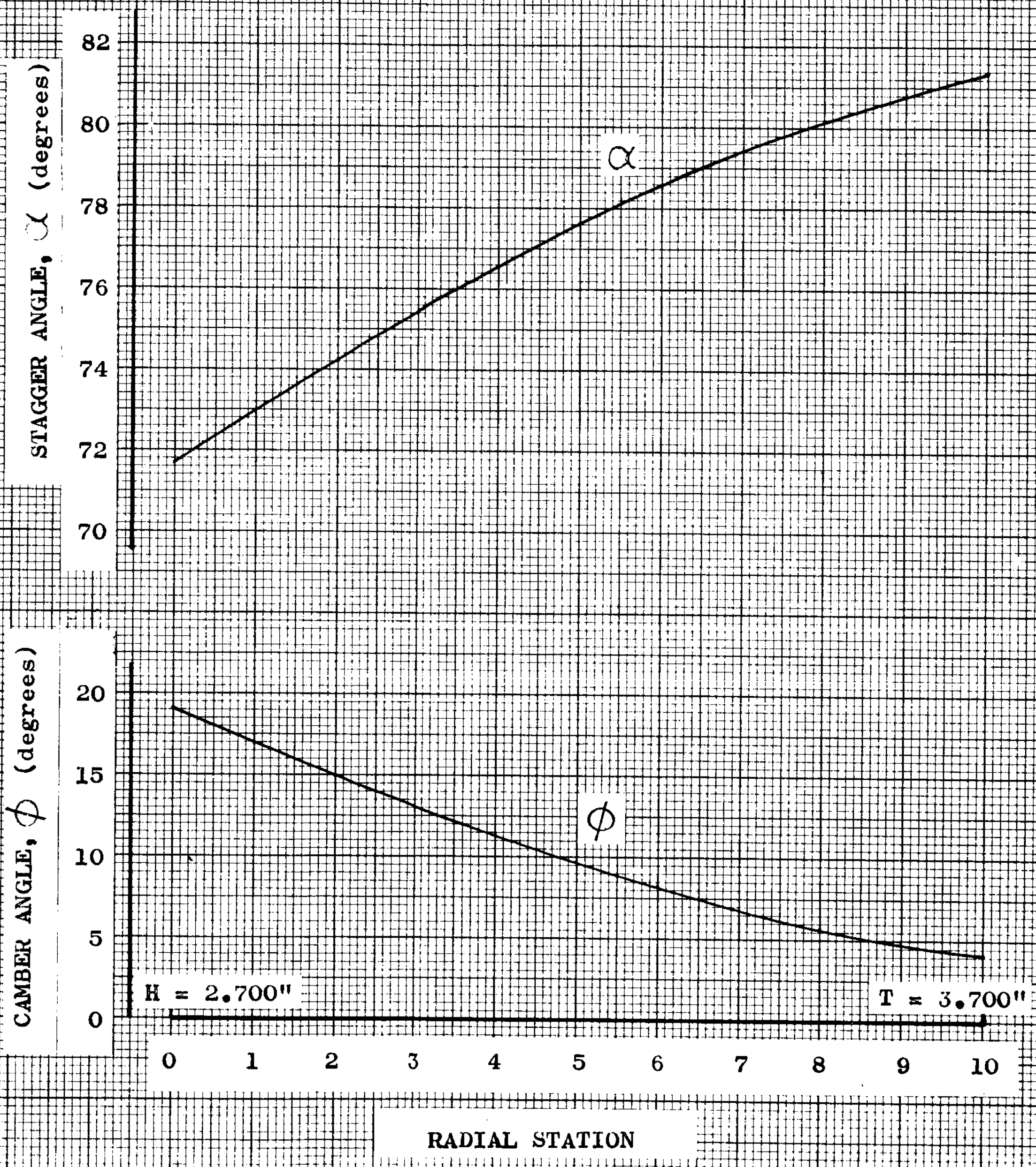

Figure 14. Low-Speed Inducer, Stagger and Camber Angle Distribution for Double-Curved Portion of Blades

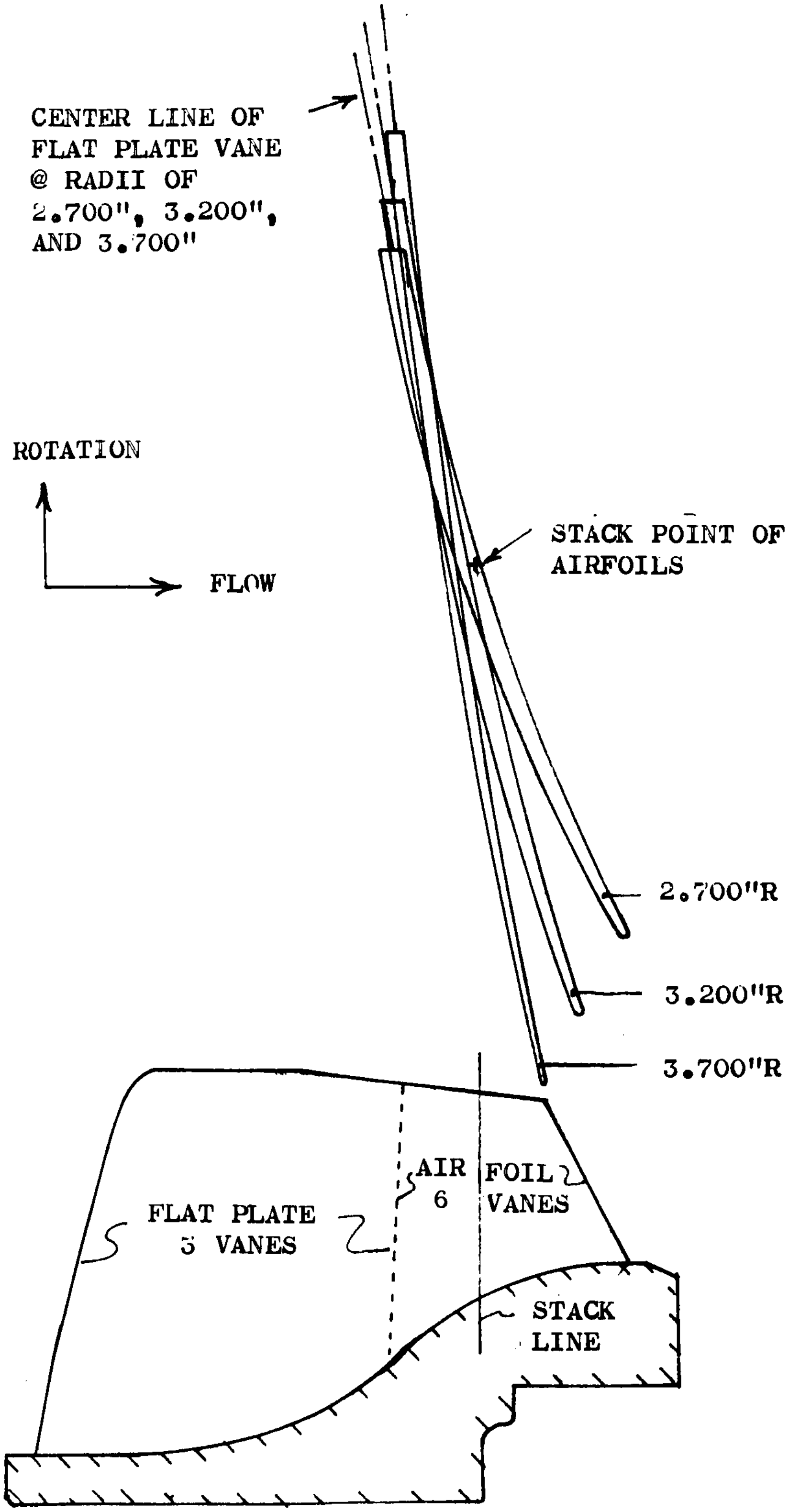

Figure 15. Low-Speed Inducer Vane Layout

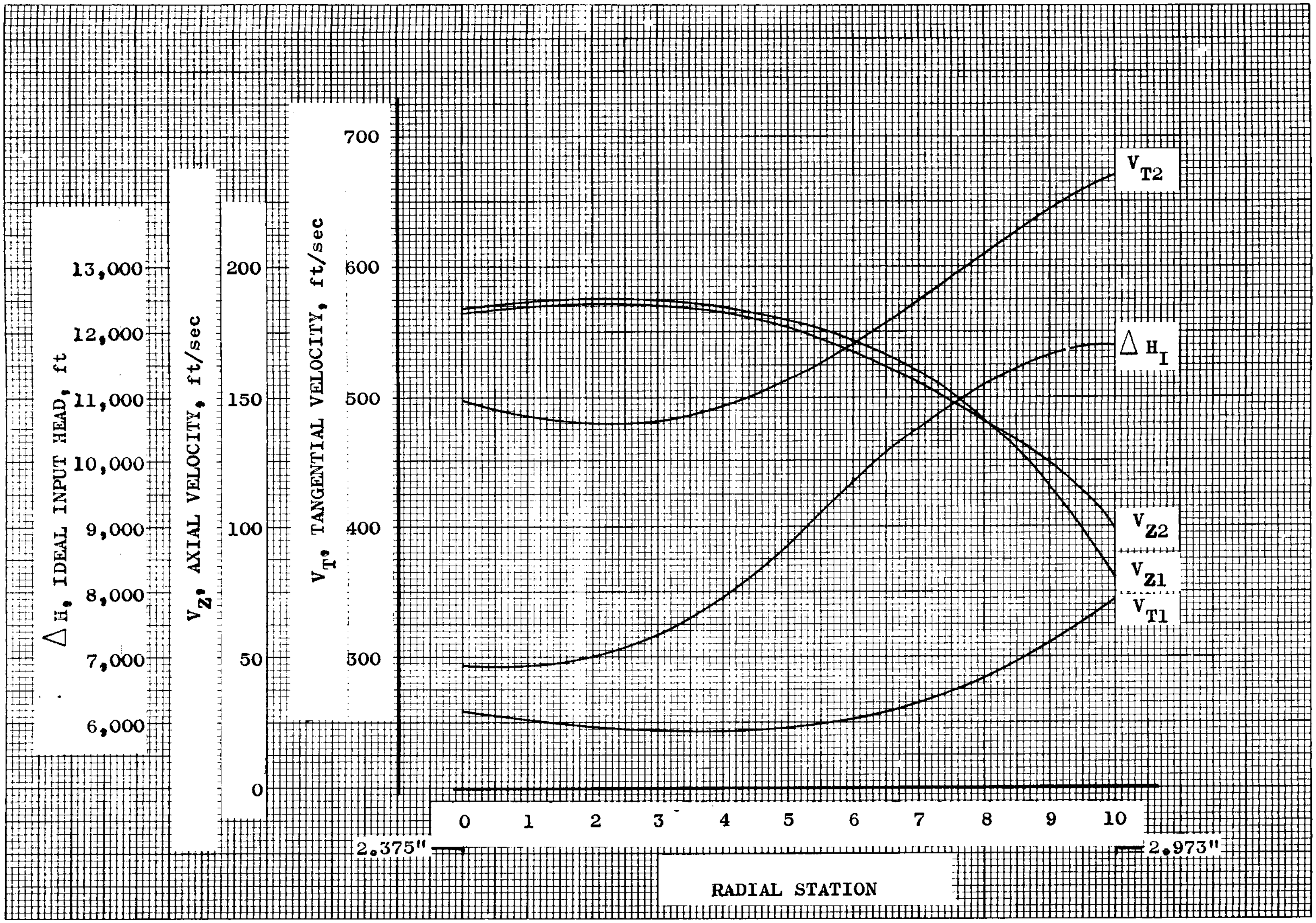

Figure 16. High-Speed Rotor Blade Element Data

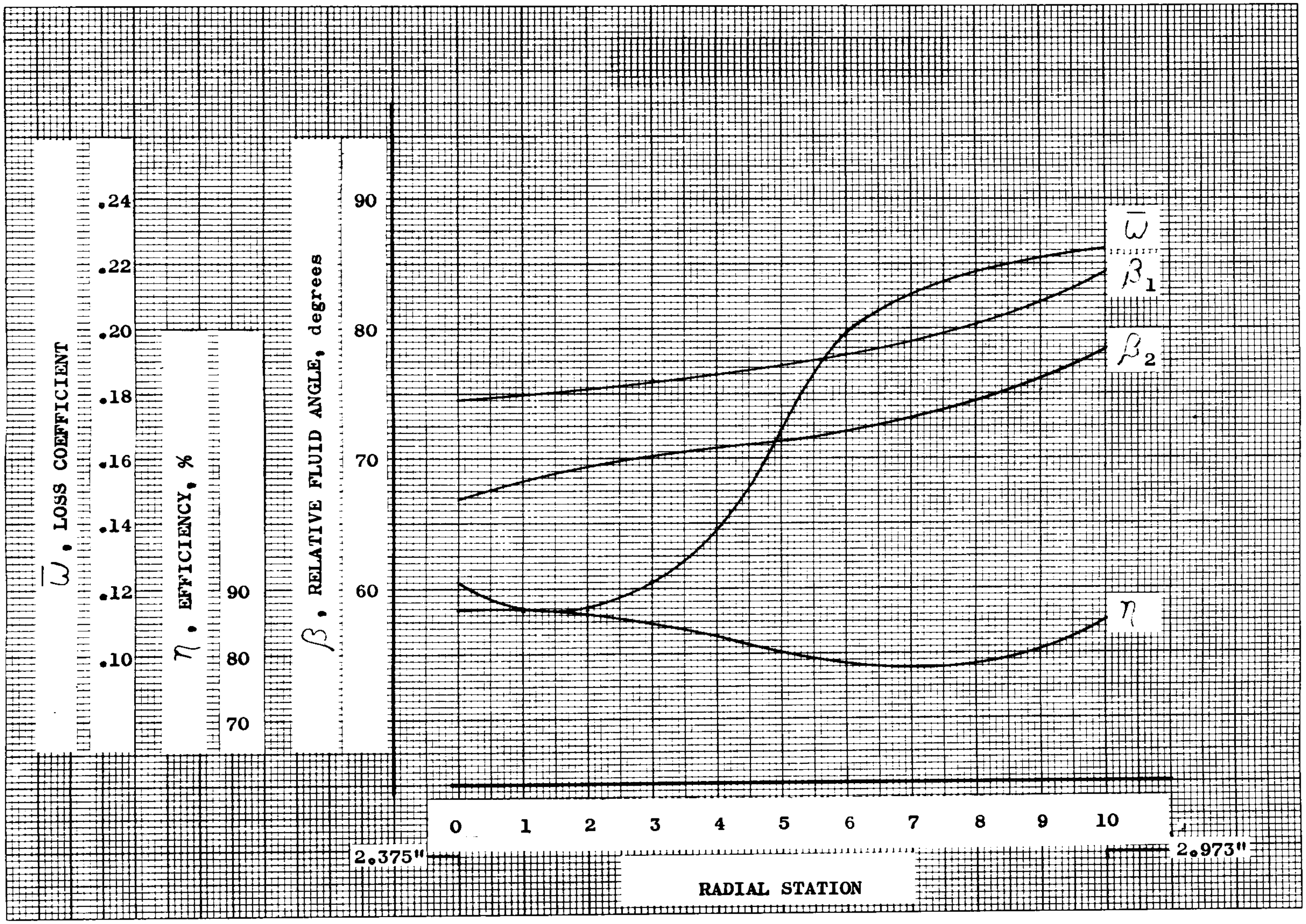

Figure 16. High-Speed Rotor Blade Element Data

distribution could be found which satisfied both radial equilibrium and continuity. This results in an axial velocity decrease from hub to tip.

The discharge axial velocity distribution was kept nearly equal to the inlet axial velocity distribution so that the streamline curvature through the blade row could be neglected. The blade loss coefficient ($\bar{\omega}$) was obtained from data for similar types of blades(37).

An existing method(38) was used to obtain the blade stagger and turning angles from the fluid relative flow angles. Figures No. 17 and No. 18 are extensions of two figures in the referenced work(39) and extrapolate the data into the high fluid inlet angle region (70-degrees to 90-degrees). The incidence angle was calculated from the following:

$$i = i_o + n\,\phi$$

where i_o is incidence at zero camber (Figure No. 17)

n slope factor (Figure No. 18

ϕ blade camber angle

The deviation angle was obtained from data for similar blade rows(40) and is shown on Figure No. 19. With both incidence and deviation angles known at each radial station, the blade stagger and camber angles could be calculated. Figure No. 20 shows stagger, camber, fluid, blade, incidence, and deviation angles at each radial station.

3. Hydraulic Turbine

The hydrodynamic design of the hydraulic turbine which drives the low-speed inducer through the outer shroud is discussed in this section.

The turbine is located directly downstream of the high-speed rotor and utilizes the full flow of the tandem inducer set. The design problem is to ascertain the blade geometry and the fluid exit conditions for a prescribed exit fluid angle and shaft power. The resulting design is a constant section untwisted blade with a blunt leading edge.

The following are the design criteria:

a. The design is weighted in favor of both simplicity and economy in construction at the expense of hydraulic efficiency.

---

(37) Sandercock, D. M. and Crouse, J. E., NASA TN D-2879, op. cit.
(38) NASA Sp-36, op. cit.
(39) Ibid., Figures No. 137 and No. 138
(40) Crouse, J.E. and Sandercock, D. M., Blade Element Performance of Two-Stage Axial-Flow Pump with Tandem-Row Inlet Stage, NASA TN-3962, May 1967

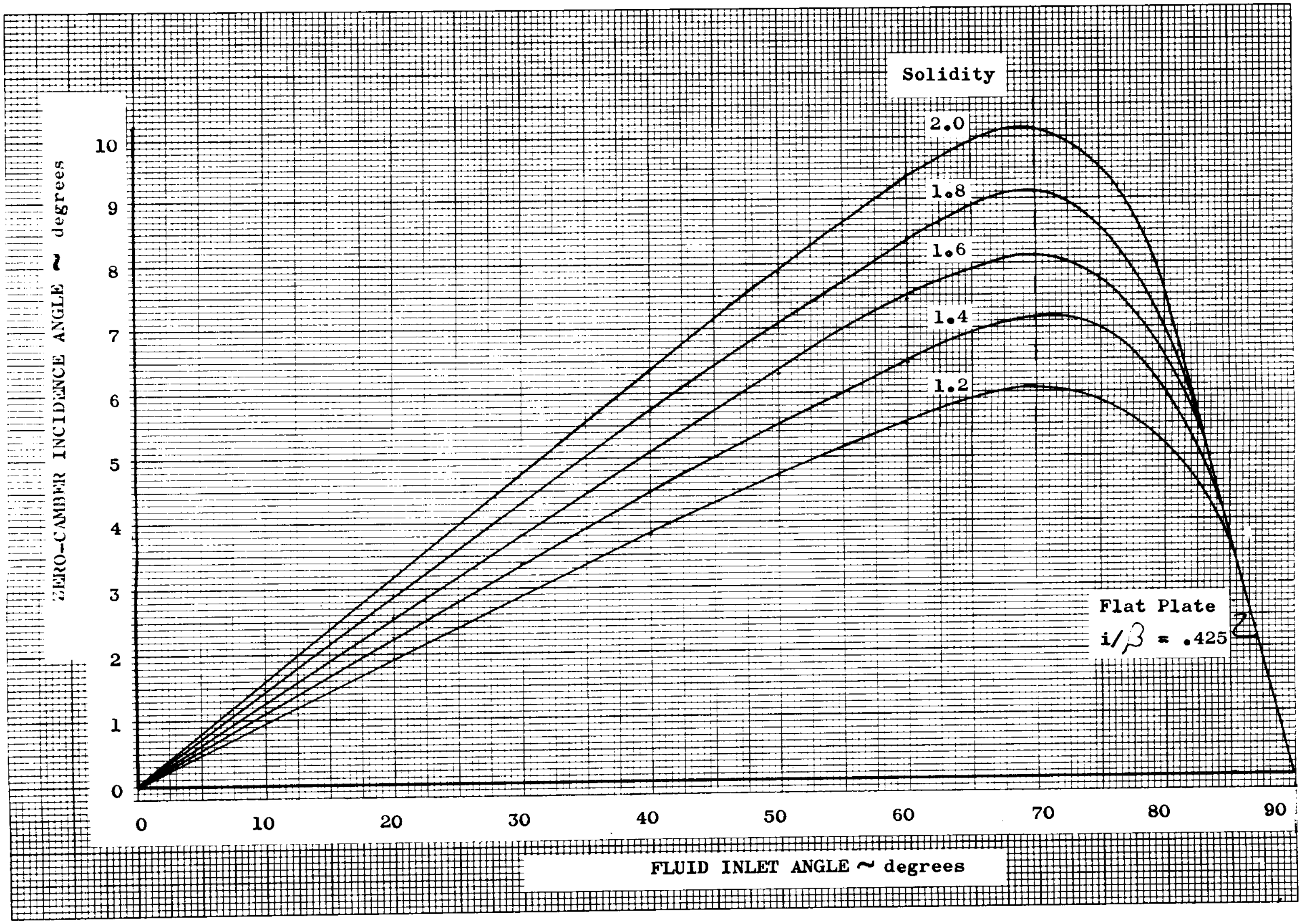

Figure 17. Extrapolation of Zero Camber Incidence Angle/Inlet Fluid Angle Curves

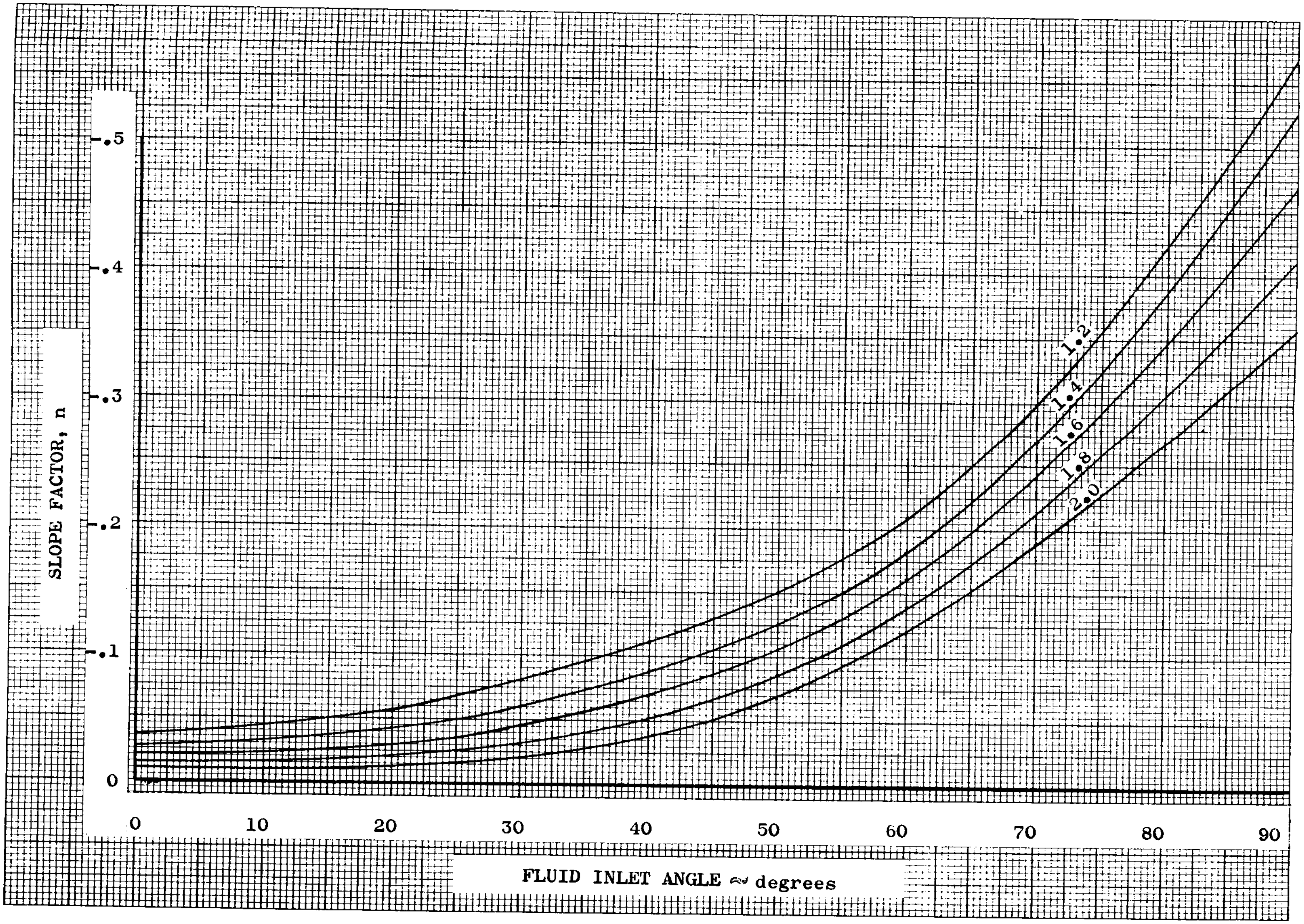

Figure 18. Extrapolation of Slope Factor/Inlet Fluid Angle Curves

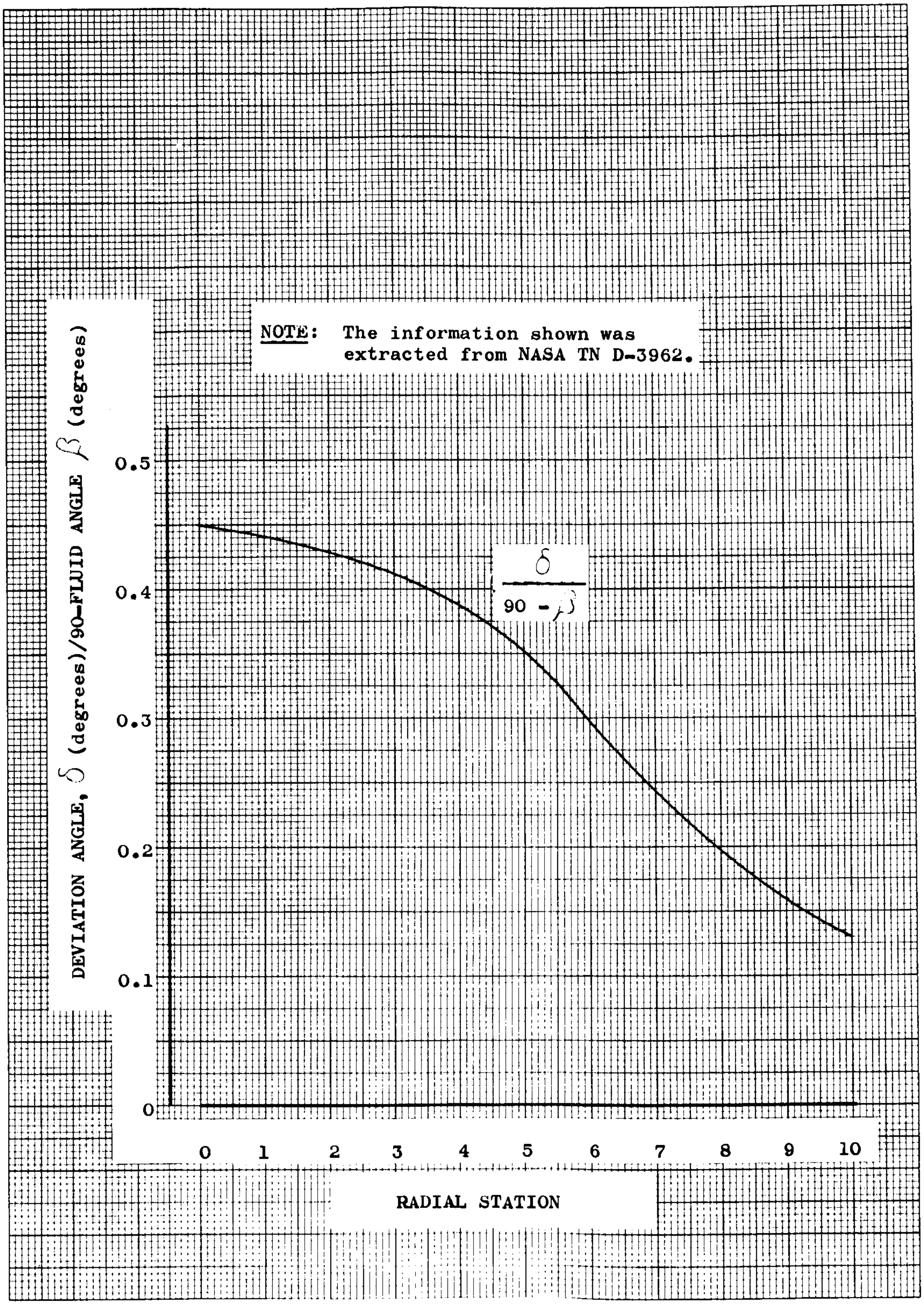

Figure 19. Blade Exit Flow Deviation Correlation Used for High-Speed Rotor Blade

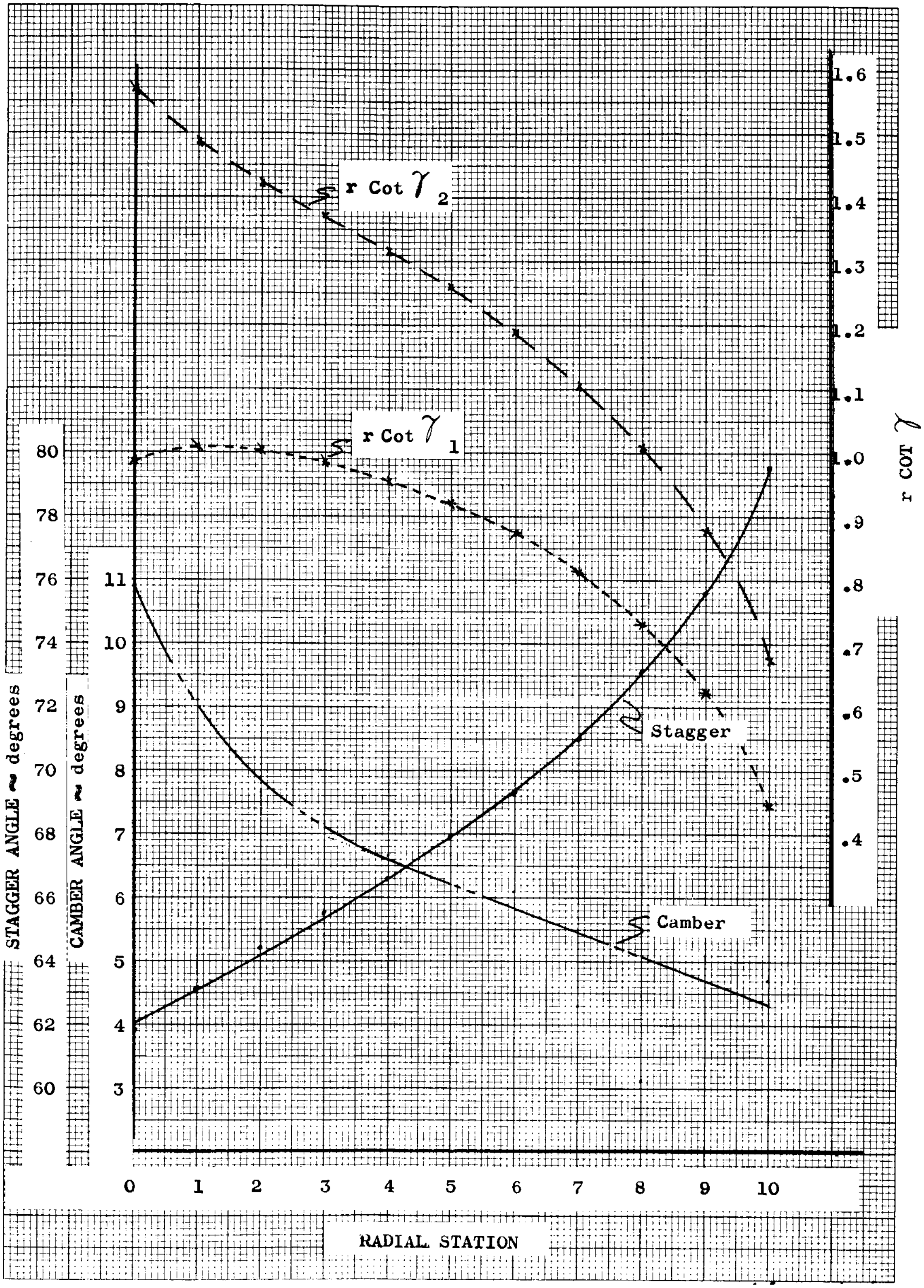

Figure 20. High-Speed Rotor Blade Element Data

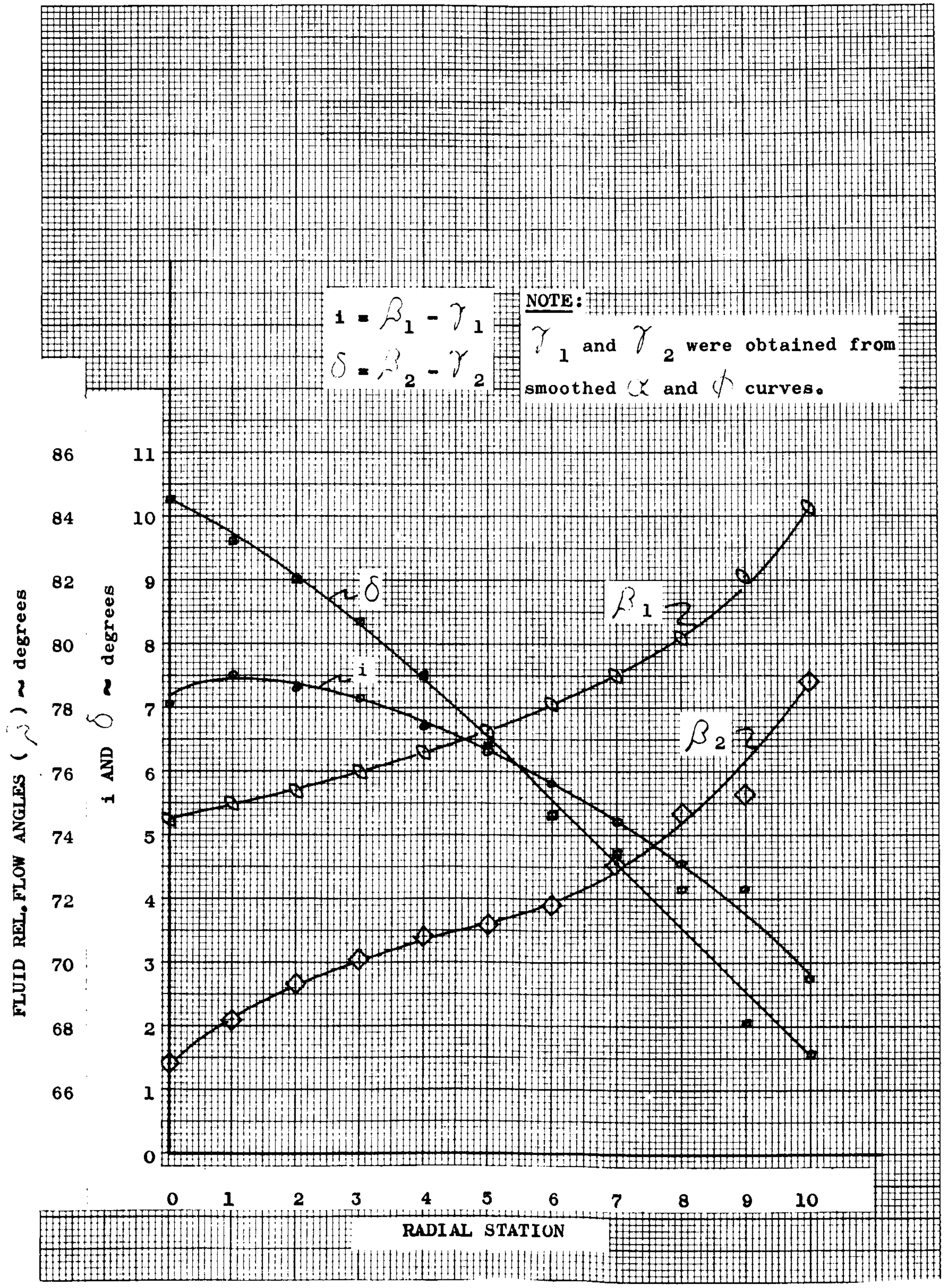

Figure 20. High-Speed Rotor Blade Element Data

b. Blade cavitation is avoided at design point operation.

c. Blade cavitation at off-design conditions is not investigated.

Both simplicity and economy in construction are achieved through the design of a constant section untwisted blade. A prime consideration in designing the profile shape is the wide variation of inlet fluid angle along the height of the blade. As illustrated by Figure No. 21, the relative fluid angle varies 40-degrees between hub and tip radii. A blunt leading edge is used to accommodate this wide variation with minimum incidence loss. This type of blunt rotor profile was utilized for the design of the oxidizer turbopump turbine of the M-1 engine(41)(42). At low relative inlet Mach number, the design point performance of blunt profiles is equal or superior to sharp blading edge profiles while the off-design performance or operation under incidence is superior.

A one-dimensional analysis is used to determine design point mean line velocity triangles and blade losses. The fluid is considered incompressible. Table VII lists the one-dimensional design point conditions.

These conditions fix the inlet velocity triangle. The exit velocity triangle is fixed by the shaft power requirement and the mass flow. A system which was developed for gas turbine design(43) is utilized for the loss estimates. The blade Reynolds Number and Mach Number are within the limitations of the system. The design point velocity triangles are shown on Figure No. 22.

Two-dimensional calculations are used to determine exit fluid conditions over the blade height. Two-dimensional inlet fluid conditions are calculated as outlined in Appendix B for the high-speed rotor design. The fluid is considered incompressible and the turbine blade calculations also are made by the method outlined in Appendix B. Blade row losses are taken from the previous one-dimensional analysis. A constant discharge blade angle was desired for simplicity and fabrication economy. Therefore, the exit through flow velocity was adjusted to produce a constant discharge fluid angle. Good agreement between the one-dimensional and two-dimensional analyses is obtained. The input heads agree within 1%. Blade and channel geometry are shown on Figure No. 23

4. Discharge Housing

The discharge housing is a nonoptimum hydraulic design. In an actual pump application, the turbine would discharge into the inlet of the

---

(41) Beer, R., NASA CR-54764, op. cit.

(42) Roelke, R. J., et.al., NASA TN D-3368, op.cit.

(43) Beer, R., NASA CR-54764, op. cit.

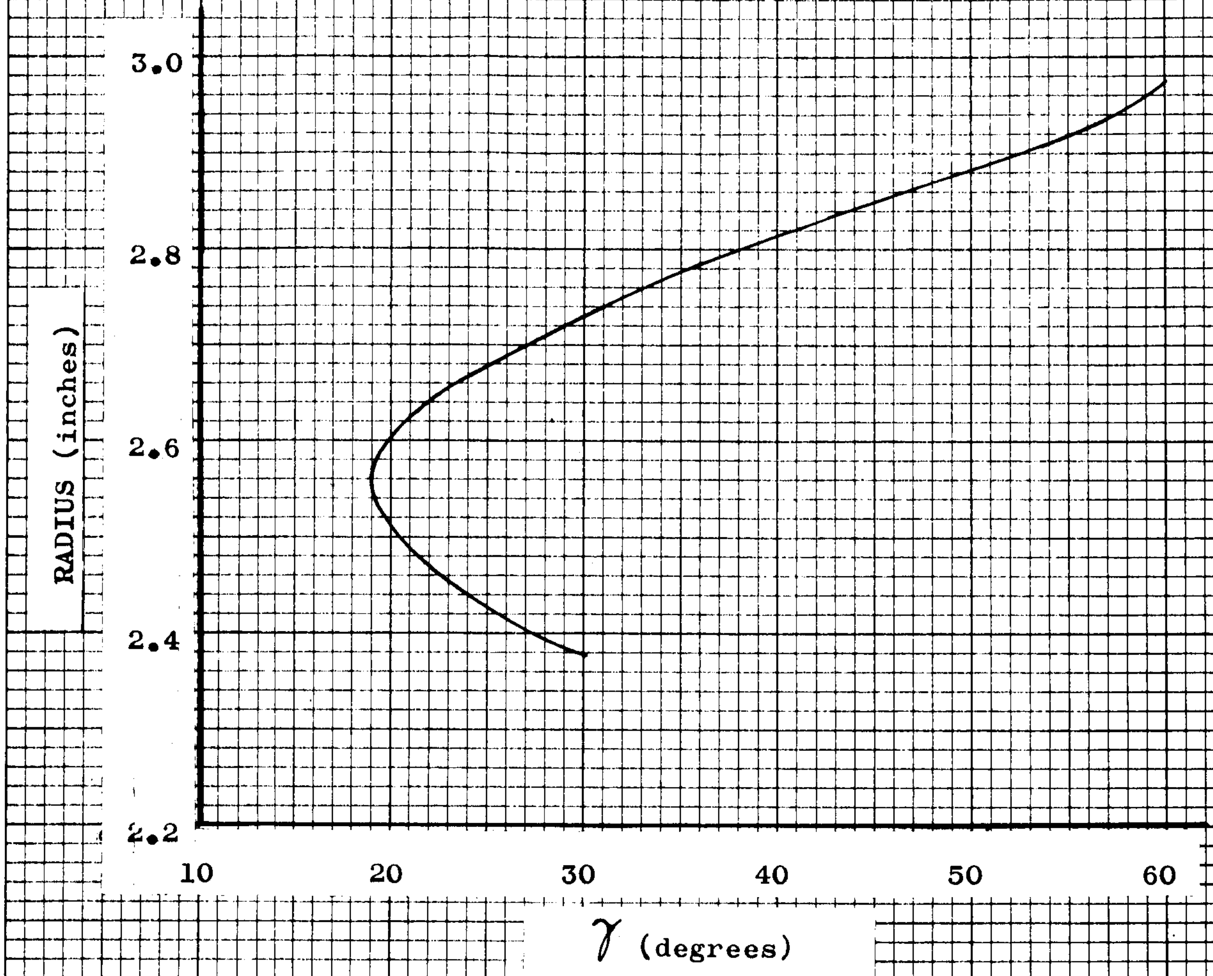

Figure 21. Hydraulic Turbine Inlet Relative Flow Angle Distribution

TABLE VII

HYDRAULIC TURBINE DESIGN POINT

FLOW CONDITIONS AT MEAN DIAMETER

Inlet Fluid Temperature	°F	-420.3
Inlet Fluid Density	lb_m/ft^3	4.35
Inlet Absolute Velocity	ft/sec	564
Inlet Relative Velocity	ft/sec	191
Rotational Speed	rpm	18,800
Mean Diameter	in.	5.38
Mean Diameter Blade Speed	ft/sec	441
Fluid Angle(*)	degrees	73.2
SHP	HP	375

(*) Measured from axial plane

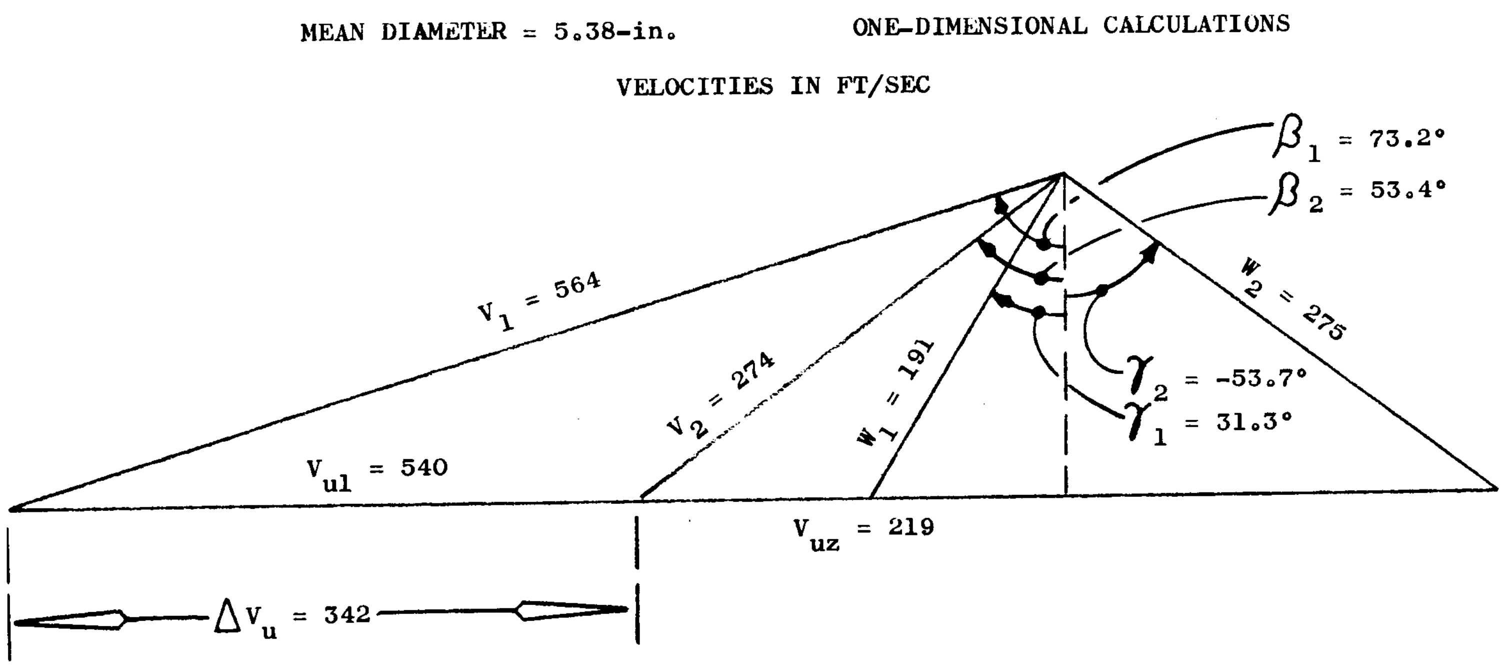

Figure 22. Hydraulic Turbine Design Point Velocity Triangle

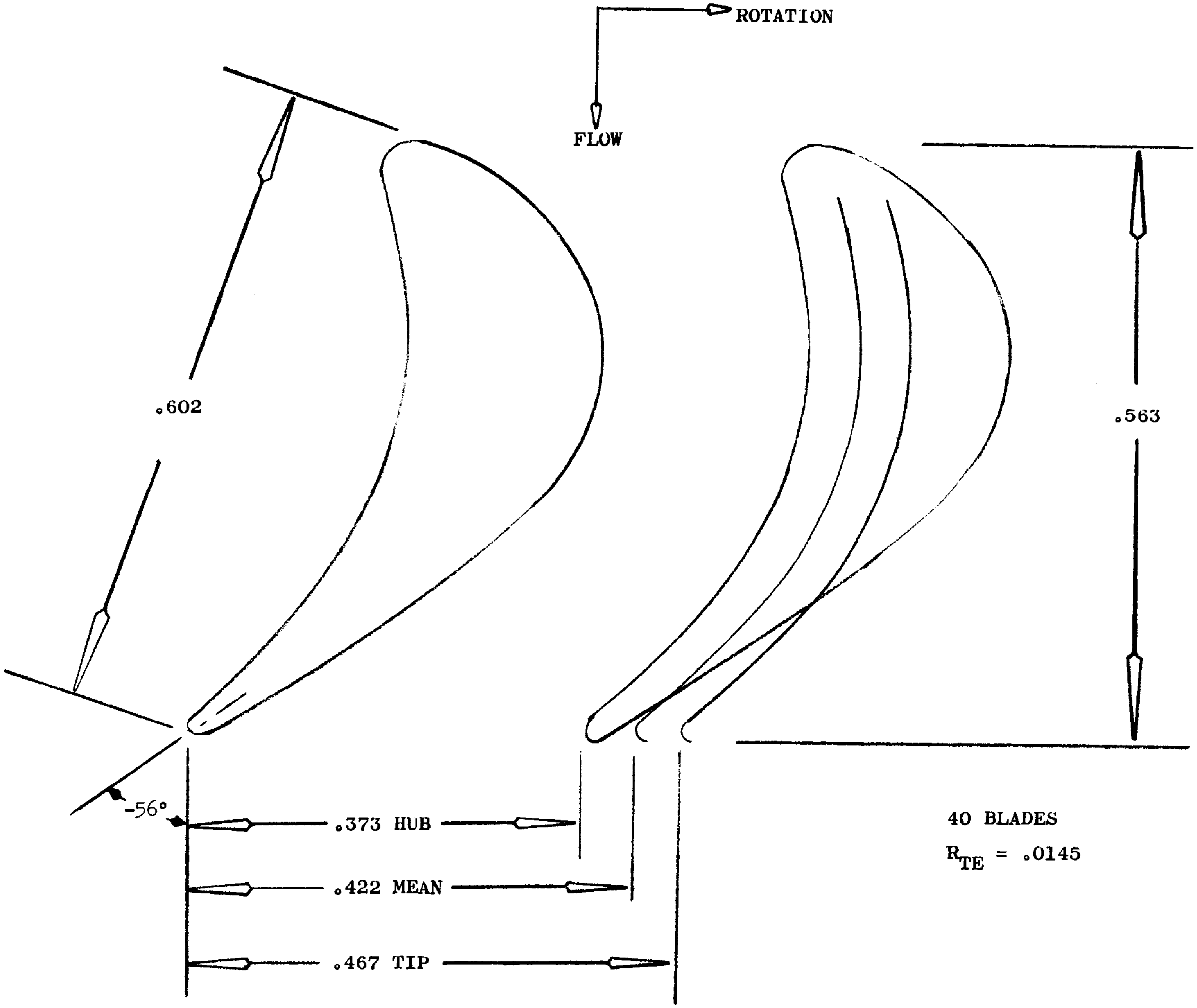

Figure 23. Hydraulic Turbine Blade and Channels

main high-speed pump, either centrifugal or axial. The housing in this application was designed to turn the flow radially in the shortest axial length to obtain minimum high-speed rotor shaft length.

The guide vanes were placed to give the housing sufficient strength and also provide a passage, through which the rear hydrostatic bearing flow could be passed. The mean camber line angle of these vanes was established to match the turbine discharge flow assuring free vortex flow in a constant height channel. The loading edge radii were deliberately made large and the blade row solidity was kept low to assure that the vanes would not stall or have large shifts in performance at off-design flow.

C. MECHANICAL LAYOUT

1. Over-All Design

Figure No. 1 shows sectional views of the major pump components. The drive unit, which is shown in phantom, is a slightly modified NERVA technology turbopump turbine/bearing housing assembly. This tester will be driven by an electric motor for the steady-state testing and driven by a turbine for the transient testing. This turbine will be the first-stage wheel of the NERVA assembly and gaseous nitrogen will be used to power it. For liquid hydrogen testing, the turbine can be powered using either gaseous nitrogen or gaseous hydrogen.

Most of the components will be fabricated from 606 Al, except for the high-speed rotor (7079 Al) and the rear instrumentation cluster (CRES 416). The 416 stainless steel was selected for the instrumentation cluster to permit the hardware to be used for liquid hydrogen operation with rolling element bearings. The 6061 Al was selected because both plate and rod can be obtained in various sizes and it has good machining as well as welding characteristics. The low-speed inducer is the highest stressed 6061 component and has an estimated fatigue safety factor of 1.59 in liquid hydrogen at the design speed. Only the high-speed rotor was stressed higher than the maximum 6061 safety limit would allow; therefore, 7079 Al was used. Operation at cryogenic temperatures will be possible because at large radii, all components are of the same material.

The pump will have a centerbody at the inlet supported by inlet vanes. This centerbody serves two purposes; it allows pressure measurements to be taken between the high-speed rotor and the low-speed inducer and provides bearing support for the back-up rolling element bearings.

Total pressure measurements at three radial stations (20%, 50%, and 80%) plus the static wall at the hub will be recorded at the high-speed rotor inlet, the high-speed rotor discharge, and the turbine discharge. These measurements will be used to determine blade row performance during the steady-state testing.

High-speed rotor rotational speed and torque will be measured on the input shaft (tester unit) and the low-speed rotor rotational speed will be measured at the shroud just ahead of the front hydrostatic bearing.

2. Prony Brake

The Prony Brake will be used to measure torque during steady-state testing. Essentially, the two rotors remain at the same speed ratio during steady-state, even at off-design conditions. It will be necessary to apply an additional load upon the hydraulic turbine by using the Prony Brake to obtain the effect of blade interaction at speed ratios which are different from that of design. In addition, the Prony Brake will be used to calibrate the turbine when the inducer is removed. The braking action is accomplished by means of caliper action on a rotating steel disc, which is an integral part of the hydrostatic axial thrust ring. After the tests requiring the use of the Prony Brake are concluded, the steel ring will be replaced with a 6061 Al ring.

The torque force will be translated into a pressure reading by means of a piston-cylinder arrangement. The piston end attaches to the brake and the cylinder end to the housing. The pressure, which will be directly proportional to torque, will be measured at the cylinder end. To null-out the effect of internal housing pressure upon the piston, a second piston-cylinder arrangement is mounted in direct opposition and the cylinder will be vented to ambient. This second piston-cylinder will be used for check-out and angular alignment.

The Prony Brake will be actuated by remote-controlled pressure supplied to six pistons mounted in the torque ring. These pistons will close the brake in a caliper-like action and compression springs will open the brake when the supply pressure is removed.

The brake consists of eight separate pads on each side of the rotating disc. These pads are made of metal-impregnated asbestos compound. With the cylinder pressure differential set at 175 psi, the normal force upon the rotating disc will be 465 lb, which results in a torque force of 93 lb at the mean radius.

The brake will be cooled by water flowing from the hydrostatic bearings into the pump discharge housing. Provision has been made to plug the passage between the Prony Brake cavity and the pump discharge housing, thereby permitting the flow to be returned to the bearing supply or dumped overboard.

3. Hydrostatic Bearings

Hydrostatic thrust bearings and journal bearings are used to support the low-speed assembly (i.e., low-speed inducer, hydraulic turbine, and connecting shroud). To verify the concept, a hydrostatic bearing parametric analysis was conducted to select fluid film bearings that would provide optimum minimum flow rate and maximum load carrying performance while satisfying the basic system geometry. The preliminary geometry of the inducer, the turbine, and the shroud assembly was designed and estimates of the axial and radial forces, weights and inertias were made so that the study would cover a useful range of expected operation.

Fluid film bearings have freedom for an infinite variety of geometry combinations; therefore, it was necessary to restrict and select appropriate parameters for investigation. First, the bearings to be analyzed were single-row, recess-orifice-compensated, hydrostatic journal and thrust bearings. For the journal bearings, the diameter and length were given as:

Inlet Journal	Diameter	8.1-in.
	Length	1.6-in.
Exit Journal	Diameter	6.5-in.
	Length	1.25-in

For the thrust bearing, the inside and outside diameters were given as:

Thrust Bearing	Inside diameter	6.9-in.
	Outside diameter	9.5-in.

The journal and thrust bearings considered had eight recesses and three recess geometries, ranging from narrow land to wide land configurations (0.2, 0.3 and 0.4). Each bearing was analyzed at one operating speed for each lubricant; 3600 rpm for water and 12,700 rpm for liquid hydrogen. For the journal bearings, a range of operating clearances was selected (0.002-in. to 0.008-in. in steps of 0.002-in.) and a range of bearing pressure drops (50 psi to 200 psi in 50 psi increments), which from preliminary estimates appeared to be adequate for load capacity and flow rate range. Three pressure ratios were used (0.2, 0.3, and 0.4). This is the ratio of recess pressure to supply pressure in the zero eccentricity position for a journal bearing obtained from previous analyses and other investigators(44). These ratios should cover the optimum design compromise for minimum flow to maximum stiffness.

The load direction was between the recesses; therefore, a minimum load capacity and stiffness value was obtained. For each parameter variation, a set of performance data was obtained at eccentricity ratios from 0.0-in. to 0.9-in. in increments of 0.1-in. where eccentricity ratio (e/c) is the ratio of eccentricity (e) to radial clearance (c). The following is a summary of the parametric cases for the journal bearings:

---

(44) Young, W. E., Investigation of Hydrostatic Bearings for Use in High Pressure Cryogenic Turbopumps, Contract AF 04(611)-11406, Semi-Annual Report AFRPL-TR-66-302, 1966

Parameters Considered	No. of Cases Per Parameter	Total Cases Considered	Added Cases Considered for Different Bearing Types and Lubricants	
1 diameter, 1 width, 1 number of recesses, 1 speed	1	144 cases	2 journal bearings (inlet and exit) 288 cases	2 lubricants (water and liquid hydrogen) 576 cases
3 recess geometries	3			
4 radial clearances	4			
4 supply pressures	4			
3 pressure ratios	3			
1 load orientation	1			

Thrust bearing data was obtained for single-acting thrust bearings at eight orifice sizes. For each parameter variation, a set of performance data was obtained at axial clearances starting at .010-in. decreasing to .001-in. in increments of .001-in. The following is a summary of the parametric cases for the thrust bearings:

Parameters Considered	No. of Cases Per Parameter	Total Cases Considered	Added Cases Considered for Different Lubricants
1 set of radii, 1 number of recesses	1	96 cases	2 lubricants (water and liquid hydrogen) 192 cases
3 recess geometries	3		
8 orifice sizes	8		
4 supply pressures	4		

For the journal bearing, data was obtained from the computer model assuming incompressible turbulent flow. For the thrust bearing, laminar or turbulent incompressible flow was assumed.

The results of the parametric study showed that hydrostatic bearings could be used in this application. Some additional analysis will be made when designing for hydrogen testing to size the orifice diameter and the pocket recess depth. The recommended running clearance of .003-in. for the journal bearing at design speed must account for the shroud growth.

The selected hydrostatic bearings for water testing were analyzed with the exact design dimension. The performance of the journal bearings is shown on Figures No. 24 and No. 25 while the performance of the axial thrust bearings is shown on Figure No. 26. The calculated axial thrust at the design condition will be 2500 lb toward the pump suction. The maximum load capacity toward suction of 5000 lb will be sufficient because the maximum axial thrust at off-design for this type of assembly is normally less than 1.5 of the design point thrust. Additional thrust capability can be realized by increasing the supply pressure. During testing, the pocket pressure will be monitored and the supply pressure increased whenever the ratio of pocket to supply pressure exceeds the design value.

4. Rolling Element Bearings

Provisions have been made to use rolling element bearings as a back-up design. For the water test, these bearings will be radial ball, water-lubricated, grease-packed, 5200 steel bearings, with non-metallic separators. The front bearing will ride on the centerbody supporting the inducer end. The back bearing will ride on the aft instrumentation cluster in the same place as the labyrinth. Both are shown on Figure No. 1.

If the rolling element bearings are used, the testing of the turbine alone will be eliminated because there is no convenient way to support the inducer end.

When the inducer assembly is tested in liquid hydrogen, the bearings will be replaced with ones made from stainless steel 440C, which will be lubricated by hydrogen flow.

Again, it should be noted that the concept of a full-flow, hydraulic-turbine-driven inducer can be better designed when hydrostatic bearings are used on the shroud. This eliminates the inlet support vanes and centerbody and does not limit the inducer-turbine speed because of high bearing DN.

5 Stress and Critical Speed

The three major components (low-speed inducer assembly, high-speed rotor, and high-speed shaft assembly) were stress analyzed at both water test speed and hydrogen test speeds. The low-speed inducer assembly has a fatigue factor of safety of 1.59. The highest stress levels were at the blade root at the inducer inlet. The high-speed rotor disc has a burst speed of approximately 86,000 rpm, which is well above the design speed of 44,500 rpm. The blades show a factor of safety of approximately 7 at a total average stress of 6.35 ksi and a alternating stress of .75 ksi. The high-speed shaft assembly has a lateral vibration critical speed of 36,000 rpm to 42,000 rpm depending upon the effective shaft stiffness. If the drive turbine (NERVA Technology Turbine Wheel P/N 294332) were redesigned for a smaller, lighter wheel, the drive assembly would be capable of operating at the design speed.

NOTES:

1. NUMBER OF POCKETS - 8
2. LOAD APPLIED BETWEEN POCKETS
3. WATER LUBRICATED
4. SUPPLY PRESSURE - 315. PSI
5. EXIT PRESSURE - 115. PSI
6. PRESSURE RATIO - .1
7. LOCAL CLEARANCE - .003-IN.

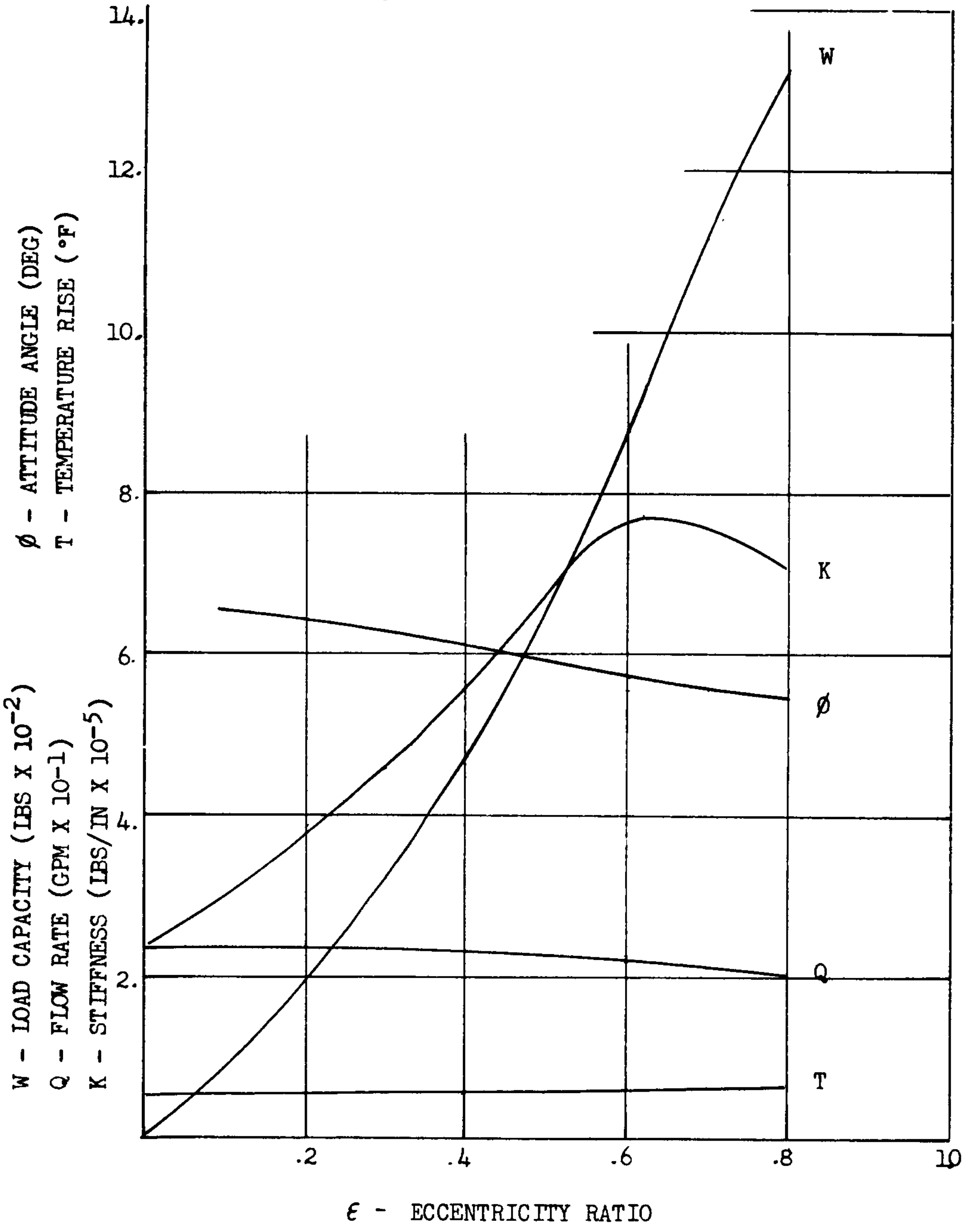

Figure 24. Inlet Hydrostatic Journal Bearing Performance

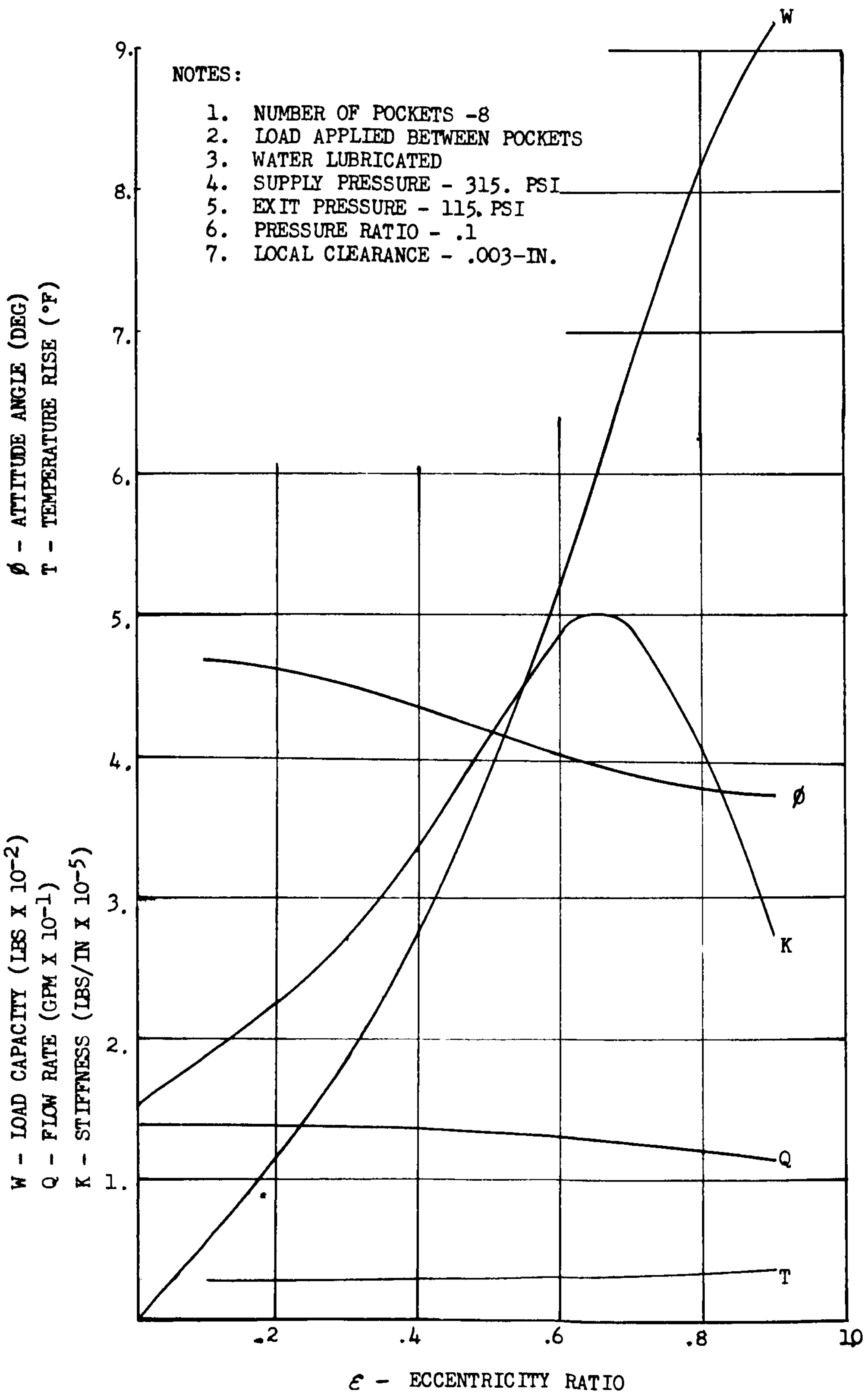

NOTES:

1. NUMBER OF POCKETS -8
2. LOAD APPLIED BETWEEN POCKETS
3. WATER LUBRICATED
4. SUPPLY PRESSURE - 315. PSI
5. EXIT PRESSURE - 115. PSI
6. PRESSURE RATIO - .1
7. LOCAL CLEARANCE - .003-IN.

Figure 25. Exit Hydrostatic Journal Bearing Performance

NOTES:

1. NUMBER OF POCKETS - 8
2. WATER LUBRICATED
3. SUPPLY PRESSURE - 315. PSI
4. EXIT PRESSURE - 115. PSI
5. TOTAL CLEARANCE - H_T = .008
6. ORIFICE DIAMETER - D_o = .080

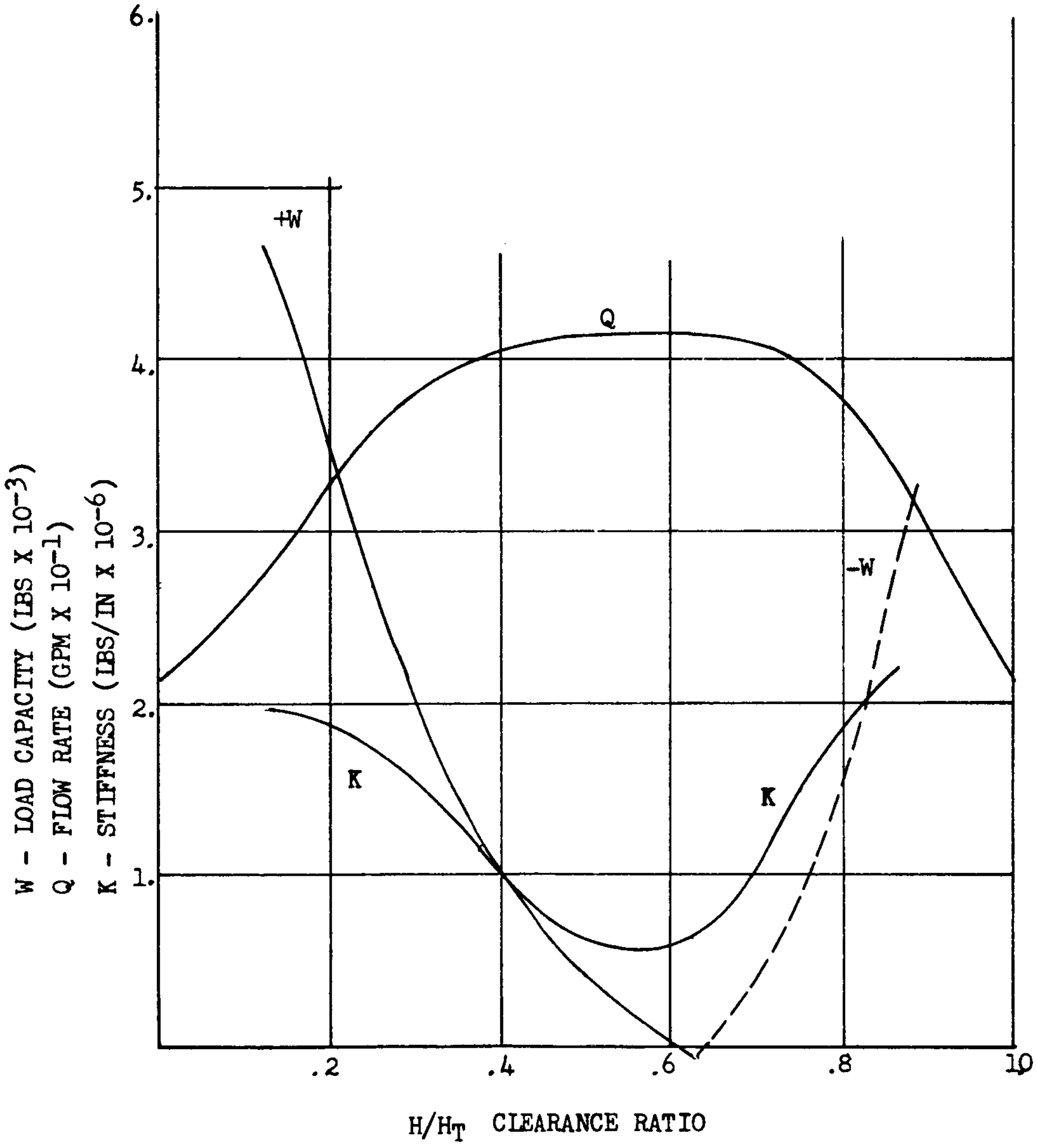

Figure 26. Double-Acting Thrust Bearing Performance

The low-speed shroud deflection at design speed operation is not uniform over the width of the forward hydrostatic bearing. The change in deflection is negligible under the rear bearing. For liquid hydrogen operation, the front hydrostatic bearing will either be machined conically for a consistent clearance on each side, or machined straight with some compromise in clearance and flow. This will compensate for an estimated coning type deflection under the bearing of .001-in. Deflection of the thrust bearing is negligible.

D. OFF-DESIGN PERFORMANCE

Performance curves to describe the non-cavitating and cavitating performance of each of the blade rows and the discharge housing were prepared. Tabular data was read from these curves for use on the computer model and the parametric studies discussed in Sections IV and V. Similar nomenclature and format were used for each blade row and the housing to simplify the handling of program input and calculations. The following is a listing of the type of plots prepared and a description of the nomenclature:

Parameters	Description
H/N^2 vs Q/N for parameters of N_2/N_1	Head rise (or reduction) flow/rate speed ratio characteristics, normalized for speed.
$T/\rho\ N^2$ vs Q/N for parameters of N_2/N_1	Torque/flow rate/speed ratio characteristics, normalized for speed and fluid density.
$\Delta H/NPSH$ vs S for parameters of N_2/N_1 and Q/N	Head loss caused by cavitation/suction specific speed/flow rate/speed ratio characteristics, normalized for speed.
$\Delta T/\rho\ NPSH$ vs S for parameters of N_2/N_1 and Q/N	Torque reduction caused by cavitation/suction specific speed/flow rate/speed ratio characteristics, normalized for speed and fluid density.

NOMENCLATURE

H	Head rise, ft
N	Blade row shaft speed, rpm
N_2/N_1	Low-speed shaft/high-speed shaft speed ratio
Q	Delivered flow rate, gpm
T	Shaft torque, ft-lb

NOMENCLATURE

ρ	Fluid density, lb/ft^3
ΔH	Head reduction caused by cavitation, ft
NPSH	Net positive suction head, ft
S	Suction specific speed, $(rpm)\,(gpm)^{1/2}/(ft)^{3/4}$

The inverse of the speed ratio discussed in Section I,A was used for convenience in calculating. (The high-speed shaft/low-speed shaft speed ratio becomes infinite when low-speed shaft speed is zero.) For the discharge housing, the high-speed shaft speed was used to obtain H/N^2, $T/\rho N^2$ and Q/N parameters.

The above design parameters are based upon assumptions of dynamic similarity. Two types of deviation from the similarity assumptions were investigated; both types having to do with boundary layer effects. One is a correction to account for variations in the blade annulus axial velocity profile caused by variations in annulus Reynolds Number under both steady-state and transient conditions. The other correction is for variations in blade loss coefficients caused by corresponding changes in blade chord Reynolds Number.

The following discussions describe the analyses and resulting performance predictions for each blade row, the discharge housing, the over-all pumping system, and the associated blade row performance dissimilarities caused by Reynolds Number effects.

1. Low-Speed Inducer

Because of the relatively high stagger angle and large secondary flows present in the helical inlet portions of the blading, empirical data (based upon available inducer test information) were used to establish off-design characteristics rather than airfoil blade cascade data. The following is a summary of these sources:

Parameters	Figure No.	Reference
$H/N^2 - Q/N$	27	(45)(46)
$T/\rho N^2 - Q/N$	28	(47)
$\Delta H/NPSH - S$	29	(48)
$\Delta T/\rho\ NPSH - S$	30	(49)

It was assumed that the ideal head rise curve followed a relationship established by a constant blade exit relative flow angle (constant fluid/blade flow deviation angle). The actual head rise for the H/N^2 parameter was obtained from a correlation of the referenced data for a mixed-flow impeller of similar specific speed. The following correlation was used:

$$\eta/\eta_{pk} = f(\psi/\psi_{i_{pk}})$$

η - efficiency

ψ - head coefficient

Subscript - i-ideal

pk refers to peak efficiency point

Data from the Marman reference was used to obtain the empirical curve, which then was applied to the low-speed inducer ideal head values to obtain the curves shown on Figure No. 27. Some extrapolation of the data in the high Q/N and negative H/N^2 region was necessary to establish predictions for extreme peripheral operation which might be encountered during start-up and shutdown. For this purpose, Swanson's performance data for a 7500 specific speed (rpm) $(gpm)^{1/2}$ $ft^{3/4}$ mixed flow pump was used as a guide.

---

(45) Marman, H. W., et al., Development Tests of the TP-1 Liquid Metal Turbopump Components, Report PWAC-318, Pratt and Whitney Aircraft, Middletown, Conn., 30 June 1961, Figure 74, p 143

(46) Swanson, W. M., "Complete Characteristics, Circle Diagram for Turbomachinery," Trans. ASME, Vol. 75, 1953, pp 819-826

(47) (U) Phase II, Final Report on the Design and Evaluation of a Low Speed Hydraulic Turbine-Driven Pump Discharge Fed Inducer Stage, Contract AF 04(611)-7446, Aerojet-General Corp. (Confidential Report)

(48) Blakis, R., et al, Initial Test Evaluation of the M-1 Liquid Hydrogen Turbopump, Including Installation, Test Procedures, and Test Results, NASA Report CR-54827, 20 July 1967

(49) (U) Phase II, Final Report on the Design and Evaluation of a Low Speed Hydraulic Turbine-Driven Pump Discharge Fed Inducer Stage, (Confidential Report), op. cit.

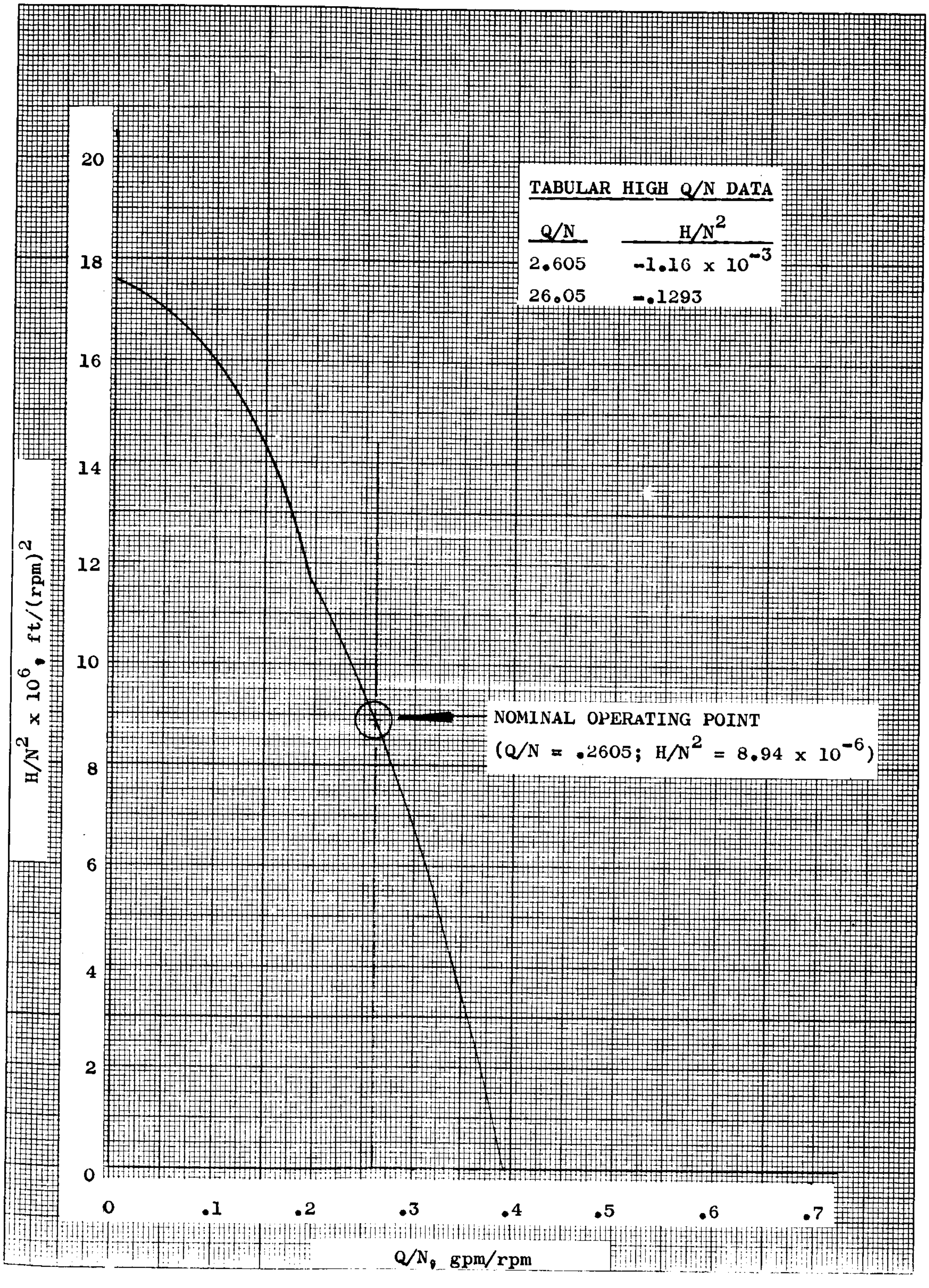

Figure 27. Low-Speed Inducer H/N^2 vs Q/N

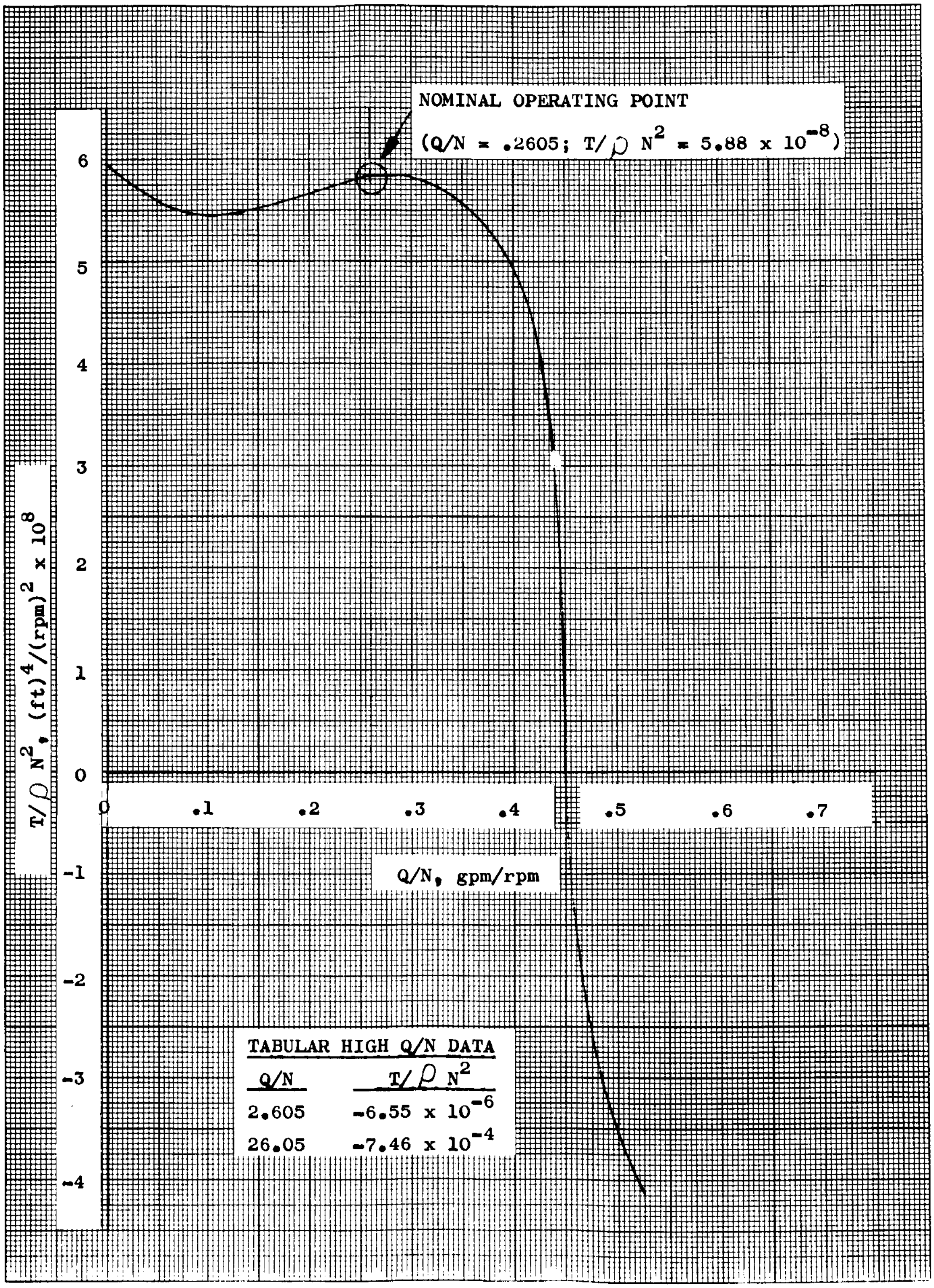

TABULAR HIGH Q/N DATA

Q/N	$T/\rho N^2$
2.605	-6.55×10^{-6}
26.05	-7.46×10^{-4}

Figure 28. Low-Speed Inducer $T/\rho N^2$ vs Q/N

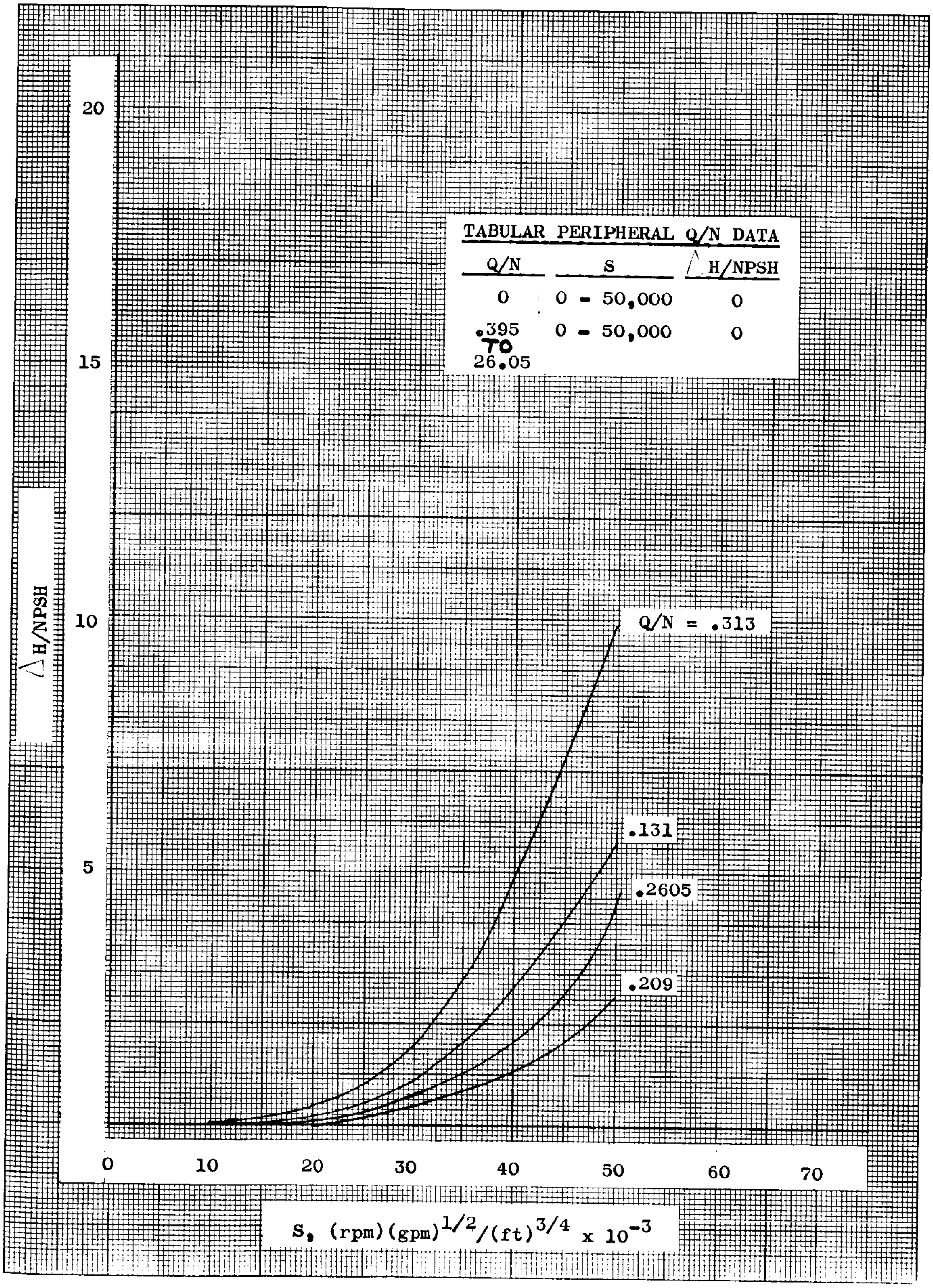

Figure 29. Low-Speed Inducer ΔH/NPSH vs S

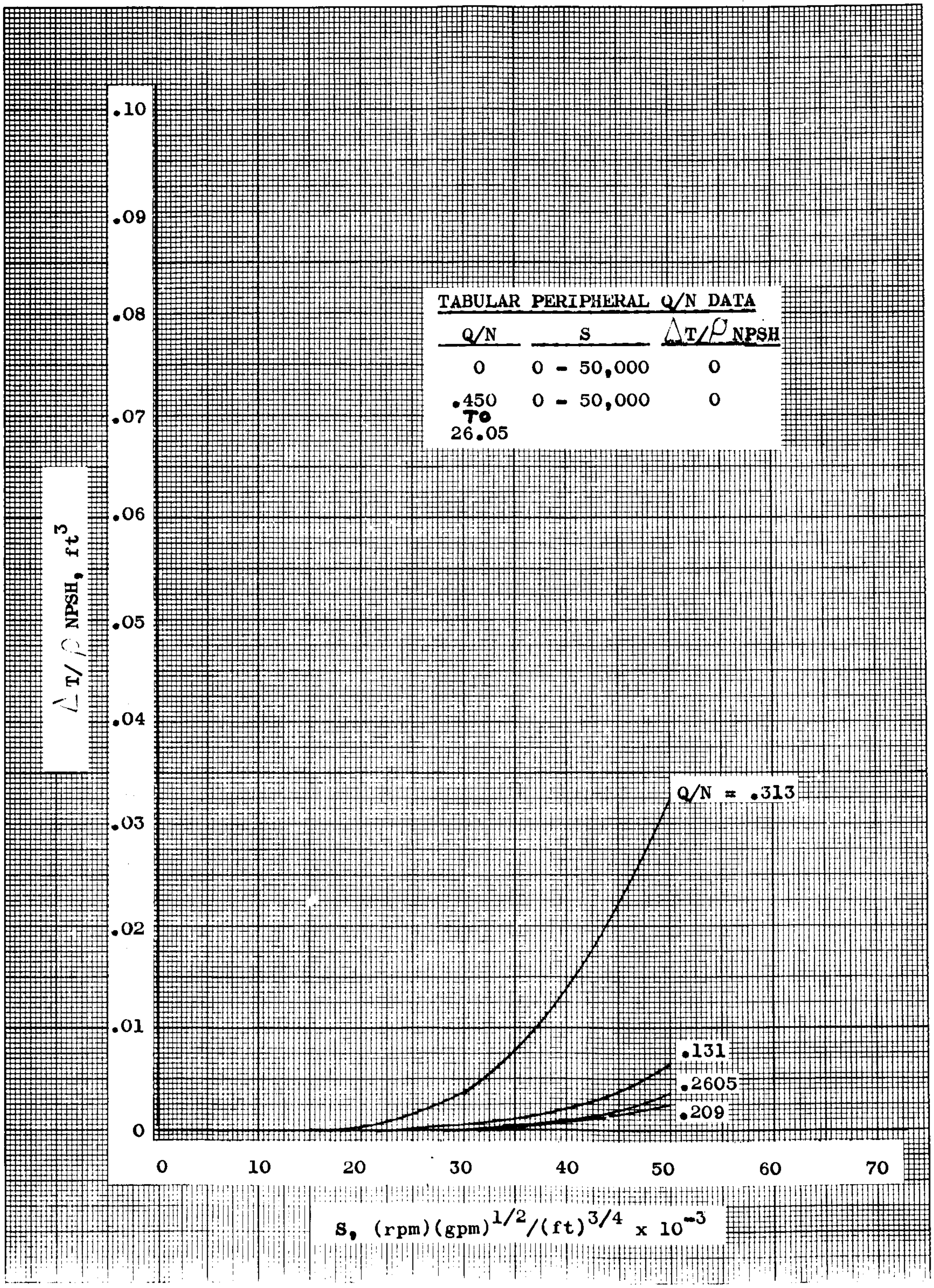

TABULAR PERIPHERAL Q/N DATA

Q/N	S	$\Delta T/\rho$ NPSH
0	0 - 50,000	0
.450 TO 26.05	0 - 50,000	0

Figure 30. Low-Speed Inducer $\Delta T/\rho$NPSH vs S

The actual inducer head rise parameter was reduced to account for losses in the inducer/high-speed rotor inter-stage passage. These losses were assumed to be 10% of the inducer mean line exit fluid velocity head at the design point. All the head parameter values were multiplied by a fixed value to obtain a consistent design point value. Consequently, the efficiency includes the effect of this added loss when calculated from the head and torque of the inducer.

To obtain the $T/\rho N^2$ predictions, the torque at less-than-design flow coefficient conditions was altered from the velocity diagram value to agree with the torque data of the partial-flow, hydraulic-turbine-driven boost pump designed and developed for another program(50). This data shows that the actual torque exceeds the velocity diagram value by increasing amounts as the zero flow coefficient point is approached. The correlation:

$$\psi_{TORQ}/\psi_i = f(\phi/\phi_{pk})$$

ψ - head coefficient

ϕ - flow coefficient

Subscripts:

TORQ - refers to value based upon actual torque

i - refers to value based upon ideal torque

pk - peak efficiency point

Data from the partial-flow, hydraulic-turbine-driven boost pump tests(51) were plotted and used to obtain torque corrections for the inducer design. Head data for the partial-flow, hydraulic-turbine driven impeller(52) alone were not available for use in the correlations discussed above.

Curves for the cavitating head loss parameter, $\Delta H/NPSH$, which are shown on Figure No. 29, were obtained from correlations of test data for a three-eighths scale model of the M-1 fuel turbopump inducer. Equivalent performance in terms of head loss as a function of suction specific speed is expected with the low-speed inducer at an equivalent percentage of design flow coefficients. An additional curve for operation at approximately 50% of the design flow coefficient (Q/N = .131) was obtained from test data at 80% of the flow coefficient by making the following assumption:

$$(S)_{Q/N = .131} - (S)_{Q/N = .209}\left(\frac{.131}{.209}\right)^{1/2}$$

---

(50) Contract Af 04(647)-7446, "Liquid Propellant Pump Investigation"
(51) Ibid.
(52) Ibid.

to obtain values of suction specific speed at equivalent $\Delta H/NPSH$ values. This extrapolation is based upon the assumption that the $NPSH/N^2$ value for equivalent amounts of $\Delta H/NPSH$ is relatively independent of Q/N at less than the design flow coefficient. For extreme peripheral operation ($Q/N = 0$ or Q/N greater than .395), the $\Delta H/NPSH$ was made zero independent of S up to values of 50,000. Actually, undetermined amount of head loss will occur in these regions. However, data is not available in this region; therefore, the zero value of $\Delta H/NPSH$ is used to "flag" the computer model output so that performance in this region can be evaluated separately from the computer.

The torque reduction resulting from cavitation was not evaluated during the M-1 scale pump tests discussed above. Data for the partial-flow, hydraulic-turbine-driven inducer(53) was utilized to obtain data correlations for performance predictions. The following correlation was used:

$$1 - \frac{(H/N^2)/\eta}{(H/N^2)_{NC}/\eta_{NC}} = f\left(1 - \frac{H/N^2}{(H/N^2)_{NC}}\right)$$

H - head rise, ft

N - shaft speed, rpm

η - efficiency

NC - non-cavitating

A curve was faired through the cavitating torque head data of the partial-flow, hydraulic-turbine-driven inducer(54) for the available flow coefficients. This curve was used to predict torque loss parameters from the head loss parameters, which were already obtained. Again, the $\Delta T/\rho$ NPSH values for extreme off-design conditions, where no data is available, were set equal to zero so as to "flag" these values for examination externally from the computer calculations.

2. High-Speed Rotor

This blade row also has an unconventionally high design inlet relative to the flow angles and the stagger angles. As with the inducer, empirical axial flow pump data were used to establish the off-design characteristics.

---

(53) Ibid.

(54) Ibid.

Parameter	Figure No.	Reference
$H/N^2 - Q/N$	31	(55)
$T/\rho N^2 - Q/N$	32	(56)
$\Delta H/NPSH - S$	33	(57)
$T/\rho NPSH - S$	34	(58)

The H/N^2 and $T/\rho N^2$ functions, which were mono-variant for the inducer, become bi-variant for the high-speed rotor because the inlet relative flow angle is a function of N_2/N_1 as well as Q/N. The H/NPSH and T/ρ NPSH functions, which were bi-variant for the low-speed inducer, become tri-variant for the same reason. In all cases, zero inlet whirl test data were used to predict the rotor performance, which is generally for finite amounts of inlet whirl. It was assumed that the zero whirl data could be extrapolated upon the basis of equivalent inlet relative flow angle.

Data taken from Stepanoff for a 5550 specific speed $\left(\frac{rpm \times gpm^{1/2}}{ft^{3/4}}\right)$, 0.7 hub to tip ratio axial pump were utilized to obtain a correlation of the loss coefficient as a function of the flow coefficient (or tangent of the inlet relative flow angle). These data were normalized to the high-speed rotor design values used to obtain the curves shown on Figure No. 31. The magnitude of the dip in the head-flow curve at the stall point was reduced somewhat because this dip was attributed to a housing rather than a rotor characteristic.

The same corrections that were applied to the low-speed inducer ideal torque curves (see Section III,D,2) were used for the high-speed rotor.

The $\Delta H/NPSH - S$ predictions were extrapolated from data for a 3800 specific speed, mixed-flow impeller (designated as RI-6A by Stepanoff) using correlations similar to those previously discussed in Section III,D,1.

---

(55) Stepanoff, A. J., Centrifugal and Axial Flow Pumps, second edition, J. Wiley & Sons, New York, 1957, Figure 8.8, p. 145

(56) (U) Phase II Final Report on the Design and Evaluation of a Low Speed Hydraulic Turbine-Driven Pump Discharge Fed Inducer Stage, (Confidential Report), op. cit.

(57) Marman, H. W., et.al., Report PWAC-318, op. cit., Figure 73, p. 143

(58) (U) Phase II Final Report on the Design and Evaluation of a Low Speed Hydraulic Turbine-Driven Pump Discharge Fed Inducer Stage, (Confidential Report), op. cit.

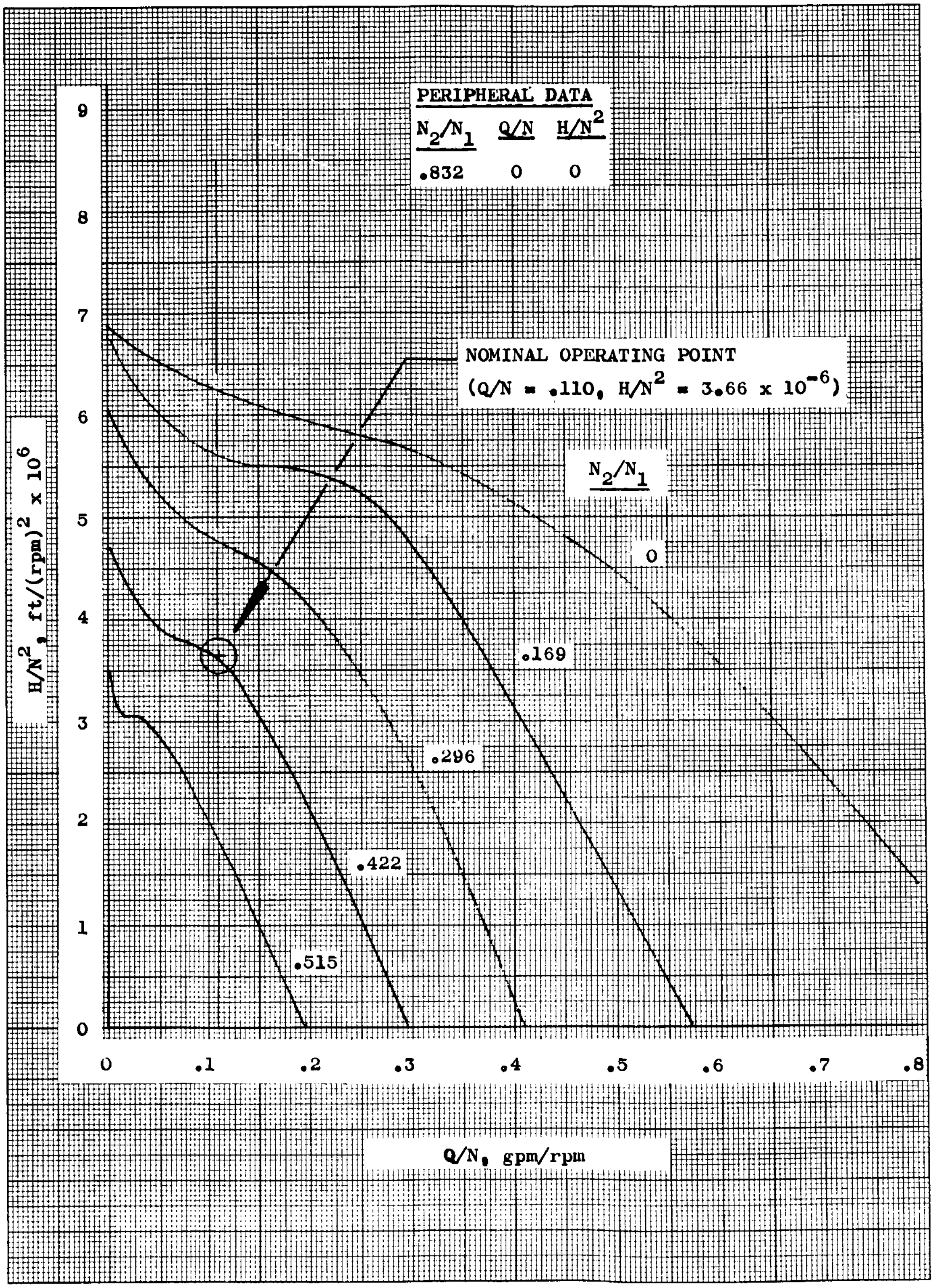

Figure 31. High-Speed Rotor H/N^2 vs Q/N

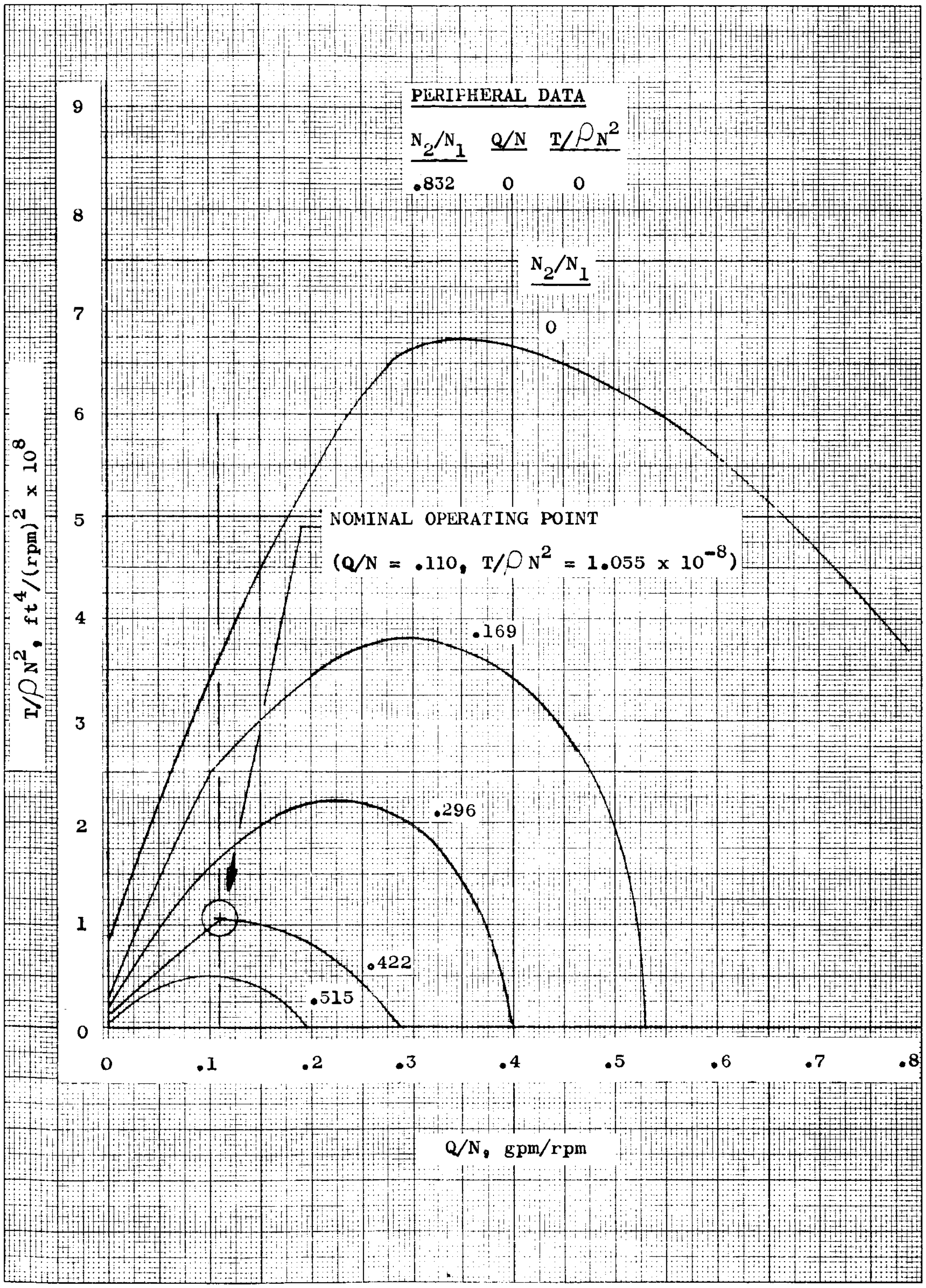

Figure 32. High-Speed $T/\rho N^2$ vs Q/N

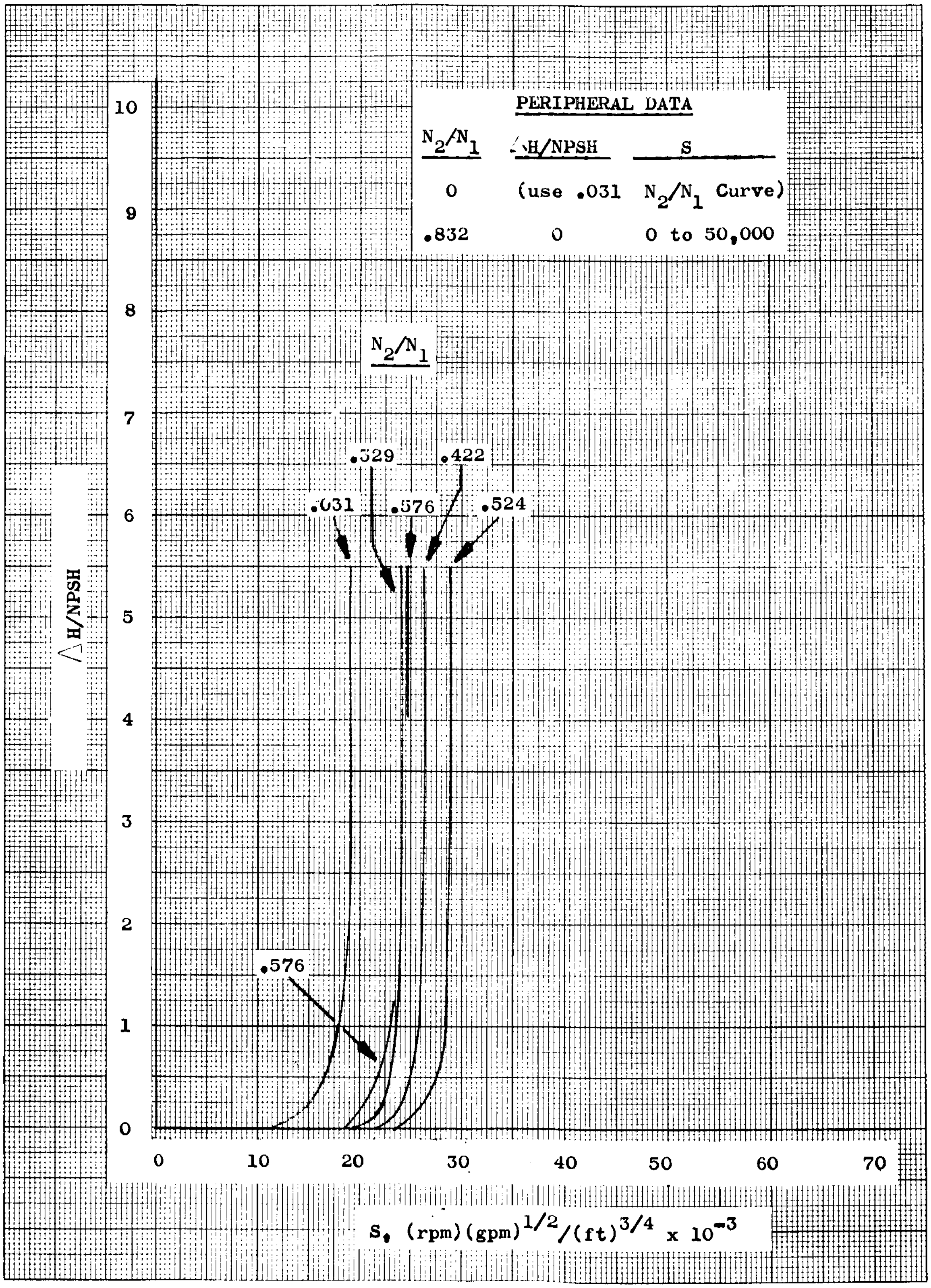

Figure 33. High-Speed Rotor ΔH/NPSH vs S (Q/N = .110)

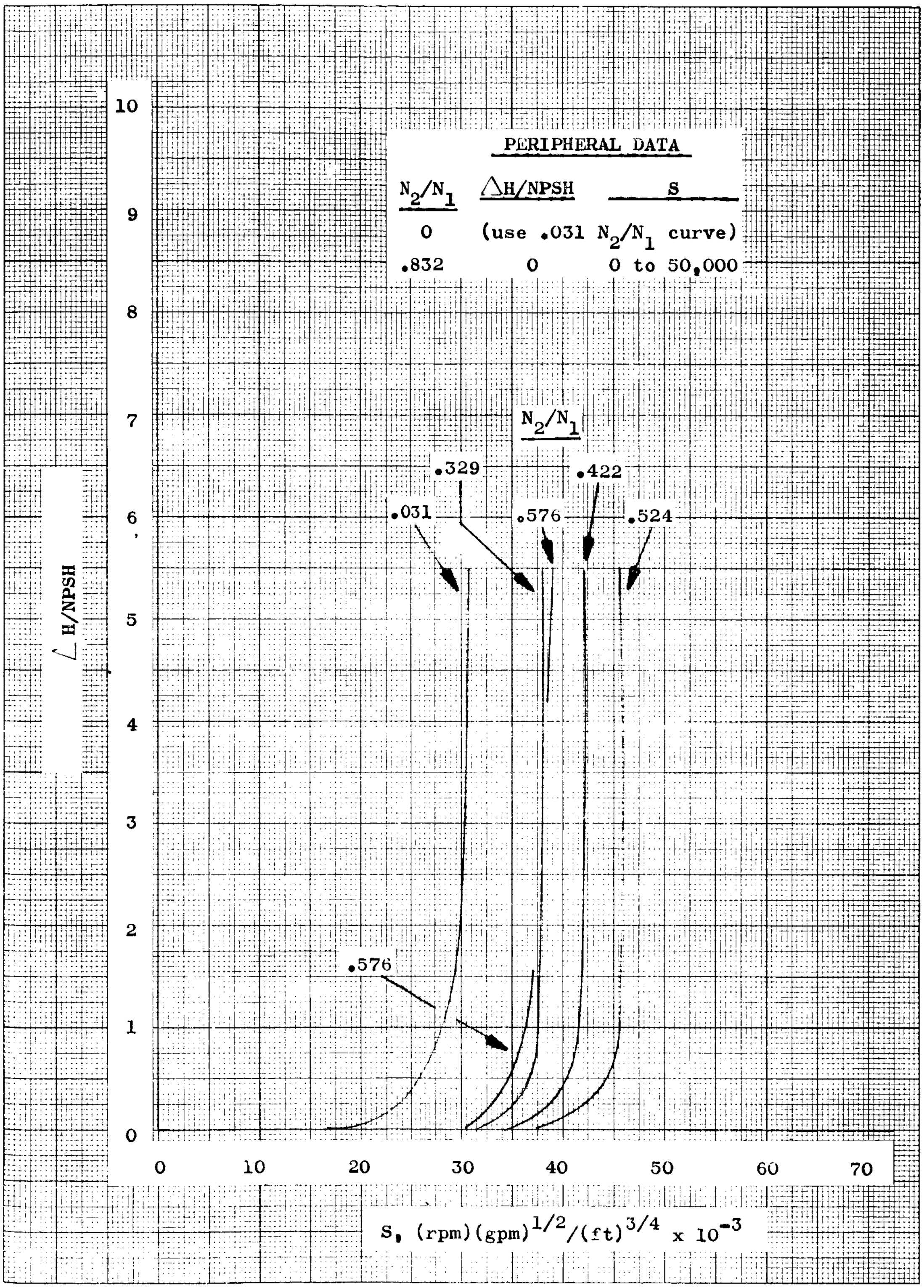

PERIPHERAL DATA

N_2/N_1	$\Delta H/NPSH$	S
0	(use .031 N_2/N_1 curve)	
.832	0	0 to 50,000

Figure 33. High-Speed Rotor ΔH/NPSH vs S (Q/N = .0688)

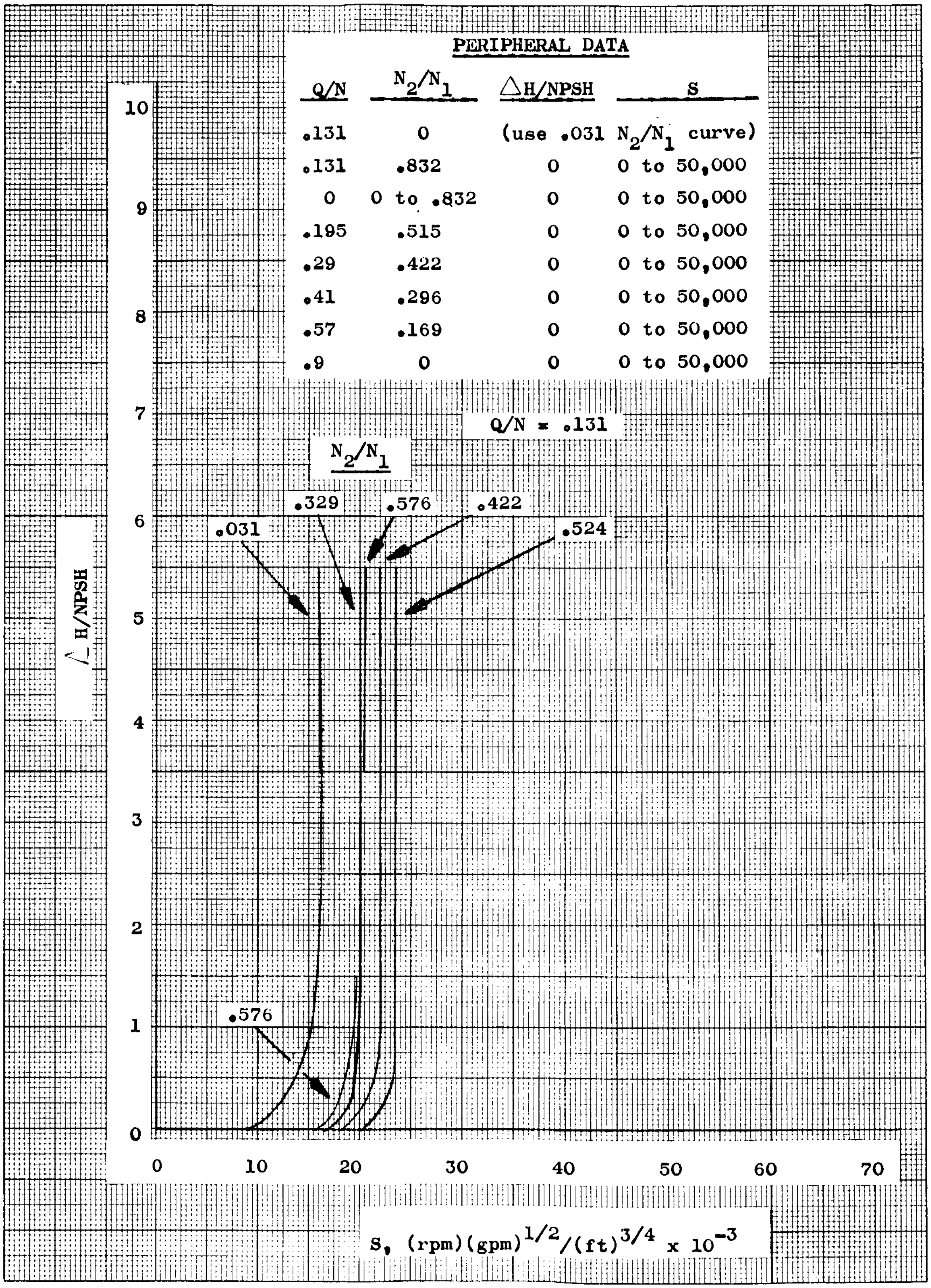

PERIPHERAL DATA

Q/N	N_2/N_1	△H/NPSH	S
.131	0	(use .031	N_2/N_1 curve)
.131	.832	0	0 to 50,000
0	0 to .832	0	0 to 50,000
.195	.515	0	0 to 50,000
.29	.422	0	0 to 50,000
.41	.296	0	0 to 50,000
.57	.169	0	0 to 50,000
.9	0	0	0 to 50,000

Figure 33. High-Speed Rotor ΔH/NPSH vs S (Q/N = 0, .131, .195, .29, .41, .57, and .9)

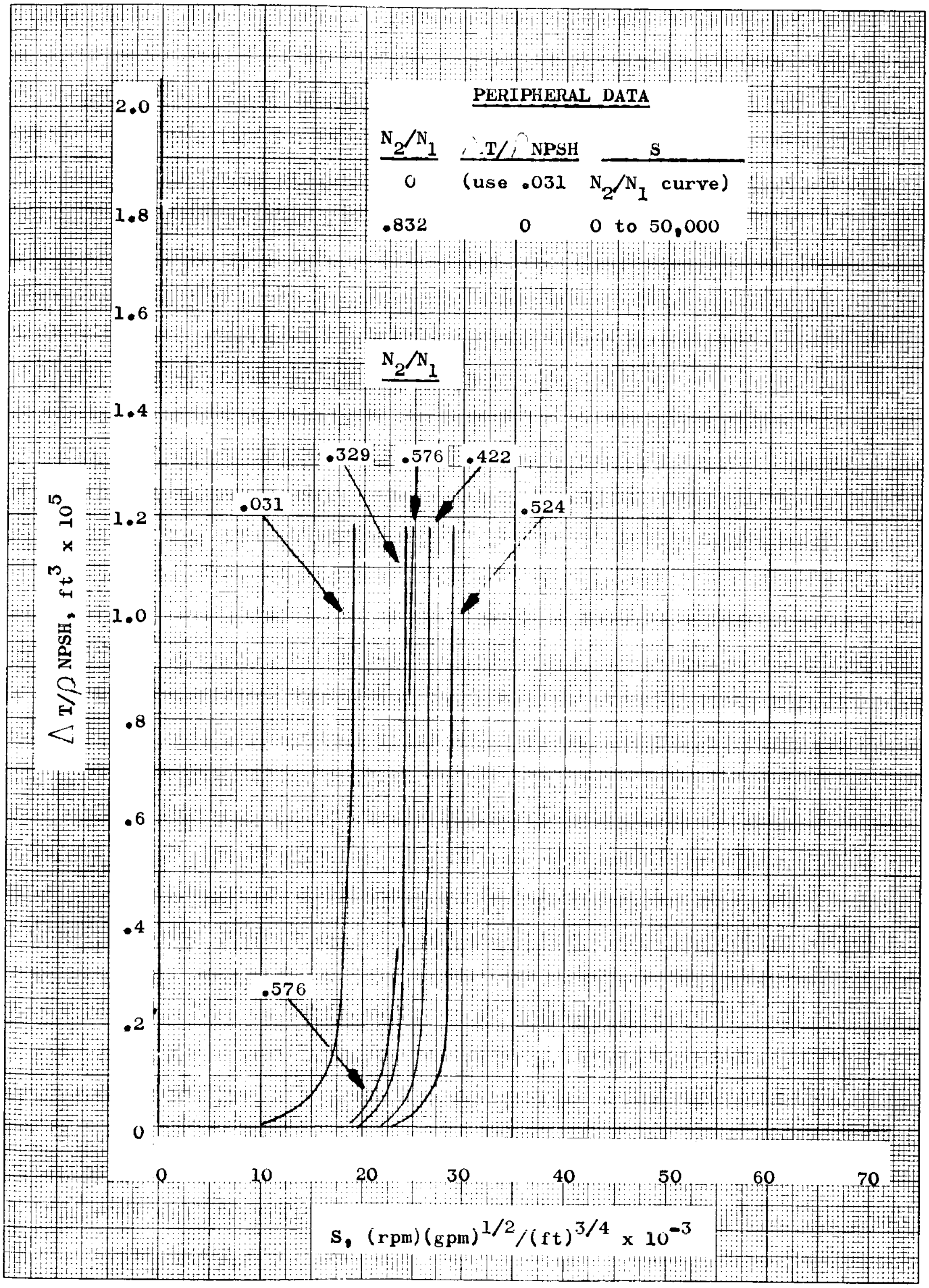

Figure 34. High-Speed Rotor $\Delta T/\rho NPSH$ vs S (Q/N = .110)

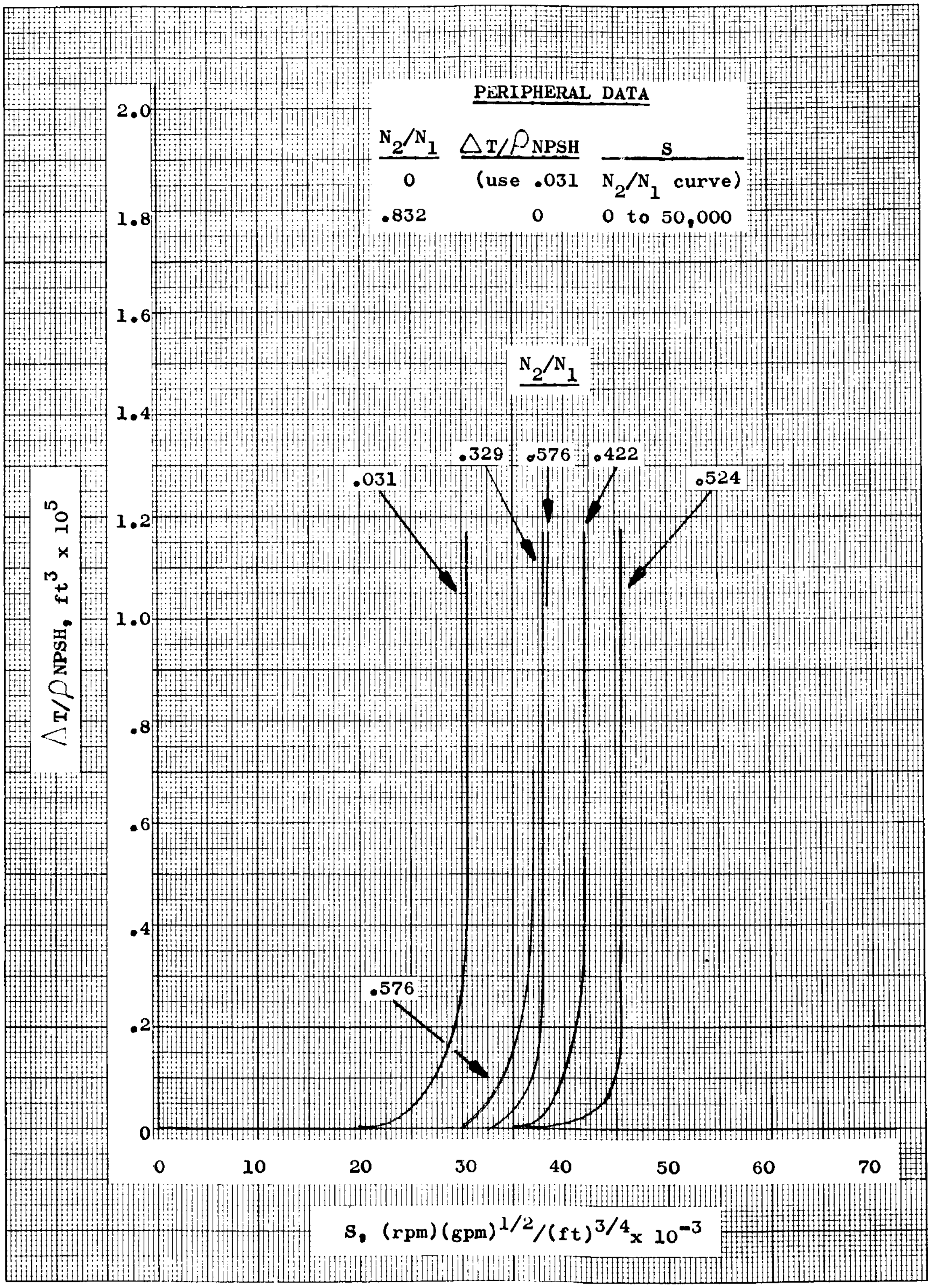

Figure 34. High-Speed Rotor $\Delta T/\rho NPSH$ vs S (Q/N = .0688)

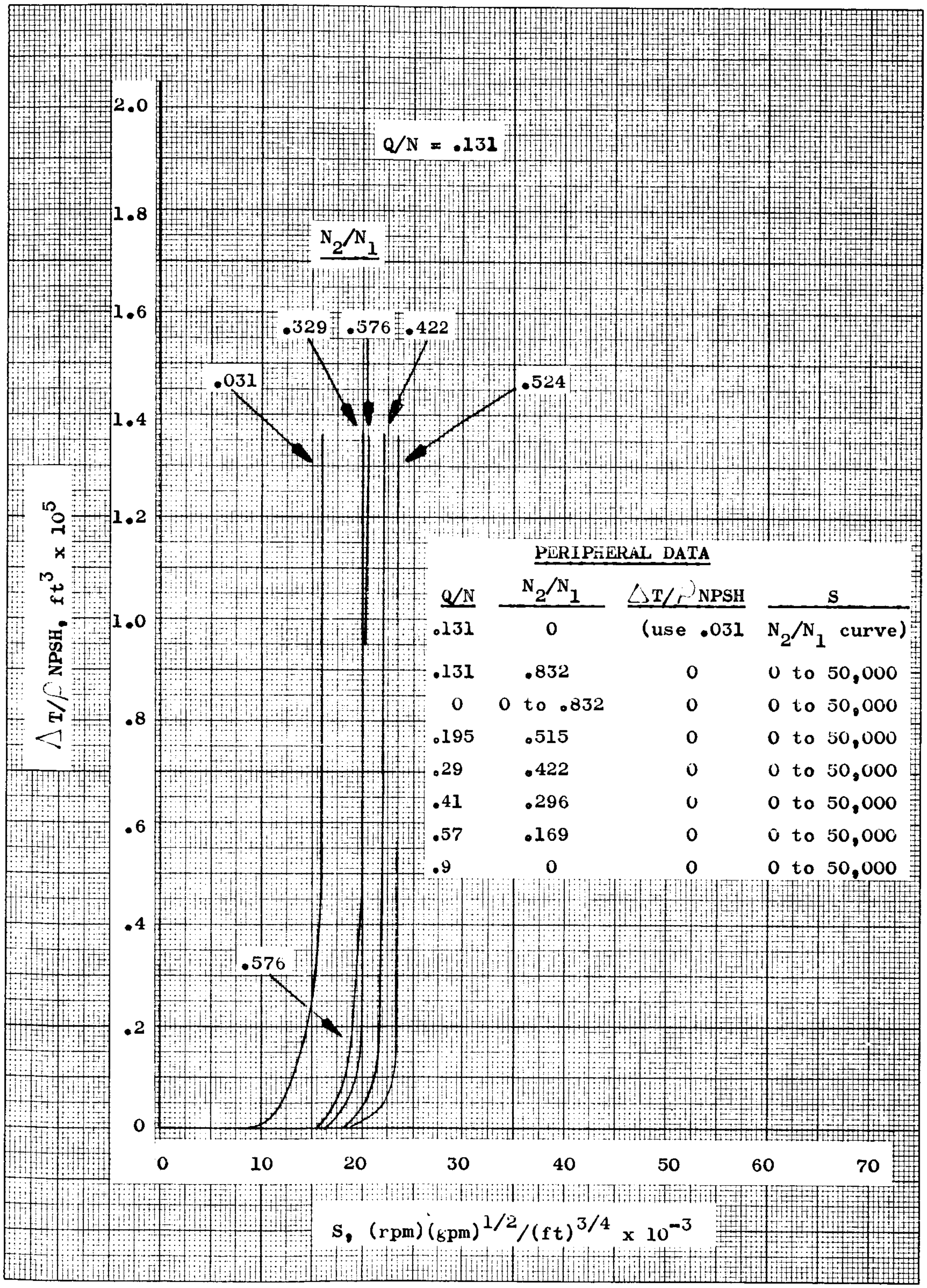

PERIPHERAL DATA

Q/N	N_2/N_1	$\Delta T/\rho$ NPSH	S
.131	0	(use .031	N_2/N_1 curve)
.131	.832	0	0 to 50,000
0	0 to .832	0	0 to 50,000
.195	.515	0	0 to 50,000
.29	.422	0	0 to 50,000
.41	.296	0	0 to 50,000
.57	.169	0	0 to 50,000
.9	0	0	0 to 50,000

Figure 34. High-Speed Rotor $\Delta T/\rho$NPSH vs S (Q/N = 0, .131, .195, .29, .41, .57, and .9)

The same correlation as was applied to the cavitating head loss data in Section III,D,2 was applied to the data shown on Figure No. 33 to obtain the T/ρ NPSH-S predictions for the high-speed rotor (Figure No. 34).

3. Hydraulic Turbine

The predicted H/N^2-Q/N and $T/\rho\ N^2$-Q/N relationships for the hydraulic turbine are shown on Figures No. 35 and No. 36, respectively. Little applicable data was available for the off-design cavitating performance of blade rows like this; therefore, no attempt was made to predict these parameters. The transient program output was examined using design point cavitation numbers (Section III,A,2,c) as a guide to verify that adequate cavitation margins existed.

As was done with the inducer blade rows, the assumption was made that the turbine exit relative flow angle was constant and independent of inlet incidence. Corrections to the static head rise across the blade were made using the estimated correction factor, K_i, shown on Figure No. 37. This curve gives somewhat more conservative loss estimates than those given by Loschge(59) or Ainley and Mathieson(60) for relatively blunt leading edge, sub-sonic profiles. Design curves used by Aerojet-General for relatively sharp leading edge, high Mach number blading are shown for comparison. The K_i is the correction to the design velocity coefficient:

$$K_i = \frac{K_V \text{ Design}}{K_V}$$

K_V - velocity coefficient

K_V Design - design velocity coefficient

used to obtain K_V values to correct the static head differential:

$$h_s = \frac{W_2^{\ 2}}{K_V^{\ 2}\ 2g} - \frac{W_1^{\ 2}}{2g}$$

h_s - static head differential, ft

W_1 - inlet relative velocity, ft/sec

W_2 - exit relative velocity, ft/sec

g - acceleration caused by gravity, ft/sec^2

---

(59) Loschge, A., Konstrucktionen aus Dampfturbinen, Springer Verlag, Berlin/Gottingen/Heidelberg, 1955

(60) Ainley, D. G. and Mathieson, G. C. R., "An Examination of the Flow and Pressure Losses in Blade Rows of Axial-Flow Turbines," Aero-Research Council R&M No. 2891, March 1951

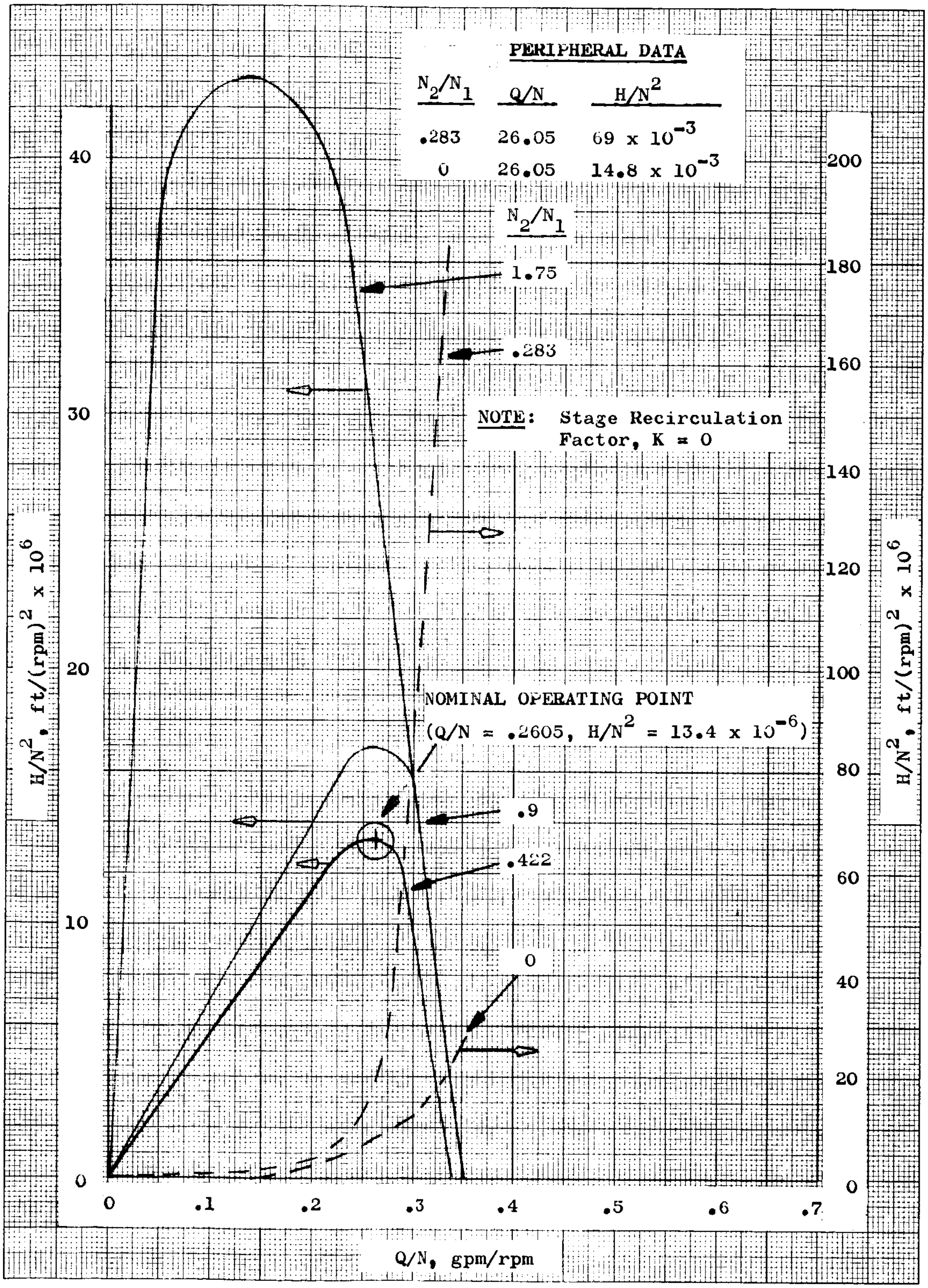

Figure 35. Hydraulic Turbine H/N^2 vs Q/N

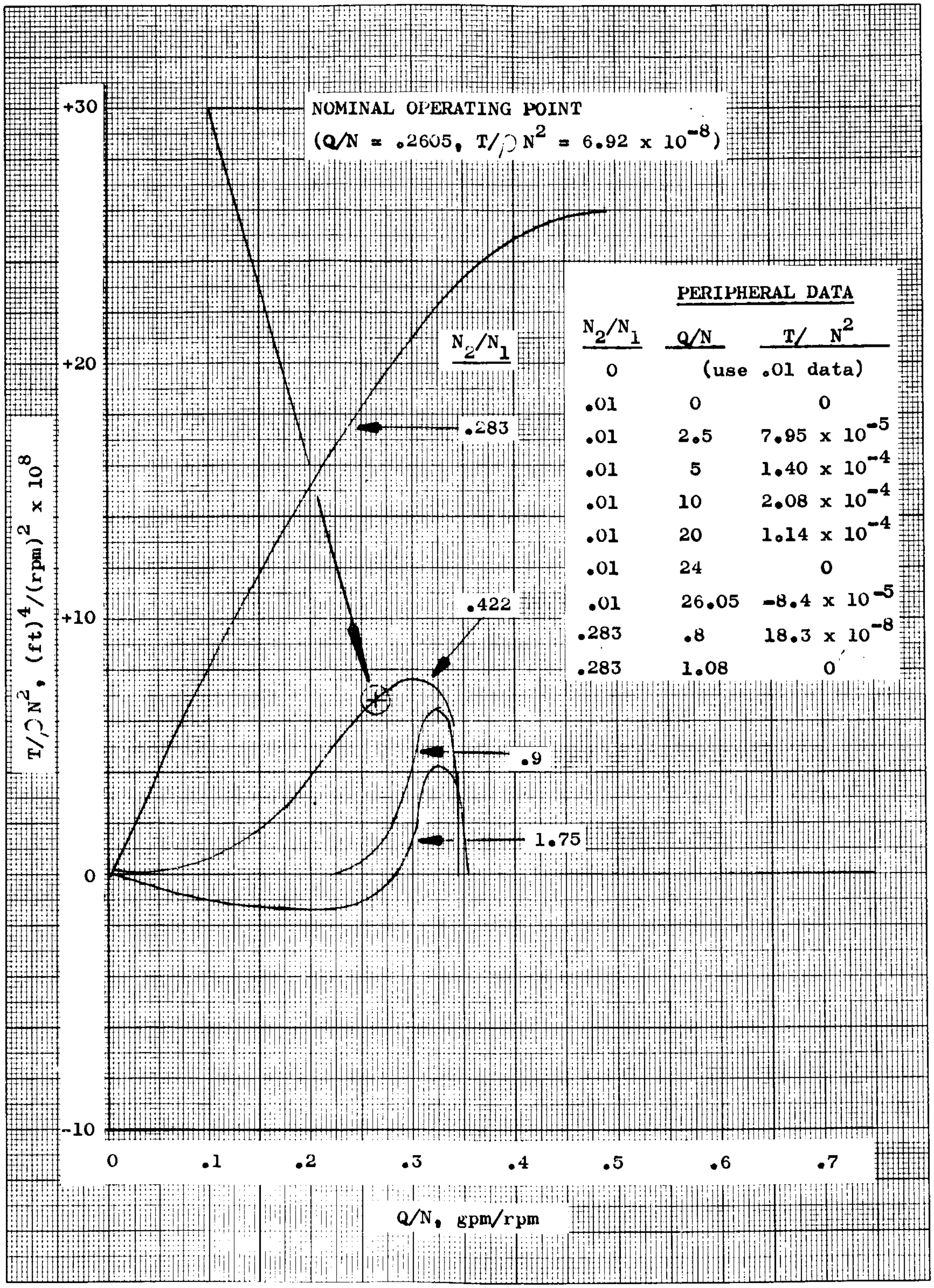

PERIPHERAL DATA

N_2/N_1	Q/N	$T/\ N^2$
0	(use .01 data)	
.01	0	0
.01	2.5	7.95×10^{-5}
.01	5	1.40×10^{-4}
.01	10	2.08×10^{-4}
.01	20	1.14×10^{-4}
.01	24	0
.01	26.05	-8.4×10^{-5}
.283	.8	18.3×10^{-8}
.283	1.08	0

Figure 36. Hydraulic Turbine $T/\rho N^2$ vs Q/N

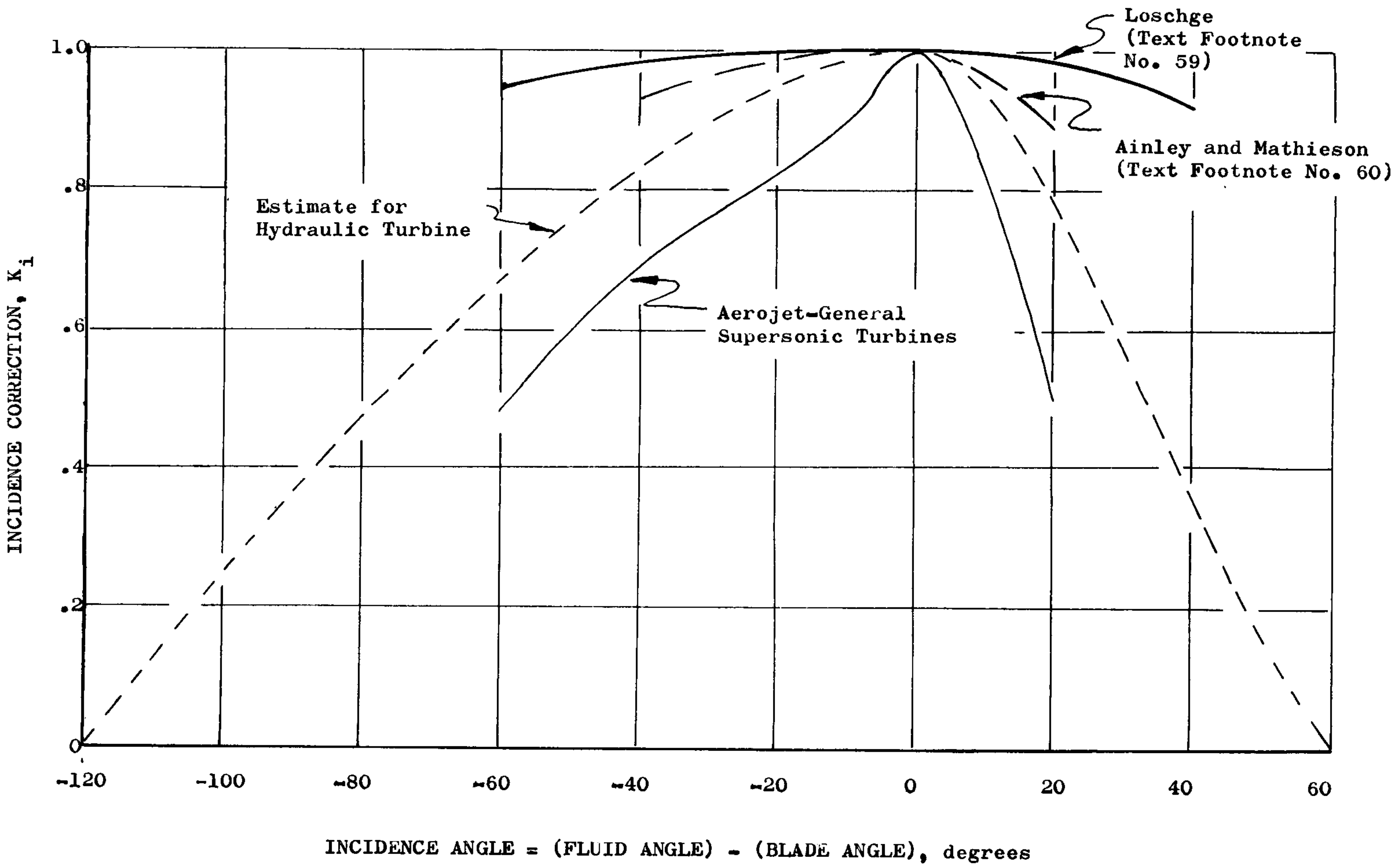

Figure 37. Hydraulic Turbine Off-Design Incidence Correction

Little data were available; therefore, no attempt was made to account for deviations in the shut-off head or stalled torque and head caused by flow separation. Consequently, it is expected that the predictions for extreme positive and negative incidence will require some corrections, which will be obtained from the Task IV test results.

4. High-Speed Drive Turbine

Figures No. 38 and No. 39 show performance estimates for the high-speed shaft gas turbine drive mass flow rate and power parameters, respectively, as functions of pressure ratio.

Nomenclature:

$\frac{\dot{W}\sqrt{T_{TO}}}{P_{TO}}$ = mass flow rate parameter

$\dot{W}$ = mass flow rate, lb/sec

P_{TO} = inlet total pressure, psia

T_{TO} = inlet total temperature, °R

$\frac{Shp}{P_{TO}\sqrt{T_{TO}}}$ = power parameter

Shp = shaft horsepower

P_{TO}/P_2 = total/static pressure ratio

P_2 = exhaust static pressure, psia

Performance has been estimated from both Aerojet-General and NASA test data(61) for two-stage and three-stage NERVA turbine designs. Calculations were performed for the 8500 rpm water test condition with a gaseous nitrogen inlet total temperature of 450°R.

5. Discharge Housing

The total pressure loss coefficients derive from impeller exit velocity surveys and housing pressure differential measurements for a

---

(61) Rohlik, H. E. and Kofsky, M. G., Performance Evaluation of Three-Stage Prototype NERVA Turbine Designed for Blade-Jet Speed Ratio of 0.107, NASA TMX 719, January 1963

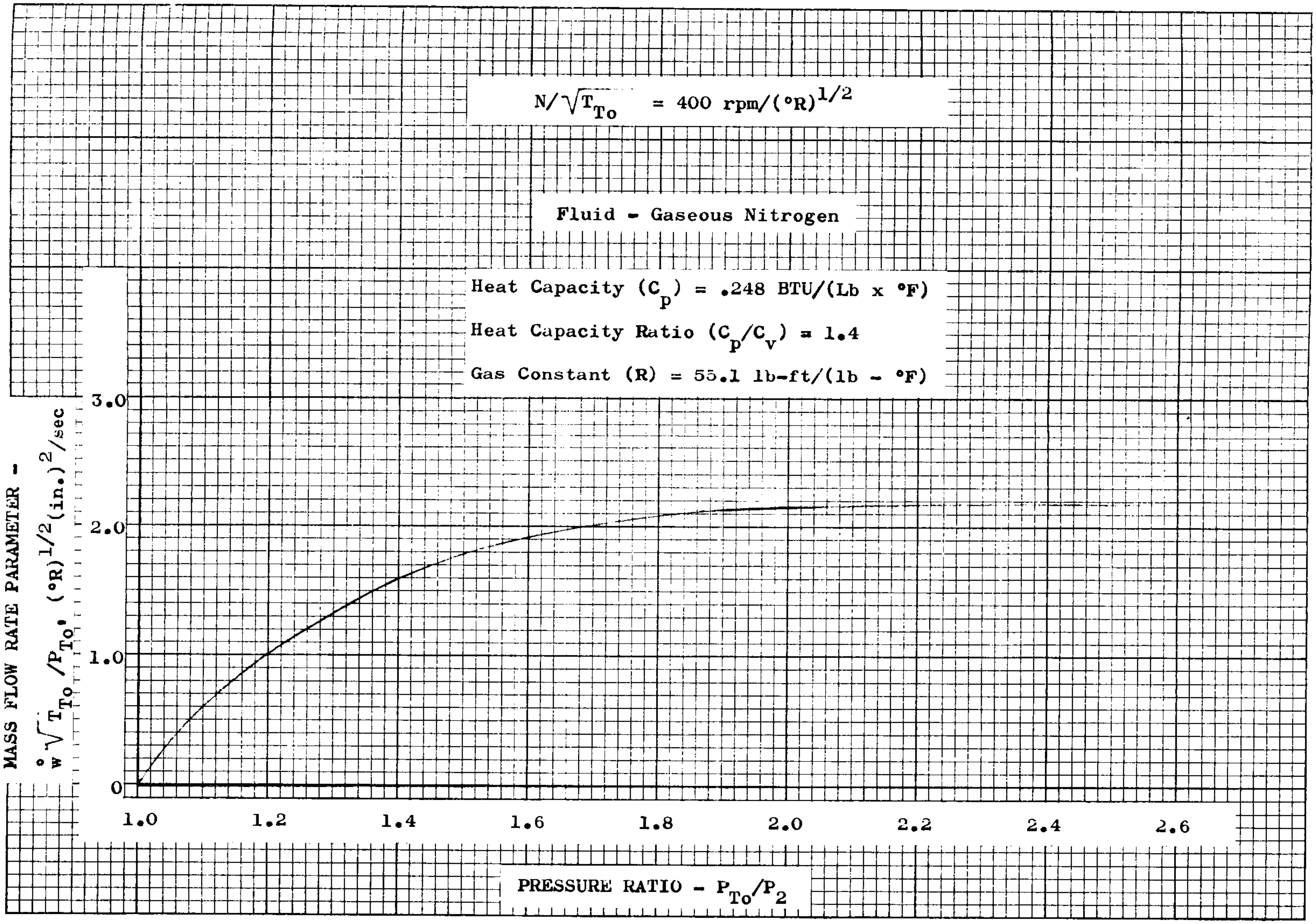

Figure 38. High-Speed Drive Turbine Mass Flow Rate Parameter vs Pressure Ratio

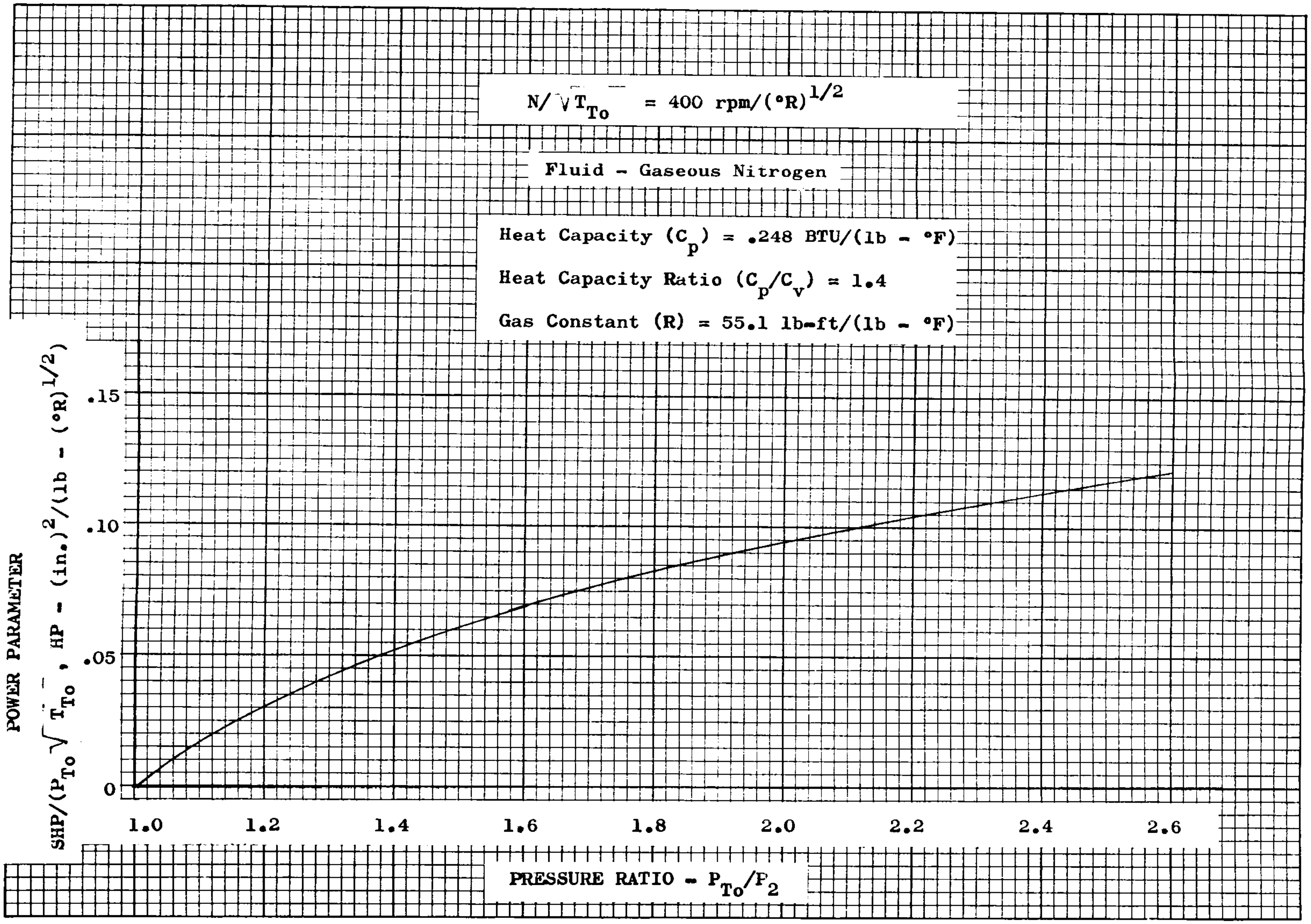

Figure 39. High-Speed Drive Turbine Power Parameter vs Pressure Ratio

mixed-flow pump(62) were used to predict off-design housing losses. Data for loss coefficient as a function of housing inlet incidence angle were normalized to the minimum loss coefficient and angle values. A design loss coefficient of 0.5 was used for the high specific speed design. The correlation is

$$\frac{K}{K_{min}} = f\ (\alpha/\alpha_{min})$$

K = loss coefficient

$K = H_T \,/\, C_1^2 /2g$

H_T = housing total pressure loss, ft

C_1 = housing inlet velocity, ft/sec

g = acceleration caused by gravity, ft/sec^2

α = housing inlet absolute fluid angle, degrees

Subscript:

min = refers to minimum loss point

The predictions of H/N^2 versus Q/N is shown on Figure No. 40. The N used is the high-speed rotor speed. The plot is bi-variant in N_2/N_1 because the housing is fed from the low-speed turbine discharge. For convenience, the high-speed rotor N was applied in the computer program so that the same input data regions used for the housing could be utilized for cases where a main stage pump is substituted for the housing.

6. Over-all Pumping System

Figure No. 41 shows H/N^2-Q/N and efficiency-Q/N curves for the over-all pumping system. Curves are shown for the head rise across the three blade rows as well as across the blade rows and housing. The estimated low-speed shaft/high-speed shaft speed ratio as a function of Q/N also is shown.

7. Reynolds Number Effects

Two types of fluid viscosity effects which could cause deviations from the usual pump dynamic similarity relationships were investigated. One was the variations in axial velocity profile at both steady-state and transient conditions. The other was the variations in blade row total pressure

---

(62) Murphy, J. S., et.al., Development of Pump Components for the Pratt & Whitney Aircraft Liquid Metal Turbopump, TP-1, Report PWAC-298, Pratt & Whitney Aircraft, Middletown, Conn., 20 October 1960, Figure 54, p 94

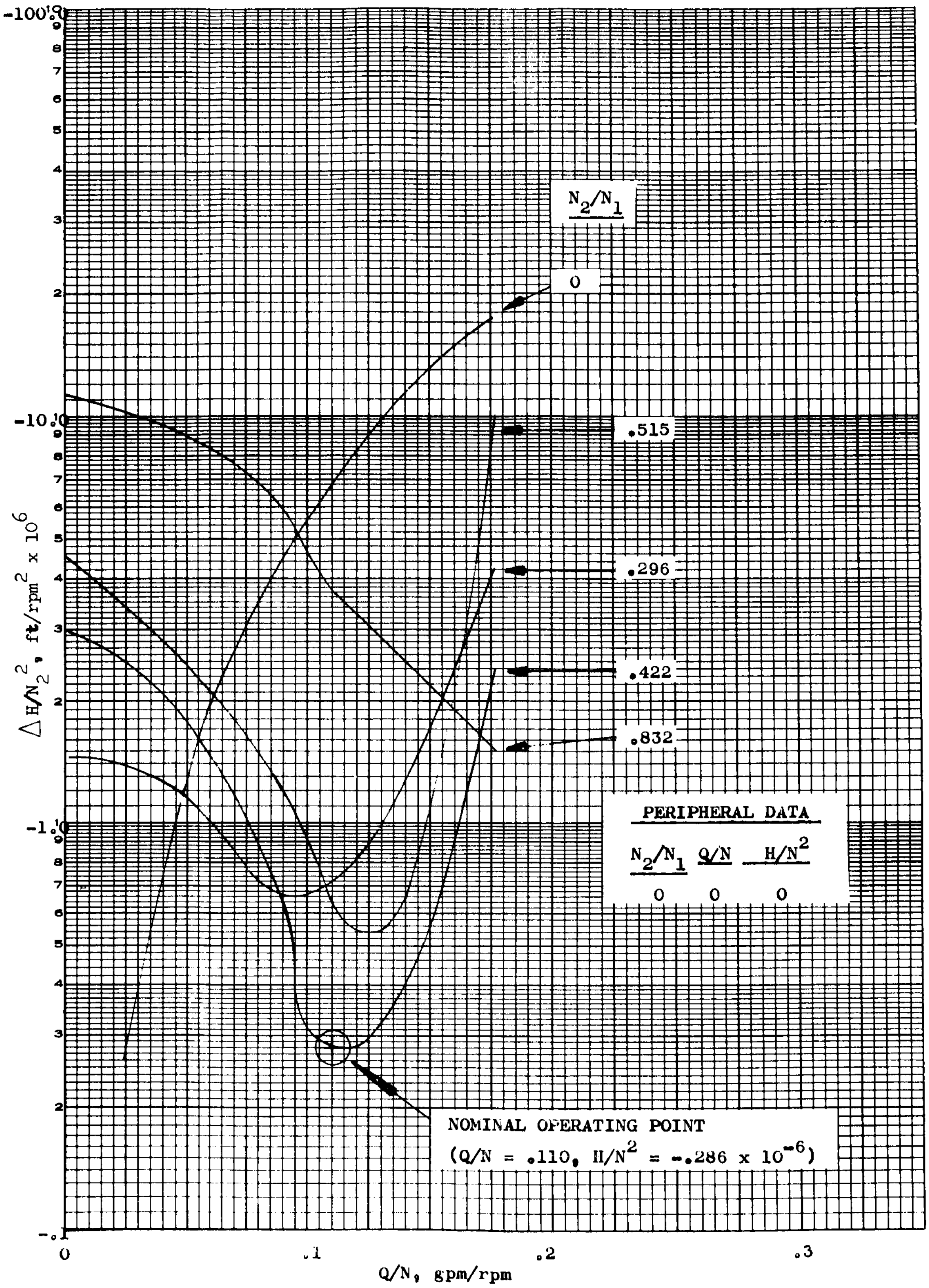

Figure 40. Discharge Housing H/N^2 vs Q/N

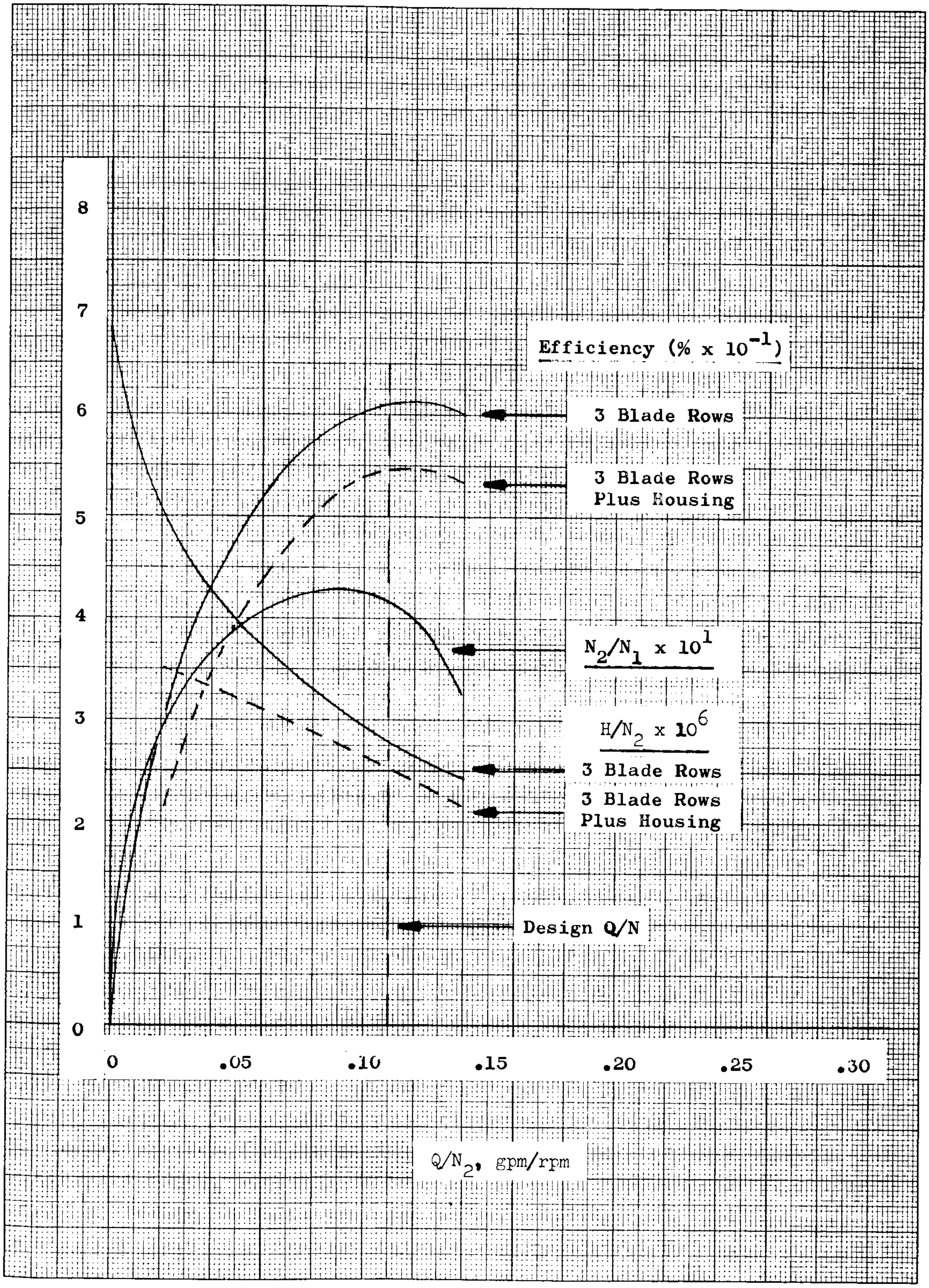

Figure 41. Over-All Pumping System H/N^2, Efficiency, and N_2/N_1 vs Q/N

loss coefficients. The latter was evaluated at steady-state conditions only because no experimental or theoretical methods are available for transient evaluations.

A fractional type correction to the actual delivered flow rate was calculated to account for the axial velocity profile variations. The adjusted flow rate was used to obtain performance data for each blade row from the curves. The blade rows had similar annulus Reynolds Numbers; therefore, the same correction curves were used for all blade rows. Curves for water and hydrogen are shown on Figures No. 42 and No. 43, respectively. The following is the nomenclature used:

DEL $(QRET)/Q_{STAGE}$

DEL (QRET) - correction to delivered flow rate, gpm

Q_{STAGE} - delivered flow rate, gpm

Q/Q_{Nom}

Q - delivered flow rate, gpm

Q_{Nom} - delivered flow rate at design nominal operating point, gpm

DEL (QT) - time rate of change of flow rate, gpm/sec

The following Reynolds Number values were assumed for the various flow regimes:

Laminar flow - less than 2.5×10^3

Laminar/turbulent transition - 2.5×10^3 to 3.5×10^3

Turbulent flow - greater than 3.5×10^3

For steady laminar flow, a parabolic velocity distribution was assumed while for steady turbulent flow, the relationship given by Schlichting(63) was used:

$$\frac{u}{U} = \left(\frac{y}{R}\right)^{1/n}$$

---

(63) Schlichting, H., Boundary/Layer Theory, fourth edition, McGraw-Hill, New York, New York, 1960, pp. 504-506

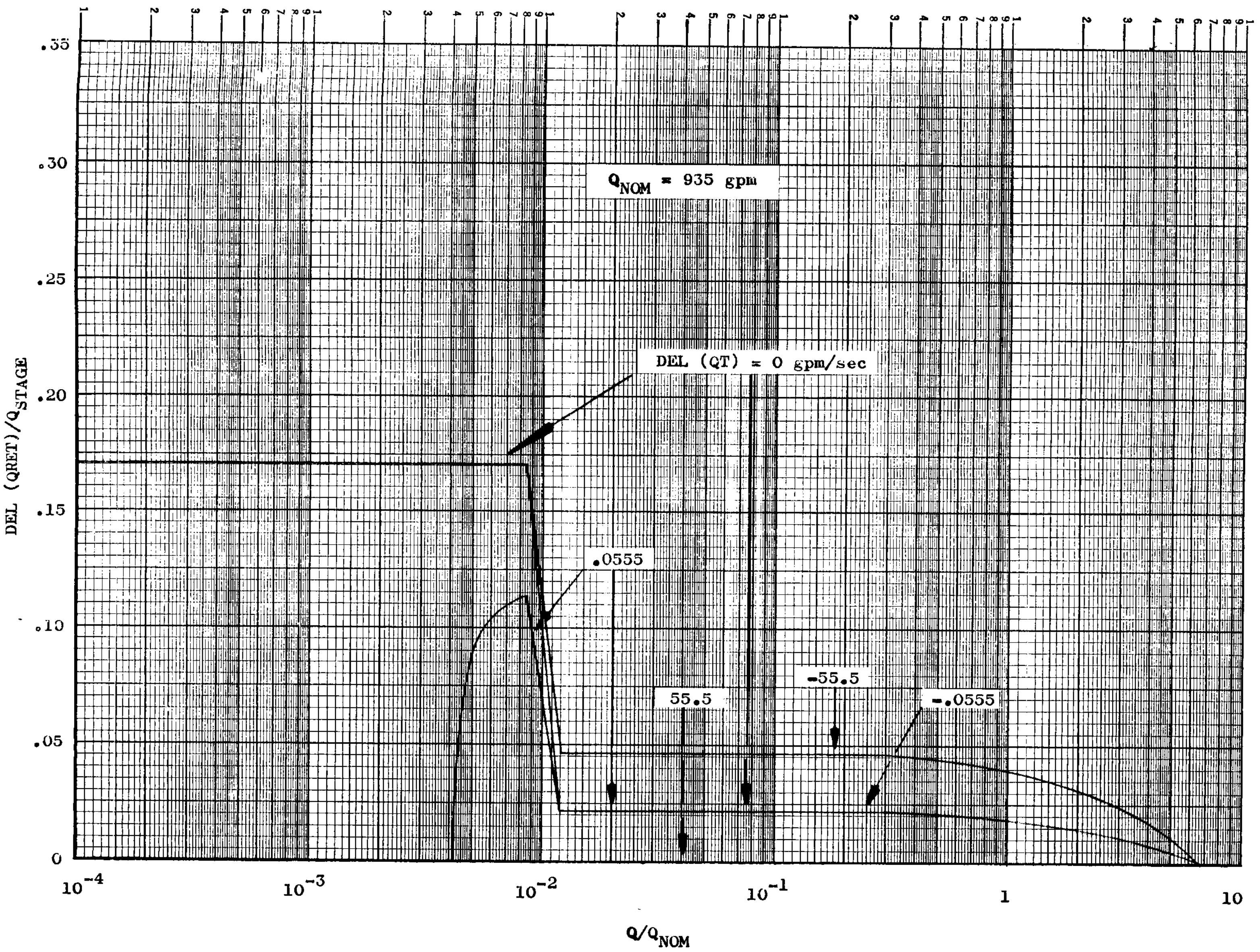

Figure 42. Axial Velocity Profile Correction - Water

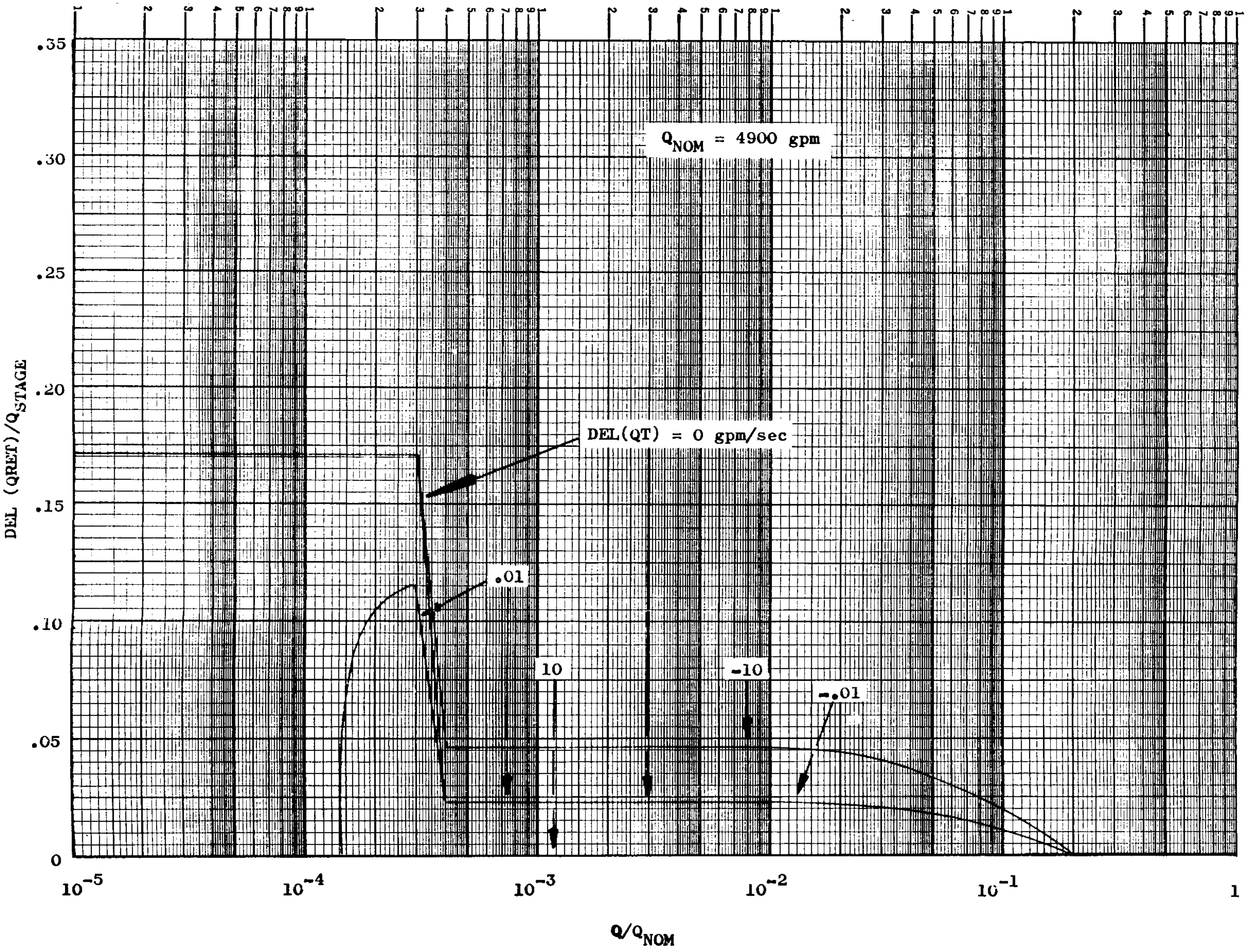

Figure 43. Axial Velocity Profile Correction - LH_2

u - velocity at distance y from wall

U - maximum velocity at pipe or annulus mid-point (distance R from wall)

n - empirically determined exponent which is a function of Reynolds Number

Numerical integrations were performed to determine a normalizing factor for the ideal head rise assuming the ideal head rise at the liquid hydrogen Reynolds Numbers at each streamline is unity. To reduce the amount of calculations involved, it was assumed that all blade rows could be treated at Reynolds Numbers greater than 3.2×10^6 as an idealized blade rows with zero entering fluid inlet whirl and an exit whirl equal to one-half the rotor velocity. This assumption was made for each streamline in performing the integrations. For the hydraulic turbine, it can be assumed that the inlet and exit stations are reversed. The tangential relative velocity for reduced Reynolds Numbers, at any given streamline, was multiplied by the normalized velocity parameter, u/U. Calculations performed for turbulent flow at a Reynolds Number of 4.0×10^3 indicated the ideal head rise would be 9.5% less than at 3.2×10^6. On a one-dimensional basis this is equivalent to a 9.2% increase in flow coefficient. This is approximately equal to the change in the one-dimensional average/pipe maximum velocity ratio between the two Reynolds Numbers. Assuming this is valid for other Reynolds Numbers, a revised blockage factor for off-design Reynolds Numbers can be obtained.

$$BF = 1 - \frac{\bar{u}/u_{max}}{(\bar{u}/u_{max})_{DESIGN}} \left[1-(BF)_{DESIGN} \right]$$

BF - Blockage Factor

$(BF)_{DESIGN}$ - Design Point Blockage Factor (.96)

$\bar{u}/u_{max}$ - one dimensional average/maximum velocity ratio

$(\bar{u}/u_{max})_{DESIGN}$ - design value

Calculated values of blockage factor and DEL $(QRET)/Q_{STAGE}$ are given below for various Reynolds Numbers.

Reynolds Number	Blockage Factor	$\frac{\text{DEL Q}_{(\text{RET})}}{\text{Q}_{\text{STAGE}}}$
4.0×10^3	.938	1.023
1.1×10^5	.9458	1.015
2.0×10^6 and higher	.96	1.0

Similar calculations for the laminar region indicate the DEL $Q/_{\text{RET}}/Q_{\text{STAGE}}$ value in this region will be 1.172.

To account for the effects of fluid inertia upon the above values during transient operation, the results of Szymanski's calculations as presented by Schlichting(64), were used. These calculations are for accelerating flow in a circular pipe under a pressure gradient which is constant with time. Values of the exponent, n, for the turbulent velocity profile equation were determined for the curves presented in Schlichting, together with the one-dimensional average velocity, time rate of change. These data were used to obtain equivalent turbulent velocity Reynolds Numbers and the associated flow rate corrections as obtained for steady flow conditions. Adjustments were made in the steady flow curves as shown on Figures No. 42 and No. 43 to obtain the required transient predictions. For decelerating flow, corresponding corrections to the steady flow predictions were made using the above accelerating flow predictions. (Corrections of equal magnitude but opposite sign were made for flow rate, time-rate-of-changes of equal magnitude, but opposite sign.) No known means for obtaining a more rigorous correction for decelerating flow is readily available.

To estimate the effect of fluid viscosity upon the head rise values obtained from the H/N^2-Q/N curves for the individual blade rows, data from blade cascade tests(65) were used. Minimum loss incidence angle loss coefficients were normalized to values for high Reynolds Numbers. These normalized ratios were used to correct both minimum loss incidence and off-minimum loss incidence loss coefficient values for the three blade rows. In this case, five operative predictions had to be prepared for each blade row because of variations in blade chord Reynolds Number and losses. The data are presented as plots of:

$$\frac{\text{DEL (HRE)}}{(\text{DEL H})_{\text{STAGE}}} \quad \text{vs} \quad Q/Q_{\text{Nom}}$$

---

(64) Ibid, p. 74

(65) NASA Sp-36, op. cit., Figure 108, p. 165

for parameters of Q/N as well as for the high-speed rotor and hydraulic turbine N_2/N_1. Similar effects in the discharge housing for axial velocity profile or losses were ignored.

DEL (HRE) - head rise correction for variations on loss coefficient

$(\text{DEL H})_{\text{STAGE}}$ - head rise obtained from H/N^2 - Q/N curves

Q - delivered flow rate

Q_{Nom} - delivered flow rate at nominal operating point

Figure No.	Blade Row	Fluid
44	Low-Speed Inducer	Liquid Hydrogen
45	Low-Speed Inducer	Water
46	High-Speed Rotor	Liquid Hydrogen
47	High-Speed Rotor	Water
48	Hydraulic Turbine	Liquid Hydrogen
49	Hydraulic Turbine	Water

Computing difficulties were experienced when the above flow rate and head corrections were applied in the transient performance computer model. In particular, trouble was experienced with the sudden flow shift in the predicted laminar/turbulent transition region for the high-speed rotor. Iterations to obtain the current time flow rate value failed. The predicted values for loss coefficients at low flow rates also appear to be excessive.

These predictions may be useful in a revised form for interpreting test data. However, it is probable that more rigorous analyses of such effects may be required. The more rigorous analyses will probably require extensive engineering and are beyond the scope of the present contract. The possible areas for further investigation are:

- the effects of increased turbulence caused by rotating blade rows.
- The effects of two-dimensional and three-dimensional flow where the various flow stream-tubes experience varying boundary layer effects (this is particularly significant for modifying the performance "steps" caused by the apparent laminar/turbulent flow transition).

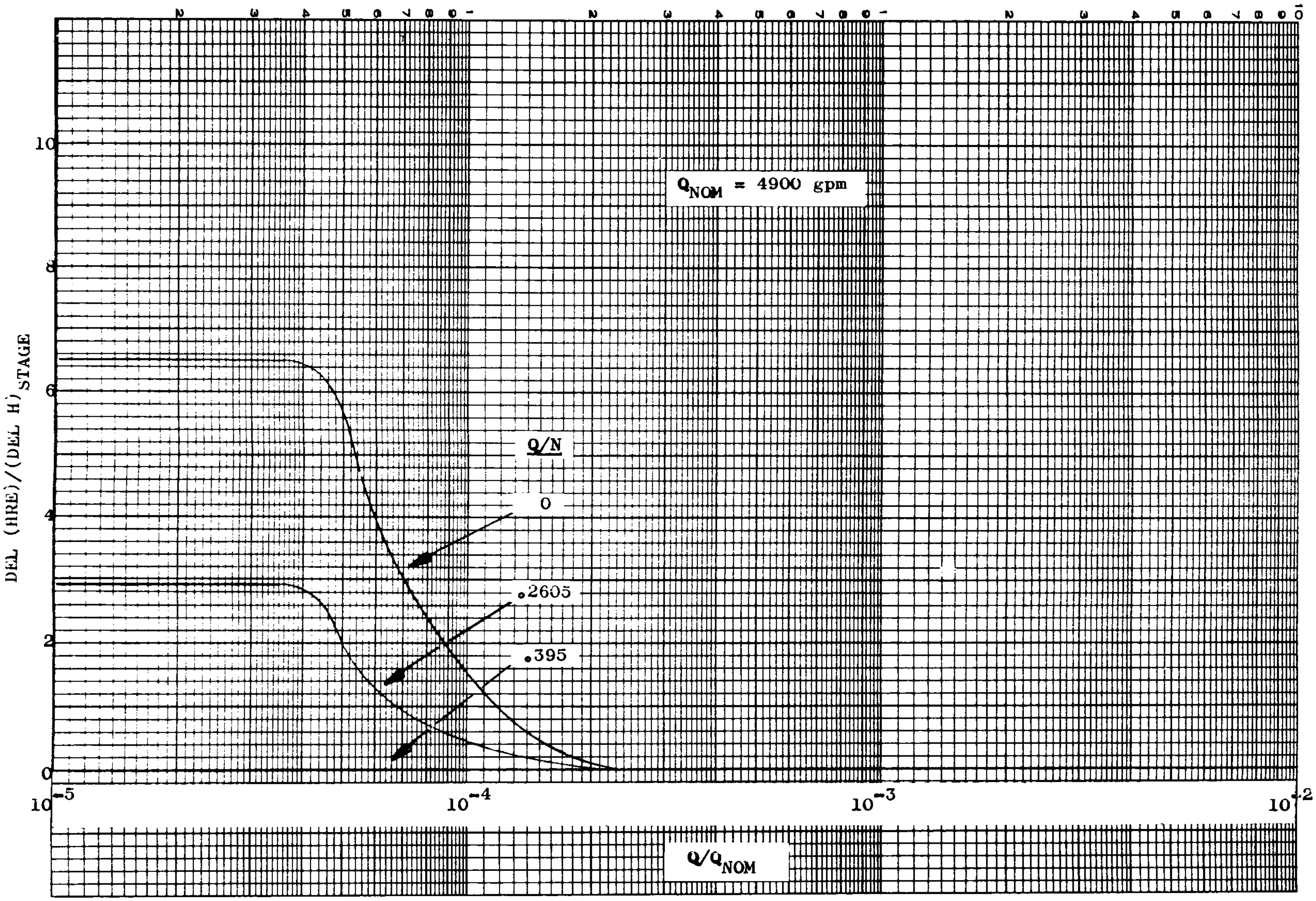

Figure 44. Low-Speed Inducer DEL (HRE)/(DELH)$_{\text{Stage}}$ vs Q/Q$_{\text{Nom}}$ - LH$_2$

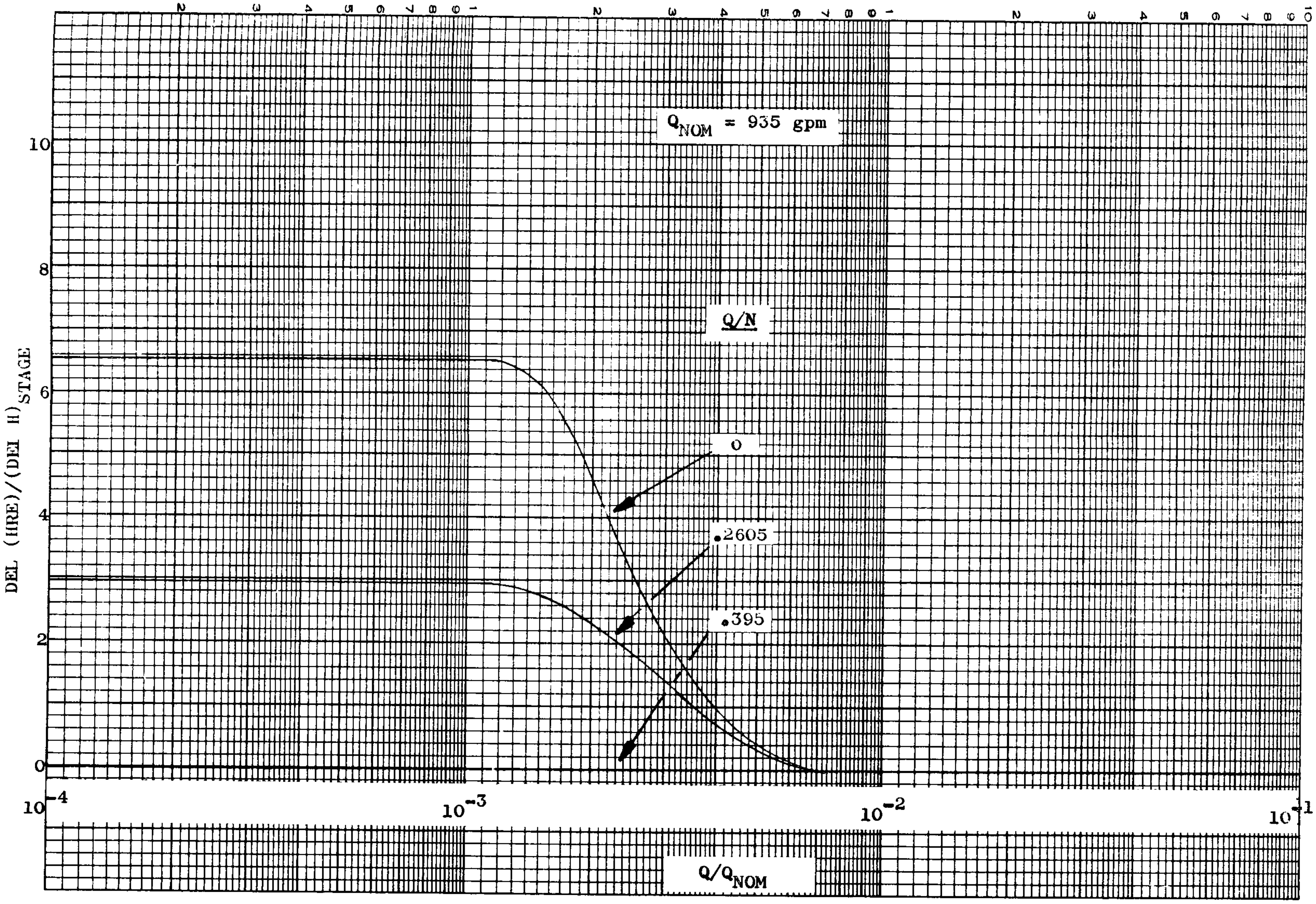

Figure 45. Low-Speed Inducer DEL (HRE)/(DELH)$_{Stage}$ vs Q/Q_{Nom} - Water

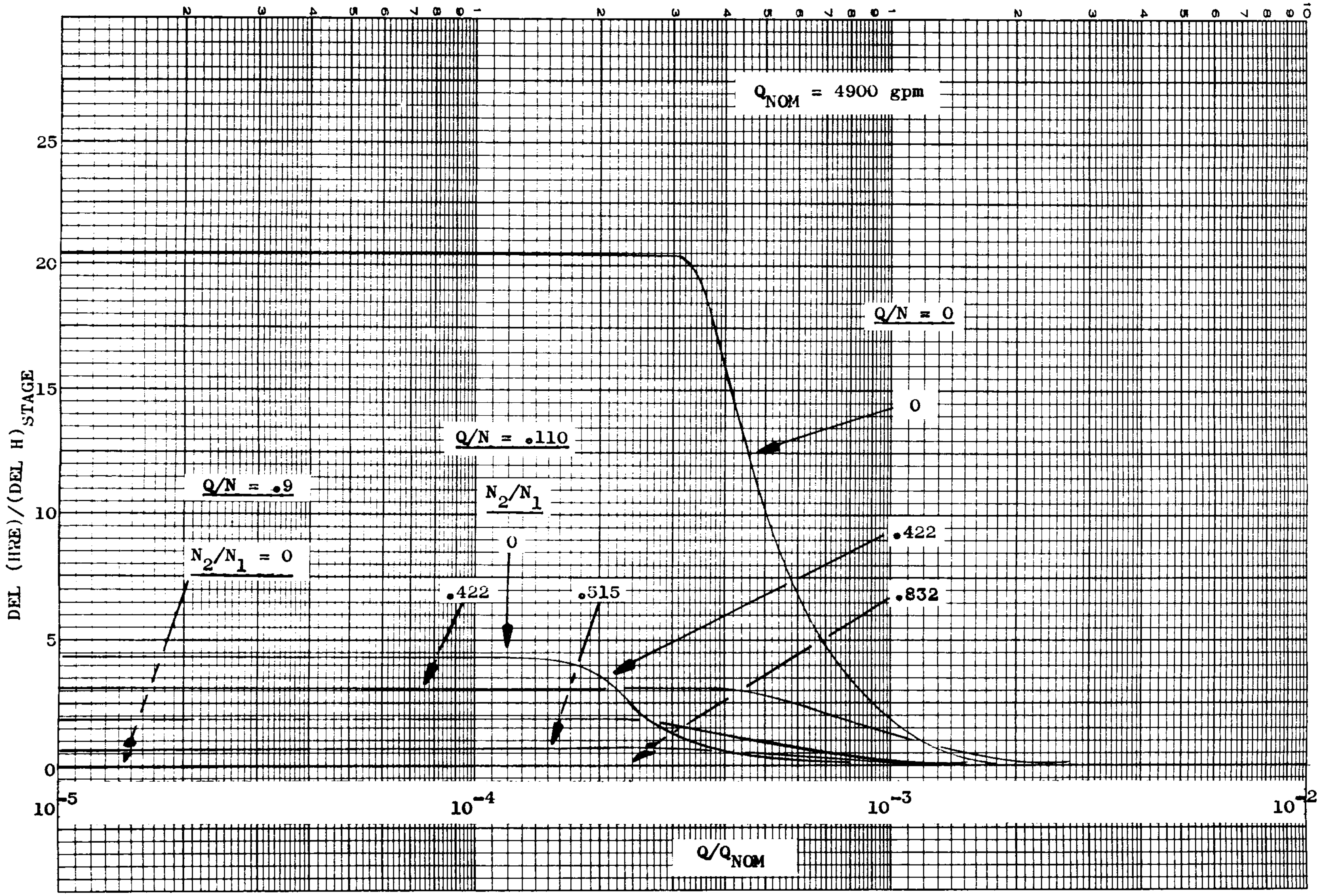

Figure 46. High-Speed Rotor DEL (HRE)/(DELH)$_{Stage}$ vs Q/Q_{Nom} - LH_2

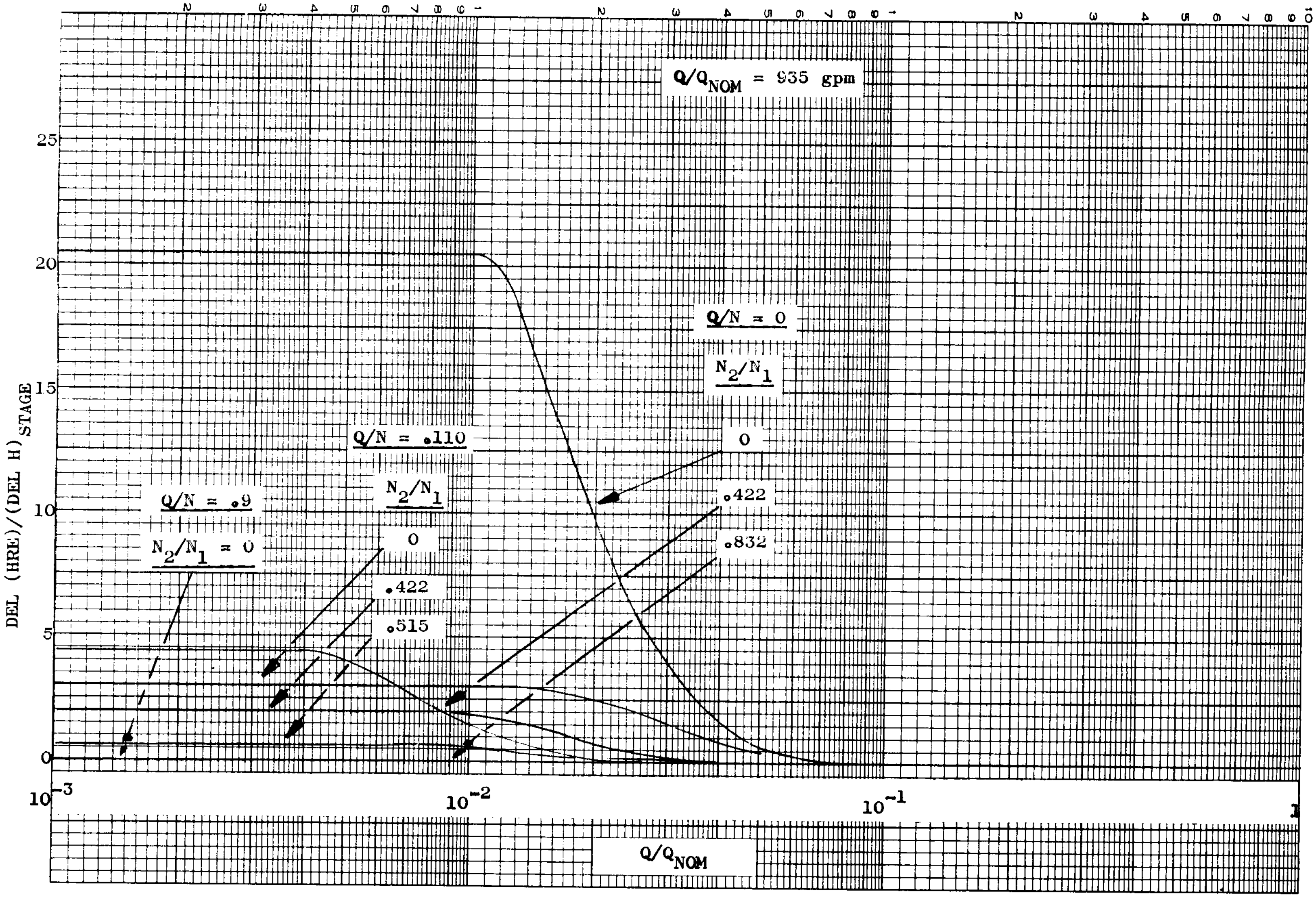

Figure 47. High-Speed Rotor DEL (HRE)/(DELH)$_{Stage}$ vs Q/Q$_{Nom}$ - Water

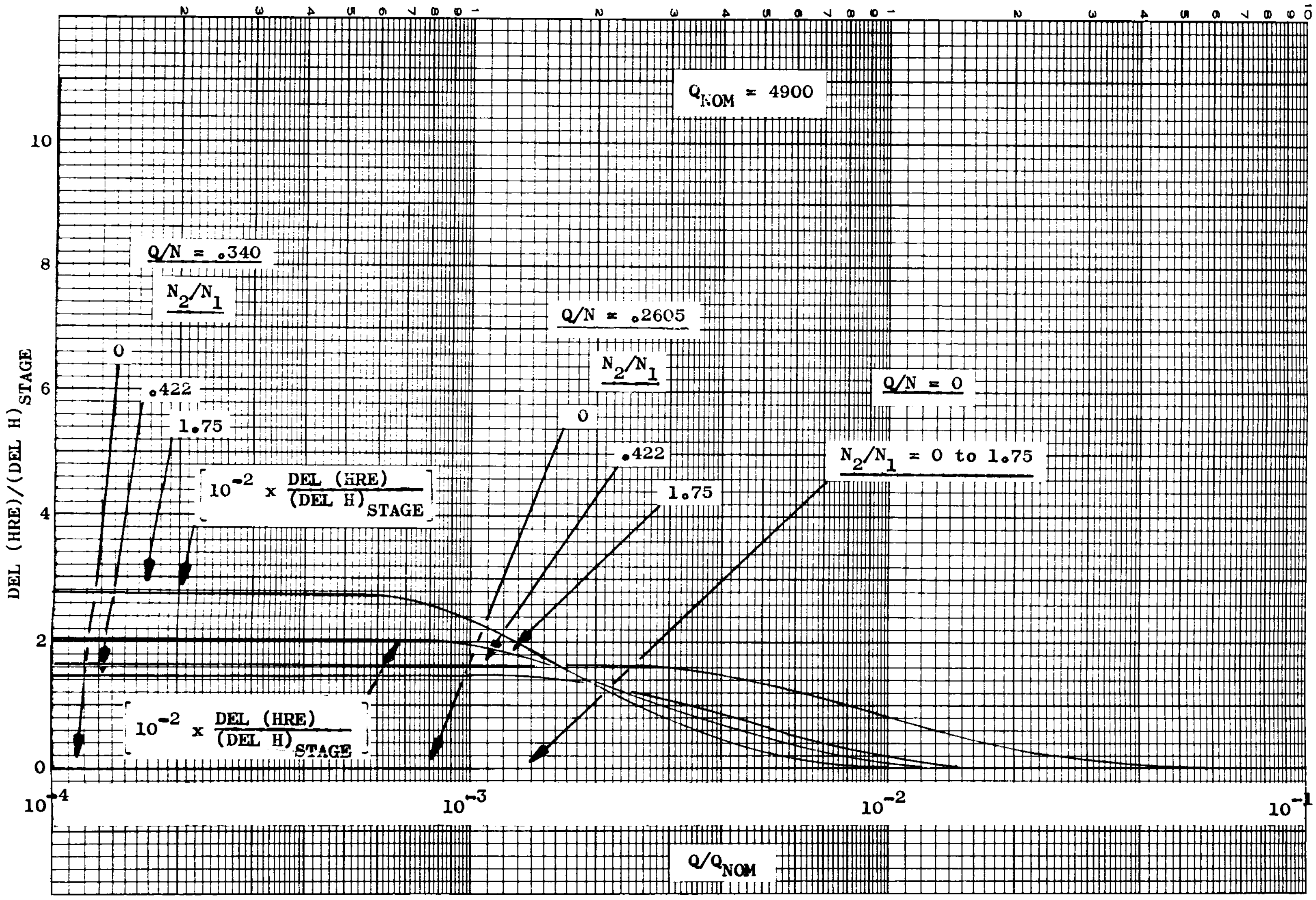

Figure 48. Hydraulic Turbine DEL (HRE)/(DELH)$_{\text{Stage}}$ vs Q/Q$_{\text{Nom}}$ - LH$_2$

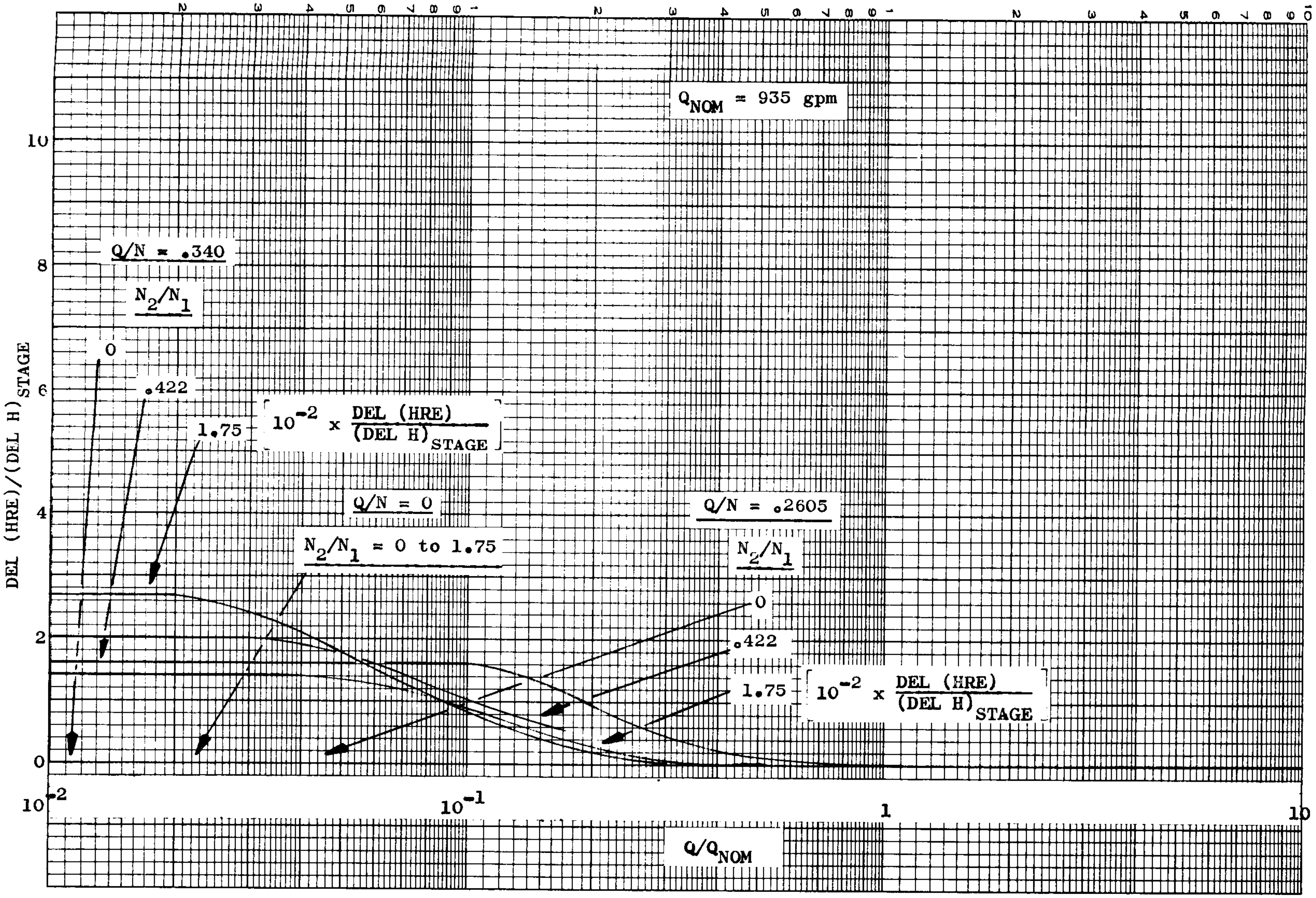

Figure 49. Hydraulic Turbine DEL (HRE)/(DELH)$_{\text{Stage}}$ vs Q/Q_{Nom} - Water

IV. TASK II - FORMULATION AND DEMONSTRATION OF COMPUTER SIMULATION

The formulation of a digital computer model for the dynamic analysis of an inducer pump with a full-flow, full-admission hydraulic turbine is presented in this section. Two systems were modeled in conjunction with the inducer; a closed-loop system for transient testing with water, which was structured after the D-3A test facility and an open-loop system which can represent either a chemical rocket engine feed system or a cryogenic pump test facility (i. e. Test Stand H-6).

The general approach in modeling the inducer was to describe the performance of the blade rows by normalized performance curves, which were obtained from separate computer programs for blade and passage design. For example, to study a change in pitch angle, the first step is to generate revised performance maps. Then, the effect of the revised blade performance upon the dynamics would be studied using this program.

The performance curves portraying the stages of the inducer can be mono-variant, bi-variant, or tri-variant functions

$$Y_i = f(X_i)$$

$$Y_j = g(X_j, Z_j)$$

$$Y_k = h(X_k, Z_k, W_k)$$

The fixed tables of input values are interpolated. The work balance on the shafts, the calculation of boundary conditions, the energy (heat) balance, and the calculation of minor losses complete the inducer model.

The system model is composed from a finite difference, method of characteristics, solution to waterhammer theory. Waterhammer theory is used to describe all hydraulic components. For right traveling waves

$$\frac{P_{x,t}}{\rho} + \frac{V_w}{gA} \frac{W_{x,t}}{\rho} = C+$$

while for left traveling waves

$$\frac{P_{x,t}}{\rho} - \frac{V_w}{gA} \frac{W_{x,t}}{\rho} = C-$$

where C+ and C- are the waterhammer constants or characteristics. These equations are solved along with non-linear friction and appropriate boundary conditions (the inducer model being one) to describe the system.(66)

---

(66) Chan, J., <u>One-Dimensional Unsteady Liquid Flow Using Waterhammer Theory</u>, Aerojet-General Computer Program No. 31403, SR40JC, July 1967

The pressure-weight flow rate form of the "characteristics" as a finite difference solution to the quasi-linear hyperbolic partial differential continuity and dynamical motion equations is convenient for direct comparison to chemical rocket engine test data.

Appendices C and D contain the detailed assumption, derivations, and equations used to portray the inducer and feed systems. The model nomenclature and digital program listings will be provided as part of the final report.

A. FINITE DIFFERENCE TECHNIQUES

1. Selection of Computing Interval

A computing interval must be selected for each system analyzed because of the finite difference approach used in formulating the model. Selection of small computing intervals (.001 sec for the advanced engine model, .005 sec for the Test Stand H-6 model, and .002 sec for the Test Stand D-3A model), was motivated by the following factors:

- For application of the waterhammer theory to the feed system, a computing interval must be selected that divides the waterhammer wave transmission times for the various lines into integers.
- The convergence on the low-speed shaft speed can be eliminated by using the first past time value in the equations.
- The time derivations of a parameter (P) can be expressed as a simple first order finite difference expression, such as

$$\frac{dP}{dt} \doteq \frac{\Delta P}{\Delta t} \doteq \frac{P_t - P_{t-1}}{\Delta t}$$

- For certain non-critical derivatives, past time values of P can be used to evaluate the derivative without loss of accuracy.

2. Explanation of First Past Time Assumptions

Transient analysis experience with a multiplicity of pump-fed engines(67) has shown that the accurate simulation of the transients can be

---

(67) Bergloff, R. A. and Olson, G. K., Engine Transients and Controls System Study of the Gas-Gas Two Stage Combustion Cycle Version of a 1500K H_2-O_2 Engine, Aerojet-General Report No. SCR-165, March 1965.

obtained by using first past time values for current time values for two general types of parameters. One is a parameter which has no discontinuities and has a definite physical limit to instantaneous change (i.e., pump speed). The other parameter is one which will be used in the calculation of a small correction to the over-all process (i.e., Equation 4 of the High-Speed Rotor Subroutine, Appendix C). This is the procedure that was followed in all of the subroutines.

3. Interpolation of Characteristic Curves

Characteristic curves are used extensively in the model with many of the curves being functions of two or three variables. While the linear, two-point interpolation method was used, each table in a map was fitted by a parabolic function. This method facilitiates the evaluation of the effect of various variables upon the over-all solution of the model.

4. Convergence Methods

The only convergence in the model is on the weight flow through the inducer. The iteration scheme is a combination of false position and the Newton-Raphson method. This iteration scheme has been used successfully for a wide variety of engine transient analyses.(68)(69)(70)(71)

The main convergence problems come from the discontinuities, maximums, and minimums in the various performance characteristic curves. Therefore, the minimum number of curves required to accurately calculate the head rise or loss are included in the convergence loop.

5. Accuracy of the Computer Model

The over-all accuracy of the model can be evaluated only in relationship to its ability to simulate the test data. Because of its complexity, a numerical estimate of the effect of specific assumptions and methods is nearly impossible. Many input curves are used in the model which are bi-variant or tri-variant. Experience has shown that the numerical methods will contribute less error than the basic error involved in the necessarily limited curve or tabular input. If more accuracy is required, an increase in the mapping of the curves will probably be required.

---

(68) Chan, J., Aerojet-General Computer Program No. 31403, op. cit.

(69) Bergloff, R. A. and Olson, G. K., Aerojet-General Report No. SCR-165, op. cit.

(70) Farr, P. F. and Olson, G. K., Performance Analysis of a Post Boost Control System, Vernier Vector Unit, Aerojet-General Report No. PTDR-9647-018, June 1965

(71) Olson, G. K., (U) A Study of the Fluid Dynamics of an Intensifier Feed System During ARES TCA Development Testing, Aerojet-General Report No. AMDR-9635-014, April 1966 (Confidential Report)

B. PUMPING SYSTEM SUBROUTINE

The pumping system subroutine is the model of the inducer dynamics and is called NASA-TP. This subroutine is designed to accommodate the transient performance calculations for four stages called the inducer, rotor, turbine, and collector or main stage. The schematic, nomenclature, assumptions, equations, and logic are presented in Appendix C. The logic was designed to take advantage of the similarity in equations for each stage. Therefore, a "do loop" was designed which uses J = 1,4 for the stages inducer through collector or main stage, respectively.

The above subroutine is used as part of the waterhammer subroutine (SR No. 11) (see Appendix D). It is called by SR No. 11 as part of the waterhammer solution of the feed system. An internal convergence upon the pump weight flow is required to establish continuity with the suction and discharge lines to the NASA-TP. In the NASA-TP, the equations describing the head-flow relationships are solved first for stages J = 1,4 and converged with the waterhammer feed line equations. After convergence, a "TORQUE FLAG" is set by SR No. 11, which allows the NASA-TP to calculate the stage torque, speed, exit temperature and exit density. This method permits the minimum number of equations to be present in the convergence loop.

The solution of the NASA-TP equations cannot begin with zero speed. This problem is handled by establishing "initial condition limits" on the solution. Before calculations are made in the NASA-TP using the characteristic curves, the high-speed shaft must exceed a minimum speed N_{1min}. Until then, no head or torque curves are used. The N_1 test FLAG (see Appendix C) is set equal to zero and tested in SR No. 11 to by-pass the torque calculations. In addition, before calculations are made with the curves for low-speed shaft components, the flow, Q, must exceed a minimum represented by

$$Q_{Min} = \frac{\%\ Q_{Min}}{100} \cdot Q_{Nom}$$

Also, a minimum speed (N_2), must be input.

1. Water Model

The NASA-TP is designed to handle the solution of the equations for operation with water as the base case. (Hydrogen operation is an option.) The basic assumptions are listed in Appendix C. It is suggested that they be reviewed thoroughly to fully understand the logic used.

2. Hydrogen Model

If hydrogen is the fluid pumped, an option flag "H_2 FLAG" must be input equal to 1, and the heat-sink heat transfer subroutine must be referenced. The heat transfer subroutine is called HTSR(M), and uses 20 data locations. It calculates the suction temperature to the first stage, T_s (see Appendix C).

When the H_2 FLAG is set, a thermodynamic properties subroutine is called, (i.e., Call PT or PH).(72) This subroutine calculates the suction fluid density for each stage from the suction pressure and temperature. Also, it calculates the exit temperature for each stage from the discharge pressure and enthalpy. Thus, this is the method used to calculate the compressibility effects of hydrogen The hydrogen data is obtained from existing literature.(73)

C. OVER-ALL SYSTEM MODELS

Two systems were modeled. One is a closed-loop system with the basic configuration of the Test Stand D-3A (water pump test) facility. This is the model which will be used for model valiation purposes because the demonstration unit will be tested at Test Stand D-3A. The other model is an open-loop system and was used to evaluate the inducer dynamics in an advanced cryogenic engine feed system as well as a cryogenic pump test facility (Test Stand H-6, the NERVA facility).

1. Feed System Subroutines

The feed system subroutines describe the various joints and lines in the systems (i.e., the tanks, valves, suction lines, and discharge lines). The method of characteristics is the basic method used in solving the differential equations. A main control subroutine, SR-40, handles the set-up of the initial conditions and the bookkeeping involved in the finite difference solution.

The components of the system are defined by numbered component routines, which when put together in a fixed order of solution establish the model. The solution begins with a known initial condition at a tank and proceeds in the established order through the components returning to the tank for the next time point

The equations and logic, are presented in Appendix D.

2. Test Stand D-3A Water Facility Model

This model describes the Aerojet-General Test Stand D-3A pump test facility. This facility is a closed-loop system for pump testing with water. The models, schematic, and order of solution are presented in Appendix E In this model, the fourth stage (J=4) is a collector; therefore, the collector option is flagged in the NASA-TP (i.e., (N + 336) = 1).

---

(72) Huser, D A., Properties of Cryogenic Fluids, Aerojet-General Memorandum No. 7830:H3153, 13 February 1967

(73) Farmer, D A , FORTRAN IV Hydrogen Property Tabular Codes, Los Alamos Scientific Laboratory Report No LA-3381, 29 October 1965

3. Engine System Model

This model describes the fuel feed system of the advanced cryogenic engine. Its schematic and order of solution are presented in Appendix E. Because the fluid is hydrogen, the NASA-TP subroutine must exercise the appropriate options. In this model, the fourth stage is an advanced cryogenic centrifugal pump. The solution begins at the known constant tank pressure at the tank outlet and ends at the known constant atmospheric pressure at the injector outlet.

4. Test Stand H-6 Hydrogen Facility Model

This model describes the Aerojet-General NERVA hydrogen pump facility. The schematic and order of solution is the same as for the engine system model. Again, the fluid is hydrogen; therefore, the correct options must be exercised. The characteristic curves describing the inducer are the same as for the water facility model (viz., the fourth stage is a collector).

D. COMPUTER SIMULATION

The closed-loop, waterhammer solution of a pump facility is not known to have ever been successfully attempted and published. Therefore, the first step was to evaluate a fictitious inducer operating in the closed-loop. This simulation was completed using a modification of an existing Aerojet-General hydrodynamics program on 17 May 1967, (see Figure No. 50). Table VIII shows the nomenclature used in this figure and those included in the ensuing Section V.

After the NASA-TP model was completed, preliminary performance data for the blade rows were input. Using this data, the program successfully simulated a 3-sec start and shutdown on 18 July 1967. These simulations were used to evaluate the preliminary design of the inducer and resulted in changes to the final design.

Next, the final design performance data were input to the program. Expansion of the program was necessary to accommodate these data. Over 11,000 data locations were required for the final input. This represents 260,000 bytes of IBM 360-65 storage. The total program with instructions requires 390,000 bytes storage out of the total of 512,000 bytes or 75%.

The previously-mentioned three system models were input and checked out. Data were validated by hand checks of curves, evaluation of key time points, and accurate steady-state balance points. Then, the verified computer simulations were used to run the parametric studies.

A typical closed-loop 3-sec duration transient will take 3 min to 3.5 min of execution time. A typical open-loop hydrogen transient will

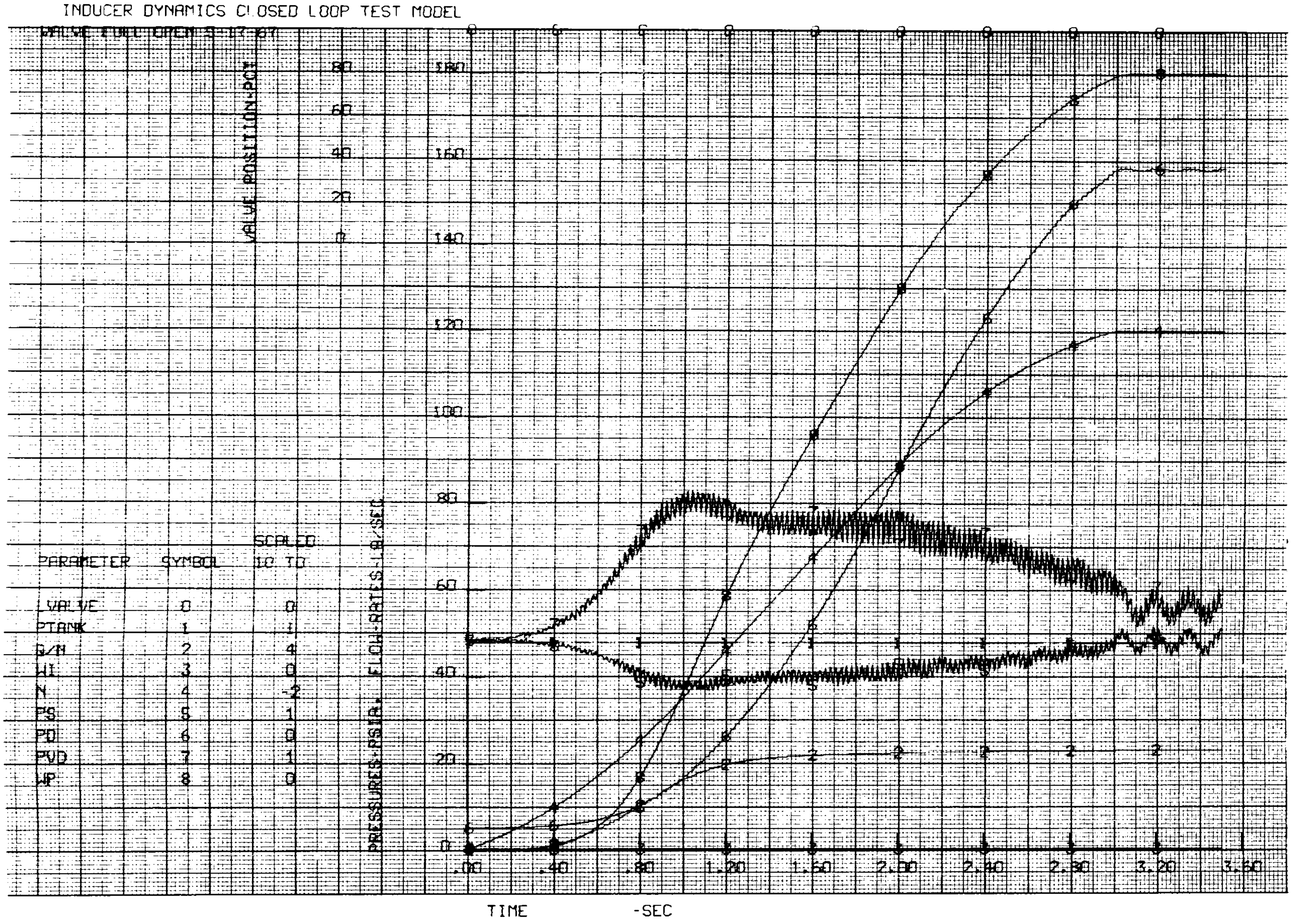

Figure 50. Inducer Dynamics Closed-Loop Test Model

TABLE VIII

NOMENCLATURE

Parameter	Units	Description
L VALVE	% open	Discharge valve position
Q/N-I	gpm/rpm	Flow coefficient - Inducer stage
Q/N-R	gpm/rpm	Flow coefficient - Rotor stage
Q/N-T	gpm/rpm	Flow coefficient - Turbine stage
Q/N-MP	gpm/rpm	Flow coefficient - Main pump stage
N_2/N_1	gpm/rpm	Speed ratio - Low/High
N_2	rpm	Speed - Low speed shaft
N_1	rpm	Speed - High speed shaft
Q	gpm	Capacity
PS	psia	Suction pressure
PD	psia	Discharge pressure - Over-all
PJ	psia	Injector pressure
PVD	psia	Valve discharge pressure
PD-I	psia	Discharge pressure - Inducer
PD-R	psia	Discharge pressure - Rotor
PD-T	psia	Discharge pressure - Turbine
PD-MP	psia	Discharge pressure - Main pump
WP	lb/sec	Weight flow rate
S-I	$\mathrm{rpm(gpm)}^{1/2}/\mathrm{ft}^{3/4}$	Suction specific speed - Inducer
S-R	$\mathrm{rpm(gpm)}^{1/2}/\mathrm{ft}^{3/4}$	Suction specific speed - Rotor
S-T	$\mathrm{rpm(gpm)}^{1/2}/\mathrm{ft}^{3/4}$	Suction specific speed - Turbine
S-MP	$\mathrm{rpm(gpm)}^{1/2}/\mathrm{ft}^{3/4}$	Suction specific speed - Main pump
NPSH	ft	Net positive suction head
TQ-I	ft-lb	Torque - Inducer stage
TQ-T	ft-lb	Torque - Turbine stage

take approximately double this time because of the added complexity of the hydrogen property data and the increased output. It was determined that the majority of the execution time resulted from the input and output of data. Therefore, the less data plotted or printed in relationship to time, the lower is the cost of analysis.

E. CONCLUSIONS FROM THE TASK II EFFORT

The following conclusions are based upon the formulation and evaluation of the computer model during Task II:

1. The characteristic curve approach to the description of the dynamic performance of a multi-stage inducer pump is workable and efficient. Basic transients can be executed in three minutes using the IBM 360-65 system.

2. Large data input is required by the characteristic curve approach. This fact necessitates careful attention to curve maps, their size, limits, number of points input, as well as the handling of maximums and minimums. Also, careful, methodical checks of program input data must be made to ensure the absence of error.

3 When checking out new data, the minimum characteristic curves that are essential to evaluation of the design should be used. Other minor correctors should be set to zero fields.

4 Small computing intervals are essential to the finite difference techniques used.

5. The waterhammer description of the closed-loop system provides an analysis of the oscillatory stability characteristics of the system as well as the over-all "inertia" characteristics of the suction and discharge lines. Therefore, the program should prove valuable as an analytical tool for the synthesis of test facilities for dynamic pump testing as well as an analytic tool for existing systems.

6. The waterhammer description of the open-loop system is particularly valuable for studies with hydrogen The compressibility effects of rapid pressure changes in the hydrogen suction and discharge lines significantly affect the pump dynamics. For example, during rapid bootstrapping of the low-speed shaft during the advance engine transient, the flow rate into the discharge line exceeds the outflow by 10%.

V. TASK III - PARAMETRIC STUDIES

The inducer dynamics were investigated parametrically in two systems. The first system was the Test Stand D-3A test facility, which is a closed-loop system. In this facility, the demonstration unit will be tested with water. The second system was an open-loop system. With this system, both an advanced cryogenic engine feed system configuration and the NERVA pump test facility, Test Stand H-6, were investigated. Liquid hydrogen was the fluid studied.

A. DEMONSTRATION UNIT IN A CLOSED-LOOP SYSTEM

1. Nominal Operating and Computation Conditions

The nominal operating conditions for the demonstration unit are listed on Table VI. In addition, there are the requirements of:

- Duration = 3.0 sec
- NPSP = 2.65 psi (NPSH = 6.1 ft)

These conditions are added to describe the transient suction performance. The higher than design value of NPSH was selected because a suction pressure oscillation of 2.75 psi peak-to-peak was predicted (by water-hammer theory) to be induced by the rapid 3 sec transient. (This oscillation of 6.0 cps superimposed upon the over-all suction fluid inertia pressure drop caused the inducer to cavitate at NPSH = 3.83 ft.)

The start transient had the following initial conditions and boundary conditions:

a. Initial low speed shaft speed, N_2 = 1 rpm.

b. No change in head through the unit until high-speed shaft speed, N_1 = 100 rpm.

c. Initial N_2/N_1 = .01.

d. No torque calculated for unit until capacity, Q, equal to 3% steady-state capacity.

e. Initial Q/N_2 = maximum = 26.

f. Vapor pressure at suction = .35 psia.

The shutdown and throttle transients were run from data written on tape for the conditions existing at the end of a 3 sec start transient with a suction pressure of 4.0 psia. Therefore, the oscillations seen on these transients represent the conditions immediately following this start.

2. Nominal Start

The nominal start and shutdown are discussed in detail as well as the parametric changes related to them (see Figures No. 51 and No. 52; see Table VIII for appropriate nomenclature).

The time sequenced order of events for the start are as follows:

a. Starting from zero, the N_1, Q/N_1, and Q build up in the unit until, at .62 sec, the low-speed shaft begins to rotate. At this time, $Q = 50$ gpm, $N_1 = 1150$, $Q/N_1 = .05$, $Q/N_2 = .50$.

b. Next, a rapid short duration acceleration of the low-speed shaft, caused by the large power input from the turbine, occurs and continues until the speed reaches 400 rpm.

c. This shaft acceleration induces a low-amplitude, water-hammer oscillation in the suction line The oscillation continues undamped throughout the transient because of the low friction loss in the suction line as well as the pump exhibiting a small gain between suction and discharge.

d. From 0.8 sec to 1.1 sec, the unit operates at an approximately constant N_2/N_1 step equal to .285 until N_2 reaches 900 rpm. After 1.1 sec, the rapid acceleration of the low-speed shaft begins. The maximum acceleration rate during this time equals 2500 rpm/sec. The corresponding maximum flow acceleration is 635 gpm/sec or 88 lb/sec/sec. The corresponding minimum non-oscillatory suction pressure is 2.2 psia (NPSP - 1.85). The corresponding minimum oscillatory suction pressure is 1.10 psia.

The steady-state balance point obtained by the computer program agrees with that specified on Table VI. The following is a comparison of the most important parameters:

Parameter	Computer Program	Design Specification	% Difference
Suction Pressure*	3.0	3.0	0
Inducer Total Head Rise, ft	111.2	112.0	-0.6
Inducer Discharge Pressure, psia	51.2	51.5	-0.6
Inducer Torque, ft-lb	55.5	55.6	-0.1
Rotor Total Head Rise, ft	263.0	264.0	-0.2
Rotor Discharge Pressure, psia	165.2	164.6	-0.2
Rotor Torque, ft-lb	47.47	47.5	0
Turbine Total Head Drop, ft	172.0	173.0	-0.5
Turbine Discharge Pressure, psia	90.7	89.9	+1.0
Turbine Torque, ft-lb	55.5	55.6	-0.2
Collector Total Head Drop*, ft	21.2	20.6	+3.0

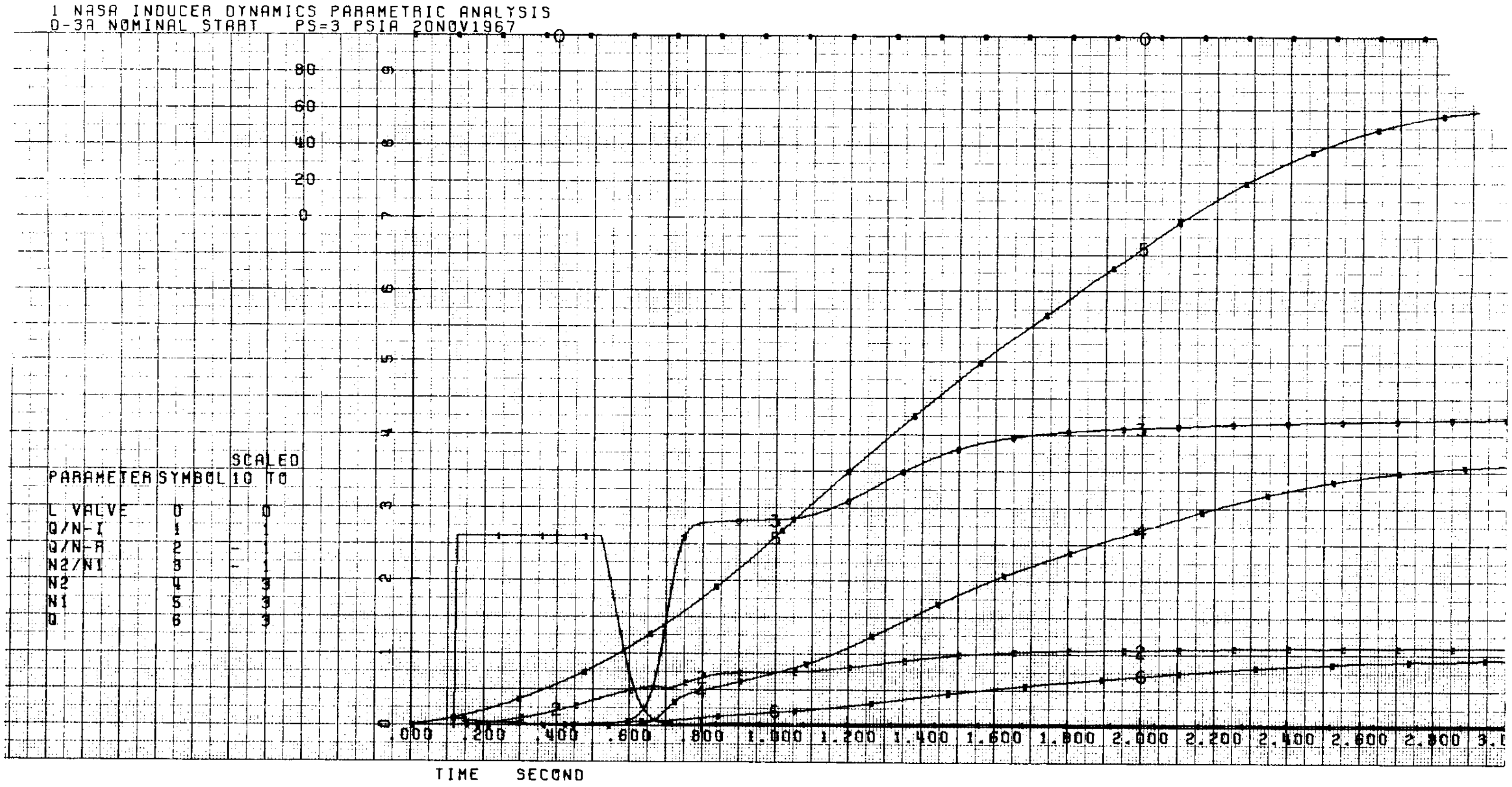

Figure 51. D-3A Nominal Start, PS = 3 psia

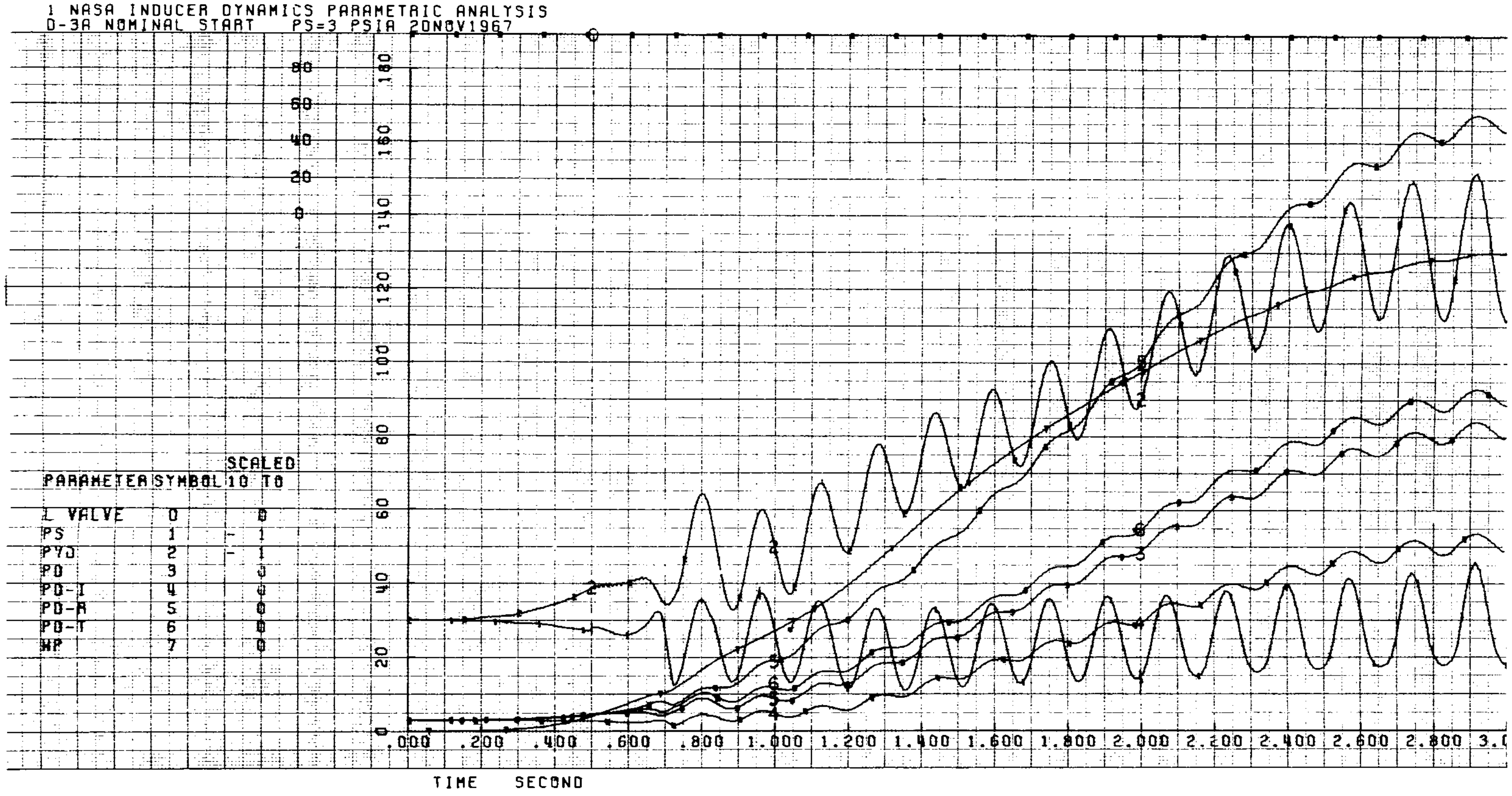

Figure 51. D-3A Nominal Start, PS = 3 psia

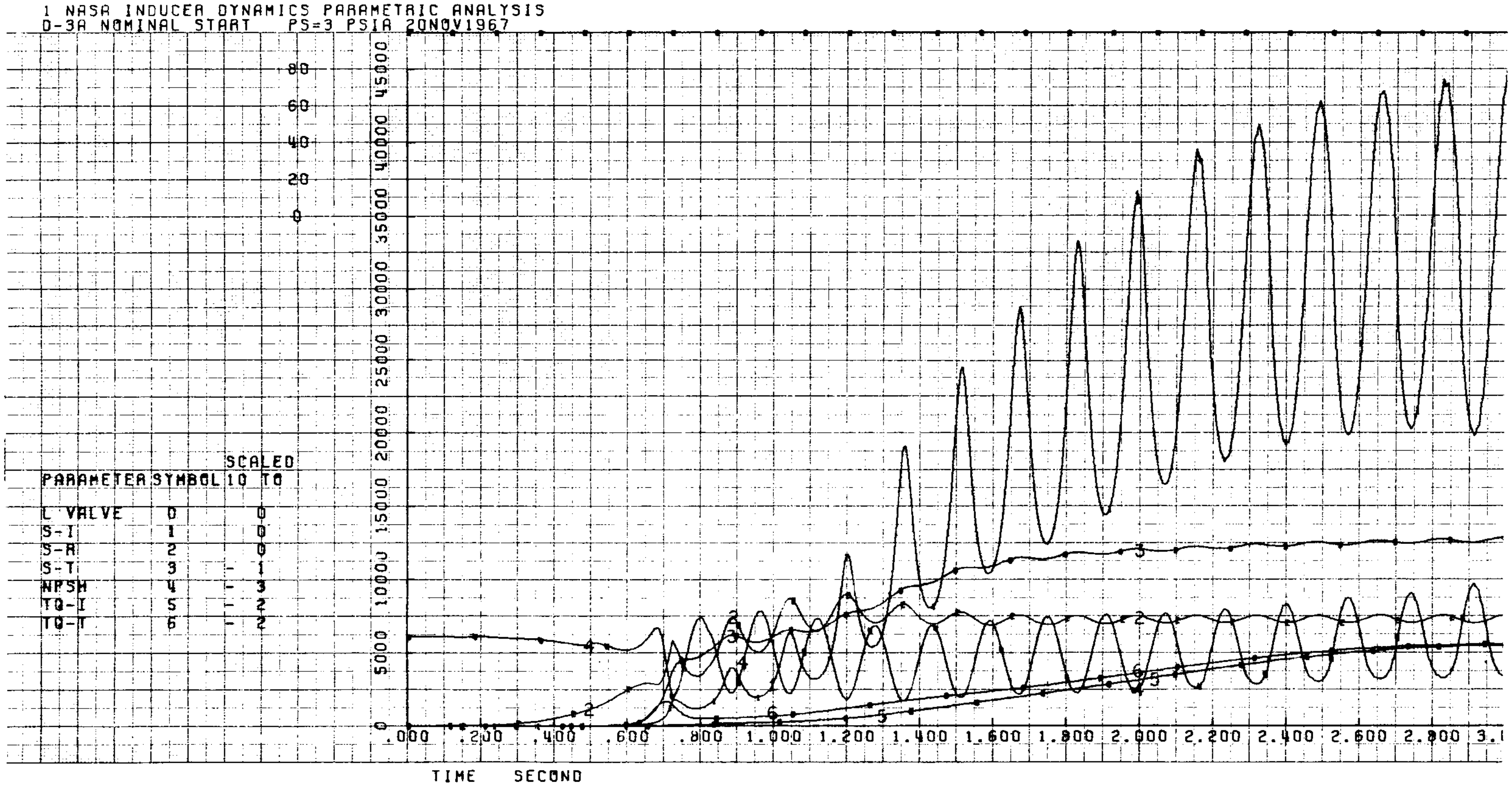

Figure 51. D-3A Nominal Start, PS = 3 psia

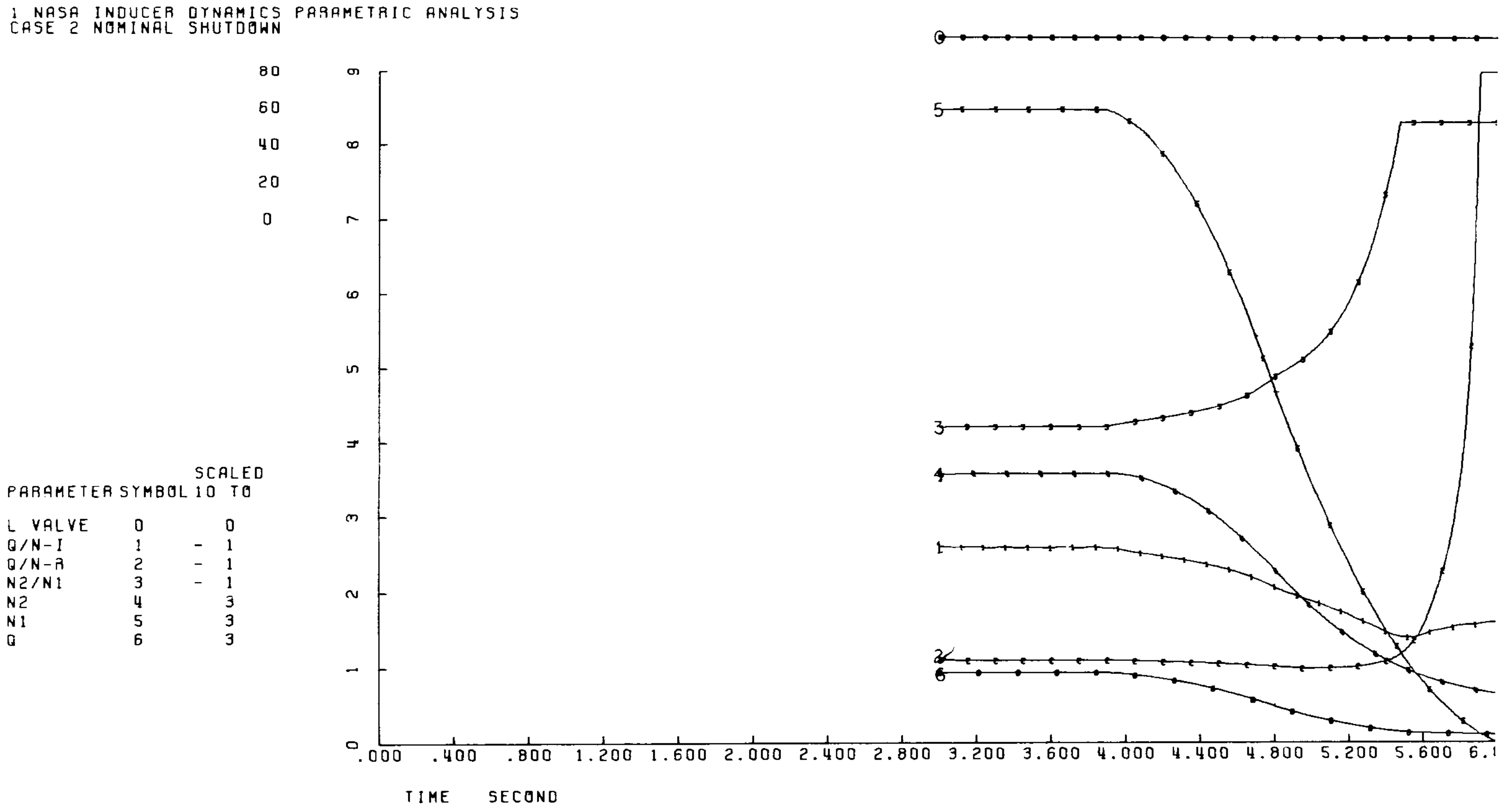

Figure 52. D-3A Nominal Shutdown

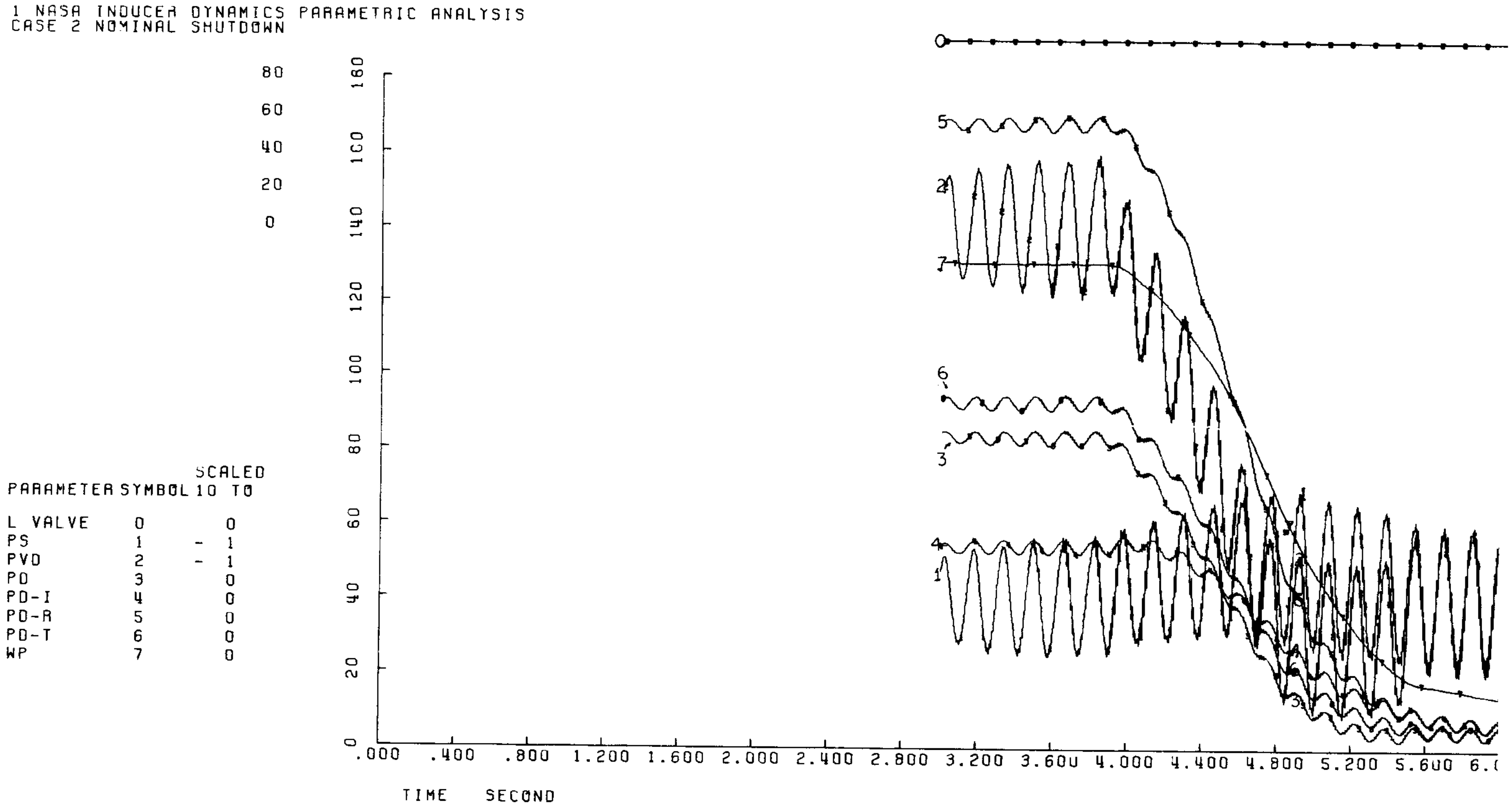

Figure 52. D-3A Nominal Shutdown

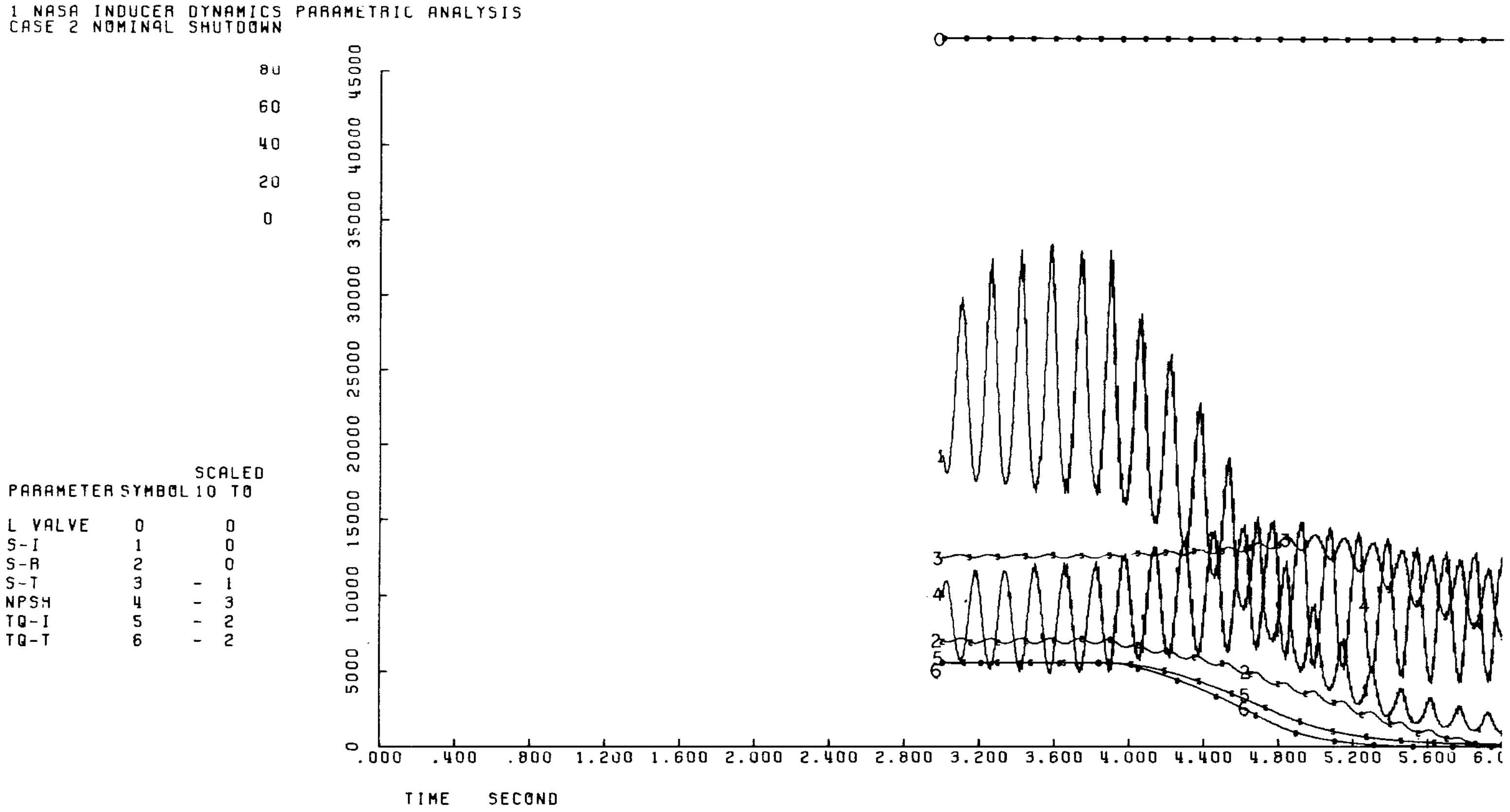

Figure 52. D-3A Nominal Shutdown

Parameter	Computer Program	Design Specification	% Difference
Collector Discharge Pressure*, psia	81.5	81.1	+0.5
Capacity, gpm	933.6	935.0	-0.1
Weight Flow, lb/sec	129.8	130.0	-0.2
High-Speed Shaft, rpm	8500.0	8500.0	0
Low-Speed Shaft, rpm	3588.0	3590.0	0.1

---

*Not included in document or revised from document.

The maximum temperature change experienced through the stages of the unit was calculated to be .14°F. The temperature profile through the unit was as follows:

	Inducer	Rotor	Turbine	Collector
Stage Suction Temperature, °R	530	530.07	530.15	530.13

Obviously, the density changes through the unit are negligible.

3. Nominal Shutdown

The time sequenced order of events for the shutdown are as follows:

a. From 3.0 sec to 3.8 sec is steady-state. The induced oscillation from the start continues and shows a small gain.

b. As N_1 decreases, N_2 decreases, but at a slower rate; therefore, N_2/N_1 increases. Q/N_1 first decreases to .10 and then rapidly increases starting at 5.4 sec. Q/N_2 steadily decreases. Both N_2/N_1 and Q/N_1 reach their input maximums at .832 and .90, respectively.

c. The maximum decelerations of flow and N_2 occur between 4.7 sec and 4.8 sec; flow deceleration equals -817 gpm/sec or -114 lb/sec/sec and speed deceleration equals -2500 rpm/sec. During these decelerations, the suction pressure increases by 0.9 psia.

d. When N_1 reaches zero, N_2 is still 690 rpm.

4. Longer Duration Starts and Shutdowns

Six second duration start and shutdowns were run. The transients exhibit lower acceleration rates and lower induced oscillations. Rotation of the low-speed shaft at start begins at 1.10 sec. General time sequence characteristics are the same. The amplitude of the induced oscillations is 0.7 psi, peak-to-peak (Pk to Pk). The percentage of the start duration resulting from the delay in bootstrapping the low-speed shaft is approximately the same for both the 3 sec and the 6 sec starts, approximately 20%.

5. Changes in Suction Pressure

A decrease in Ps to 2.0 psia leads to cavitation at the pump suction. Cavitation occurs at .71 sec, just after the low-speed shaft begins to rotate. The cavitation is caused by the induced oscillation of Ps. The conditions at the time of cavitation are N_1 = 1400 rpm, N_2 = 320 rpm, and Q = 84 gpm.

An increase in Ps to 4.0 psia lowers the suction specific speed and decreases the amount of cavitation losses of the inducer blade row. The inducer blade row is the only one that experiences cavitation losses during any of the start transients for the closed-loop system.

6. Changes in Valve Position

The valve at the end of the pump discharge line was open and closed 20% from its nominal admittance, Kw, to achieve off-design start transients, approaching 120% Q/N and 80% Q/N. The following are the resulting steady-state operating points achieved:

Case	Q	% Q/QN	N_2	Q/N_1	Q/N_2	ΔH_1	ΔH_R	ΔH_T	ΔH_C
120% Q/N	980	+5%	3710	.1153	.263	118	240	-187	-24
Nominal	935	0	3590	.110	.260	111	263	-172	-21
80% Q/N	830	-11%	2500	.0977	.237	122	274	-156	-26

As shown, the inducer undergoes larger performance shifts from valve closure. The steepness of the rotor head-capacity performance curves with increasing Q/N_1 and N_2/N_1 is the dominant factor.

7. Throttle Cycle

Two throttle cycles were run to the same operating points but with different durations. Using the steady-state point (at 3 sec) obtained from the 3 sec start with Ps = 4 psia, the following two cycles were run: Cycles (1) and (2) were run at steady-state for 0.5 sec, then throttled down to 65% N_1 and 95% Q/N_1 in (2 sec) or (4 sec), then ramped to 100% N_1 and 100% Q/N_1 in (1.5 sec) or (3.0 sec).

Both the short and long throttle cycles were accomplished without any difficulties. The maximum low-speed shaft acceleration was 1750 rpm/sec, which is lower than the nominal start.

8. Effect of Acoustic Velocity

Previous test experience with the Test Stand D-3A facility has shown that various amounts of air are entrained or dissolved in the water. Air entrainment has been demonstrated to have a marked influence upon the wave velocity in liquids.(74) As little as 0.4% air content can decrease the effective acoustic velocity by a factor of 4. Two cases were compared with the nominal, which assumed zero air content. These were one-half and one-quarter the velocity in pure water. The following are the results as pertains to the amplitude and frequency of the induced suction pressure oscillations:

Cases	Acoustic Velocity (ft/sec)	Pk to Pk Amplitude P_s (psi)	P_{vD} (psi)	Frequency (cps)
Nominal	4300	2.8	4.1	5.88
1/2 Nominal	2300	2.0	2.5	3.34
1/4 Nominal	1170	1.5	1.7	1.43

A significant drop in amplitude of the induced oscillations occurs with lower acoustic velocities (see Figure No. 53).

9. Effect of Geometry Changes

Increasing the length of suction or discharge line results in a pressure drop, dP, as a result of fluid inertia. This is related to weight flow acceleration, dw/dt, by

$$dP \propto \frac{\ell}{gA} \frac{dw}{dt}$$

where, ℓ = length, A = area, and g is the gravitation constant.

The nominal suction line length is 38.5 ft. At the maximum dw/dt = 80 lb/sec/sec, the dP for the nominal start was 0.8 psi. When the line was increased by 16 ft, cavitation occurred as a result of the induced pressure oscillation.

A longer discharge line slightly retarded the build-up of flow through the pump. Initial rotation of the low-speed shaft was delayed 30 millisec by increasing the line by 16 ft, which is 75% of the nominal 21.5 ft. The most significant effect of the change was to decrease the amplitude of the induced suction pressure oscillations by 1.0 psi. This demonstrates the widely-known fact that changes in line length can have a significant effect upon resonance in pumping systems.(75) The longer discharge line can be used in testing if necessary.

---

(74) Streeter, V. L. and Wylie, E. B., Hydraulic Transients, McGraw-Hill Inc., 1967

(75) Ibid.

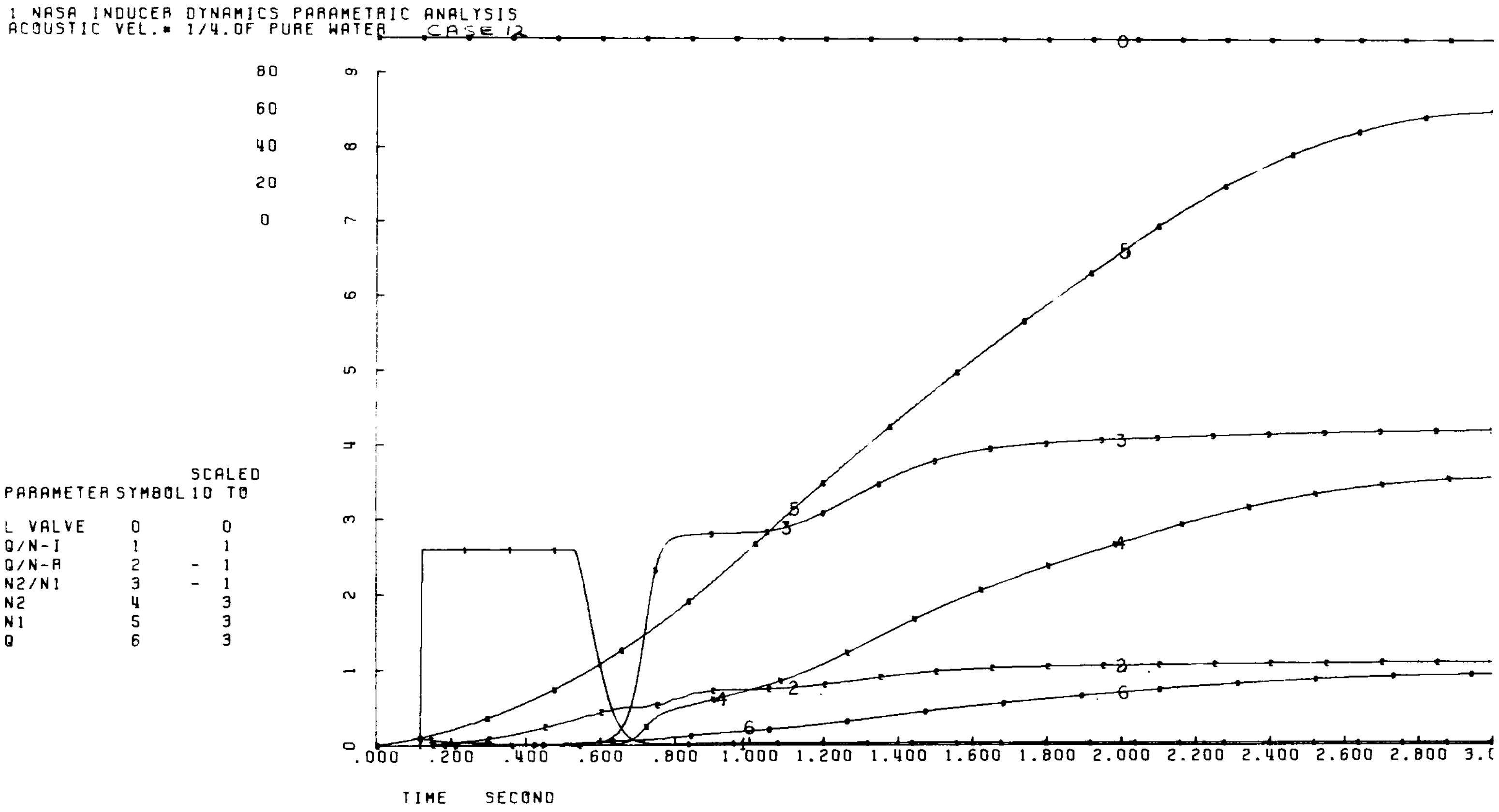

Figure 53. D-3A Acoustic Velocity = 1/4 of Pure Water

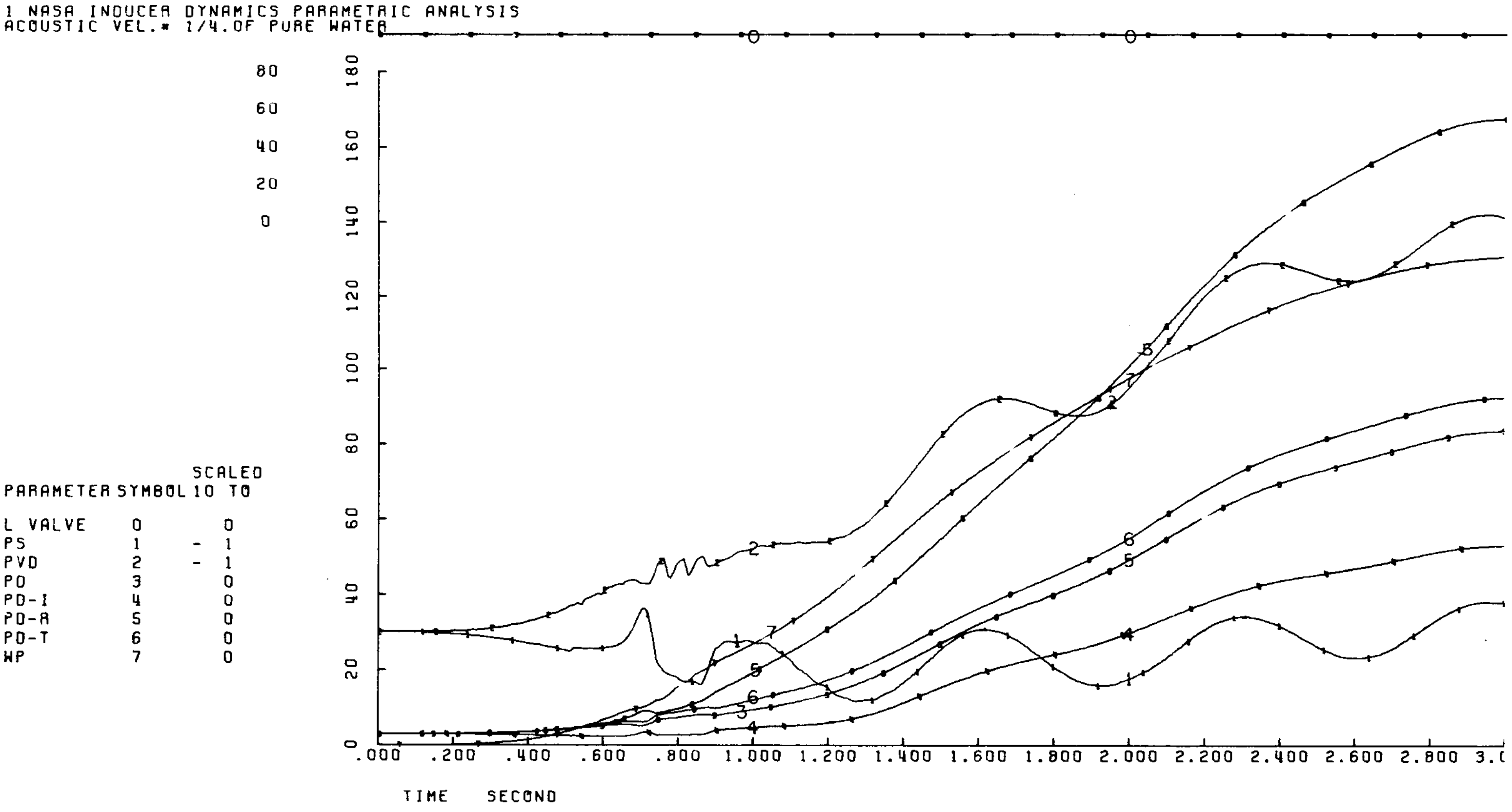

Figure 53. D-3A Acoustic Velocity = 1/4 of Pure Water

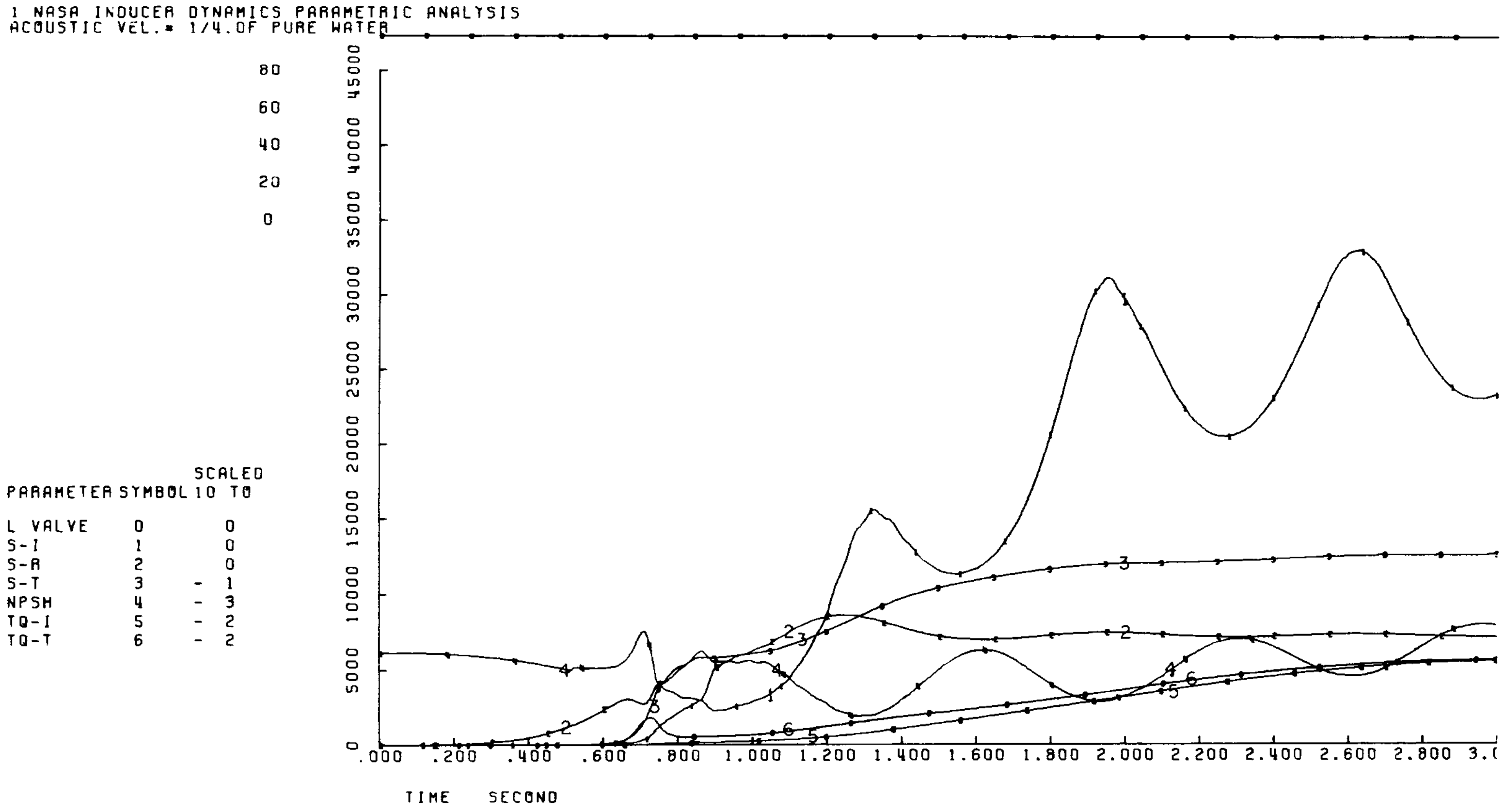

Figure 53. D-3A Acoustic Velocity = 1/4 of Pure Water

10. Effect of Polar Moment of Inertia

The effect of a 25% decrease in the polar moment of inertia from the nominal value of .0317 ft-lb-sec^2 was small. The time of initial rotation of the low-speed shaft remained the same. The lower inertia produced a slightly faster acceleration of the shaft during the middle of the transient. However, 100 rpm is the maximum difference in low-speed shaft speed between the two cases at any time during the transient.

11. Comparison of Cases

Significant parameters of each case were compared with the values from the selected nominal start and shutdown. They are presented on Table IX. The list of the most significant cases studied for Test Stand D-3A is as follows:

Parametric Study: Test Stand D-3A Facility

Case No.	
1	Nominal start, duration = 3.0 sec
2	Nominal shutdown, duration = 3.0 sec
3	6-sec start
4	6-sec shutdown
5	120% Q/N, valve opened 20%
6	80% Q/N, valve closed 20%
7	Higher Ps, Ps = 4.0 psia
8	Lower Ps, Ps = 2.0 psia
9	Short duration throttle cycle
10	Long duration throttle cycle
11	Acoustic velocity equal to one-half of nominal
12	Acoustic velocity equal to one-quarter of nominal
13	Longer discharge line
14	Longer suction line

B. DEMONSTRATION UNIT IN AN OPEN-LOOP SYSTEM

1. Configurations

The two open-loop configurations studied were an advanced cryogenic engine hydrogen feed system and the NERVA pump test facility (Test Stand H-6). The general open-loop configuration is presented in Appendix E. The geometry and pressure schedule for the systems are as follows:

TABLE IX

D-2A WATER TEST FACILITY - PARAMETRIC STUDY OF NASA INDUCER DYNAMICS

Case	Description	Configuration	Duration	Ps	Steady State Q/N_1	Steady State N_1	Boot-strap Time	N_1 at Boot-strap	Max $\frac{dN_1}{dt}$	Max $\frac{dQ}{dt}$	Max $\frac{d\dot{w}}{dt}$	Min. Overall Ps	Min. NPSP	Min. Oscillitory Ps	pk-pk Max. Ampl. Ps	pk-pk Max. Ampl. Pvd	Freq. of Press. Oscillations
			Sec	PSIA		RPM	SEC	RPM	RPM/SEC	GPM/SEC	LB/SEC/SEC	PSIA	PSI	PSIA	PSI	PSI	CPS
1	Nominal Start	Nominal	3	3	100%	100%	.62	1150	2500	635	88	2.1	1.75	1.1	2.8	4.10	6.0
2	Nominal Shutdown	"	"	4	"	"	-	-	-2500	-817	-114	4.0	3.65	2.5	4.0	4.0	6.0
3	6 Sec. Start	"	6	3	"	"	1.1	700	1000	280	39	2.35	2.00	2.2	0.7	0.8	6.0
4	6 Sec. Shutdown	"	6	4	"	"	-	-	-1300	-384	-54	4.0	3.65	1.8	5.0	5.0	6.0
5	120% Q/N_1 Start	"	3	4	105%	103.2	.62	1150	2500	670	92	3.2	2.85	1.9	3.0	4.3	6.0
6	80% Q/N_1 Start	"	3	3	89%	98%	.62	1150	2450	590	81	2.2	1.85	1.3	1.5	1.6	6.0
7	Higher Ps	"	3	4	100	100	.62	1150	2500	635	88	3.2	2.85	2.1	2.0	2.3	6.0
8	Lower Ps	"	3	2	"	"	.55	950	-	-	-	.35	0	-	-	-	-
9	Short Dur. Throttle Cycle	"	5	4	"	"	-	-	1750	470	65	3.5	3.15	2.3	3.5	3.7	6
10	Long Dur. Throttle Cycle	"	6	4	"	"	-	-	1000	235	32	3.7	3.35	2.3	3.6	3.6	6
11	1/2 Acoustic Velocity	"	3	3	"	"	.63	1175	2500	635	88	2.1	1.75	.9	2.0	2.5	3.34
12	1/4 Acoustic Velocity	"	3	3	"	"	.65	1250	2500	635	88	2.1	1.75	1.2	1.5	1.7	1.43
13	Longer Discharge Line	Inc. disch. line by 16 ft.	3	3	"	"	.65	1250	2500	635	86	2.1	1.75	1.3	1.8	1.9	5.25
14	Longer Suction Line	Inc. Suction Line by 16 ft.	3	3	"	"	.65	1250	2500	635	88	.35	0	-	-	-	-

Test Stand H-6 Facility

Component	W lb/sec	P_i psia	Delta P psi	L ft	th in.	D in.	V_ω ft/sec
Tank	29.2	50	0	-	-	-	-
Suction Line	29.2	50	-24	106	.148	8.125	3461
Pump	29.2	26	+57	-	-	-	-
Discharge Line	29.2	83	-6	25	.5	7.625	3487
Valve	29.2	77	-49	-	-	-	-
Dump Line	29.2	28	-4	195	.322	7.625	3481
Outlet	29.2	24	-1	-	-	-	-
			Advanced Engine				
Tank	47	70	-	-	-	-	-
Suction Line	47	70	-4.00	28	.1	8	3374
Pump*	47	66	+5704	-	-	-	-
Discharge Line	47	5770	-10	2	.3	3	3464
Valve	47	5760	-90	-	-	-	-
Injector Feed Line	47	5650	-1000	3.5	.3	3	3475
Injector		4650	-4627	-	-	-	-

---

*Includes advanced cryogenic main stage pump

2. Hydrogen Pump Test Facility Transients

Table V is an enumeration of the nominal operating point studied for the Test Stand H-6 test facility. Some changes were made to the pressure schedule to minimize the change of induced oscillations experienced in the water test facility analysis. An orifice was inserted into the system line to provide damping and the tank pressure was raised to accommodate this change.

The nominal high-speed shaft transient was a 3 sec "S" shaped build-up. The deviation was the same as for the nominal water facility start. However, the shaft maximum accelerations were greater, 17,000 rpm/sec as compared with 4500 rpm/sec for the Test Stand D-3A start. The computational boundary conditions for the start were the same as the Test Stand D-3A start.

The start transient is presented on Figure No. 54. Significant characteristics of the start are summarized as follows:

a. After N_1 = 100 rpm, the low-speed shaft flow coefficients, Q/N-I and Q/N-T, are at their input maximums while the high-speed shaft coefficient, Q/N-R, ranges between .036 to .053 before bootstrapping occurs at 1.70 sec. This range is in the high head rise performance region of the rotor stage. This mode of operation would be desirable in an engine. It was accomplished by opening the control valve slowly. The control valve actuation time was 2.95 sec to its steady-state position, 95% open. (This position was required, using the design test area valve, to obtain the steady-state balance point.)

b. The long slip region did not detrimentally affect the inducer operation; actually, it helped to maintain the discharge pressure of the unit greater than, or equal to the suction pressure over the entire start. At bootstrapping, the pressure profile across the unit was as follows:

	Inducer	Rotor	Turbine	Collector
Pd, psia	42.5	104.5	103.8	90.3
Ps, psia	47.5	42.5	104.5	103.8
ΔP, psi	-5.0	62.0	-0.7	-13.5

Ignoring the effect of the test area line losses, it can be seen that a NPSP of 5 psi would be required for this start to avoid cavitation of the unit.

c. The percentage of total duration represented by the slip region was 57%. When compared to the nominal Test Stand D-3A slip region at 20% of total duration, a distinct difference is noted. This difference is attributable to the higher high-speed shaft acceleration. This fact was proven by running a Test Stand H-6 start of 9 sec duration which produces the same acceleration as the nominal Test Stand D-3A transient. With the same acceleration, the same percentage slip of 20% was produced.

d. At bootstrapping, other important conditions were Q = 946 gpm and N_1 = 17,972 rpm. Their steady-state values are 3040 and 27,500 respectively.

e. After bootstrapping, the unit makes a smooth, continuous transition to steady-state.

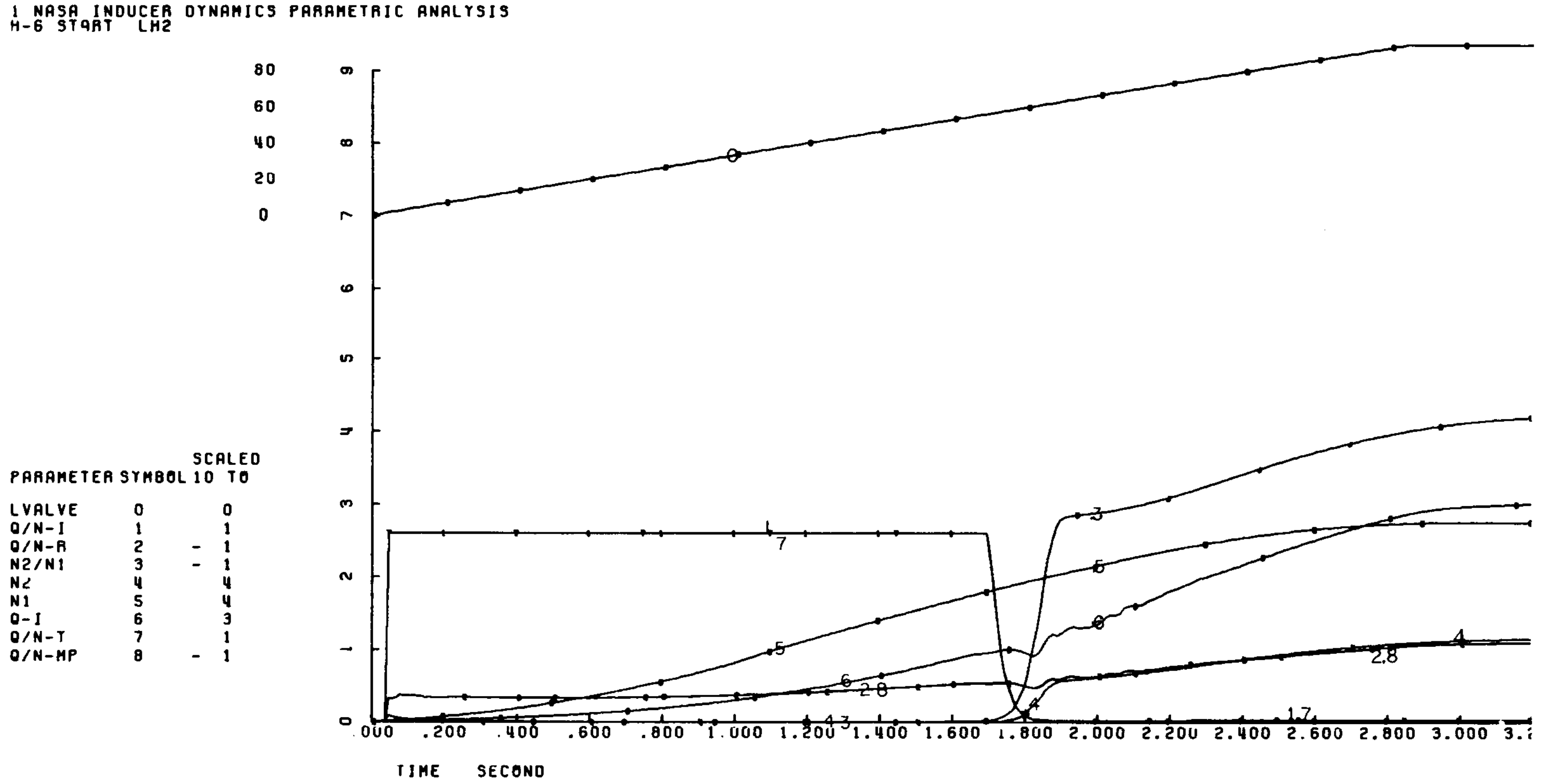

Figure 54. H-6 Start, LH_2

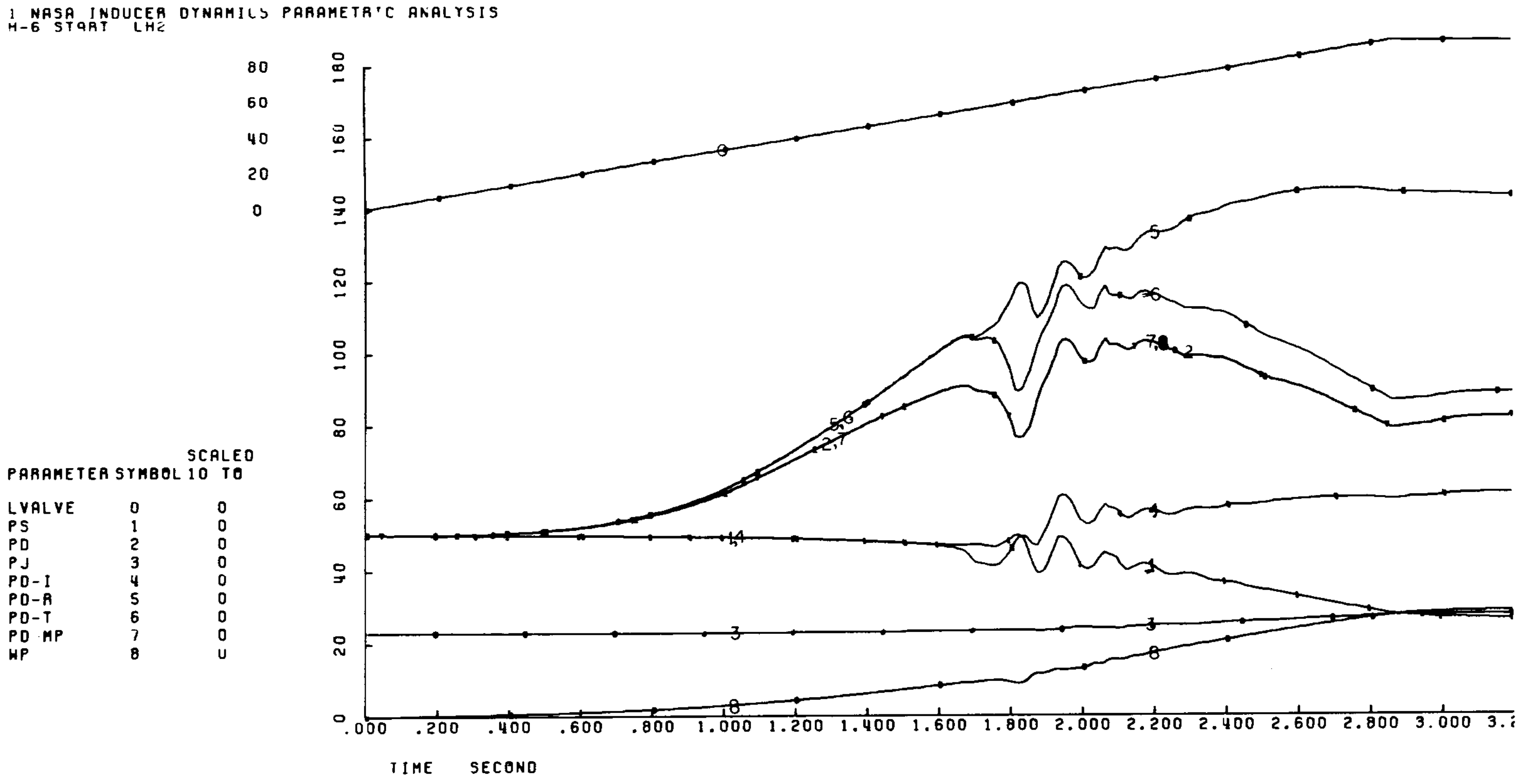

Figure 54. H-6 Start, LH_2

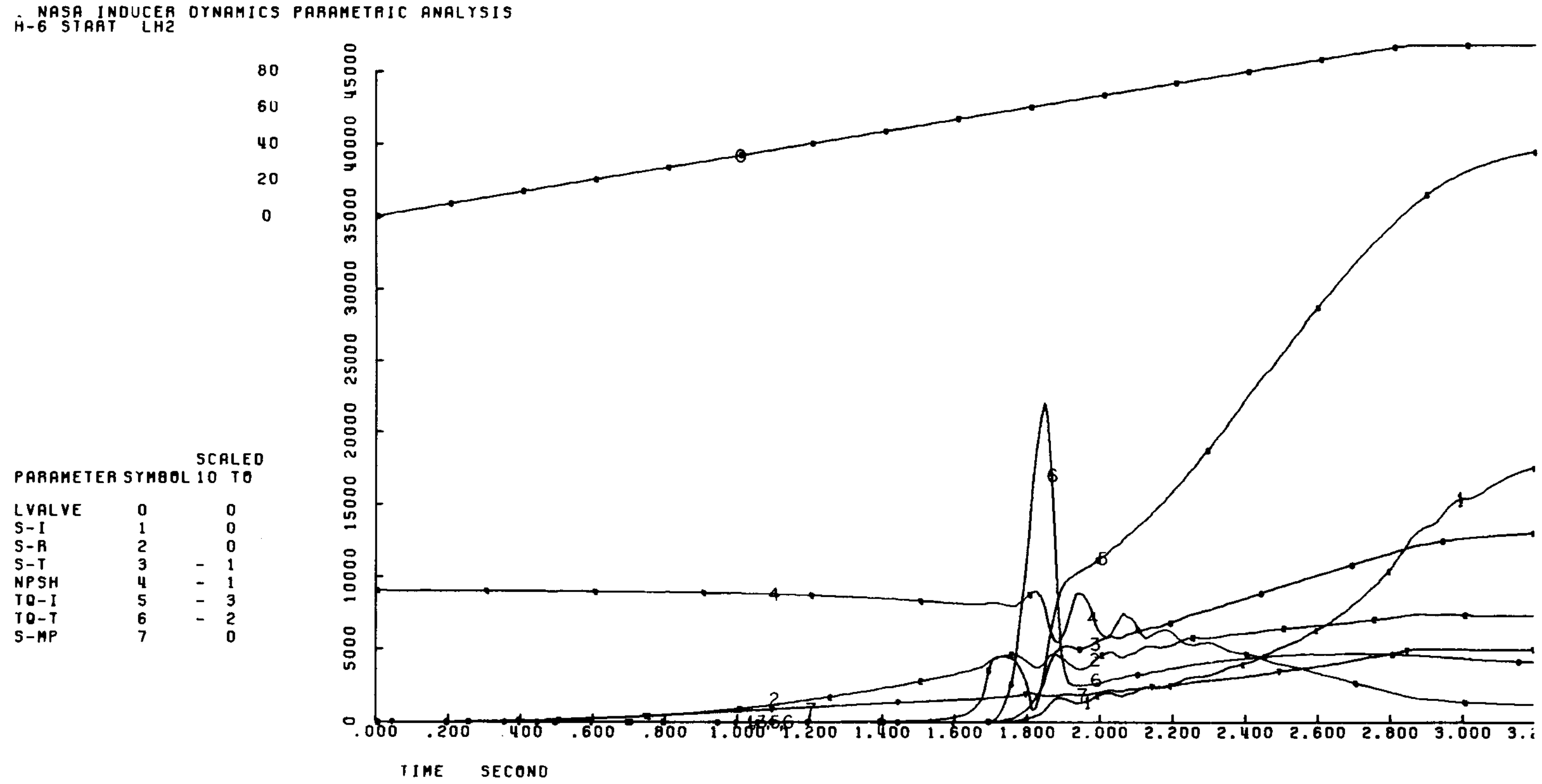

Figure 54. H-6 Start, LH_2

f. The maximum temperature rise across the unit occurs at 1.70 sec, the time at which bootstrapping occurs. The temperature profile and stage inlet densities are as follows:

	Inducer	Rotor	Turbine	Collector
Stage Inlet Temp, °R	40	39.9	42.46	42.55
Stage Inlet Press, psia	47.5	42.5	104.5	103.8
Stage Inlet Density, lb/ft^3	4.300	4.263	4.228	4.223

The values were obtained from thermodynamic tables of hydrogen properties.

g. The steady-state balance point agreed with 0.4% for the low-speed shaft speed and within 0.8% for the flow when compared with Table V.

Another transient run for the Test Stand H-6 facilities was a 3 sec transient with a faster opening time. The valve opened in 1.45 sec, twice as fast as the previously described start. The over-all effect was a large drop across the unit at bootstrapping, 10 psi as compared with the previous 47.8 psi pressure rise. Also, bootstrapping occurred earlier, at 48% of duration.

3. Advanced Engine Transients

Table IV is an enumeration of the nominal operating point of an advanced engine hydrogen feed system with an advanced centrifugal hydrogen main stage pump. The main stage pump performance curves are presented on Figures No. 55 through No. 58. Some changes were made in the pressure schedule to facilitate the obtaining of the transients.

The basic type of transient studied was the tank head start similar to that required by a two-stage combustion cycle advanced engine. In these transients, the discharge valve is opened before power is supplied to the pump. Both the high-speed and low-speed shafts of the inducer start from infinite or maximum flow coefficient for the blade rows.

The valve is opened rapidly to a "step" position. Then this valve position is maintained for the period of time required to fill the injector manifolds and to obtain ignition in the combustion chambers. After ignition, the valve opens at the rate required to control chamber pressure and pump build-up. This sequence was studied. The shape of the speed build-up of the high-speed shaft and the control valve contour were taken from the ARES engine start(76).

---

(76) Gibb, J. A., ARES Predicted Start and Shutdown Transients, Aerojet-General Memorandum No. 9350:66:0218, 21 September 1966.

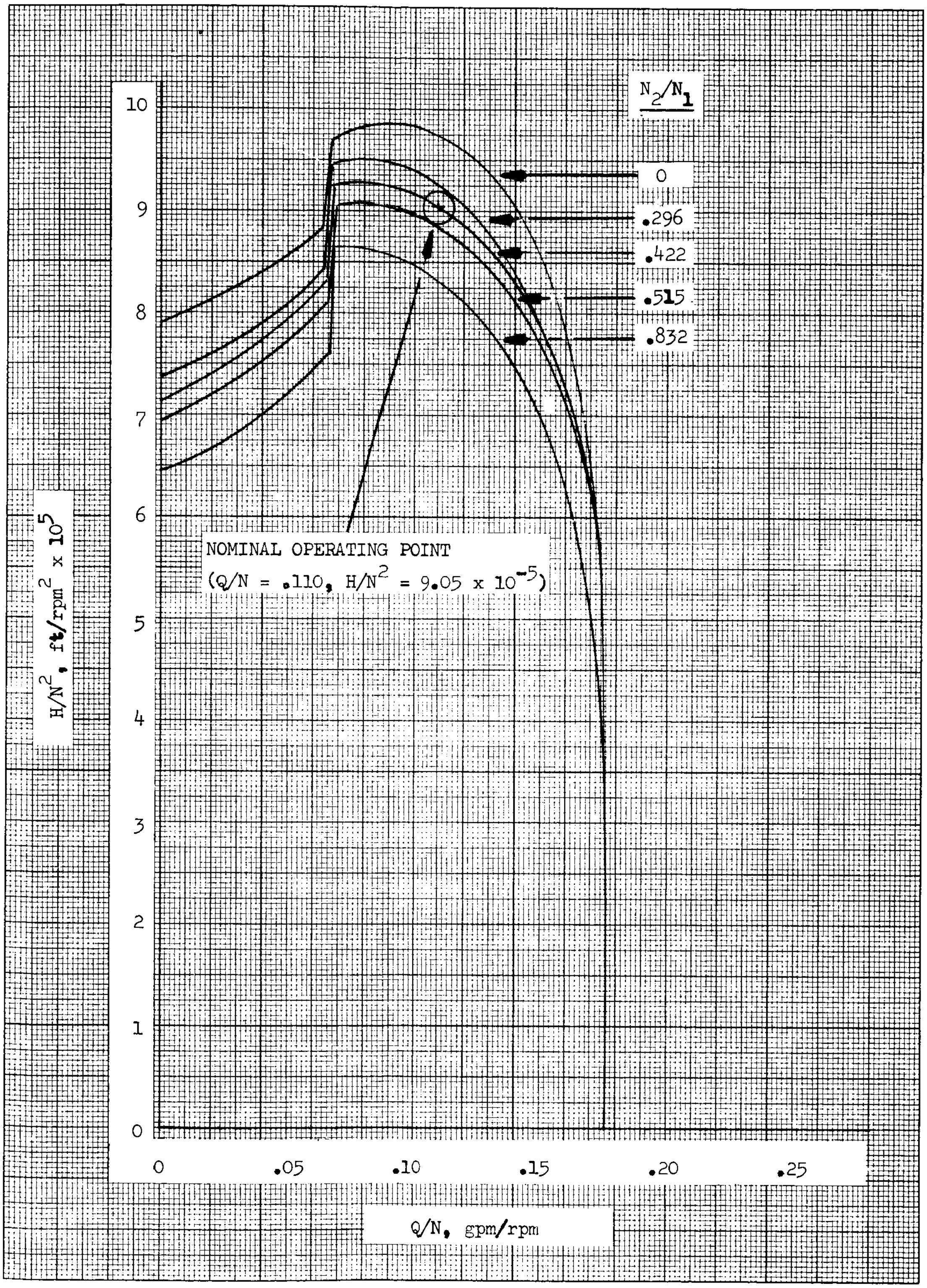

Figure 55. Main Stage Pump H/N^2 vs Q/N

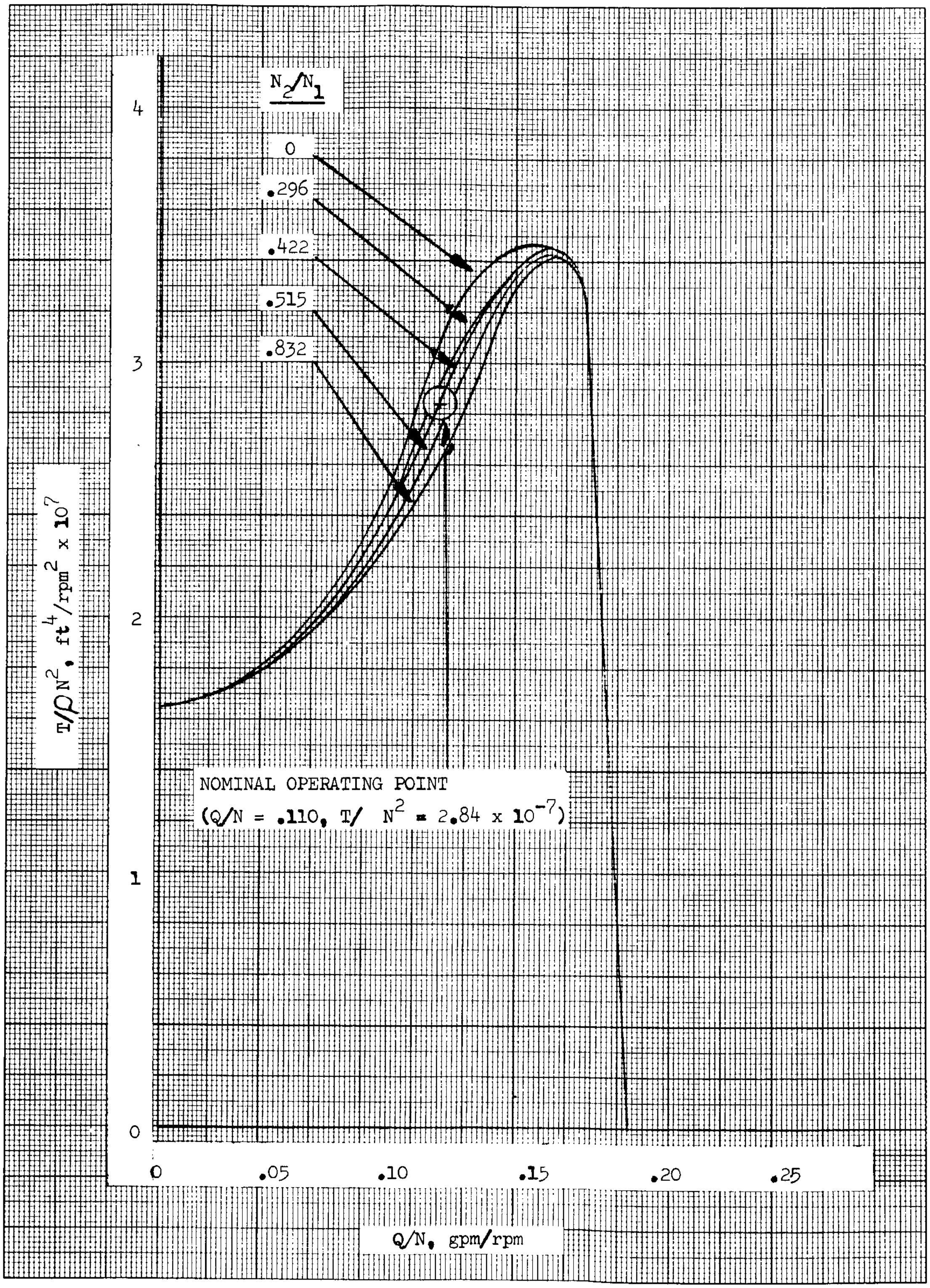

Figure 56. Main Stage Pump $T/\rho N^2$ vs Q/N

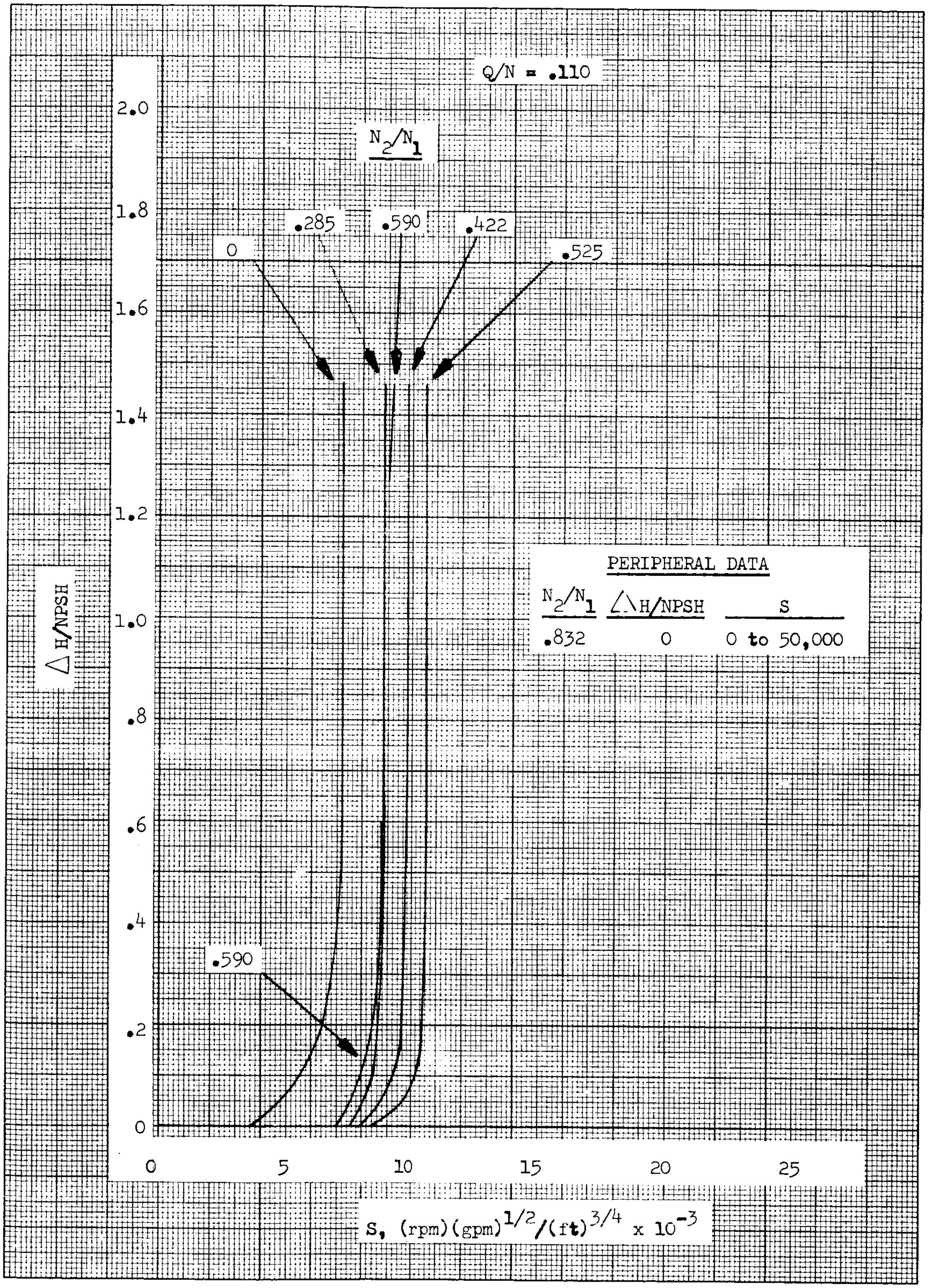

PERIPHERAL DATA

N_2/N_1	△H/NPSH	S
.832	0	0 to 50,000

Figure 57. Main Stage Pump ΔH/NPSH vs S (Q/N = .110)

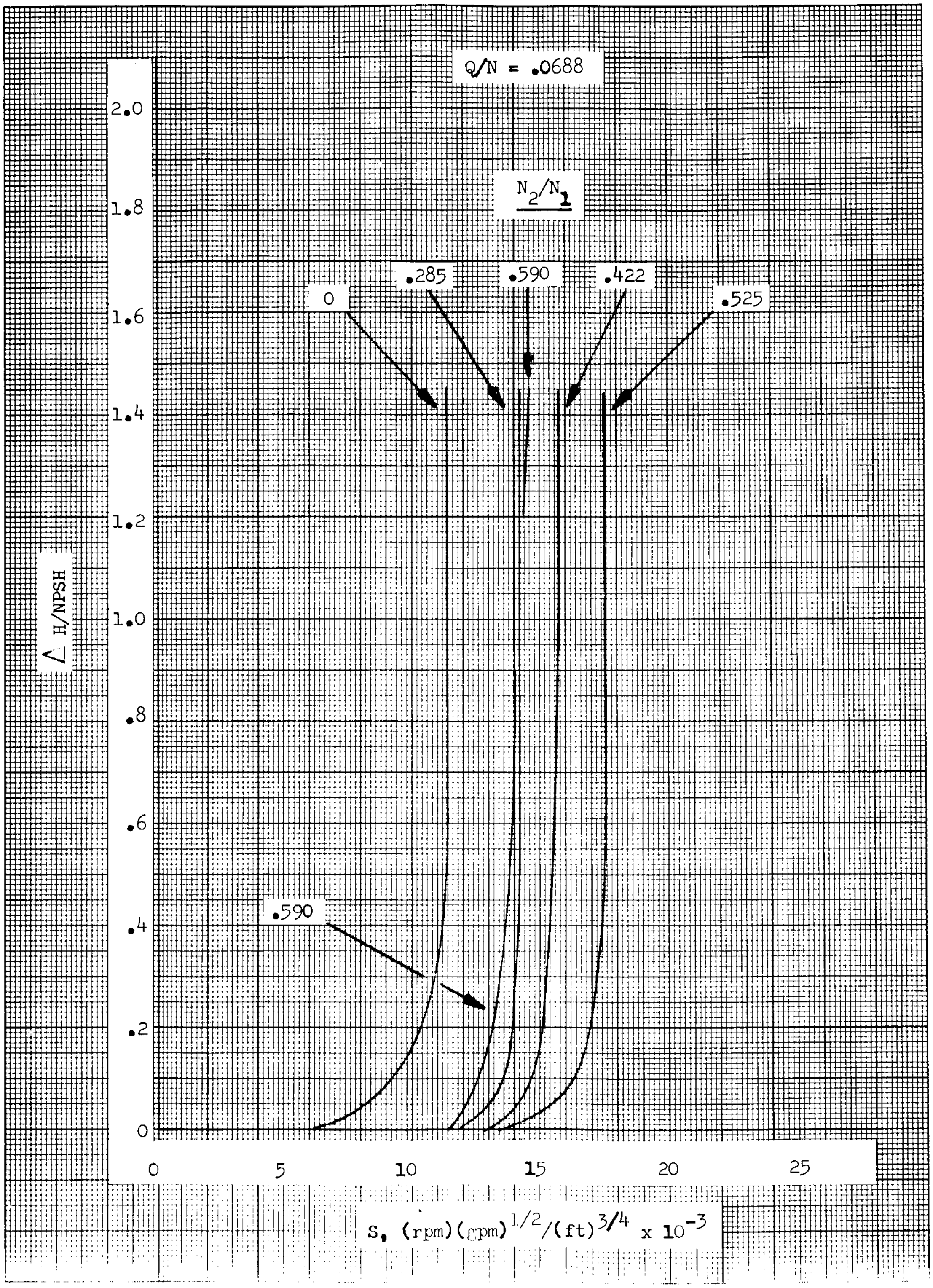

Figure 57. Main Stage Pump ΔH/NPSH vs S (Q/N = .0688)

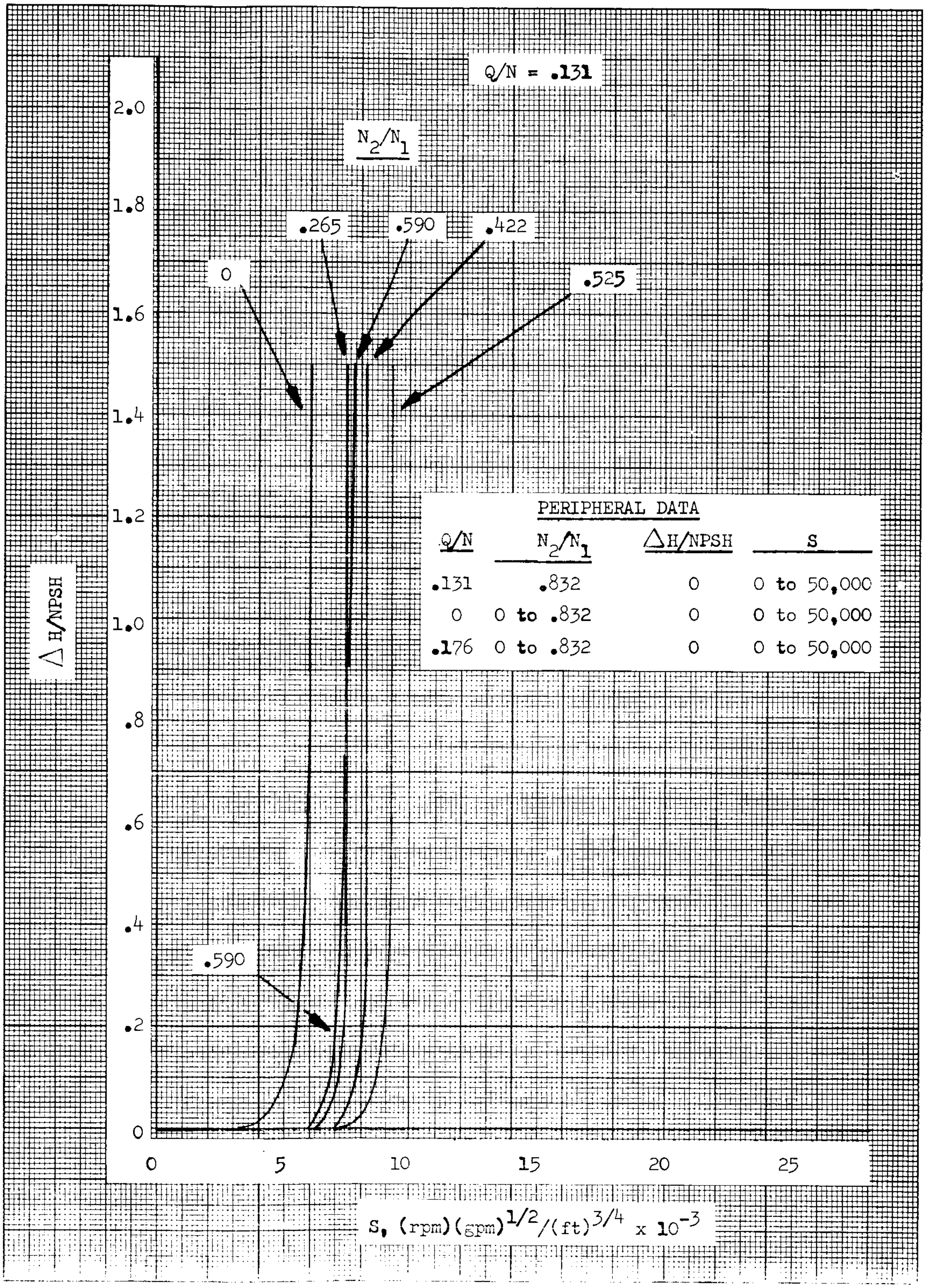

PERIPHERAL DATA

Q/N	N_2/N_1	ΔH/NPSH	S
.131	.832	0	0 to 50,000
0	0 to .832	0	0 to 50,000
.176	0 to .832	0	0 to 50,000

Figure 57. Main Stage Pump ΔH/NPSH vs S (Q/N = 0, .131, .176)

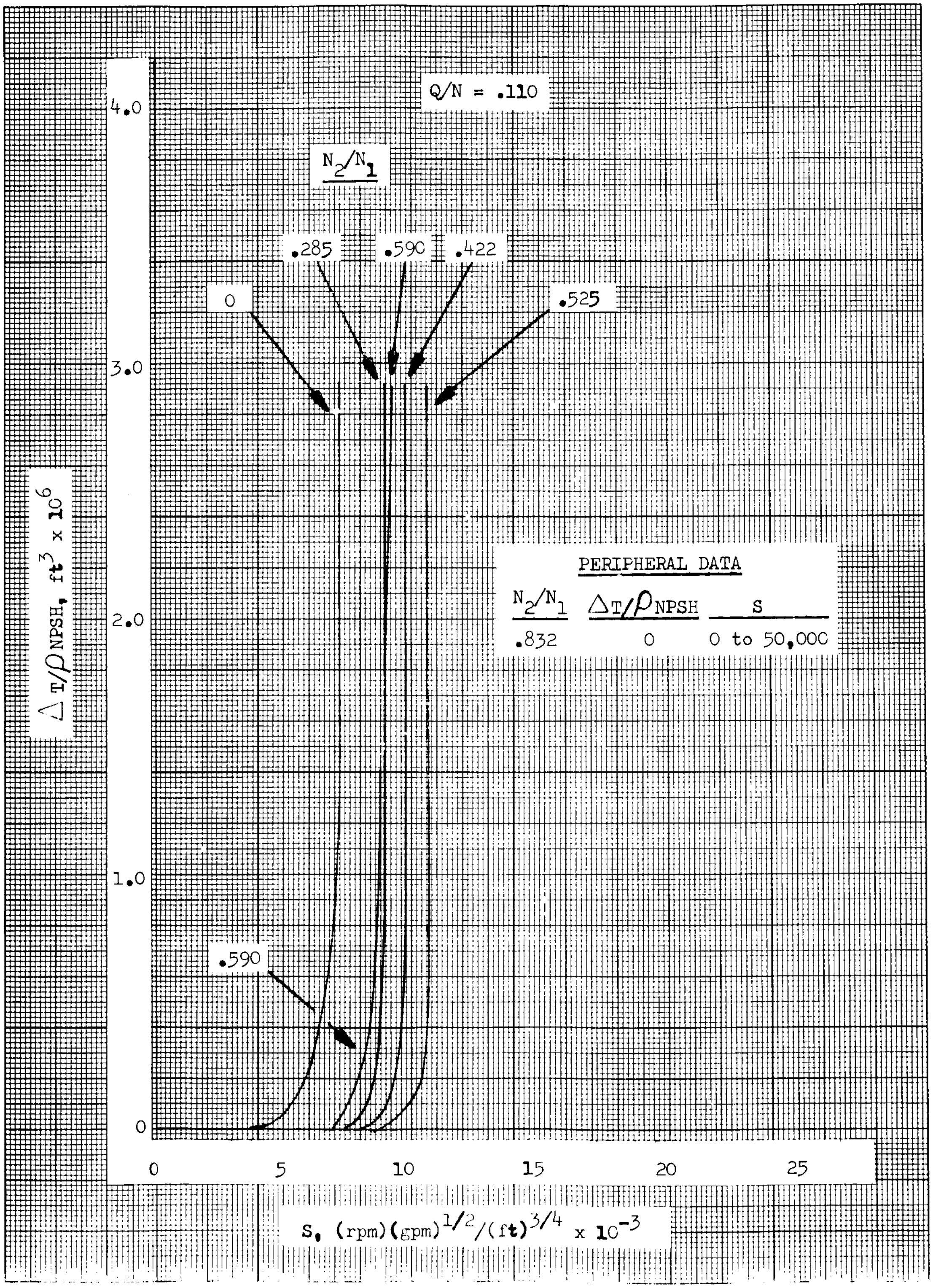

Figure 58. Main Stage Pump ΔT/ρNPSH vs S (Q/N = .110)

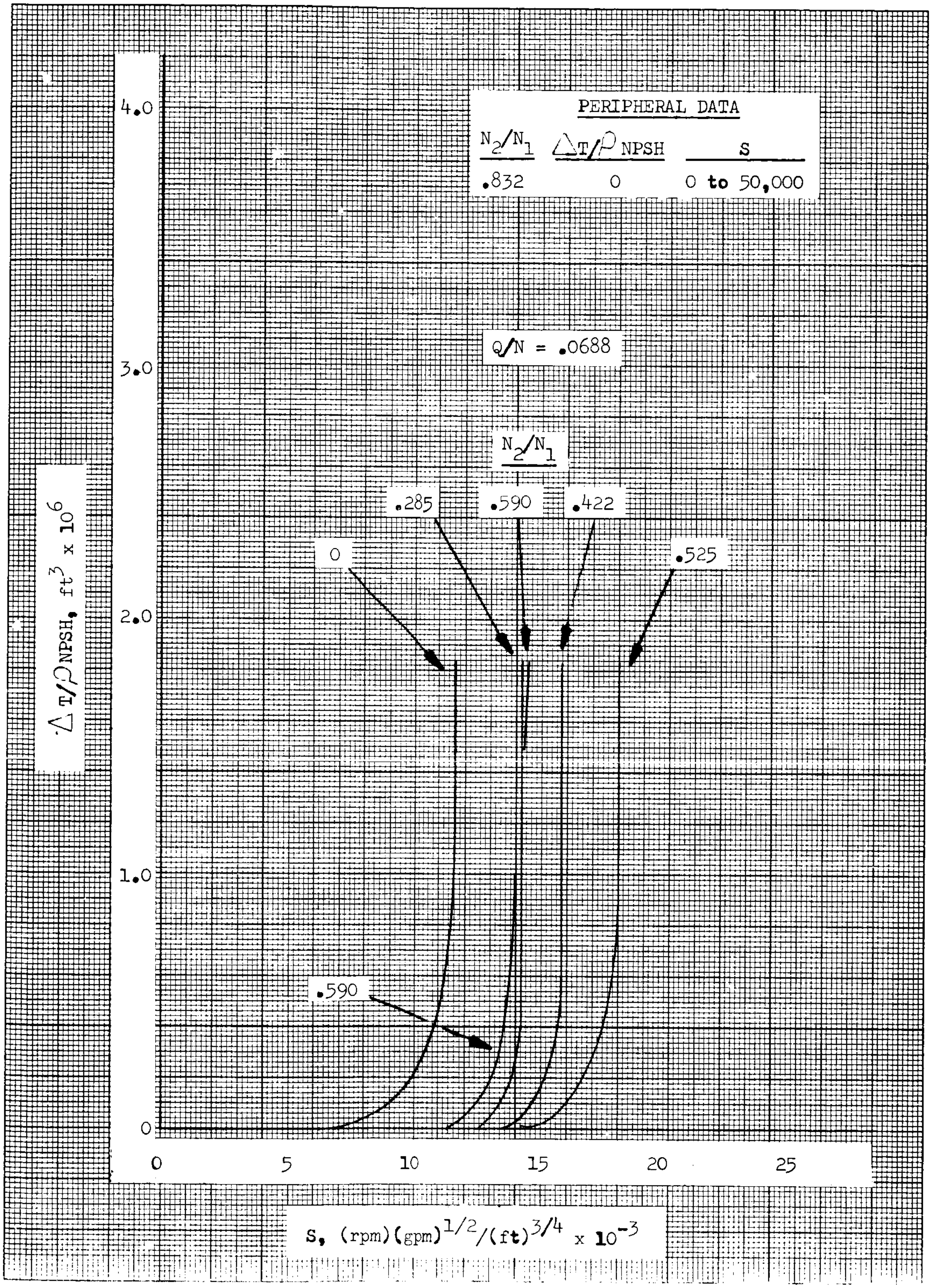

Figure 58. Main Stage Pump ΔT/ρNPSH vs S (Q/N = .0688)

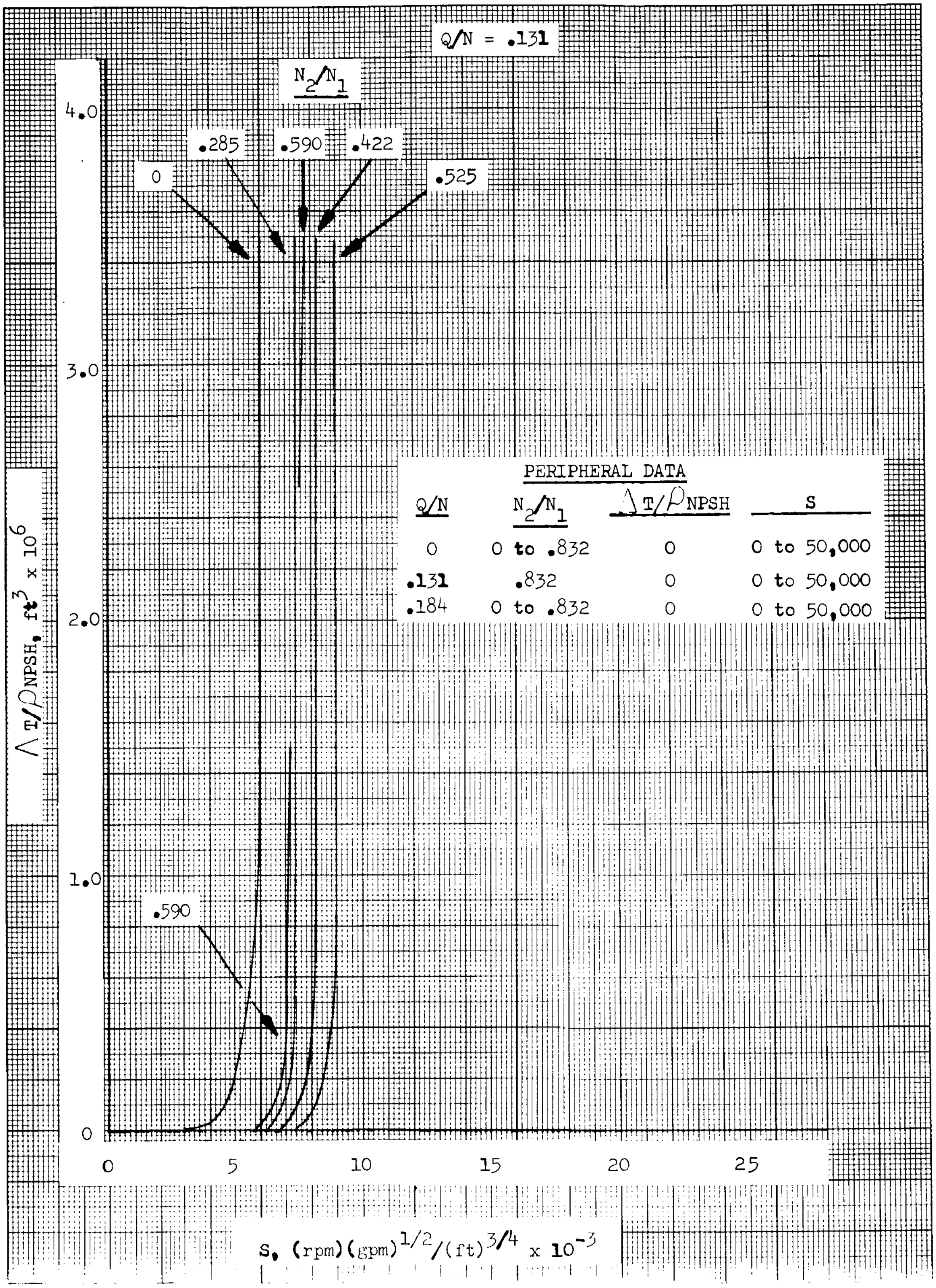

PERIPHERAL DATA

Q/N	N_2/N_1	$\Delta T/\rho NPSH$	S
0	0 to .832	0	0 to 50,000
.131	.832	0	0 to 50,000
.184	0 to .832	0	0 to 50,000

Figure 58. Main Stage Pump ΔT/ρNPSH vs S (Q/N = 0, .131, .184)

The start transient was developed from a parametric study wherein the valve "step" position was the primary variable.

Case	Valve Step Position
1	10%
2	20%
3	30%
4	100%

Convergence problems were encountered on the pump weight flow. These problems were partially the result of the discontinuities in the hydrogen property data used. This data was utilized inside the convergence loop to account for density change with changing pressure. The following is an example of the convergence problem for Case 2:

	W_j	W_{j-1}	W_{j-2}	W_{j-3}	W_{j-4}
Assumed Weight Flow	5.44052	5.43299	5.43298	5.43294	5.43301
Difference Between Assumed & Calculated	-.14771	-.13610	-.13621	-.13621	-.13621

Allowable Difference equals (.001) $W_j = \pm.0054405$.

The convergence shows that no root exists closer than -.13610. This error is 2.5% and was considered too high to be allowed.

The hydrogen property data was removed from the convergence loop but the convergence problem continued. A small window seems to be present for tank head starts with <u>this</u> main stage pump. Evidently, precise manipulation of flow by the control valve flow resistance contour is required and is probably of a different shape than the step contour studied.

The longest computer run, 1 sec of a 3 sec transient, was obtained with the valve 100% open. However, the discharge of the turbine cavitates in this start beginning at 0.87 sec; therefore, the start is unsatisfactory (see Figure No. 59), but it does demonstrate that it is possible to bootstrap the inducer with an advanced main stage pump.

It should be noted that this open-loop model does not completely simulate an actual engine start. The orifice downstream of the control valve acts as a fixed constant load while an actual engine has a variable load resulting from such considerations as combustion and manifold filling. This fact could account for some of the difficulty in obtaining a complete transient. Because difficulty was encountered in obtaining a satisfactory tank-head start modeled after the ARES engine start, a different start was investigated using a transient similar to that studied for Test Stand H-6. In this transient, the high-speed shaft begins rotation at the same time that the control valve is opened and has a "S" shaped characteristic.

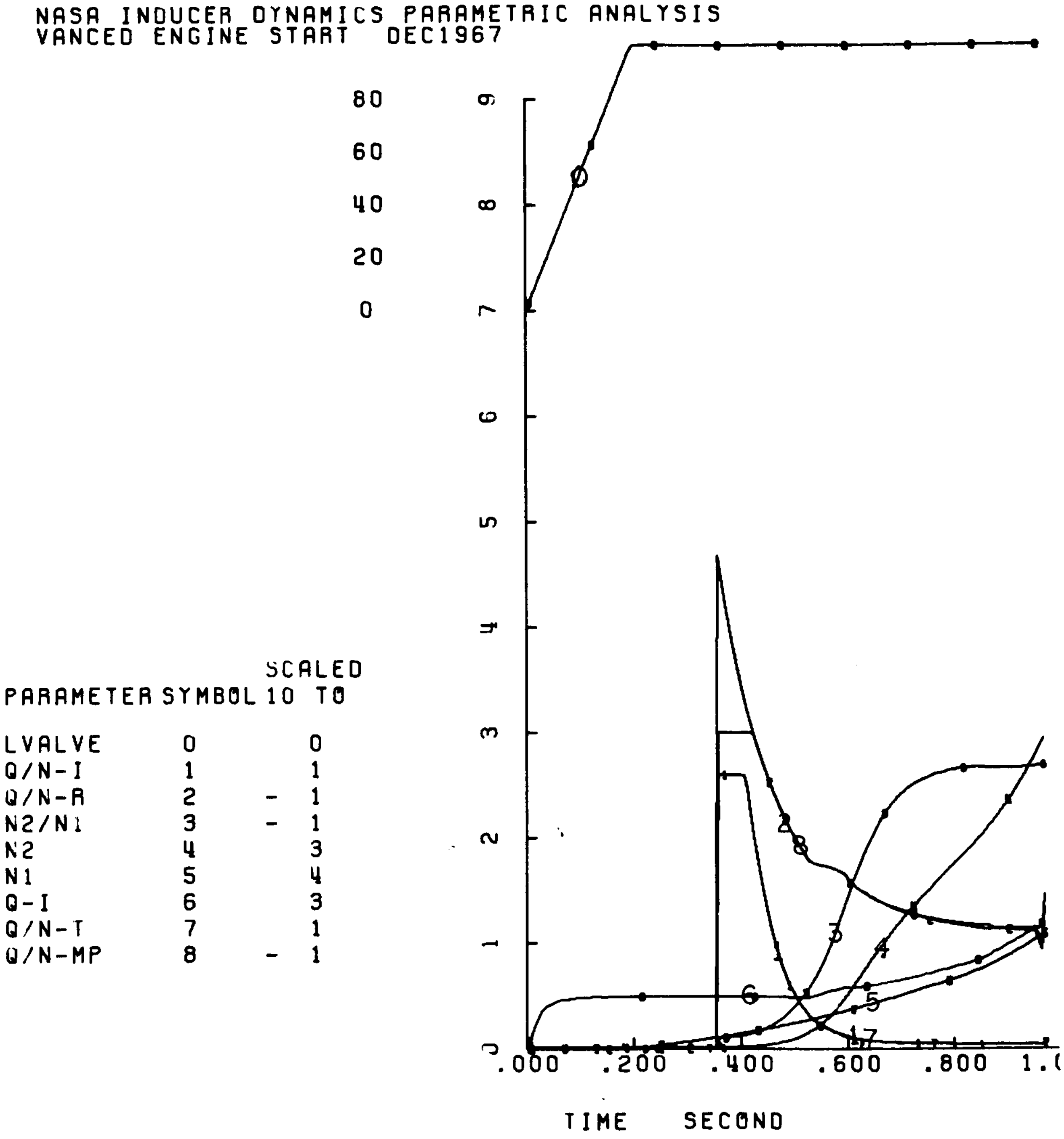

PARAMETER	SYMBOL	SCALED 10 TO
LVALVE	0	0
Q/N-I	1	1
Q/N-R	2	- 1
N2/N1	3	- 1
N2	4	3
N1	5	4
Q-I	6	3
Q/N-T	7	1
Q/N-MP	8	- 1

Figure 59. Advanced Engine Start - Tank Head Start

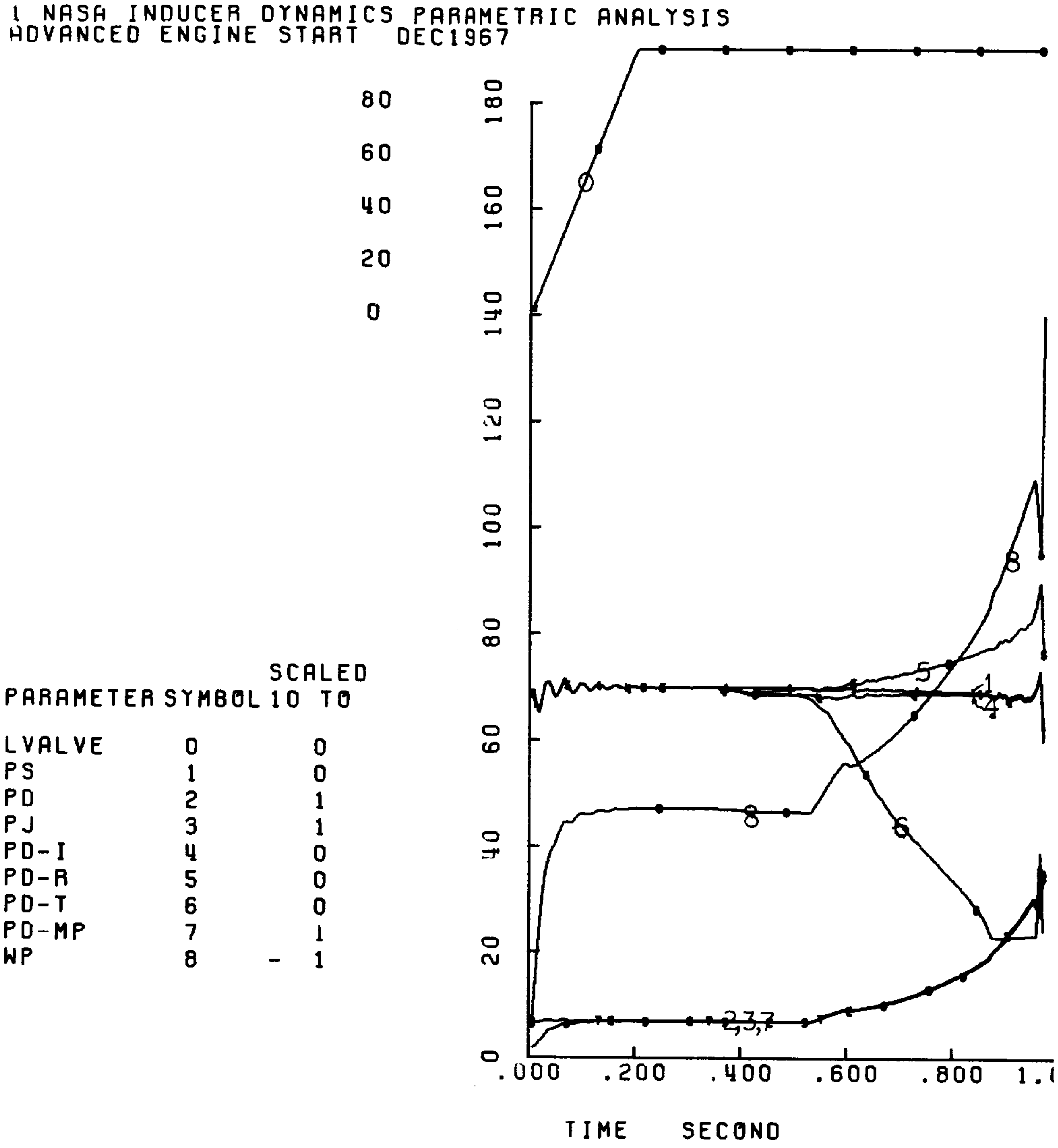

Figure 59. Advanced Engine Start - Tank Head Start

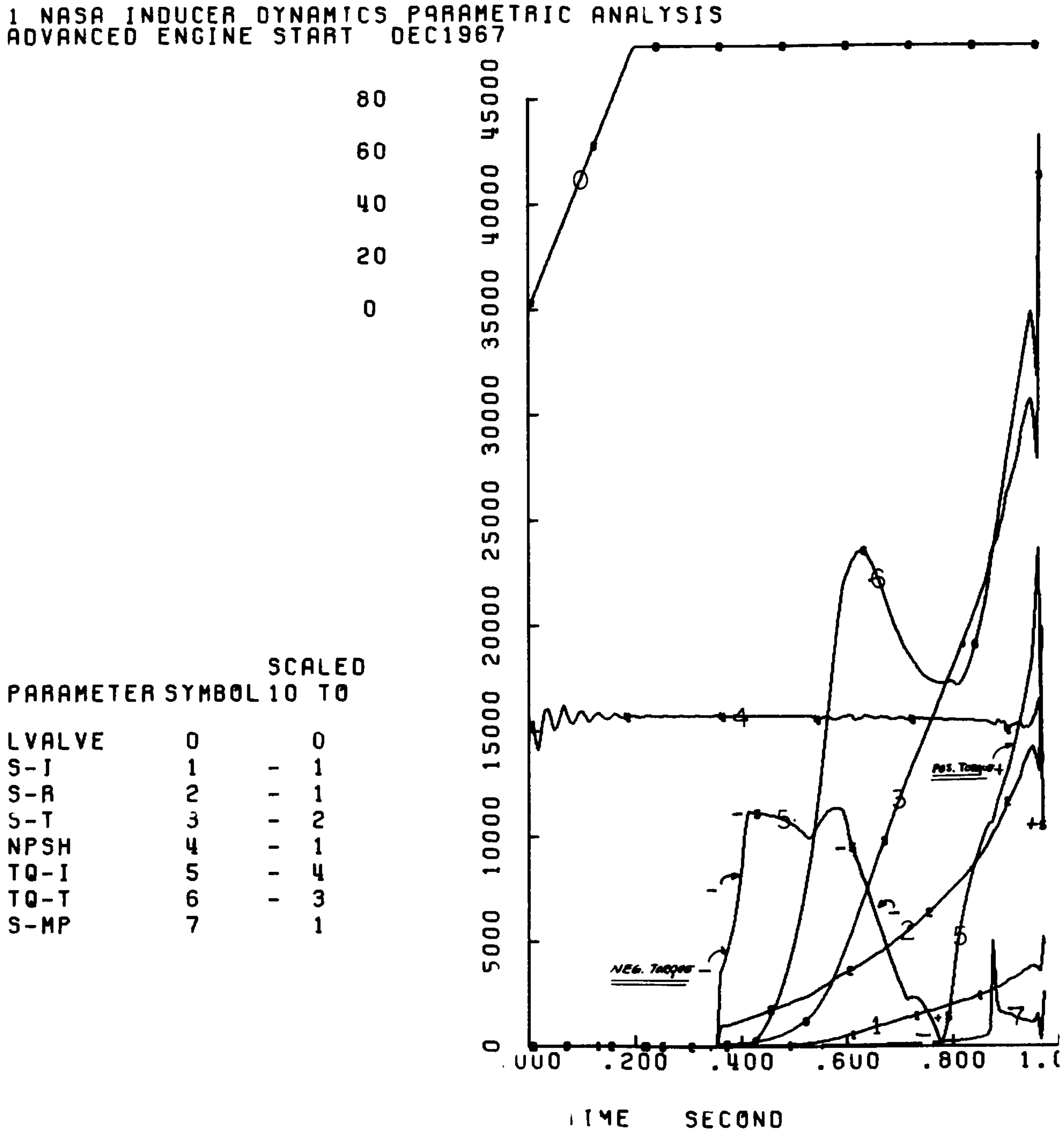

Figure 59. Advanced Engine Start - Tank Head Start

The control valve opens at two rates. Initially, it opens slowly, throttling the flow until the low-speed shaft bootstraps. Then, it is opened rapidly to its steady-state position, allowing the flow to build-up rapidly with the speed.

The results of this study are presented on Figure No. 60.

From the aspect of over-all rocket engine operation, the control of the pressure and flow rate transients are of prime importance. Flow rate control is required to regulate the transient heat flux to the thrust chamber by controlling the mixture ratio and chamber pressure. Pump discharge pressure control is required to provide coolant to the thrust chamber at pressures sufficiently high to suppress vaporization. Of course, the pump must operate under these controls with sufficient margins at blade stall and cavitation (viz., generally satisfactory performance). Therefore, in evaluating a start, the pressure and flow transients must be carefully scrutinized with regard to the application considered.

C. EFFECT OF REYNOLDS NUMBER CORRECTIONS UPON UNIT IN A CLOSED-LOOP

Viscous effects upon the flow through the blade rows produces velocity gradients which have an effect upon their performance. This effect will be termed "Reynolds Number Corrections" (RNC). Two forms of RNC were investigated. A flow correction

$$Q_{CORR} = Q(1 + \frac{dQ_{Re}}{Q})$$

where

$$\frac{dQ_{Re}}{Q} = f\ (\frac{Q}{Q_{NOM}},\ \frac{dQ}{dt})$$

and a head correction

$$dH_{CORR} = dH(1 - \frac{dH_{Re}}{dH}$$

where

$$\frac{dH_{Re}}{dH} = g\ (\frac{Q}{Q_{NOM}},\ \frac{Q}{N})$$

or

$$\frac{dH_{Re}}{dH} = h\ (\frac{Q}{Q_{NOM}},\ \frac{Q}{N},\ \frac{N_2}{N_1})$$

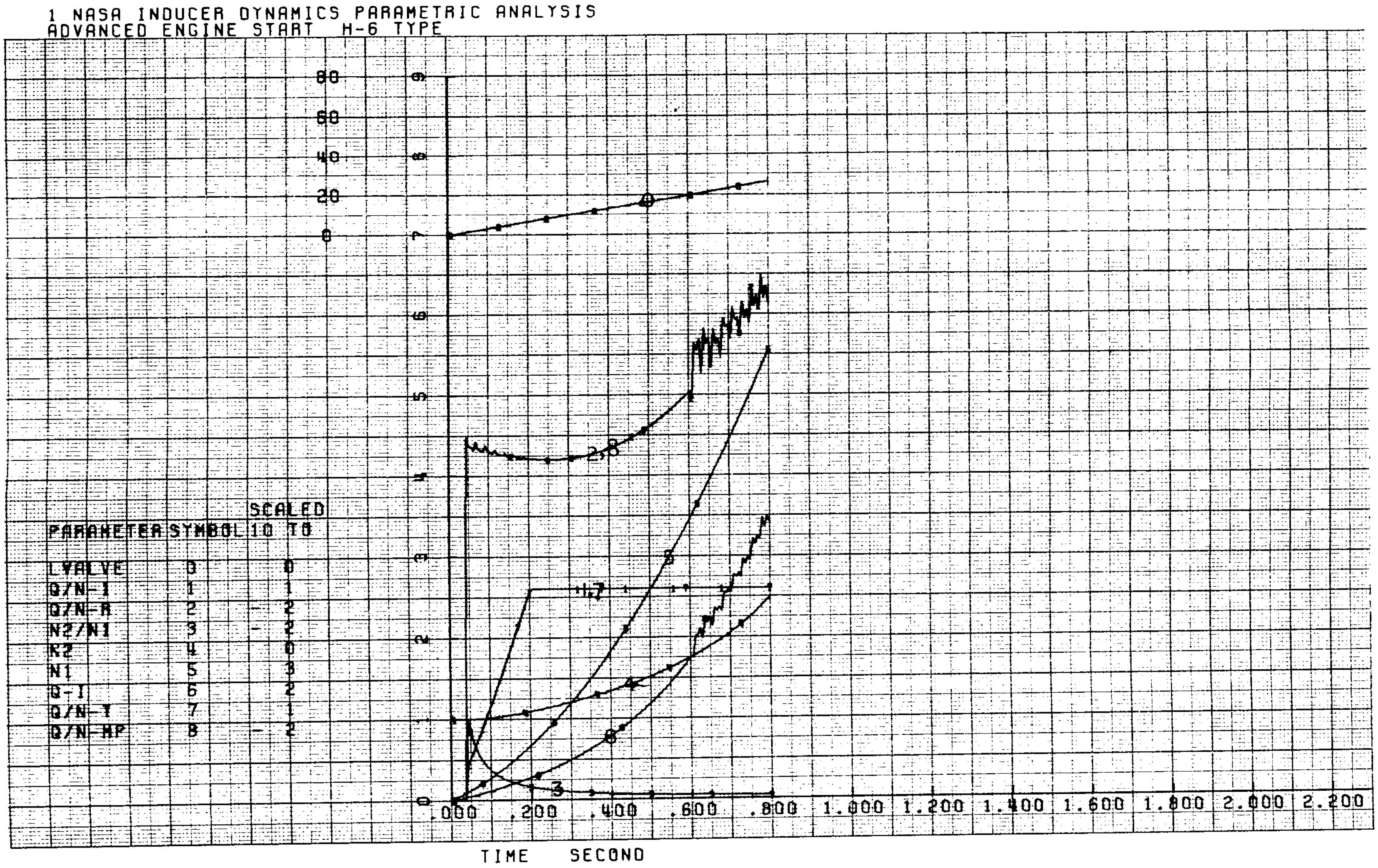

Figure 60. Advanced Engine Start - H-6 Type

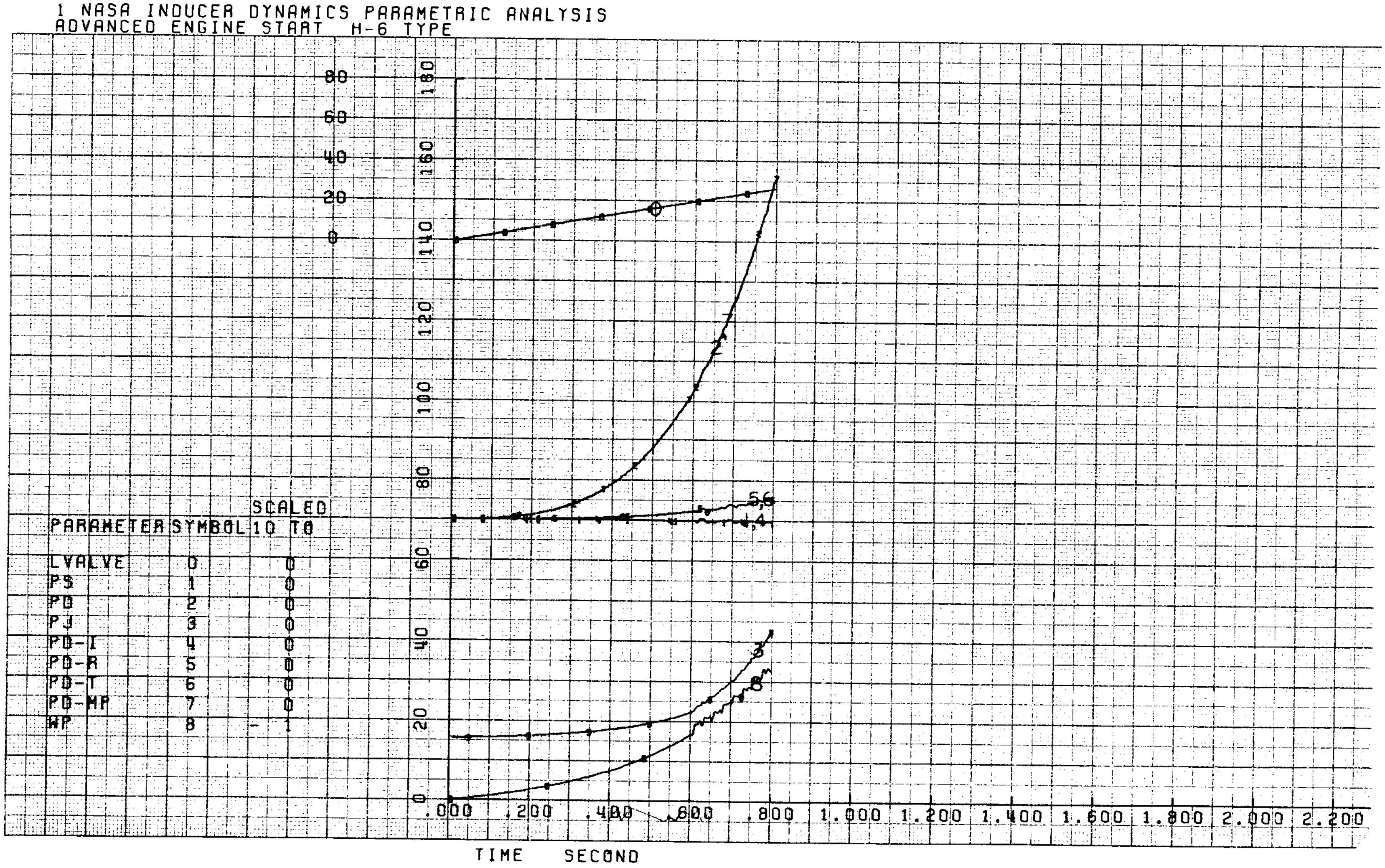

Figure 60. Advanced Engine Start - H-6 Type

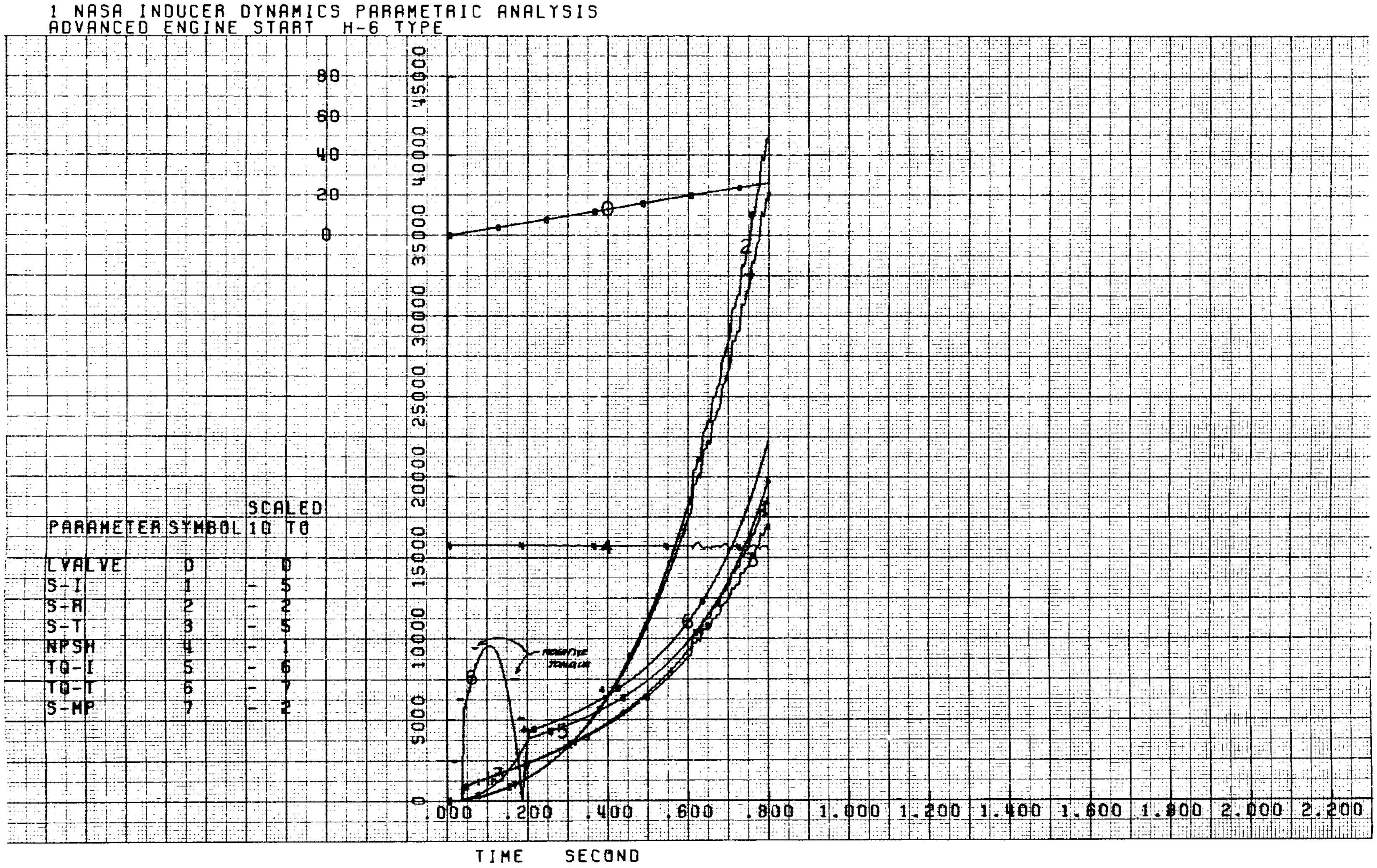

Figure 60. Advanced Engine Start - H-6 Type

The flow RNC always increases the effective flow while the head RNC always increases the head loss across a blade row.

A 3 sec duration start was studied. The conditions and configuration were the same as for the nominal Test Stand D-3A study except that the suction pressure was increased to 70 psia. The RNC curves investigated are presented on Figures No. 42, No. 45, No. 47, and No. 49. The following results were obtained:

1. The RNC for the rotor, shown on Figure No. 47, could not be successfully used. Note that at the initial conditions for the rotor,

$$\frac{Q}{N} \simeq 0, \ \frac{N_2}{N_1} = .01, \ \frac{Q}{QN} \simeq 0$$

the dH_{Re}/dH is greater than 1. For the closed-loop, this would require flow in the negative direction (by convention). No negative flow at the pump was a boundary condition under which the model was formulated although this was an arbitrarily imposed artificial boundary condition. With some additional complexity, its solution could have been accommodated.

2. The other RNC were used for a start transient. The RNC exhibited some minor effects upon the over-all transient. However, difficulty was encountered in using the flow correction shown on Figure No. 42. At the point in the transient where the flow is decelerated, (approximately .68 sec), a flow oscillation was introduced. From this point on, the flow correction introduced a discontinuity as a result of alternate reading of positive and then negative dQ/dt for adjoining time points. Therefore, the flow and pressures oscillated at 500 cps. The flow oscillation reached an amplitude of 6 lb/sec peak to peak.

3. Because of the oscillation, the RNC were deemed unsatisfactory in their present form. A different form of flow correction will be needed to account for Reynolds Number effects.

D. EXAMINATION OF TRANSIENT CHARACTERISTICS OF HYDRODYNAMICALLY-SIMILAR SYSTEMS

For the study of hydrodynamic scaling effects upon the performance of the inducer, the design is considered to be the "reduced size pumping system." Therefore, the scaling requirements for a larger unit were explored. The system studied was the open-loop, advanced engine model.

Dynamic similarity is realized when the ratio of forces acting upon a particle in one flow is the same as the ratio of forces acting at a corresponding point and time in a scaled unit. The relationships used in scaling the feed lines and their assumptions are as follows:

1. To maintain the same head and velocity at a fixed location and time, the static and dynamic relationships of the geometry to the head and velocity must be maintained constant:

Static Relationships:

a. Velocity head - $\frac{Q}{D^2}$ = constant

b.* Total head losses, friction - $\frac{LQ^2}{D^5} \simeq \frac{LQ}{D^2}$ = constant

Dynamic Relationships:

a. Waterhammer pressure waves

frequency - L and $\frac{th}{D}$ = constant

amplitude - Q/D^2 and $\frac{th}{D}$ = constant

Over-all Relationships:

a. Required for dynamic similarity - L = constant

$\frac{th}{D}$ = constant

$\frac{Q}{D^2}$ = constant

---

*Assumes rough pipe and fully-turbulent flow.

2. The over-all relationships are valid for the lines as long as the hydraulic resistances (frictional terms) are approximately constant over the range of Reynolds Numbers studied.

3. The over-all relationships are valid for comparison of the same fluid and pipe material only. If different fluids or materials are used, the additional similarity relationship required is

$$\frac{B_K}{\left(1 + \frac{B_K}{E}\frac{D}{th}\right)} = \text{constant}$$

where: B_K = fluid bulk modulus
E = modules of elasticity of the material

4. The over-all relationships and the additional relationship specified in 3 are valid only if no Poisson effects are included in the calculation of wave velocity. (That is, the line must have expansion joints or be rigidly-supported at the ends so that only lateral expansion is allowed.)

The comparison of a scaled engine to the designed demonstration unit according to the stated dynamic scaling relationships is presented below for a unit with double the flow rate.

Parameter	Demonstration Unit Engine	Scaled Engine
Flow rate, lb/sec	47	94
Suction line, length, L, ft	28	28
Suction line, diameter, D, in.	8	11.3
Suction line, thickness th, in.	.1	.129
Discharge line, length, L, ft	2	2
Discharge line, diameter, D, in.	3	4.24
Discharge line, thickness, th, in.	.3	.424
Injector feed line, length, L, ft	3.5	3.5
Injector feed line, diameter, D, in.	3	4.24
Injector feed line, thickness, th, in.	.3	.424

In summary, the larger engine could be expected to start-up and shutdown in the same time duration as the smaller engine. The various pressure parameters would have the same time traces as would occur for the smaller engine. The flow rate and speed parameters would be proportionally higher by a ratio of two. This is believed to be a realistic representation because line lengths do not vary greatly between large and small rocket engines.

E. CONCLUSIONS FROM THE PARAMETRIC STUDY OF THE DEMONSTRATION UNIT IN A CLOSED-LOOP

The following conclusions are based upon the results of this study:

1. The unit, as designed, will operate as required over the range of test conditions specified (i.e., duration, throttling, off-design flow, and speed). However, because of induced oscillations in the closed-loop system, testing at a NPSH of less than 6.1 ft may not be feasible for most 3 sec duration start-up tests.

2. A negligible temperature rise occurs in the water during any of the transients studied.

3. The induced waterhammer oscillation predicted by the model have been experienced previously in the Test Stand D-3A test facility at similar frequencies. Therefore, it is believed that the prediction of their existence is true. However, the actual amplitude and frequency must be verified by test experience because critical variability could exist in the purity (i.e., lack of inert gas) of the water.

4. The model has demonstrated that significant changes in amplitude of the induced oscillations can be obtained by increasing the discharge line size or increasing the inert gas content in the system. These changes can be made in the system to control the induced oscillations during testing.

F. CONCLUSIONS FROM THE PARAMETRIC STUDY OF THE DEMONSTRATION UNIT IN AN OPEN-LOOP

The following conclusions are based upon the study of the NERVA pump test facility transients. Hydrogen was the pumped fluid.

1. The demonstration unit will bootstrap satisfactorily for both a short duration (3 sec) and a long duration (9 sec) transient if tested in the Test Stand H-6 facility with hydrogen.

2. No sustained induced pressure oscillations are present in these transients.

3. The maximum temperature rise through the induced stages, as calculated using liquid hydrogen thermodynamic properties, was a 2.5°R rise above a suction temperature of 40°R.

4. A rocket engine main stage pump could be run with the inducer at a minimum NPSP = 5 psi with the transient presented on Figure No. 54, ignoring the losses caused by the long Test Stand H-6 facility suction line.

5. The transient presented on Figure No. 54 is not the optimum start for this unit. An optimization study, contouring the control valve hydraulic resistance versus time to achieve the lowest possible minimum NPSP, was beyond the scope of this analysis. It is reasonable to believe that such a study would achieve operation of the unit at the NPSP specified in the design document.

6. The following conclusions were drawn from the study of the advanced engine transients:

a. The demonstration unit can be made to bootstrap with an advanced centrifugal hydrogen main stage pump on a tank-head start.

b. For a satisfactory tank-head start with the inducer, precise control of the pump flow by contouring the flow control valve is required. The study indicates a narrow window of flow control is required for satisfactory operation with a tank-head start.

such head coefficients simplifies the high-speed rotor inlet design. Also, the flatter tandem row head-flow characteristics provide improved above-design-flow coefficient cavitation performance for the high-speed rotor. For these reasons, the tandem blade row should be considered for full-flow, hydraulic-turbine-driven inducers.

G. To simplify design, the high-speed rotor and hydraulic turbine use axial-flow, constant annulus dimension blading. Generally, systems with mixed-flow, variable annulus dimension blading will be required for rocket engine application. A mixed-flow hydraulic turbine, wherein the exit annulus is smaller than the inlet annulus should be evaluated because this type of design more readily matches the downstream elements.

H. For high head-rise applications, which includes this program, the use of more highly-loaded, high-speed rotor staging offers design advantages because the annulus dimensions can be made almost equal to those of the main stage pump suction annulus. Tandem blade rows can offer advantages for such applications; however, this type of design was not selected in this program because of the need to simplify design and fabrication. The tandem blade row has a disadvantage in that its added length and weight can provide high-speed shaft assembly critical speed problems. Compact (short axial length), highly-loaded staging would have application for the high-speed rotors of full-flow, hydraulic-turbine-driven inducer systems.

I. Analytical investigations of the transient start-up and shutdown as well as the throttling characteristics of the full-flow, hydraulic-turbine-driven inducer system indicate that satisfactory operation is obtained. The low-speed shaft speed does lag behind the high-speed shaft speed during a start-up transient. However, this could be a problem for very rapid starting applications. Analyses were based upon the type of starting experienced by a rocket engine pumping system using a centrifugal pump in a so-called "tank-head" start, wherein the pumping system is required to operate at relatively high (above-design) flow coefficients during the initial portions of the transient. It is recommended that other types of operation, including those wherein the pumping system initially operates at low or zero flow coefficient, be considered for future investigations. In addition, the use of other main stage pumping systems, including axial flow pumps, should be considered.

J. The conclusions and recommendations associated with the details of formulating the computer model as well as the results of the parametric analysis have been itemized at the end of each discussion (Sections II and III).

VI. CONCLUSIONS AND RECOMMENDATIONS RESULTING FROM TASK I, TASK II, AND TASK III EFFORTS

A. The full-flow inducer concept provides a feasible hydrogen boost pumping system for rocket engines, based upon the design and off-design analyses (including transient analyses) performed to date. These analyses also are applicable to other propellants with boost pumping systems of equivalent specific speed.

B. Low-speed inducer head rise capability and low-speed inducer/hydraulic turbine torque/speed stability characteristics place an approved limit on the high-speed shaft/low-speed shaft speed ratio values that can be used.

C. Systems with lower design head rise values than the minimum (5000 ft) specified in this program would have more conventional blading and could be more easily matched to the suction geometry of main stage pumping systems. This system is convenient for experimental investigations because the relatively large diameter exit annulus provides for rolling element bearings and instrumentation systems; however, this annulus size is greater than found in axial or centrifugal main stage pumping system inlets.

D. The existing contractual requirement for cavitation-free operation of the high-speed rotor at 120% of the design flow coefficient is a rather severe one because of the relatively steep low-speed inducer head flow characteristic. This results in comparatively large high-speed rotor inlet relative flow angle (measured from the axial direction) design values which are outside the range of existing axial airfoil blade, cascade, compressor, and pump test data. Lower angles can be used if the pump cavitation performance is allowed to be limited by the high-speed rotor rather than the low-speed inducer cavitation performance at flow coefficients of less than 120% of design.

E. Cavitating and non-cavitating test data for airfoils with varying blade profiles and blade thicknesses as well as non-airfoil blading in the range of inlet relative flow angles from 75 degrees to 85 degrees (measured from the axial direction) are needed to eliminate some of the uncertainty associated with the design of the inlet portions of the high-speed rotor. Generally, this blade row must operate with some pre-whirl and the available pump test data is for zero pre-whirl; therefore, a requirement also exists for investigating geometries designed for inlet pre-whirl.

F. It is estimated that the inducer design for this program has the largest, reasonable ideal head coefficient for an axial discharge rotor of a single blade row design. Tandem blade row designs also can be used; however, they were not selected because it was expedient to retain simplicity in the design and fabrication of the initial demonstration unit. The tandem blade row design can furnish larger over-all head coefficients and the use of

BIBLIOGRAPHY

1. Anderson, D. A., Soltis, R. F., and Sandercock, D. M., Performance of 84° Flat-Plate Helical Inducer and Comparison with Performance of Similar 78° and 80.6° Inducers, NASA TN D-2553, December 1964

2. Ball, C. J., Meng, P. R., and Reid, L., (U) Cavitating Performance of 84° Helical Pump Inducer Operated in 37° and 42°R Liquid Hydrogen, NASA TMX-1360, February 1967 (Confidential Report)

3. Beer, R., Aerodynamic Design and Estimated Performance of a Two-Stage Curtis Turbine for the Liquid Oxygen Turbopump of the M-1 Engine, NASA CR-54764, 1965

4. Bergloff, R. A. and Olson, G. K., Engine Transients and Controls System Study of the Gas-Gas Two Stage Combustion Cycle Version of a 1500K H_2-O_2 Engine, Aerojet-General Report No. SCR-165, March 1965

5. Beveridge, J. H., Campbell, W. E., and Fitts, J. J., NPSP Selection for a Nuclear Rocket, AIAA Paper No. 67-467, July 1967

6. Blakes, R., et al, Initial Test Evaluation of the M-1 Liquid Hydrogen Turbopump, Including Installation, Test Procedures, and Test Results, NASA CR-54827, 20 July 1967

7. Brumfield, R. G., Optimum Design for Resistance to Cavitation in Centrifugal Pumps, U. S. Naval Ordnance Test Station, Inyokern, California, 1948

8. Campbell, W. E., (U) NPSP Evaluation, Aerojet-General Report No. RN-S-388, March 1967 (Confidential Report)

9. Chan, J., One-Dimensional Unsteady Liquid Flow Utilizing Waterhammer Theory, Aerojet-General Computer Program No. 31403, SR40JC, July 1967

10. Chlapek, J. D., Start Transient Testing of a Low-Speed Hydraulic Turbine Driven Inducer Stage in Combination with a Rocket Engine Turbopump, AFRPL-TR-66-124, June 1966

11. Crouse, J. E. and Sandercock, D. M., Blade Element Performance of Two-Stage Axial-Flow Pump with Tandem-Row Inlet Stage, NASA TN-3962, May 1967

12. Crouse, J. E. and Sandercock, D. M., Design and Over-all Performance of an Axial-Flow Pump Rotor with a Blade Tip Diffusion Factor of 0.43, NASA TN D-2295, May 1964

13. Crouse, J. E., Soltis, R. F., and Montgomery, J. C., Investigation of the Performance of an Axial Flow-Pump Stage Designed by the Blade Element Theory, NASA TN D-1109, December 1966

14. Farmer, O. A., et al, FORTRAN IV Hydrogen Property Tabular Codes, Los Alamos Scientific Laboratory Report No. LA-3381, 29 October 1965

15. Farquhar, J. and Lindley, B. K., Hydraulic Design of the M-1 Liquid Hydrogen Turbopump, NASA CR-54822, 15 July 1966

16. Farr, P. F. and Olson, G. K., Performance Analysis of a Post Boost Control System, Vernier Vector Unit, Aerojet-General Report No. PTDR-9647-018, June 1965

17. Lary, F. B., (U) Advanced Cryogenic Rocket Engine Program, Aerospike Nozzle Concept, Contract AF 04(611)-11399, Quarterly Progress Reports, RPL TR-66-138, June 1966; RPL TR-66-242, September 1966; RPL TR-66-348, December 1966; RPL TR-67-91, March 1967; RPL TR-67-188, June 1967 (Confidential Reports)

18. Lieblein, S., Schwenk, F. C., and Broderick, R. L., Diffusion Factor for Estimating Losses and Limiting Blade Loadings in Axial-Flow Compressor Blade Elements, NASA RME53D01, 8 June 1953

19. Lindley, B. K., Test Report, M-1 Fuel Subscale Pump Water Tests 1.2-05-EHP-008 through -019 (Inducer Stage, Transition Stage Configuration), Aerojet-General Report No. TPR 0028, August 1965

20. Loschge, A., Konstrucktionen aus Dampfturbinen, Springer Verlag, Berlin/Gottingen/Heidelberg, 1955

21. Marman, H. W., et al, Development Tests of the TP-1 Liquid Metal Turbopump Components, Report PWAC-318, Pratt & Whitney Aircraft, Middletown, Conn., 30 June 1961, Figure 74, p. 143

22. Miller, M. J. and Crouse, J. E. Design and Over-All Performance of an Axial-Flow Pump Rotor with a Blade Tip Diffusion Factor of 0.66, NASA TN D-3024, September 1965

23. Murphy, J. S., et al, Development of Pump Components for the Pratt & Whitney Aircraft Liquid Metal Turbopump, TP-1, Report PWAC-298, Pratt & Whitney Aircraft, Middletown, Conn., 20 October 1960, Figure No. 54, p. 94

Bibliography (cont.)

24. Olson, G. K., (U) A Study of the Fluid Dynamics of an Intensifier Feed System During ARES TCA Development Testing, Aerojet-General Report No. AMDR-9635-014, April 1966 (Confidential Report)

25. Roelke, R. J., Stabe, R. G., and Evans, D. G., Cold Air Performance Evaluation of Scale Model Oxidizer Pump Drive Turbine for the M-1 Hydrogen-Oxygen Rocket Engine, NASA TN D-3368, March 1966

26. Rohlik, H. E. and Kofsky, M. G., Performance Evaluation of Three-Stage Prototype NERVA Turbine Designed for Blade-Jet Ratio of 0.107, NASA TMX 719, January 1963

27. Sandercock, D. M. and Crouse, J. E., Design and Over-All Performance of a Two-Stage Axial-Flow Pump with a Tandem-Row Inlet Stage, NASA TN D-2879, June 1965

28. Sandercock, D. M., Soltis, R. F., and Anderson, D. A., Cavitation and Non-Cavitation Performance of an 80.6° Flat-Plate Helical Inducer at Three Rotational Speeds, NASA TN D-1439, November 1962

29. Sandercock, D. M., Soltis, R. F., and Anderson, D. A., Investigation of the Performance of a 78° Flat-Plate Helical Inducer, NASA TN D-1170, March 1962

30. Schlichting, H., Boundary Layer Theory, fourth edition, McGraw-Hill, New York, New York, 1960, pp. 504-506

31. Stepanoff, A. J., Centrifugal and Axial Flow Pumps, second edition, J. Wiley & Sons, New York, 1957, Figure No. 8.8, p. 145

32. Streeter, V. L. and Sylie, E. B., Hydraulic Transients, McGraw-Hill Inc., 1967

33. Young, W. E., Investigation of Hydrostatic Bearings for Use in High Pressure Cryogenic Turbopumps, Contract AF 04(611)-11406, Semi-Annual Report AFRPL-TR-66-302, November 1966

34. Aerodynamic Design of Axial Flow Compressors, NASA Sp-36, 1965, Figure No. 203

35. (U) Phase II Final Report on the Design and Evaluation of a Low Speed Hydraulic Turbine-Driven, Pump Discharge Fed Inducer Stage, Aerojet-General Corp., Sacramento, California, Contract AF 04(611)-7446 (Confidential Report)

Bibliography (cont.)

36. Acosta, A. J., "An Experimental Study of Cavitating Inducers," Second Symposium on Naval Hydrodynamics, Washington, D. C., August 1958

37. Ainley, D. G. and Mathieson, G. C. R., "An Examination of the Flow and Pressure Losses in Blade Rows of Axial-Flow Turbines," Aero-Research Council R&M No. 2891, March 1951

38. Edlebeck, N. A., "(U) The Design and Testing of Axial-Flow Blading for High-Head, High Capacity Liquid Hydrogen Pumps," AIAA Propulsion Specialists Conference, Colorado Springs, Colorado, June 1965 (Confidential Paper)

39. Gongwer, C. A., "A Theory of Cavitation Flow in Centrifugal Pump-Impellers," Trans. ASME, Vol. 66, 1941, pp. 29-40.

40. Stripling, L. B., "Cavitation in Turbopumps - Part 2," Trans. ASME, Journal of Basic Engineering, Vol. 84, 1962, pp. 339-350

41. Swanson, W. M., "Complete Characteristics, Circle Diagram for Turbomachinery," Trans. ASME, Vol. 75, 1953, pp. 819-826

42. Wood, G. M., Murphy, J. S., and Farquhar, J., "An Experimental Study of Cavitation in a Mixed Flow Pump Impeller," Trans. ASME, Journal of Basic Engineering, Vol. 82, Series D, December 1960, pp. 929-940

43. Gibb, J. A., ARES Predicted Start and Shutdown Transients, Aerojet-General Memorandum No. 9350:66:0218, 21 September 1966

44. Huser, D. A., Properties of Cryogenic Fluids, Aerojet-General Memorandum No. 7830:H3153, 13 February 1967

APPENDIX A

STAGE WORK SPLIT
AND
HIGH-SPEED ROTOR CAVITATION ANALYSIS
PROGRAM LISTING

```
ONE  D  1130 PROGRAM FOR THE FULL FLOW INDUCER  NAS 3-7977

XNI-INDUCER RPM  RI-INDUCER MEAN DISCHARGE RADIUS  SR-SPEED RATIO H/L
DH-INC OF HEAD  W2W1-W2/W1  C3-TURBINE CONSTANT  DHDF-DRUM FRICTION H.C.
HCI-INDUCER MEAN H.C.  C4-TURBINE LEAKAGE FACTOR  RI1-IND MEAN INLET RAD.
RT-MAX IND. RAD  Q-FLOW GPM        C5-LOSS FACTOR ON VELOCITY HEAD INTER
STAGE LOSS  SIG- SOLIDITY OF HIGA SPEED ROTOR  C6-SPEE RATIO STABILITY
MARGIN
XX(1)    WBAR  VS  HCI
XX(2)    W2/W1  VS  HCI
XX(3)    HCI AT FC=1.2*DESIGN  / HCI AT FC DESIGN    VS HCI
XX(4)    DEL HCI(DUE TO INPUT HEATING, CAVITATION, INLET NPSH)  VS  HCI
XKP  CAVITATION CONSTANT (GONGWER, BRUMFIELD)  VS INLET FLUID FLOW ANGLE
PARR   WBAR AVERAGE  VS D
DIMENSION XX(5)
CALL LOSS (0,UI,UR)
 1 READ(2,106)XNI,RI,SR,DH,W2W1,C3,DHDF,HCI,C4,RI1,RT,Q,C5,SIG,C6,FC1
   WRITE(3,100)XNI,Q,HCI,SR,C6,RI1,RI,RT,W2W1,DHDF,C3,C4,C5
   WRITE(3,101)
   Q=Q/448.8
   DHIP=0.
   FLAG=0.
60 DHIP= DHIP+ DH
   UI=XNI*RI/114.5
   RRT=(390000./(SR*XNI))**.333
   RRT=RRT*C3/RI
15 RRR=SQRT(HCI/SR+DHIP*32.2 /((1.-W2W1)*UI**2*SR**2))
   IF(C3-.1)10,10,20
10 RRT=RRR
20 UR=UI*SR*RRR
   DHCR=DHIP*32.2  /UR**2
   HCR1=HCI/SR/RRR**2
   HCR2=HCR1+DHCR
   HCT2=(HCR2*RRR**2*SR-(HCI+DHDF)/C4)/RRT**2
   SSR=((1.-HCI)/C4+(1.-HCT2)*RRT**2+DHDF/C4)/((1.-HCR2)*RRR**2)
   HCT1= HCR2*SR*(RRR/RRT)**2
   DHCT= HCT1-HCT2
   D=SR*RRR**2*(1.-HCR2)-RRT**2*(1.-HCT2)-(1.-HCI)/C4
```

```
C     ONE  D  1130 PROGRAM FOR THE FULL FLOW INDUCER  NAS 3-7977

      A=SR*RRR**2-1.2*D
      B=1./C4+RRT**2
      C=-DHDF/1.2 /C4
      E=B**2-4.*A*C
      R1=(B+SQRT(E))/(2.*A)
      SSR12=((1.-HCI)/C4+(1.-HCT2)*RRT**2+DHDF/C4/(1.2*R1)**2)/((1.-HCR2
     X)*RRR**2)
      DEL2=(SR-SSR/C6)/SR
      IF(FLAG)300,300,320
  300 IF( DEL2 ) 310,310,320
  320 FLAG =1.
      CALL ITER(2,DHIP,.005,10.,DEL2,DHIP,A2)
      IF(A2)  1,15,310
  310 CONTINUE
      DO 30 I=1,4
   30 CALL LOSS(I,HCI,XX(I))
      UI1=XNI*RI1/114.5
      WI1=UI1*SQRT(1.+FC1**2)
      WI2=WI1*XX(2)
      WTI2 = UI*(1.-HCI)
      A=3.14/ 72.*(RT**2 -RI**2)
      CMI2=Q/A
      WI2P=    SQRT(CMI2**2+WTI2**2)
      IF(WI2-WI2P)50,40,40
   40 CMI2= SQRT(WI2**2-WTI2**2)
      A=Q/CMI2
      GO TO 70
   50 WI2=WI2P
   70 RTI=SQRT(RI**2+A*72./3.14)
      RHI=SQRT(RI**2-A*72./3.14)
      FCI2=CMI2/UI
      BETAI=ATAN((1.-HCI)/FCI2)
      DL1= C5/2.*((CMI2/UI)**2+HCI**2)
      PP=1.+5.*(1.-XX(3))*(1.-1.2*R1)
      HCIA = HCI-XX(1)*(WI1/UI)**2/2.-DL1
      EFI=HCIA/HCI
      HCI12=(HCIA+DL1)*PP-DL1-XX(4)
      HT=HCI12*UI**2/32.2
      CUI2= HCI*UI
```

```
C     ONE  D  1130 PROGRAM FOR THE FULL FLOW INDUCER  NAS 3-7977

      CUR1= CUI2/RRR
      CUR12= (UI-1.2* R1        *(UI-CUI2))/RRR
      WTR1=(1.-HCR1)*UR
      WTR12=1.-CUR12/UR
  200 CALL ITER(1,BETA,.005,10.,DEL1,78.,A1)
      IF(A1)  1,210,220
  210 BET = BETA /57.2958
      TANB=SIN(BET )/COS(BET )
      FCR1= (1.-HCR1)/TANB
      CMR1=FCR1*UR
      A=Q/CMR1
      RTR=SQRT((RI*RRR)**2+A*72./3.14)
      RHR=SQRT((RI*RRR)**2-A*72./3.14)
      URT=XNI*SR*RTR/114.5
      FCR12= FCR1*1.2
      BET12= 57.2958* ATAN(WTR12/FCR12)
      UR2G=UR**2/64.4
      C22G=(FCR12**2+(CUR12/UR)**2)*UR2G
      W22G=(FCR12**2+ WTR12**2)*UR2G
      XK= (HT-C22G)/W22G
      CALL LOSS(7,BETA,XKP)
      DEL1=(XK-XKP)/XK
      GO TO 200
  220 D=1.-W2W1 +(WTR1- UR*(1.-HCR2))/(2.*SIG*FCR1/COS(BET)*UR)
      CALL LOSS(8,D,PARR)
      WBAR=PARR * 2.*SIG *SQRT(FCR1**2+(1.-HCR2)**2)/FCR1
      DHCRA= DHCR-WBAR*(FCR1/COS(BET))**2/2.
      EFR =      DHCRA /DHCR
      FCT1= FCR1*SR
      EFT=1./(1.+(.177*(FCT1**2+(1.-HCT2)**2))/(2.*DHCT))
      EFA=HCI*EFI/RRR**2/SR**2+EFR*DHCR-DHCT/SR**2*(RRT/RRR)**2/EFT
      EFA=EFA/DHCR
      H=DHIP *EFA
      WRITE(3,102)SSR,DHCR,HCR2,DHCT,HCT2,SSR12,EFI,EFR,EFT,EFA,BETA,
     XBET12,RTI,RHI,RTR,RHR,XK,D,WBAR,H
      WRITE(3,103)RRR,RRT,FC1,FCI2,BETAI,XX(4),FCR1,URT,PARR
      IF(FLAG) 60,60,1
  100 FORMAT(1H1,10HIND SPEED=,F9.0,/,10HFLOW     =,F9.3,/,10HIND H.C. =
     X,F9.4,/,10HSPEED RAT=,F9.3,/,10HSR STA MR=,F9.4,/,16HIND R M1,M2,M
```

```
C     ONE  D  1130 PROGRAM FOR THE FULL FLOW INDUCER  NAS 3-7977

     XAX=,3F9.3,/,10HW2/W1     =,F9.3,/,10HDRUM FHC =,F9.4,/,10HTURB R FA
     X=,F9.3,/,10HTURB L FA=,F9.3,/,10HI.STAGE F=,F9.3,////)
  101 FORMAT (1X,' SSR   DHCR   HCR2   DHCT   HCT2   SR12   EFFI   EFFR   EFFT
     XEFFA   BETR  BE12   RTI    RHI    RTR    RHR    K NO   D* R   W-B    DH',
     X//,      1X,' RRR    RRT   FCI1   FCI2   BETI   DHCL   FCR1    URT   LPR
     X',///)
  102 FORMAT(1X,F5.3,9F6.3,2F6.2,7F6.3,F6.0)
  103 FORMAT(1X,F5.3,6F6.3,F6.0,F6.3,///)
  106 FORMAT(16F5.0)
      END
```

APPENDIX B

TWO-DIMENSIONAL FLOW
WITH
SIMPLE RADIAL EQUILIBRIUM

Appendix B

A computer program was written using the method described in NASA Report RME56003a, "Aerodynamic Design of Axial Flow Compressors - Volume 2." Existing Aerojet-General computer program, Job No. 10001, essentially does the same calculation but was not used because of its complexity.

The new program was an eleven streamline solution for the flow distribution forward and aft of a single rotating blade row. The assumptions were:

1. Incompressible flow, no heat transfer.
2. Simple radial equilibrium.
3. Flow axially symmetric with no streamline curvature.

The program was written in FORTRAN III and ran approximately 4 min per case using an IBM 1130 computer.

The method of iteration was modified from the normal scheme in that the axial velocity distribution was set and the input head at the hub streamline was assumed until the mass averaged input head equaled that required. The axial velocity distribution was arbitrary and could be input to the program. This program scaled the input distribution at each streamline until continuity was satisfied. The program was checked against the existing Computer Job No. 10001 using a test case of the same input. The results showed negligible differences which were well within the iteration tolerance.

APPENDIX C

PUMPING SYSTEM SUBROUTINES

Appendix C

I. NOMENCLATURE

Parameter	Description	Units
A	Flow Area	Ft^2
B	Bulk Modulus	Psi
C	Waterhammer Characteristic Constant	Ft
Cp	Heat Capacity	Btu/lb °R
d	Inside Diameter	In.
E	Modulus of Elasticity	Psi
f	Function of	-
g	Gravitational Constant	$32.2\ ft/sec^2$
H	Head	Ft
J	Polar Moment of Inertia	$Ft\text{-}lb\text{-}sec^2$
K	Constant bias	-
Kr	Flow Recirculation Constant	-
Kv	Valve Flow parameter	$Lb^{1/2}\text{-}in./sec$
L	Constant Length	Ft
N	Speed	Rpm
P	Pressure - Unless Otherwise Spec.	Psia
Q	Flow Rate	Gpm
R	Hydraulic Flow Resistance	$Sec^2/ft^3\text{-}in.^2$
T	Temperature	°R
t	Time	Sec
t*	Past Times	Sec
th	Thickness of Conduit	in.
Vw	Sonic Velocity in Fluid	Ft/sec
$\dot{W}$	Weight Flow	Lb/sec

Appendix C

Parameter	Description	Units
ε	Error	-
ΔH	Total Differential Head	Ft
μ	Torque	Ft-lb
$\Delta\mu$	Correction to Torque	Ft-lb
$\Delta(H/N^2)$	Correction to Dimensional Head Coeff.	$Ft/(rpm)^2$
$\Delta(\mu/\rho N^2)$	Correction to Dimensional Torque Coeff.	$Ft\text{-}lb/lb/ft^3/(rpm)^2$
$\Delta N/\Delta t$	Shaft Acceleration	Rpm/sec
$\Delta Q/\Delta t$	Flow Acceleration	(Gpm)/sec
ΔQ	Flow Rate Correction	Gpm
NPSH	Net Positive Suction Head	Ft
ρ	Weight Density	lb/ft^3

Subscripts	Description
1	High Speed Shaft
2	Low Speed Shaft
I	Low Speed Inducer
M	Collector or Main Stage Pump
R	High Speed Rotor
T	Turbine
C	Cavitation Condition
NC	Non-cavitation Condition
NOM	Nominal
R_e	Reynolds Number
V	Sat Vapor Condition
A	Assumed Value

Appendix C

Subscripts	Description
e	Exit
i	Inlet
r	Recirculation
tr	Transient

APPENDIX C

INDUCER SCHEMATIC AND MODEL

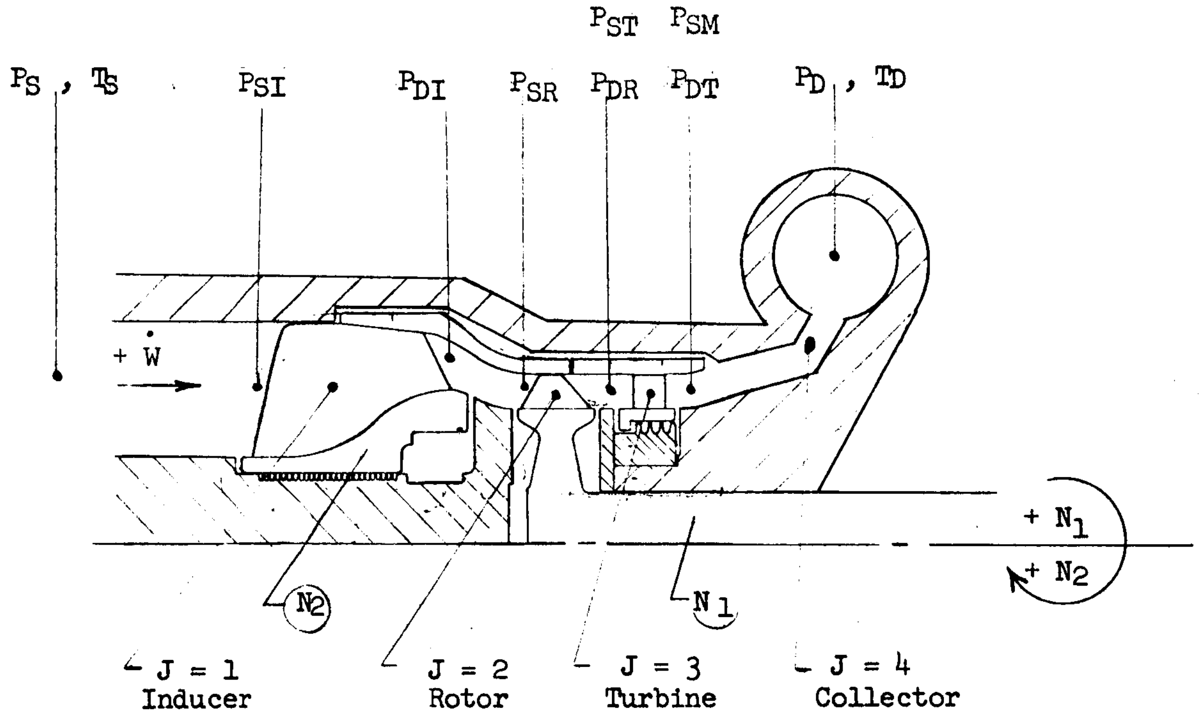

BASIC ASSUMPTIONS

1. Constant weight flow rate - no storage.
2. Flow in positive direction only.
3. Rotation in positive speed direction only.
4. All characteristic curves dealing with head rise or loss are expressed as total head or enthalpy.
5. N_1 is known as a function of time.

II. INDUCER SUBROUTINE (J=1)

A. ASSUMPTIONS

1. All head heat and torque characteristics are independent of high-speed rotor speed, N_1.
2. No recirculating flow.
3. A correction in stage flow and head rise exists because of Reynolds Number.
4. Constant density through the stage, inlet density is used, ρ_I.
5. Flow through the inducer is in a positive direction only $(\dot{\omega}_I \geq 0)$.

B. INDUCER: ORDER OF SOLUTION

Equation No.	Equation	Boundary Conditions or Limits
1.	Predict a Value of $\dot{\omega}_{wh}$ = lb/sec	$\dot{\omega} \geq 0$
2.	$Q = \frac{448.831\ \dot{\omega}_{wh}}{\rho} =$ gpm	
3.	If $N_1 \leq$ Min, Set $P_d = P_S$, Exit $\Delta Q/\Delta t = (Q_{(t-1)} - Q_{(t-2)})/\Delta t$	
4.	$\frac{\Delta Q_{Re}}{Q} = f_1(\frac{\Delta Q}{\Delta t}, \frac{Q}{Q_{Nom}})$ (Sec Curve 67-146)	$\frac{\Delta Q}{\Delta t} =$ MAX $Q/Q_{Nom} =$ MAX
5.	$Q^1 = Q(1 + K_1 \frac{\Delta Q_{Re}}{Q}$	If $Q^1 < 0$: ERROR MESSAGE = 140
6.	$NPSH = 144 (\frac{P_S - P_V}{\rho}) + {\frac{Q}{A_S}}^{2} \frac{2.482 \times 10^{-6}}{g}$	$NPSH \geq .01$

Appendix C

Equation No.	Equation	Boundary Conditions or Limits
7.	Using first past time value of N_2 $N_2 = N_2^*$ $S = \frac{N_2^* \sqrt{Q^1}}{(NPSH)^{3/4}}$	$0 \leq S \leq MAX$
8.	$\frac{\Delta H_c}{NPSH} = f_2 \ (S, \frac{Q^1}{N_2^*})$ $\Delta H_c = K_2 \ (NPSH) \ f_2$ (See Curve 67-116)	$0 \leq \frac{Q^1}{N_2^*} \leq MAX$
9.	$\frac{\Delta H_{nc}}{N_2^{*2}} = f_3 \ (\frac{Q^1}{N_2^*})$ $\Delta H_{nc} = K_3 \ N_2^{*2} \ f_3$ (See Curve 67-114)	
10.	$\frac{\Delta H_{Re}}{\Delta H_{nc}} = f_5 \ (\frac{Q^1}{N_2^*}, \ \frac{Q^1}{Q_{Nom}})$ (See Curve 67-120)	$0 \leq Q^1/Q_{Nom} \leq MAX$ $-1 \leq K_5 \frac{\Delta H_{Re}}{\Delta H_{nc}} \leq +1$
11.	$\Delta H^1_{nc} = \Delta H_{nc} \ (1 - K_5 \ \frac{\Delta H_{Re}}{\Delta H_{nc}})$	
12.	$\Delta H = \Delta H^1_{nc} - \Delta H_c = ft$	
13.	$P_{dI} = P_S + \frac{\Delta H \ \rho}{144} = psia$	$P_d \geq P_v$

Equation No.	Equation	Boundary Conditions or Limits
	BEFORE $\dot{\omega}A$ CONVERGENCE: BYPASS TO ROTOR SUBROUTINE, AFTER CONVERGENCE: CONTINUE	
14.	$\frac{\Delta\mu_c}{\rho\ (NPSH)} = f_6\ (S, \frac{Q^1}{N_2*})$ (See Curve 67-117) $\Delta\mu_c = K_6\ \rho\ NPSH\ f_6$	
15.	$\frac{\mu^1}{\rho\ N_2*^2} = f_7\ (\frac{Q^1}{N_2*})$ (See Curve 67-115) $\mu^1 = K_7\ \rho\ N_2*^2\ f_7$	
16.	$\mu = \mu^1 - \Delta\mu_c$	
17.	Test Option H_2 Flag If H_2 Flag = 0 Incompressible Go to Equation 19 If H_2 Flag = + Compressible Go to Equation 18	
	COMPRESSIBLE	
18.	Compressibility effects are taken into account by changing density from stage to stage using a NBS thermodynamic subprogram. The suction density to the stage is taken as the stage density.	

Equation No.	Equation	Boundary Conditions or Limits

For Inducer Stage

T_s is calculated from Heat Transfer Subroutine HTSR(M)

Call PT

$$\rho_J = f(P_{s_{t-1}}, T_{s_{t_1}}) =$$

$$En_s = \text{enthalpy - Btu/lb}$$

$$Ens = f(P_{s_{t-1}}, T_{s_{t-1}})$$

For all the other Stages

Call PT

$$\rho_J = f(P_{d(J-1)_{t-1}}, T_{e(J-1)_{t-1}})$$

$$En_s = f(P_{d(J-1)_{t-1}}, T_{e(J-1)_{t-1}})$$

For all the Stages

The exit enthalpy if calculated from the torque

$$\Delta E_\mu = \frac{\mu \frac{\Pi}{30} N_J *}{778\, Q_J\, \rho_J}$$

$$En_e = En_s + \Delta En_\mu$$

The exit temperature and density are then calculated from thermodynamic properties

$$T_e = f(En_e, P_d)$$

$$\rho_e = f(En_e, P_d)$$

Equation No.	Equations	Boundary Conditions or Limits
19.	INCOMPRESSIBLE: Calc. T_e, ρ_e	
	$T_e = T_o + \frac{1}{C_p} \frac{\mu \frac{\Pi}{(30)} N_J{}^*}{778\eta\, Q_J \rho_J} - \frac{\Delta H}{778}$	$T_c \geq T_o$
	$\rho_e = f_{\rho_e}(T_e)$	
	RETURN	

III. HIGH-SPEED ROTOR SUBROUTINE (J=2)

A. ASSUMPTIONS

1. All head and torque characteristics are a function of speed ratio, N_2/N_1
2. Recirculation exists in the pump
3. A correction in stage flow and head rise exists because of Reynolds Number.
4. Constant density through the stage, inlet density to the high-speed rotor is used.
5. Flow through the rotor is in a positive direction only.
6. A correction to head and torque characteristics may exist because of high-speed shaft acceleration. (Optional)
7. First past time value of N_2, $N_2 \equiv N_2^*$ is used.

B. HIGH-SPEED ROTOR: ORDER OF SOLUTION

Equation No.	Equation	Boundary Conditions or Limits
1.	$\rho = \rho_R = \rho_{eI_{(t-1)}}$ (Incompressible)	
2.	$Q_R = \frac{\rho_{I(t-1)}}{\rho_{R(t-1)}} Q_I = Q = gpm$	
3.	$P_{SR} = P_{dI}$	
	<u>Using First Past Time Value of $\Delta H_R = \Delta H^*$</u>	
4.	$Q_r = K_r \ (\Delta H^*)^{1/2}$ $\frac{\Delta Q}{\Delta t} = \frac{Q_{(t-1)} - Q_{(t-2)}}{\Delta t}$	
5.	$\frac{\Delta Q_{Re}}{Q} = f_1 \left(\frac{\Delta Q}{\Delta t}, \frac{Q}{Q_{Nom}}\right)$ (See Curve 67-146)	$\Delta Q/\Delta t \leq MAX$ $Q/Q_{Nom} \leq MAX$

Appendix C

Equation No.	Equation	Boundary Conditions or Limits
6.	$Q^1 = Q\left[1 + K_1 \frac{\Delta Q_{Rc}}{Q}\right] + Q_r$	If $Q^1 < 0$ Error Message = 140
	$T_{s_{t-1}} = T_{eI_{t-1}}$	
7.	$P_v = f_{te}(T_{s_{t-1}})$	
8.	$NPSH = \frac{144\ (P_{sr} - P_v)}{\rho_R}$	$NPSH \geq .01$
9.	$S = \frac{N_1\sqrt{Q^1}}{(NPSH)^{3/4}}$	$0 \leq S \leq MAX$
10.	$\frac{\Delta H_c}{NPSH} = f_2\ (S, \frac{Q^1}{N_1}, \frac{N_2^*}{N_1})$	$0 \leq \frac{Q^1}{N_1} \leq MAX$ $0 \leq \frac{N_2^*}{N_1} \leq MAX$
	(See Curve 67-123)	
	$\Delta H_c = K_2\ NPSH\ f_2$	
11.	$\frac{\Delta H_{nc}}{N_1^2} = f_3\ (\frac{Q^1}{N_1}, \frac{N_2^*}{N_1})$	
	(See Curve 67-121)	
	$\Delta H_{nc} = K_3\ N_1^2\ f_3$	
	Test Option Flag B	
	If Flag B = 0	
	Go to Equation 13	
	If Flag B = +	
	$\Delta N_1/\Delta t = N1_{(t)} - N1_{(t-1)}/\Delta t$	

Equation No.	Equation	Boundary Conditions or Limits
12.	$\frac{\Delta H_{tr}}{N_1^2} = f_4 (\frac{\Delta N_1}{\Delta t}, N_1)$	
	(Optional Curve)	
	$\Delta H_{tr} = K_4 N_1^2 f_4$	
13.	$\frac{\Delta H_{re}}{\Delta H_{nc}} = f_5 (\frac{Q^1}{N_1}, \frac{N_2^*}{N_1}, \frac{Q^1}{Q_{Nom}})$	$-1 \leq K_5 \frac{\Delta H_{re}}{\Delta H_{nc}} \leq 1$
	(See Curve 67-127)	
14.	$\Delta H_{nc}^1 = \Delta H_{nc} (1 - K_5 \frac{\Delta H_{re}}{\Delta H_{nc}})$	
15.	$\Delta H = \Delta H_{nc}^1 - \Delta H_c - \Delta H_{tr}$	
16.	$P_{dR} = P_{sR} + \frac{\Delta H \rho_r}{144}$	
	BEFORE $\dot{\omega}_A$ CONVERGENCE: BYPASS TO TURBINE SUBROUTINE, AFTER CONVERGENCE: CONTINUE	
17.	$\frac{\Delta \mu_c}{\rho (NPSH)} = f_6 (S, \frac{Q^1}{N_1}, \frac{N_2^*}{N_1})$	
	(See Curve 67-124)	
	$\Delta \mu_c = K_6 \rho (NPSH) f_6$	
18.	$\frac{\mu^1}{\rho N_1^2} = f_7 (\frac{Q^1}{N_1}, \frac{N_2^*}{N_1})$	
	(See Curve 67-122)	
	$\mu^1 = K_7 \rho N_1^2 f_7$	

Equation No. | Equation | Boundary Conditions or Limits

Test Option Flag B

If 0: Go to Equation 20

If +: Continue

19. $$\frac{\Delta\mu_{tr}}{\rho N_1^{2}} = f_8 \left(\frac{\Delta N_1}{\Delta t}, N_1, \frac{Q}{N_1}\right)$$

(See Curve VIII)

$$\Delta\mu_{tr} = K_8 \rho N_1^{2} f_8$$

20. $$\mu = \mu^{1} - \Delta\mu_c - \Delta\mu_{tr}$$

21. Test Option H_2 Flag

If H_2 Flag = 0, Incompressible

Go to Equation 23

If H_2 Flag = 1, Compressible

Continue

22. COMPRESSIBLE: Calc. Te, Ene ρ_e

<u>Methods is the same as Outlined under Inducer</u>

RETURN

23. INCOMPRESSIBLE: Calc T_e, ρ_e

$$T_e = T_s + \frac{1}{C_p}\left[\frac{\mu \frac{\pi}{(30)} N_1}{778\,\dot{\omega}} - \frac{\Delta H}{778}\right]$$ $T_e \geq T_o$

$$\rho_e = f\rho_e (T_e)$$

RETURN

Appendix C

IV. TURBINE SUBROUTINE

A. ASSUMPTIONS

1. All head and torque characteristics are a function of speed ratio, N_2/N_1.
2. A bypass flow exists in the turbine.
3. A correction in stage flow and head rise exists because of Reynolds number.
4. Constant density through the stage, inlet density to the turbine is used.
5. Flow through the turbine is in a positive direction only.
6. First past time value of N_2, $N_2 \equiv N_2{}^*$ is used.

B. TURBINE: ORDER OF SOLUTION

EQUATION NO.	EQUATION	BOUNDARY CONDITION OR LIMITS
1	$\rho = \rho_T = \rho_{er(t-1)}$ (Incompr.)	
2	$Q = Q_T = \frac{\rho r(t-1)}{\rho T(t-1)} Q_r = CPM$	
3	$P_{ST} = P_{dR}$	
	Using past time value of $\Delta H_T = \Delta H^*$	
4	$Q_r = -K_T \left(\lvert \Delta H^* \rvert\right)^{1/2}$	
	$\lvert \Delta H^* \rvert$ = absolute value of ΔH^*	
	$\Delta Q/\Delta t = (Q(t-1) - Q(t-2))/\Delta t$	
5	$\frac{\Delta QRe}{Q} = f1 \left(\frac{\Delta Q}{\Delta t}, \frac{Q}{Q_{NOM}}\right)$ (See Curve 67-146)	$\Delta Q/\Delta t \leq MAX$ $Q/Q_{NCM} \leq MAX$
6	$Q^1 = Q \left(1 + K_1 \frac{\Delta QRe}{Q}\right) + Qr$	

EQUATION NO.	EQUATION	BOUNDARY CONDITION OR LIMITS
7	$T_{s(t-1)} = T_{er(t-1)}$	
	$Pv = f_{Te}(T_{e(t-1)})$	
8	$NPSH = 144 \frac{(Pst - Pv)}{\rho}$	$NPSH \geq .01$
	Using first past time value $N_2 \equiv N_2^*$	
9	$S = \frac{N_2^* \sqrt{Q^1}}{(NPSH)^{3/4}}$	$0 \leq S \leq MAX$
10	$\frac{\Delta Hc}{(NPSH)} = f_2 \left(S, \frac{Q}{N_2^*}, \frac{N_2^*}{N_1}\right)$	$0 \leq \frac{Q^1}{N_2} \leq MAX$
	(See curve 67-116 for type)	$0 \leq \frac{N^2}{N_1} \leq MAX$
	$\Delta H_c = K_2 \, (NPSH) \; f_2$	
11	$\frac{\Delta H_{nc}}{N_2} = f_3 \left(\frac{Q^1}{N_2^*}, \frac{N_{2^*}}{N_1}\right)$	This will be a negative value, at steady state.
	$\Delta H_{nc} = K_3 \, N_2^{*2} \, f_3$	
	$(K_3 \equiv - X.XX)$	
12	$\frac{\Delta H_{re}}{\Delta H_{nc}} = f_5 \left(\frac{Q^1}{N_2^*}, \frac{N_2^*}{N_1}, \frac{Q^1}{Q_{NOM}}\right)$	$-1 \leq K_5 \frac{\Delta H_{re}}{\Delta H_{nc}} \leq + 1$
	(See Curve 67-130)	
13	$\Delta H_{nc}^{1} = \Delta H_{nc} \left(1 - K_5 \frac{\Delta H_{re}}{\Delta H_{nc}}\right)$	
14	$\Delta H = \Delta H_{nc}^{1} - \Delta H_c$	

EQUATION NO.	EQUATION	BOUNDARY CONDITIONS OR LIMITS

15 $$\rho_{dt} = P_{ST} + \frac{\Delta H_{\rho}}{144}$$

BEFORE $\dot{W}$a CONVERGENCE: BYPASS TO MAIN PUMP SUBROUTINE

AFTER CONVERGENCE: CONTINUE

16 $$\frac{\Delta \mu c}{\rho (NPSH)} = f_6 \; (S, \frac{Q^1}{N_2*}, \frac{N_2*}{N_1})$$

(See Curve 67-117 for type)

$$\Delta \mu c = K_6 \; \rho (NPSH) \; f_6$$

17 $$\frac{\mu^1}{\rho N_2*} = f_7 \; (\frac{Q^1}{N_2*2}, \frac{N_2*}{N_1})$$

(See Curve 67-128)

$$\mu^1 = K_7 \; \rho N_2*^2 \; f_7$$

18 $$\mu = \mu^1 - \Delta \mu c$$

19 Test Option H_2 Flag

If H_2 flag = 0, incompressible go to equation 20

If H_2 flag = 1, compressible - continue

COMPRESSIBLE: CALC. T_c, E_{ne}, ρe

The equations are the same as described in the Inducer Subroutine except, the definition

$$\Delta En_{\mu} \equiv - \frac{\mu_T \frac{\Pi}{30} N_2}{778 \; Q_J \; \rho_J}$$

EXIT

EQUATION NO.	EQUATION	BOUNDARY CONDITIONS OR LIMITS
20	INCOMPRESSIBLE: CALC. Te_{γ} ρe	
	$T_e = T_s + \frac{1}{C_\rho} \left[\frac{\Delta H}{778} + \frac{\mu \frac{\pi}{(30)} N_{2*}}{778\, \dot{w}}\right]$	$T_e \geq T_o$
	NOTE: $\Delta H \equiv -$ at steady state $T_e < T_s$ at steady state	
	$\rho_e = f_{\rho e} (T_e)$	
	WORK BALANCE ON LOW SPEED ROTATION	
21	$HP_{loss} = f_{loss} (Q)$	HP = horse power
22	$\mu_{loss} = \frac{5253.1\, HP_{loss}}{N_2*}$	
23	$N_2 = N_2* + \frac{30\ \Delta t}{\pi J} \left(\frac{\mu_t + \mu_{t*}}{2} - \frac{\mu_I + \mu_{I*}}{2} - \frac{\mu_{loss} + \mu_{loss*}}{2}\right)$	$N_2 \geq 0$
	EXIT	

V. MAIN PUMP SUBROUTINE

The following two options were considered:

Option I: Main pump as collector--no rotating parts.
Option II: Main pump as a pump.

A. ASSUMPTIONS

1. All head and torque characteristics are a function of speed ratio, N_2/N_1.
2. Recirculation exists if used as a pump.
3. A correction in stage flow and head rise exists because of Reynolds number.
4. Constant density through the stage, inlet density is used.
5. Flow through the rotor is in a positive direction only.
6. A correction to head and torque may exist because of high speed shaft acceleration. (Optional)

B. MAIN PUMP: ORDER OF SOLUTION

Equation No.	Equation	Boundary Conditions or Limits
1.	$\rho = \rho_M = \rho_{eT(t-1)}$	
2.	$Q = Q_M = \dfrac{\rho_{T(t-1)}}{\rho_{M(t-1)}} Q_T = \text{GPM}$	
3.	$P_{SM} = P_{dT}$	
4.	$T_{s_{t-1}} = T_{eT_{t-1}}$	
	$P_V = f_{Te}(T_{eT_{t-1}})$	
5.	$\text{NPSH} = 144 \dfrac{(P_{SM} - P_V)}{\rho}$	NPSH $\geq$ .01

Appendix C

Equation No.	Equation	Boundary Conditions or Limits
6.	Test Option Flag C If Flag C = 0, Pump Go to Equation 13. If Flag C = 1, Collector Continue.	
7.	$S = \frac{N_1^* \sqrt{Q}}{(NPSH)^{3/4}}$	
8.	$\frac{\Delta H_C}{NPSH} = f_2 \left(S, \frac{Q}{N_1^*}, \frac{N_2^*}{N_1}\right)$ (See Curve 67-135 as example) $\Delta H_C = K_2 (NPSH)\ f_2$	$\text{Min} \le \frac{Q}{N_2^*} \le \text{Max}$
9.	$\frac{\Delta H_{NC}}{N_1^{*2}} = f_3 \left(\frac{Q}{N_1^*}, \frac{N_2^*}{N_1}\right)$ (See Curve 67-132) $\Delta H_{NC} = K_3\ N_1^{*2}\ f_3$	These will be negative if collector
10.	$\Delta H = \Delta H_{NC} - \Delta H_C$	
11.	$P_d = P_{SM} + \frac{\Delta H\ \rho}{144}$	$P_d \ge P_V$
12.	$T_{e_J} = T_{s_J}$ EXIT	

Main Pump Equations

Using first past time value of ΔH_M

$$\Delta H_M \equiv \Delta H^*$$

Equation No.	Equation	Boundary Conditions or Limits
13.	$Q_r = K_r\ (\Delta H^*)^{1/2}$ $\Delta Q/\Delta t = (Q_{(t-1)} - Q_{(t-2)})/\Delta t$	
14.	$\frac{\Delta Q_{Re}}{Q} = f_1 \left(\frac{\Delta Q}{\Delta t}, \frac{Q}{Q_{nom}}\right)$ (See Curve 67-131 as example)	

Appendix C

Equation No.	Equation	Boundary Conditions or Limits
15.	$Q^1 = Q\ [1 + K_1 \frac{\Delta Q_{Re}}{Q}] + Q_r$	If $Q^1 < 0$, <u>error</u>
16.	$S = \frac{N_1 \sqrt{Q^1}}{(NPSH)^{3/4}}$	$0 \leq S \leq Max$
17.	$\frac{\Delta H_C}{NPSH} = f_2\ (S, \frac{Q^1}{N_1}, \frac{N_2^*}{N_1})$ (Curve 67-135) $\Delta H_C = K_2 (NPSH)\ f_2$	$0 \leq \frac{Q^1}{N_1} \leq Max$ $0 \leq \frac{N_2^*}{N_1} \leq Max$
18.	$\frac{\Delta H_{NC}}{N_1^2} = f_3\ (\frac{Q^1}{N_1}, \frac{N_2^*}{N_1}$ (See Curve 67-133) $\Delta H_{NC} = K_3\ N_1^2\ f_3$	
19.	Test Option Flag B If Flag B = 0 Go to Equation 21. If Flag B = + Continue. $\Delta N_1/\Delta t = (N_{1(t)} - N_{1(t-1)})/\Delta t$	
20.	$\frac{\Delta H_{tr}}{N_1^2} = f_4\ (\frac{\Delta N_1}{\Delta t}, N_1, \frac{Q}{N_1})$ (Optional Curve) $\Delta H_{tr} = K_4\ N_1^2\ f_4$	
21.	$\frac{\Delta H_{Re}}{\Delta H_{NC}} = f_5\ (\frac{Q'}{N_1}, \frac{N_2^*}{N_1}, \frac{Q^1}{Q_{nom}})$ (See Curve 67-125 as example)	$-1 \leq K_5 \frac{\Delta H_{Re}}{\Delta H_{NC}} \leq +1$
22.	$\Delta H_{NC}' = \Delta H_{NC}\ (1 - K_5 \frac{\Delta H_{Re}}{\Delta H_{NC}})$	

Equation No.	Equation	Boundary Conditions or Limits
23.	$\Delta H = \Delta H_{NC}^{1} - \Delta H_C - \Delta H_{tr}$	
24.	$P_d = P_{SM} + \frac{\Delta H\ \rho}{144}$	$P_d \geq P_V$
	Before $\dot{w}_a$ Convergence: Bypass to waterhammer pump. **After $\dot{w}_a$ Convergence:** Continue.	
25.	$\frac{\Delta\mu_C}{\rho\ NPSH} = f_6\ (S, \frac{Q^1}{N_1}, \frac{N_2^*}{N_1})$ (Curve 67-136) $\Delta\mu_C = K_6\ \rho(NPSH)\ f_6$	
26.	$\frac{\mu^1}{\rho\ N_1^2} = f_7\ (\frac{Q^1}{N_1}, \frac{N_2^*}{N_1})$ (See Curve 67-134) $\mu^1 = K_7\ \rho\ N_1^2\ f_7$	
27.	Test Option Flag B If Flag B = 0 Go to Equation 29. If Flag B = + Continue.	
28.	$\frac{\Delta\mu_{tr}}{\rho\ N_1^2} = f_8\ (\frac{\Delta N_1}{\Delta t}, N_1, \frac{Q}{N_1})$ (Optional Curve) $\Delta\mu_{tr} = K_8\ \rho\ N_1^2\ f_8$	
29.	$\mu = \mu^1 - \Delta\mu_C - \Delta\mu_{tr}$	
30.	Test Option H_2 Flag If H_2 Flag = 0, Incompressible Go to Equation 32. If H_2 Flag = 1, Compressible Continue.	

Equation No.	Equation	Boundary Conditions or Limits
31.	COMPRESSIBLE: Calculate T_e, Ene, ρ_e Method is the same as outlined under Inducer Subroutine, except $\Delta E_{n_\mu} = \frac{\mu (\frac{\pi}{30}) N_1}{778 \dot{w}}$ EXIT INCOMPRESSIBLE: Calculate T_e, ρ_e	
32.	$T_e = T_s + \frac{1}{C_p} \left[\frac{\mu (\frac{\pi}{30}) N_1}{778 \dot{w}} - \frac{\Delta H}{778} \right]$ $\rho_e = f_{\rho_e} (T_e)$ EXIT	$T_e \geq T_o$

APPENDIX D

FEED SYSTEM SUBROUTINES

Appendix D

I. GENERAL ASSUMPTIONS

A. Constant density in all lines.

B. Constant area in each section.

C. Pressure waves travel at sonic velocity (i.e., the flow velocity is negligible compared to sonic velocity).

D. Constant elevation and length.

E. Conduit walls are elastic laterally but not axially. (No Poisson's ratio effects.)

F. Fixed computing internal, with wave propagation times for each section being an integral number of this interval.

G. Static pressure equal to total pressure (for simplified presentation of equations only, program includes effect).

H. No friction in line, instead it is lumped at the joints.

II. BASIC EQUATIONS

Using the above assumptions, the basic equations for a simple elastic conduit are

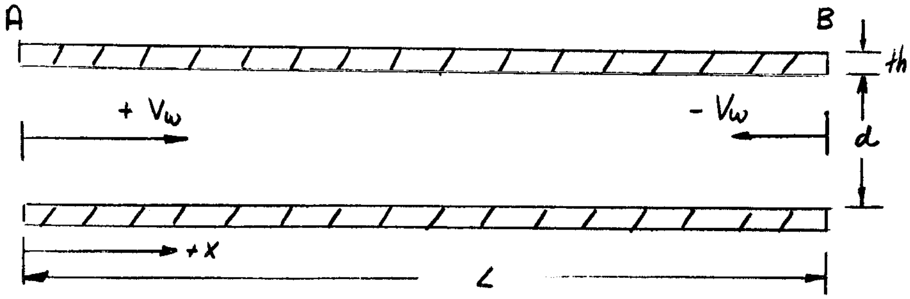

Equation of Motion:

$$(1) \quad \frac{\partial H}{\partial X} = - \frac{1}{g} \frac{\partial V}{\partial t}$$

Appendix D

Equation of Continuity: Where:

$$(2)\quad \frac{\partial H}{\partial t} = - \frac{V_w^{\,2}}{g} \frac{\partial V}{\partial X}, \qquad (3)\quad V_w^{\,2} = \frac{Bk}{\rho\ (1 + \frac{Bk.d}{E.th})}$$

By methods suggested by L. Bergeron, "Waterhammer in Hydraulics and Waves Surges in Electricity" translated by AsME, 1961, Wiley, New York, these equations can be solved in a finite difference form

Let

$$(4)\quad \frac{\Delta X}{\Delta t} = \frac{L}{\Delta t} = V_w,\ \Delta t = \frac{L}{V_w}, \qquad (5)\quad S = \frac{V_w}{gA}$$

for right traveling waves

$$(6)\quad \frac{P_{B,t}}{\rho} + S\,\frac{\dot{w}_{B,t}}{\rho} = C^{+} = \frac{P_{A,t*}}{\rho} + S\,\frac{\dot{w}_{A,t*}}{\rho}$$

for left traveling waves

$$(7)\quad \frac{P_{A,t}}{\rho} - S\,\frac{\dot{w}_{A,t}}{\rho} = C^{-} = \frac{P_{B,t*}}{\rho} - S\,\frac{\dot{w}_{B,t*}}{\rho}$$

where t = current time

$$t* = (t - \Delta t) = t - \frac{L}{V_w}$$

Equations (6) or (7) can be solved with a known boundary condition or another equation relating $P_{x,t}$ and $\dot{w}_{x,t}$.

A computing interval, $(\Delta t)_{min}$, is selected which when multiplied by an interger (I_i) will equal the Δt of each section,

$$\Delta t_1 = \frac{L_1}{V_{ws}}, \quad I_1\ (\Delta t)_{min} = \Delta t_1$$

$$\Delta t_2 = \frac{L_2}{V_{wd}}, \quad I_2\ (\Delta t)_{min} = \Delta t_2$$

$$\Delta t_3 = \frac{L_3}{V_{wj}}, \quad I_3\ (\Delta t)_{min} = \Delta t_3$$

III. DESCRIPTION OF COMPONENTS

A. TANK AND INLET LINE, SR NO. 1

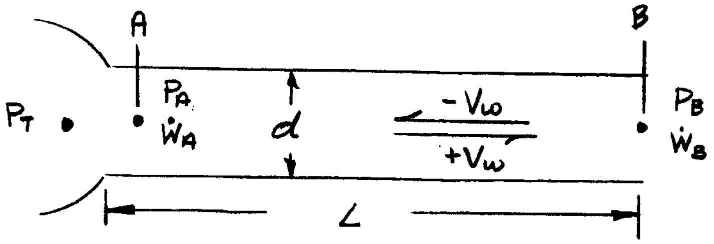

1. Boundary Conditions

(1) (i) PT = PA or (ii) $P_A = P_T - \frac{\dot{w}A^2}{\rho} R$

(2) Known past time conditions of P_B, $\dot{w}B$

2. Initial Conditions

(1) $\dot{w}_A = 0$

(2) $\dot{w}_B = 0$

(3) $P_A = P_B = P_T$

(i) $P_A = P_T$ calculate $\dot{w}_A$, C_A^-

3. Equations

(1) $t^* = t - \frac{L}{V_w}$

(2) $C_A^- = \frac{P_T}{\rho} - S\,\frac{\dot{w}A,t}{\rho}$

(3) $C_A^- = \frac{P_{B,t^*}}{\rho} - S\,\frac{\dot{w}B,t^*}{\rho}$

Solving for $\dot{w}A,t$ from eq (2)

(4) $\dot{w}A,t = \frac{\rho}{S}\left(\frac{P_T}{\rho} - C_A^-\right)$

Note: the sign of $\left(\frac{P_T}{\rho} - C_A^-\right)$ determined the direction at the flow. Flow out of tank is assumed positive.

(ii) $P_A = P_T - \frac{\dot{w}_A{}^2}{\rho} R$ (Friction loss at tank exit)

4. <u>Equations</u>

(1) $t^* = t - \frac{L}{V_w}$

(2) $P_{A,t} = P_T - \frac{(\dot{w}_{A,t})^2}{\rho} R$

(3) $\frac{P_{A,t}}{\rho} - S \frac{\dot{w}_{A,t}}{\rho} = C_A{}^-$

(4) $C_A{}^- = \frac{P_{B,t*}}{\rho} - S \frac{\dot{w}_{B,t*}}{\rho}$

Solving equations (2) and (3) for $\dot{w}_{A,t}$, gives the solution to the quadratic

$$(5) \quad |\dot{w}_{A,t}| = \left| \frac{\rho S}{2R} \left\{ -1 + \sqrt{1 + \frac{4R}{S^2} \left| \left(\frac{P_T}{\rho} - C_A{}^- \right) \right.} \right\} \right|$$

Because friction represents a loss the positive root is selected.

Also, the direction of the flow is determined by

$$(6) \quad \dot{w}_{A,t} = \text{SIGN} \left\{ \left(\frac{P_T}{\rho} - C_A{}^- \right) \right\} |\dot{w}_{A,t}|$$

as was shown previously.

Then,

$$(7) \quad P_{A,t} = \rho \left(C_A{}^- + S \frac{\dot{w}_{A,t}}{\rho} \right)$$

B. INTERNAL POINT WITH OR WITHOUT FRICTION, SR NO. 2

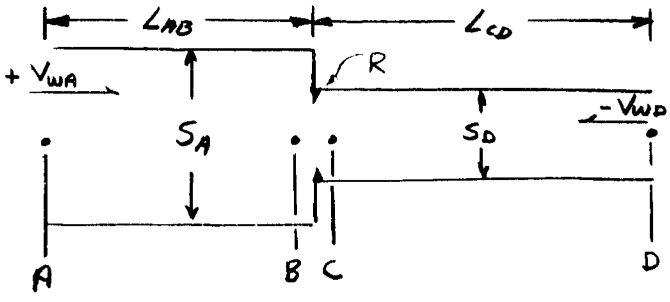

Appendix D

1. Known Conditions

a. Without Friction

(1) $\dot{w}_B = \dot{w}_C$

(2) $P_B = P_c$ (velocity head neglected)

(3) Known past time values at A and D

b. With Friction

(1) $\dot{w}_B = \dot{w}_C$

(2) $P_c = P_B - \frac{\dot{w}_B{}^2}{\rho} R$

(3) Known past time values at A and D

2. Equations

a. Without Friction

(1) $t_A{}^* = t - \frac{L_{AB}}{V_{wA}}$

(2) $t_B{}^* = t - \frac{L_{CD}}{V_{wD}}$

(3) $\frac{P_{B,t}}{\rho} + S_A \frac{\dot{w}_{B,t}}{\rho} = C_A{}^+ = \frac{P_{A,t*A}}{\rho} + S_A \frac{\dot{w}_{A,t*A}}{\rho}$

(4) $\frac{P_{c,t}}{\rho} - S_D \frac{\dot{w}_{B,t}}{\rho} = C_D{}^- = \frac{P_{D,t*D}}{\rho} - S_D \frac{\dot{w}_{D,t*D}}{\rho}$

(5) $P_{B,t} = P_{c,t}$

Solving eq's 1 (3), (4), and (5) for $\dot{w}_{B,t}$ gives

(6) $\dot{w}_{B,t} = \rho \left[\frac{C_A{}^+ - C_D{}^-}{SA + SD} \right]$

then

(7) $P_{B,t} = P_{c,t} = \rho\, C_A{}^+ - S_A\, \dot{w}_{B,t}$

b. With Friction

(1) - (4) are the same.

$$(5)\quad P_c = P_B - \frac{\dot{w}_B^{\,2}}{\rho} R$$

Solving eq's (3), (4), and (5) for $\dot{w}_{B,t}$ gives

$$(6)\quad |\dot{w}_{B,t}| = \left|\frac{\rho}{2R}(S_A + S_D)\left\{ -1 + \sqrt{1 + \frac{4R}{(S_A - S_D)^2}\,|(C_A^{+} - C_D^{-}}\right\}\right|$$

the sign or direction of the flow is determined by the difference between the characteristics.

$$(7)\quad \text{SIGN} = \text{SIGN}\left\{(C_A^{+} - C_D^{-})\right\}$$

therefore

$$(8)\quad \dot{w}_{B,t} = \text{SIGN}\ |\ \dot{w}_{B,t}\ |$$

then

$$(9)\quad P_B = \rho\ (C_A^{+} - S_A\frac{\dot{w}_{B,t}}{\rho})$$

$$(10)\quad P_c = \rho\ (C_D^{-} + S_D\frac{\dot{w}_{B,t}}{\rho})$$

C. BRANCH POINT, SR NO. 3

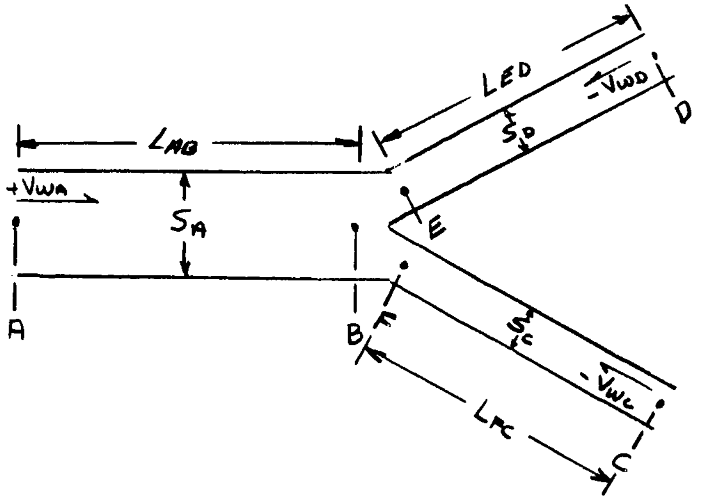

Appendix D

(a) Equations

(1) $\dot{w}_B = \dot{w}_E + \dot{w}_F$

(2) $P_B = P_F = P_E$ (change in Kinetic energy neglected)

(3) $t_A{}^* = t - \dfrac{L_{AB}}{V_{wA}}$

(4) $t_D{}^* = t - \dfrac{L_{ED}}{V_{wD}}$

(5) $t_c{}^* = t - \dfrac{L_{Fc}}{V_{wc}}$

(6) $\dfrac{P_{B,t}}{\rho} + S_A \dfrac{\dot{w}_{B,t}}{\rho} = C_A{}^+ = \dfrac{P_{A,tA^*}}{\rho} + S_A \dfrac{\dot{w}_{A,tA^*}}{\rho}$

(7) $\dfrac{P_{B,t}}{\rho} - S_D \dfrac{\dot{w}_{B,t}}{\rho} = C_D{}^- = \dfrac{P_{D,tD^*}}{\rho} - S_D \dfrac{\dot{w}_{D,tD^*}}{\rho}$

(8) $\dfrac{P_{B,t}}{\rho} - S_c \dfrac{\dot{w}_{F,t}}{\rho} = C_c{}^- = \dfrac{P_{c,tc^*}}{\rho} - S_c \dfrac{\dot{w}_{c,tc^*}}{\rho}$

Solving (1), (6), (7) and (8) simultaneously

(9) $$P_{B,t} = \rho \left\{ \frac{\dfrac{C_A{}^+}{SA} + \dfrac{C_D{}^-}{SD} + \dfrac{C_c{}^-}{Sc}}{\dfrac{1}{SA} + \dfrac{1}{SD} + \dfrac{1}{Sc}} \right\}$$

then,

(10) $\dot{w}_{B,t} = \dfrac{C_A{}^+ - P_{B,t}/\rho}{SA/\rho}$ (from eq (6))

(11) $\dot{w}_{E,t} = (\frac{P_{B,t}}{\rho} - \bar{C_D}) \frac{\rho}{S_D}$ (from eq (7))

(12) $\dot{w}_{F,t} = \dot{w}_{B,t} = \dot{w}_{E,t}$ (from eq (7))

Note: The equations as presented are in the form used in the computer. This was determined to be convenient form. It is recognized that some of the equations could be simplified by algebraic manipulations.

Also Note: The units of pressure (P) in these equations are lb/ft^2. In the program the units are $lb/in.^2$.

therefore

$$P_{(eq'ns)} = P_{(program)} \times 144 \frac{in.^2}{ft^2}$$

D. CONTROL VALVE, SR NO. 8

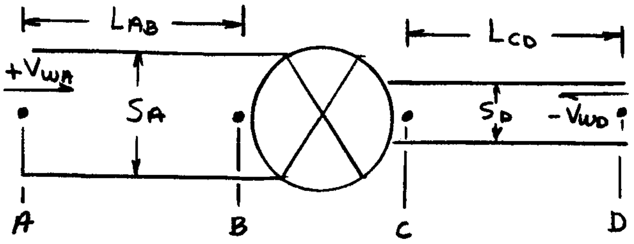

a. Equations

(1) $\dot{w}_B = \mathring{w}_c$

(2) $\mathring{w}_{B,t} = K_w \sqrt{(P_{B,t} - P_{c,t}) \frac{\rho}{62.4}}$

(3) $K_w = K_w'(t)$, (K_w is a known function of time)

(4) $R = \frac{62.4}{K_w^2}$

(5) $\dot{w}_{B,t}^2 = \frac{\rho}{R} (P_{B,t} - P_{c,t})$

(6) $t_A^* = t - \frac{L_{AB}}{V_{WA}}$

(7) $t_D^* = t - \frac{L_{CD}}{V_{WD}}$

(8) - (12) These equations are the same as those listed in, SR #2, (b)(ii). Equations with friction, Equations (6), (7), (8), (9), and (10).

E. WATER-HAMMER PUMP, SR NO. 11

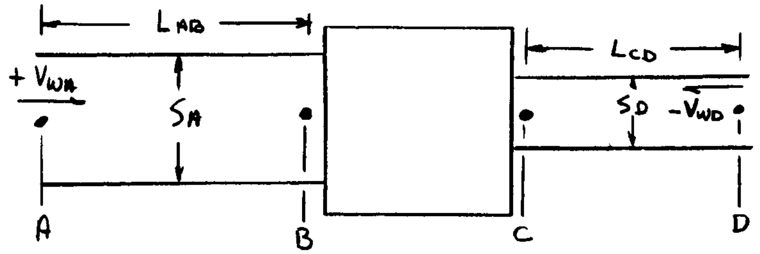

a. Known Conditions

(1) $N_1 = N(t)$ (known pump speed or speeds)

(2) $T_o = K$ (constant inlet temperature)

(3) $\dot{w}_B = \dot{w}_c \geq 0$

b. Equations

(1) $\dot{w}_P = \dot{w}_B = \dot{w}_c$, $P_{B,t} = P_S$, $P_{c,t} = P_d$

(2) $$t_A^* = t - \frac{L_{AB}}{V_{wA}}$$

(3) $$t_D^* = t - \frac{L_{CD}}{V_{wD}}$$

(4) $$\frac{P_S}{\rho} + S_A \frac{\dot{w}_P}{\rho} = C_A + = \frac{P_{A,tA^*}}{\rho} + S_A \frac{\dot{w}_{A,tA^*}}{\rho}$$

(5) Call NASA-TP

$$P_d = P_s + f(\dot{w}_{P,t}, N_1, N_2, T_o, \ldots\ldots)$$

The head rise in the pump can be calculated as a function of $\dot{w}_{P,t}$, with known value of speed, temperature, etc.

(6) $$\frac{P_d}{\rho} - S_D \frac{\dot{w}_P}{\rho} = C_D^- = \frac{P_{D,tD*}}{\rho} - S_D \frac{\dot{w}_{D,tD*}}{\rho}$$

Equations (4), (5), and (6) can be solved simultaneously for P_S, P_d, $\dot{w}_P$ by internal iteration as follows.

i) Assume $\dot{w}_P$

ii) From equation (4) calculate P_S

iii) Call NASA-TP Subroutine, and calculate P_d

iv) Using calculated value of P_d, calculate $\dot{w}_P$ from Equation (6)

$$\dot{w}_P = \frac{\rho}{S_D}\left(\frac{P_d}{\rho} - C_D^-\right)$$

v) Compare calculated value of $\dot{w}_P$ with assumed value until

$$\dot{w}_P - \dot{w}_{P(\text{assumed})} \leq \varepsilon$$

vi) Call Iteration 2, the convergence subroutine and iterate until the allowable error (ε) is less than or equal to

$$\varepsilon = \text{Max}\left(|\varepsilon|, \frac{\%\ \varepsilon}{100} \times \dot{w}_P\right)$$

F. OUTLET SR NO. 12

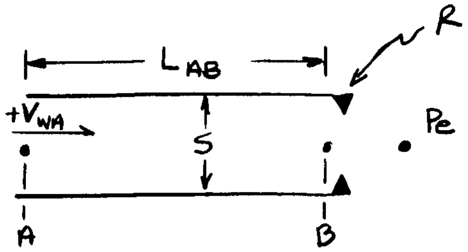

1. Boundary Conditions

(1) $P_e = P_a$ (known exit or atmospheric pressure)

(2) Known hydraulic resistance, R (friction or orifice)

2. Equations

a. Without Friction

(1) $t^* = t - \frac{L_{AB}}{V_{wA}}$

(2) $\frac{P_{B,t}}{\rho} + S_A \frac{\dot{w}_{B,t}}{\rho} = C_A + = \frac{P_{A,t^*}}{\rho} + S_A \frac{\dot{w}_{A,t^*}}{\rho}$

(3) $P_{B,t} = \text{MAX}\ (P_V, P_a)$ (P_V = vapor pressure)

(4) $\dot{w}_{B,t} = \frac{\rho}{S_A} (C_A{}^* - \frac{P_{B,t}}{\rho})$

b. With Friction

(1) and (2) are the same

(3) $P_{B,t} = \text{MAX}(P_e, P_V) + \frac{(\dot{w}_{B,t})^2}{\rho}\ R$

(4) $|\dot{w}_{B,t}| = \frac{\rho S_A}{2R} \left\{ -1 + \sqrt{1 + \frac{4R}{S_A{}^2}\ \left|C_A + - \frac{P_e}{\rho}\right|} \right.$

(5) $$\mathrm{SIGN} = \mathrm{SIGN}\left\{(C_A - \frac{P_e}{\rho})\right\}$$

(6) $$\dot{w}_{B,t} = \mathrm{SIGN}\,|\dot{w}_{B,t}|$$

(7) $$P_{B,t} = \rho(C_A - S_H \frac{\dot{w}_{B,t}}{\rho})$$

NOTE: All points are tested in the program for vapor pressure

$$\mathrm{TEST}\ (P_{i,t} \geq P_v)$$

If the pressure is less than P_V, it is set equal to P_V

$$P_{i,t} = \mathrm{MAX}\ (P_{i,t},\ P_V)$$

and all equations using it are re-evaluated.

APPENDIX E

SYSTEM MODELS

APPENDIX E

CLOSED LOOP SCHEMATIC

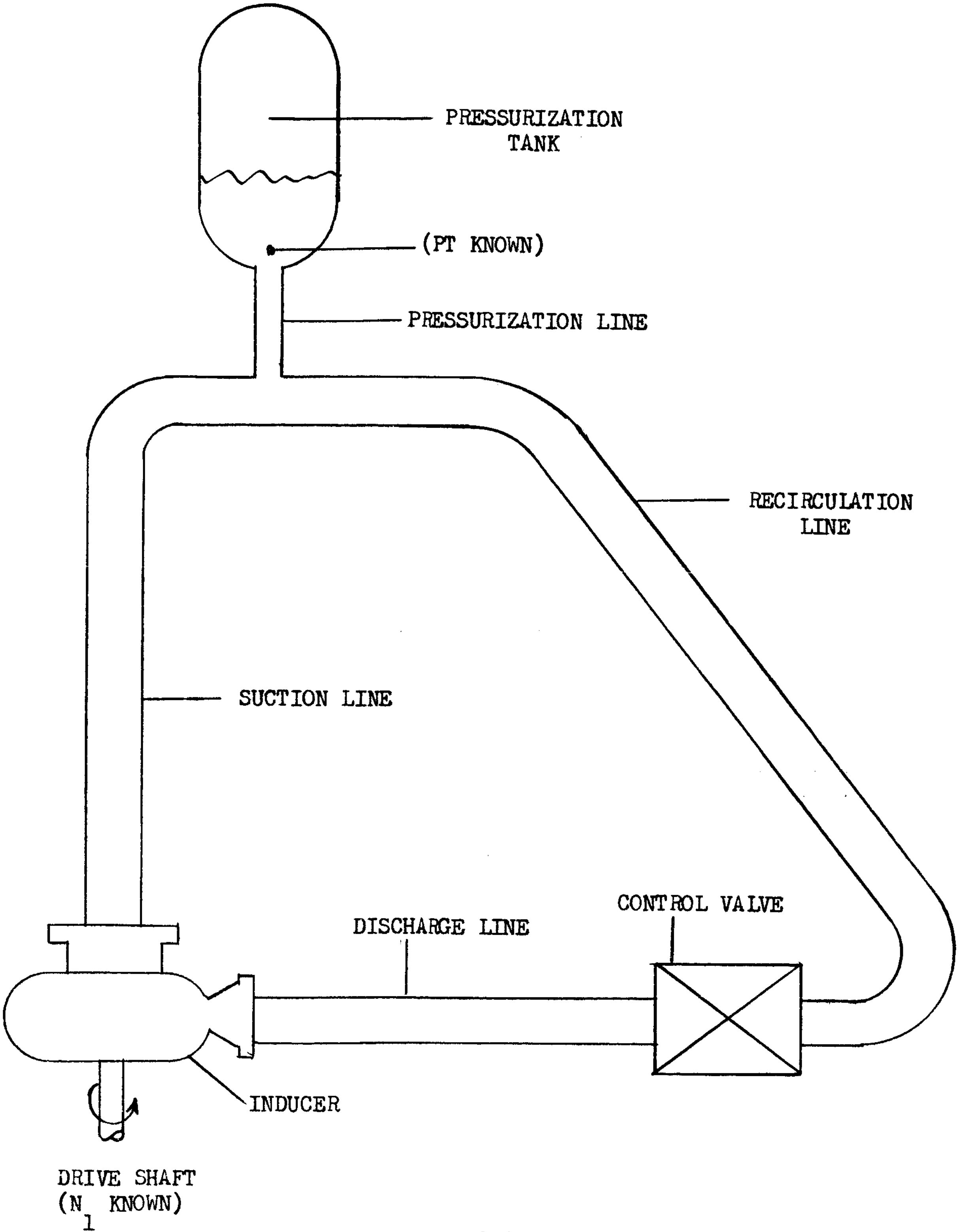

Appendix E

OPEN LOOP SCHEMATIC

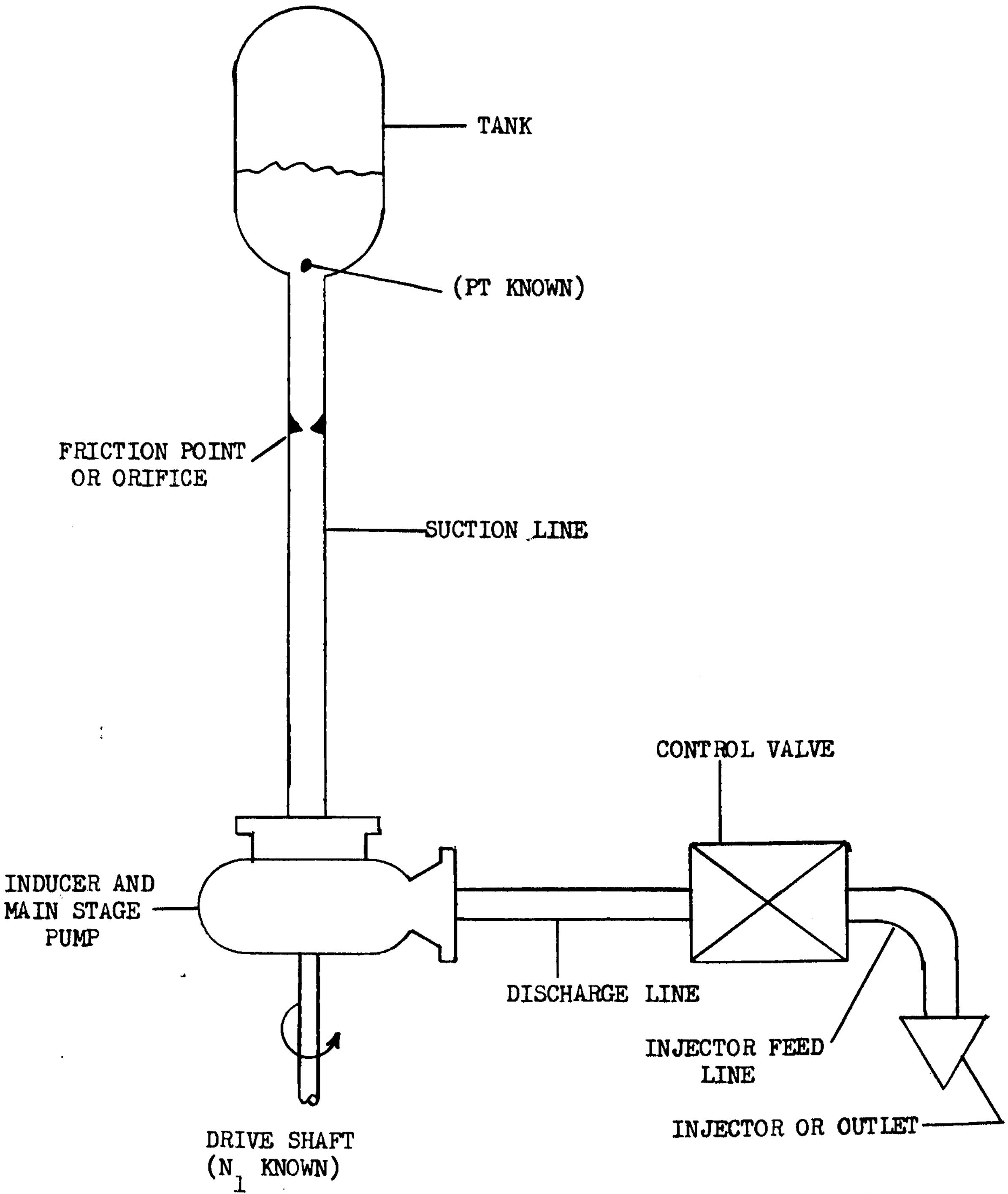

(Pa KNOWN)